Analytical forward models for magnetic induction of asymmetric, icy ocean worlds with implications for spacecraft investigations

Marshall J. Styczinski

A dissertation
submitted in partial fulfillment of the
requirements for the degree of

Doctor of Philosophy

University of Washington

2021

Reading Committee:

Erika M. Harnett, Chair

Steven D. Vance

David B. Pengra

Miguel F. Morales

Program Authorized to Offer Degree:
Physics

University of Washington

Abstract

Analytical forward models for magnetic induction of asymmetric, icy ocean worlds with implications for spacecraft investigations

Marshall J. Styczinski

Chair of the Supervisory Committee:
Affiliate Associate Professor Erika M. Harnett
Earth and Space Sciences

Oscillating magnetic fields are screened within electrically conducting materials by induced currents, which generate secondary, induced magnetic fields. Induced fields are measurable outside the conducting body, and adopt a strength and spatial structure dependent on both the excitation field and the conductivity structure of the body. This dependence has been exploited to sound the interior and ionospheric structure of Earth and the Galilean moons of Jupiter, providing the strongest evidence yet for the presence of Europa's subsurface ocean. Forward models of magnetic induction are essential to magnetic investigations by *Europa Clipper* and *JUICE,* two missions in development that intend to characterize the oceans of Europa and Ganymede, respectively. These forward models will also be vital elements of future missions to explore the moons of the ice giants. Until the present work, all ocean induction models have adopted simplified structure for the conductivity, with a single, spherically symmetric, uniformly conducting layer for the ocean and sometimes additional layers for the ionosphere, mantle, and/or core. Such an approach neglects the altitude-dependent density of charge carriers in the ionosphere and depth-dependent pressure and temperature within the ocean, all of which contribute to radial dependence of conductivity. Also neglected are the effects of layer asymmetry on the induced magnetic fields, which result in modifications to the magnetic moments that can bias the inversion of measurements necessary to constrain interior structure.

This dissertation details recent advances in magnetic induction forward models and their application to magnetic sounding of icy moons. The impacts of depth-dependent conductivity structure within ocean layers are examined in application to Europa, Ganymede, and Callisto, informed by self-consistent geophysical models generated with the open source framework *PlanetProfile*. Analytical forward models for asymmetric conducting layers are derived and applied to Europa, Callisto, the uranian moon Miranda, and the neptunian moon Triton based on descriptions of possible asymmetry found in the literature. Implications for magnetic investigations by future spacecraft missions are discussed. The products of the present work permit investigation of realistic depth-dependence and asymmetry within ocean worlds for the first time. Open source software is provided to facilitate application of the presented models.

TABLE OF CONTENTS

LIST OF FIGURES

Figure Number Page

ACKNOWLEDGMENTS

Thank you to Elena Amador-French for sharing your story during your Final Exam. If I had not heard your words that fateful day, this project would never have begun. Thank you to Matt Tilley for encouraging me to ask Erika for advice and for being a great companion during that transition. Thank you to Erika Harnett for offering me consistently valuable advice from day 1, and for taking a big gamble on agreeing to work with me. And thank you to Aziz Khan for seeing me through it all. The character of support you've offered me through several major trials has been surprising and touching and so, so welcome. I can never thank you enough for the frequent experience of your amazing company.

Carol Paty and Steve Vance have been amazing mentors regarding a great many things, but participating in mission science most of all. Thank you both very much for the time and energy you have invested in me and my career. I also wish to thank the UW Astrobiology Program for the excellent educational experiences they have crafted and the wonderful community they support. I would have traveled on a very different track if not for discovering this program.

This work was supported by NASA Headquarters under the NASA Earth and Space Science Fellowship Program — Grant 80NSSC18K1236. Portions of this work were funded by Washington NASA Space Grant Consortium, NASA Grant #NNX15AJ98H.

DEDICATION

For Aziz.

You taught me how to understand myself.

You showed me what it's like to feel my science passions to their fullest.

You walked with me down many a dark street.

You were there when I needed it most. Again and again.

I am forever indebted to you for sharing your time, your wisdom, and your enthusiasm with me so freely.

This project is for you. I would never have made it here if not for you.

Chapter 1

INTRODUCTION

All life on Earth requires liquid water to survive, to grow, and to reproduce (Rothschild and Mancinelli, 2001). In the search for life beyond Earth, "following the water" is useful as a guiding principle (Hubbard et al., 2002), but water is not the only necessary ingredient for an environment to be considered habitable (Jones and Lineweaver, 2010). In brief, the elements C, H, N, O, P, and S are also known to be required (to construct DNA and proteins, Hoehler et al., 2020), as well as a source of energy to drive microbial metabolism and an environment conducive to survival (*i.e.* between extremes of temperature, pressure, *etc.*). The large icy moons in our solar system are exciting targets for study because they may host all of these requirements in concert in protected environments, beneath their icy shells (Domagal-Goldman et al., 2016). All of the giant planets host at least one icy moon.

1.1 The astrobiological interest of icy moons

These moons have evolved over their lifetimes. Heating from various sources such as impacts and gravitational contraction, tidal forcing, and radioactive decay has led them all to at least partially differentiate (Barr and Canup, 2008), with denser materials sinking and the less dense water and ice resting on top. The icy moons of the giant planets are likely composed of a combination of chondritic material, which has a significant iron component, and cometary material, which is mostly made up of more volatile compounds (including water) that condense far from the Sun (Néri et al., 2020). The geologic and chemical history of possible oceans within these moons dictates the present-day composition of dissolved compounds within their waters, and hence their potential habitability. In particular, the chemical state and concentration of dissolved salts such as

NaCl and $MgSO_4$—which each result from water–rock reactions under differing conditions (Hand and Chyba, 2007; Vance et al., 2018)—determines the fluid's electrical conductivity along with its physical state (temperature and pressure). Critical to this work, the electrical conductivity of ocean fluids within the moons causes them to interact with the magnetic field of their parent planet.

The large moons of Jupiter—Io, Europa, Ganymede, and Callisto, known as the Galilean moons after their discoverer—are among the most accessible bodies in our solar system for the exploration of potentially habitable environments. A preponderance of water ice on the surfaces of Europa, Ganymede, and Callisto (Showman and Malhotra, 1999) and their likely chondritic–cometary compositions (Néri et al., 2020) suggest they may contain all the ingredients needed to support habitable environments even today. Gravitational interactions between the moons and with their parent planet combine to support active heating by tidal dissipation, warming the bodies by straining their ice shells and their mantles of silicate rock (Showman and Malhotra, 1997; Tobie et al., 2005). These features couple with Jupiter's relative proximity to Earth (among the giant planets) to make the Jupiter system a prime target for astrobiology-focused missions.

The Uranus system offers important contrasts to other planetary systems that can help understand how these systems evolve. Uranus has five large moons: Miranda, Ariel, Umbriel, Titania, and Oberon. These moons orbit near the uranian equator, marking them as likely natural satellites that formed from the same disk of material as the planet. They appear to have engaged in orbital resonances that placed them in their current orbital arrangement (Ćuk et al., 2020). The closest analogue for the moons of Uranus appears to be Saturn's mid-sized moons, which have undergone orbital migration that created mutual tidal heating (Neveu and Rhoden, 2019). From recent discoveries there, and at distant Pluto (Nimmo et al., 2016), the prospect for oceans in some uranian moons seems plausible even at their great distance from the Sun ($\sim$ 19 AU), but we do not yet have any direct evidence for extant oceans there. Possible evidence for relict tidal heating can be seen in Miranda's 1 Gyr-old coronae features (Plescia, 1988; Beddingfield and Cartwright, 2020).

Although models assuming simple compositions of silicates and water predict an ocean in Miranda would have frozen out by the present era (Hussmann et al., 2006), the presence of volatile clathrates or other insulating materials could support the persistent presence of fluids by providing

thermal insulation and adding rigidity to the ice, both of which lower the Rayleigh number and thus inhibit solid-state convection (Croft, 1987; Castillo-Rogez et al., 2019; Kamata et al., 2019). In Saturn's moon Titan and the dwarf planets Ceres and Pluto, methane clathrates may impede solid state convection in ice, leading to inefficient cooling that slows the freeze-out of subsurface oceans. Similarly, the presence of ammonia on the surface of Ariel is indicative of recent geological activity and suggests a role for volatiles that might aid in retaining heat (Cartwright et al., 2020).

1.2 Magnetic sounding across the solar system

Extant oceans within the icy moons scattered across the solar system may be hidden from view, but they are not invisible to our instruments. All of the giant planets have strong intrinsic (internally generated) magnetic fields (Schubert and Soderlund, 2011), each likely driven by a dynamo in their interior (Stanley and Glatzmaier, 2010) akin to that within the Earth. These internally driven fields have magnetic moments that rotate with the planet. Each planet has a strong dipole moment. For all but Saturn, their dipole moments are directed $\sim$10° or more away from their rotation axes. The strong, rapidly rotating, tilted magnetic moments subject the icy moons of each planet to a rapidly time-varying magnetic field that interacts with their electrically conducting ocean fluids.

The oscillating magnetic fields induce electric currents within the conductive materials that act to screen the interior from these oscillations. These induced electric currents are known as eddy currents. Greater electrical conductivities support greater eddy currents, thereby more rapidly screening the magnetic oscillations with depth. The eddy currents give rise to their own secondary, induced magnetic field that can be measured outside the material. With knowledge of the applied oscillating field, known as the excitation field, measurements of the net field (excitation + induced) can be used to infer the conductivity structure within which the eddy currents flow. This is the central principle behind *magnetic sounding,* upon which this work is based.

1.2.1 Magnetic sounding of the Earth

Daily variations in the magnetic field of the Earth have long been exploited to study the conductivity structure of its interior (*e.g.* Schuster, 1889). Magnetic measurements distributed over a very wide range of latitudes, longitudes, and altitudes, and extending over great lengths of time, have supported detailed analyses constraining the electrical properties of the core, mantle, crust, ionosphere, and even oceanic flows (Wait, 1972; Constable and Constable, 2004a; Kuvshinov, 2008). Eddy currents will be induced within electrically conducting layers by any magnetic oscillation with sufficient strength and a short enough period of oscillation. This phenomenon has proven valuable for petroleum prospecting with *active* magnetic sounding (*e.g.* Constable and Srnka, 2007), where a strong oscillation is generated and the response from buried conducting layers is measured. Active magnetic sounding has not yet been applied to other planetary bodies due to prohibitive power and mass requirements.

Passive magnetic sounding instead relies on excitation by natural magnetic oscillations. The study of induced fields of the Earth through passive magnetic sounding is often termed *magnetotellurics.* The field of magnetotellurics has been revolutionized by modern computational techniques (see *e.g.* Fainberg and Zinger, 1980; Zhang and Schultz, 1992; Velímský and Martinec, 2005; Weiss, 2010). Common in such studies are numerical simulations that solve the governing differential equations, which stem from Maxwell's laws combined with Ohm's law, over a grid of nodes that may be related to points in space. Such simulations are computationally expensive to run and rely on the great wealth of data available from across the globe (and beyond) and extensive field campaigns. These data can be used to hone and refine a model, testing its accuracy against accepted benchmarks (Egbert and Kelbert, 2012). However, magnetic data from other planetary bodies is more limited. A lack of seismic data from the icy moons hampers our understanding of their interiors. Therefore, it is most advantageous for magnetic sounding investigations regarding icy moons to consider a wide range of possibilities against which to compare measurements. This large-parameter-space approach renders numerical simulations for the purpose of matching the measured induced field to the interior structure potentially very time-consuming. Fortunately,

electromagnetic theory and mathematical methods for solving differential equations enjoy a long heritage and fast, approximate solutions are available that may be applied to sound other bodies (Section 1.3).

1.2.2 Considerations for magnetic sounding of icy moons

The primary factors that influence the viability of magnetic sounding investigations of icy moons are:

- The strengths and periods of the magnetic oscillations applied by the parent planet
- The character of the surrounding plasma and ionospheric environment
- Wide coverage of spacecraft measurements over varying planet/moon orbital configurations (*i.e.* true anomaly and parent planet longitude)

Stronger magnetic oscillations, and with shorter periods drive stronger responses from a given conducting body. The plasma environment within which a moon is immersed contributes its own magnetic signals that make the global induced field more difficult to distinguish in the analysis of magnetic measurements. Of more practical concern, magnetic sounding on a global scale is most effective when the spacecraft encounters the body under a variety of magnetic and plasma conditions. This ensures that the induced magnetic field is distinguishable from any intrinsic field that may be present (Kivelson et al., 2002; Schilling et al., 2004).

Europa and Callisto are both ideal candidates for magnetic sounding. Jupiter's magnetic field is the strongest of any planet in the solar system (Schubert and Soderlund, 2011). It has a dipole moment tilted about 9.6° away from its spin axis and has a sidereal period of about 10 hr. The combination of these features means that strong magnetic oscillations are applied to all of the Galilean moons, though Ganymede's intrinsic field presents separate challenges. The great strength of Jupiter's magnetic field also causes it to trap large amounts of plasma sourced from volcanic eruptions on Io that become ionized (Bagenal and Dols, 2020). The resulting current sheet and

"Io plasma torus" extend out to Europa, creating dynamic plasma conditions that impact the interpretation of magnetic measurements there. In spite of the challenging plasma conditions, magnetic sounding has provided strong evidence of the presence of an ocean at Europa (Section 1.3; Kivelson et al., 2000). Callisto experiences milder upstream plasma conditions than Europa, but is expected to harbor a substantial, asymmetric ionosphere (Hartkorn et al., 2017; Hartkorn and Saur, 2017) that has prevented a conclusive assessment of whether it too contains an ocean (Liuzzo et al., 2016, 2017). The upcoming *JUICE* mission[1] plans several flybys of Callisto en route to its final orbit around Ganymede—the analysis of data obtained from these flybys is likely to be able to settle the matter (Liuzzo et al., 2018).

Ganymede resides between Europa and Callisto in its orbit of Jupiter, and is also subject to strong magnetic oscillations from Jupiter. Indeed, some constraints on induced magnetic moments of Ganymede have been determined from analysis of data from the *Galileo* mission (Kivelson et al., 2002). However, Ganymede also has its own intrinsic magnetic field, which drastically changes the magnetic environment near the moon (Paty and Winglee, 2004; Payan et al., 2015). New features appear, such as a magnetopause and auroras (Feldman et al., 2000). In recent years, rocking of the auroras due to the oscillating induced field has been identified as a valuable line of evidence that supports magnetic sounding (Saur et al., 2015). Ganymede's strong intrinsic field and unique plasma environment render it a difficult target for magnetic sounding—converging lines of evidence will be critical for future characterization of its interior structure. A wealth of new measurements taken by the *JUICE* mission, not just of magnetic fields but by an array of instruments, will lead to a much better understanding of the moon and its nested magnetosphere.

Enceladus is a small moon of Saturn well-known for its active and ongoing plume eruptions (*e.g.* Hansen et al., 2011). This moon is expected to host a global subsurface ocean (Thomas et al., 2016) of substantial astrobiological interest (Waite et al., 2017; Ray et al., 2021). The dipole moment of Saturn is very nearly aligned with its axis of rotation (Schubert and Soderlund, 2011), which results in very small magnetic oscillations at Saturn's rotation period relative to Enceladus

[1] JUpiter ICy moons Explorer, in development by the European Space Agency.

(its *synodic* period). However, non-zero eccentricity and inclination in Enceladus's orbit contribute variations in distance from Saturn that will drive magnetic oscillations at the orbital period. Small additional magnetic oscillations may also be driven by libration (Rambaux et al., 2010; Van Hoolst et al., 2016). The ice shell of Enceladus exhibits pronounced asymmetry, with a thinner crust covering the south polar terrain near the plumes (Nimmo et al., 2011; Tajeddine et al., 2017; Hemingway and Mittal, 2019). Accounting for asymmetry in the ice shell is likely to pose additional challenges to magnetic sounding investigations, but the present work enables asymmetry effects to be modeled (Section 1.4).

Miranda and Ariel are excellent candidates for magnetic sounding. Uranus has a strongly tilted dipole moment (60°) and a comparably rapid rotation (17.3 hr, Ness et al., 1986), but also possesses quadrupole and octupole moments with a spectral power similar to the dipole moment (Herbert, 2009). These features create strong magnetic oscillations at a variety of periods, with an especially strong excitation at the synodic period (Cochrane et al., 2021). The magnetospheric plasma environment in the Uranus system is not nearly as intense as in the Jupiter system (Bridge et al., 1986), potentially enabling spacecraft investigations to undertake more sensitive analyses of magnetic data.

Umbriel, like Callisto (Hibbitts et al., 2002), hosts a substantial fraction of CO_2 ice on its surface (Grundy et al., 2006). The excitation field applied to Umbriel is also similar to Callisto (Zimmer et al., 2000; Arridge and Eggington, 2021; Cochrane et al., 2021). Unlike Uranus's outer moons Titania and Oberon, Umbriel orbits entirely interior to the Uranus magnetopause (Arridge et al., 2014), and at a greater distance than Miranda and Ariel. The substantial quadrupole and octupole moments in the uranian field of internal origin decay quickly with distance from the planet, resulting in a larger influence of magnetospheric structures with distance (Paty et al., 2020). Magnetospheric oscillations (*e.g.* magnetopause movement due to variations in solar wind conditions) are therefore likely to influence the excitation spectrum at Umbriel (Arridge and Eggington, 2021). Future modeling efforts will need to account for the full range of significant magnetic excitations at this moon.

Triton is a large moon of Neptune and likely a captured Kuiper belt object (Agnor and Hamilton, 2006). Like Uranus, Neptune has a strongly tilted dipole moment (47°) and rotates rapidly

(16.1 hr), applying strong magnetic oscillations to Triton (Connerney et al., 1991). Active cryovolcanism at Triton may support a plasma torus similar to that of Io (Belcher et al., 1989; Richardson et al., 1991), which could complicate magnetic sounding investigations. Triton also has an extended ionosphere (Tyler et al., 1989) that could mimic or mask induction signals from a subsurface ocean, especially if it contains substantial asymmetry (see Chapter 4.3.2). A combination of models involving magnetospheric plasma and detailed accounting of the internal field of Neptune is likely to play an important role in studying induction signals from this moon.

1.3 Past studies applying magnetic sounding to icy moons

The scarcity of measurements near icy moons encourages an approach that considers the conductivity structure in aggregate, on a global scale. Thermodynamics and self-gravity will tend to drive ocean layers within these bodies toward a near-spherical shape that is global in extent (Tobie et al., 2003). It is customary to assume that each layer (including the ocean) is perfectly spherical, as this simplifies the solution to the governing differential equations substantially. All studies of icy moons prior to this work have applied some variant of the recursive method developed by Srivastava (1966) for determining the induced magnetic field from a layered spherical conductor. Parkinson (1983, Ch. 5) presents a derivation of this method with updated and simplified notation that is often referenced in these studies. Unfortunately, the Parkinson derivation contains errors that have been repeated by high-profile publications (*i.e.* Zimmer et al., 2000; Hand and Chyba, 2007) and continue to propagate (Arridge and Eggington, 2021). Fortunately, these errors do not affect calculations of the final induced field or interpretation of measurements. In the present work, we carefully detail each step in our derivations so as to clarify the sources of the errors and their consequences.

Owing to the well-supported evidence of a global ocean there (*e.g.* Sarid et al., 2002; Schenk et al., 2020) and the extended *Galileo Europa Mission,* Europa has received the greatest share of attention among magnetic sounding investigations of icy moons. Europa has long been thought to have an extant subsurface ocean (Ross and Schubert, 1987). Early results from the *Galileo* mission supported this theory (Carr et al., 1998; Pappalardo et al., 1999) with gravity and geomorphological evidence. Several flybys near Europa provided strong evidence of a local magnetic field from the

moon (Kivelson et al., 1997; Khurana et al., 1998; Kivelson et al., 1999), but it was not until the E26 flyby, *Galileo's* last pass near Europa, that the observed magnetic moments were confirmed to be time-varying, and therefore most likely due to an ocean (Kivelson et al., 2000; Zimmer et al., 2000). Small constraints have subsequently been placed on the intrinsic moments of Europa (Schilling et al., 2004), suggesting that perhaps all of the magnetic moments measured near the moon are due to induction by the ocean.

Later studies by Schilling et al. (2007) and Hand and Chyba (2007) each took different approaches toward studying the same goal: characterization of Europa's interior using the *Galileo* data. Schilling et al. used magnetohydrodynamic (MHD) simulations to model the flow of jovian plasma past the moon at 8 points in time, equally distributed throughout the synodic period, and compared the results against the *Galileo* measurements from near flybys. They used the MHD simulations as a perturbation atop the induced field predicted by the Srivastava (1966) layer method for several candidate interior models with varying ocean conductivity and a fixed ice shell thickness of 25 km. Ultimately, these authors concluded that Europa's total ocean conductance must be greater than 50 kS for their model to agree with the *Galileo* data. Hand and Chyba opted instead to consider laboratory measurements of the conductivity of possible ocean fluids and attempted to constrain the salinity of Europa's ocean, for a range of induction responses guided by the results of Zimmer et al. (2000) and Schilling et al. (2004). These authors considered a variety of layer models to represent the interior, including influence of a possible iron core, but assigned a fixed conductivity for the ocean for each model based on laboratory studies performed at ambient pressure with temperatures of 0 or 25 °C (which they all scaled to 0 °C). They found that the combination of salinities and ice shell thicknesses necessary to match the results of Schilling et al. (2004) were unrealistic, requiring dissolved salts near the saturation limit and ice shells thinner than suggested by non-magnetic constraints (*e.g.* Billings and Kattenhorn, 2005).

The Galilean moons have been studied together by Seufert et al. (2011), who examined the induced magnetic fields that result from each moon for various interior layer models and at a variety of periods in the spectrum of magnetic oscillations Jupiter applies to the moons. These authors were chiefly concerned with the impacts on the induced field of (1) a possible conducting core and (2)

the assumed conductivities for ice and mantle layers. Seufert et al. contributed the first analysis making a rigorous determination of the phase delay predicted from their selected interior models. All prior work had inferred from the conclusion of Zimmer et al. (2000), who found "no evidence" for a non-zero phase delay, that a zero phase delay may be supposed. As shown throughout the work of Seufert et al. (2011), all finite ocean conductivities will result in a non-zero phase delay.

Possible induced magnetic moments have been identified for Ganymede by the analysis of Kivelson et al. (2002), but these authors note that quadrupole-and-higher intrinsic moments may account equally well for the signal they attribute to induction. The intrinsic field of Ganymede has discouraged magnetic sounding investigations to some degree, while inspiring numerous studies of plasma interactions with its embedded magnetosphere (*e.g.* Paty and Winglee, 2004; Jia et al., 2009; Payan et al., 2015; Poppe et al., 2018; Carnielli et al., 2019). Blending the two topics, Duling et al. (2014) created an MHD model with what they termed the *insulating boundary method,* for which they developed a new process for modeling insulating surfaces (such as the planetary surface) in plasma simulations. These authors supposed a single value for each of the ocean depth, layer thickness, and conductivity in Ganymede; their primary focus was to demonstrate the viability of their model for combining forward-model predictions of the induced field using the Srivastava (1966) layer method with plasma simulations that self-consistently use the same conducting layers to model diffusion of the global magnetic fields. UV observations of Ganymede's auroras using the *Hubble Space Telescope* have also been used to study the interior of this intriguing moon. Saur et al. (2015) recorded numerous images of the auroras to track their position as they rock back and forth in response to changing magnetic conditions applied by Jupiter. They found that statistical predictions for the variation in the location of the auroral ovals better matched the observations when a subsurface ocean was included in the model—the induction response from the ocean reduces the movement of the ovals. Saur et al. concluded that Ganymede likely has a subsurface ocean no deeper than 330 km and an intrinsic field that has nearly nonexistent quadrupole moments. Their results favor an interpretation of the possible induced moments identified by Kivelson et al. (2002) as resulting from the presence of an ocean and not from the intrinsic field.

Callisto has an ancient, heavily cratered surface that shows little indication of geological activity

(McKinnon, 2006). Gravity measurements used to infer a high moment of inertia (axial moment $C/MR^2 = 0.3549 \pm 0.0042$) suggest that it may not be fully differentiated (Anderson et al., 2001). Even with these considerations, Callisto has become an important target for study in astrobiology (Vance et al., 2018). Magnetic measurements were first used to identify a putative ocean within Callisto early in the *Galileo* mission (Khurana et al., 1998; Zimmer et al., 2000). However, subsequent analyses determined that the case for an ocean in Callisto is not clear, as the moon supports a substantial ionosphere that may account for part or all of the observed induced field (Liuzzo et al., 2016, 2017). Indeed, Callisto's ionosphere likely hosts a day–night dichotomy (Hartkorn et al., 2017) as solar EUV photons are thought to be the dominant source of ionization of ionospheric plasma there. Determining whether Callisto has an ocean will likely require measurements by future missions, and interpreting those measurements will require a careful accounting of ionospheric structure, including its asymmetry.

Recently, gathering attention has been focused on the moons of Uranus (Arridge and Eggington, 2021; Cochrane et al., 2021). The *Uranus Orbiter and Probe* mission concept was rated as one of the highest priorities for a NASA Flagship mission in the 2013–2022 Planetary Science Decadal Survey (National Research Council, 2011). The Decadal Survey included among its goals to "assess tidal evolution within giant-planet systems"—including moons of Uranus—and highlighted questions of how the thermal and orbital evolution of the satellites relates to their interior structures, and what drives the endogenic activity on Ariel and Miranda. Subsequent mission concepts (*e.g.* Hofstadter et al., 2019) have included magnetic field investigations intended for magnetic sounding of subsurface oceans. Recent work by Weiss et al. (2020), Arridge and Eggington (2021), and Cochrane et al. (2021) has shown a rich spectrum of excitations applied to each of the moons by the exotic field of Uranus. The studies by Arridge and Eggington (2021) and Cochrane et al. (2021) each considered a range of possible configurations for extant oceans and the induction signals they would create, and each supported the conclusion that a future spacecraft mission to this system may be able to distinguish between models from magnetic measurements alone. Of course, measurements near the moons are required, of which we have none. Future missions touring the Uranus system will likely also contribute additional observations that will help to constrain interior models

and better inform magnetic sounding investigations.

1.4 Advancing models of planetary interiors

In the present work, we compile our recent studies improving on past models of global magnetic induction. We endeavor to create a single, cross-disciplinary model capable of predicting the induced magnetic field of an icy moon while simultaneously incorporating as many constraints as possible. In this way, we support future magnetic sounding investigations that are informed by diverse *in situ* instrumentation and remote observations, such that they may be able to place the most rigorous constraints on the characterization of subsurface oceans.

Each of Chapters 2–4 consists of a published or submitted manuscript, presented in the order in which the work was completed. These chapters have seen minimal edits from the content of the individual manuscripts. However, several apparent errors in Chapter 2 have been identified; these have been marked with footnotes referring to the updated derivation in Chapter 4. Similar mathematical derivations appear in each of these chapters; some portions are necessarily repeated as the process has been honed and refined over years of research. Due to changing notation between the chapters, we recommend the reader refer to Chapter 4.6 for the most complete, general derivation of the induced magnetic field from an asymmetric, layered conductor. The forms applied in Chapters 2 and 3 may be viewed as special cases of the more general solution from Chapter 4.

1.4.1 Self-consistent geophysics in conductivity models

Magnetic sounding investigations of icy moons prior to this work have all assigned a uniform conductivity throughout the ocean layer. Convection currents within the ocean are expected to maintain a uniform composition (salinity) throughout, with the possible exception of a buoyant, low-salinity layer at the melting temperature just under the ice shell (Melosh et al., 2004). Even with a uniform salinity in the ocean, the electrical conductivity will not be uniform, as this important property is dependent on temperature and pressure, as well as composition (*e.g.* Horne and Frysinger, 1963; Larionov and Kryukov, 1984; Pawlowicz, 2012). We have therefore adopted the *PlanetPro-*

file framework[2] to connect geophysical models of icy moon interiors to rigorously supported values of electrical conductivity based on laboratory measurements of fluids under pressure (Vance et al., 2018). *PlanetProfile* incorporates spacecraft measurements of a body's surface temperature, moment of inertia, mass, and radius with an assumed, uniform ocean composition and an assumed ice–ocean interface temperature to calculate radial profiles of relevant geophysical quantities self-consistently, including electrical conductivity. The body is divided radially into a series of many layers, and measured quantities are propagated downward from the surface.

The primary consequences of our multi-layered-ocean approach are (1) slightly longer runtimes for computer programs, which are generally still negligible for modern systems and (2) a shift in forward modeling from treating conductivity, ice thickness, and ocean thickness as independent variables to instead treating solute composition and temperature at the ice–ocean interface as independent variables. In Chapter 3, we detail our application of this method. We ultimately conclude that, for the Galilean moons, our multi-layered approach with *PlanetProfile* predicts significant differences (on the order of nT) as compared to an analogous, single ocean layer with a uniform conductivity. We also find that a choice of uniform conductivity equivalent to the value at the ice–ocean interface yields a greater difference from the multi-layered approach than choosing a conductivity matching the radial average value. Among these, only the multi-layer approach forms a self-consistent interior model. Our model is available as open-source software (see Chapter 3).

The definition of Seawater

The properties of Earth seawater under varying physical conditions have been the subject of a considerable amount of research, in service of a better understanding of our own planet. The availability of information regarding Earth seawater and its dominance on this inhabited world have led many researchers to suppose this composition for the oceans of other worlds for comparison purposes. Earth seawater contains more than simply 3.5 wt% NaCl dissolved in water. For clarity, in this work we define Seawater (with a capital 'S') to mean Standard Seawater as defined by Millero et al.

[2] https://github.com/vancesteven/PlanetProfile

(2008). Further, the definition of salinity in an oceanographic context is notoriously contentious (*e.g.* Ponte et al., 2021). Throughout this work, we interpret salinity to be a simple ratio of mass of the solute to the mass of solution in a fixed volume; we report values in wt% or as a fraction of Standard Seawater.

1.4.2 Asymmetry in conductivity models

Real ocean worlds are not perfectly symmetric. This work fills an important gap in the literature: Until now, to determine the induced magnetic field from an ocean that is not perfectly spherical required numerical simulations. Such simulations are time-consuming and computationally expensive, and so impractical for a parameter-space exploration. With scarce data along limited trajectories, magnetic sounding of icy moons relies on forward models from a wide parameter space against which to compare. These factors have entirely prevented any consideration of the effects of asymmetric conducting layers on magnetic sounding investigations. As gravity and thermodynamic asymmetries are fully the expected case (*e.g.* Tobie et al., 2003), this is a worrying omission. Therefore, we embarked on a quest to find an analytic solution, such that may be evaluated expediently for a wide variety of considered cases, to the magnetic induction problem for an asymmetric ocean world.

We first found such a solution under the extreme limit of high conductivity in the ocean, which we cover in Chapter 2. This limit was applied in some early studies of *Galileo* data for Europa (*e.g.* Kivelson et al., 2000). We later succeeded in deriving the analytical solution we sought: The predicted magnetic moments resulting from a given excitation field for a layered conductor, where each boundary takes an arbitrary, near-spherical shape and each layer has an arbitrary, finite conductivity. The derivation and its application to examples of expected asymmetry within Europa, Miranda, Callisto, and Triton are presented in Chapter 4. Software to run our model is available as a Zenodo archive: `https://zenodo.org/record/5002956`.

Together, the theoretical developments described in this work, and the tools we supply for their application, support improved integration between non-magnetic constraints and magnetic sounding investigations. Eventual new measurements will only increase the importance of this integra-

tion. Future work is now poised to take advantage of the rich literature on these exciting bodies and determine What Lies Below with greater fidelity than ever before.

Chapter 2

MAGNETIC INDUCTION FROM ASYMMETRIC OCEANS IN THE HIGH-CONDUCTIVITY LIMIT

This chapter consists of a peer-reviewed publication in the planetary science journal *Icarus*. The original version is available open-access with the publisher at https://doi.org/10.1016/j.icarus.2020.114020. The main text and figures are reproduced here in their entirety with changes mainly to the formatting; several footnotes have been added where the methods and results of this chapter have been corrected by the more rigorous derivation in Chapter 4. Cited references appear in the Bibliography at the end of this dissertation. Computer programs contained in the Supplemental Material are available from the publisher along with the main text at the link above.

Reference

"Induced magnetic moments from a nearly spherical ocean." M. J. Styczinski and E. M. Harnett, 2021. *Icarus* **354**, pp. 114020, copyright ©2021 the Authors.

Induced magnetic moments from a nearly spherical ocean

M. J. Styczinski[1,2] and E. M. Harnett[2,3]

[1] Department of Physics, University of Washington

[2] UW Astrobiology Program, University of Washington

[3] Department of Earth and Space Sciences, University of Washington

Abstract

The five largest planets all have strong intrinsic magnetic fields that interact with their satellites, many of which contain electrically conducting materials on global scales. Conducting bodies exposed to time-varying magnetic fields induce secondary magnetic fields from movement of eddy currents. In the case of spherically symmetric conducting bodies, matching magnetic solutions at the boundary results in relatively simple relations between the excitation field and the induced field. In this work, we determine the more complicated induced magnetic field from a near-spherical conductor, where the outer boundary is expanded in spherical harmonics. Under the approximations that the excitation field is uniform at a single frequency, the product of wavenumber and radius for the body is large, and the average radius of the body is large compared to the perturbation from spherical symmetry, we find that each spherical harmonic in the shape expansion induces discrete magnetic moments that are independent from the other harmonics in the expansion. That is, simple superposition applies to the magnetic moments induced by each perturbation harmonic. We present a table of the magnetic moments induced by each spherical harmonic up to degree 2 in the perturbed shape. We also present a simple formula by which the induced magnetic field may be evaluated for any arbitrary shape described by expanding the radius of the conducting body in spherical harmonics. Unlike the Earth, many moons in the solar system are tidally locked to their parent bodies, and many also contain saline, subsurface oceans. Conductive material in these moons is therefore expected to be non-spherical. Accounting for the boundary shape of Europa's ocean will be critical for interpretation of *Europa Clipper* magnetic measurements near the moon, where the effects of quadrupole-and-higher magnetic moments will be most apparent. The results of this work permit

magnetic studies considering non-spherical oceans of satellites for the first time.

2.1 Introduction

Induced magnetic fields result when a conducting body is subjected to a time-varying electromagnetic field. The time-varying magnetic field generates electric fields in accordance with Maxwell's laws, which in turn drive currents in the conducting body, producing a secondary magnetic field. Because currents can only flow where there is conducting material, the shape of the conducting body affects the form of the resulting induced field.

The induced magnetic field for the configuration of a spherically symmetric conductor has been described by Lahiri and Price (1939) and Srivastava (1966), and summarized in application to planetary bodies by Parkinson (1983). Each of these authors examine cases of finite conductivity that vary only with radius. A significant body of work exists in the study of non-uniform conductivity structures within the Earth, but much of it is of limited application to other solar system bodies. Some studies focus on inverting measurements to find induced magnetic moments for the Earth, *e.g.* Egbert and Kelbert (2012). Numerous authors consider forward modeling of a heterogeneously conducting Earth, especially in designing numerical solutions intended to aid in magnetic sounding (Fainberg and Zinger, 1980; Zhang and Schultz, 1992; Velímský and Martinec, 2005; Weiss, 2010). All geomagnetic studies benefit from the wealth of magnetic measurements taken over long periods of time in, on, and near the Earth. These extensive reservoirs of data help inform the variety of models that may be applied and make numerical simulations for this purpose far more practical.

In contrast, magnetic measurements of most solar system bodies are very sparse. Earth's moon is the only moon in the solar system that, as yet, has had any spacecraft orbiting it. Past geocentric studies relying on a wealth of training data are of limited use in application to bodies with data-limited magnetic surveys—there is a need for techniques capable of constraining global-scale conductivity structures with sparse magnetic measurements. No previous work has evaluated the effect on induced magnetic moments from perturbing the outer surface of the conducting body. Crucially, as we will demonstrate in Section 2.3.3, deviations from spherical symmetry can alter the induced dipole moments, and result in induced magnetic moments of higher order than that of

the excitation field, even when the excitation field is uniform. Although the signal from magnetic moments of greater than dipole order is expected to be small for existing spacecraft measurements (*e.g.* those from the *Galileo* mission), future missions are more likely to be able to resolve higher-order magnetic moments. For example, the *Europa Clipper* mission plans numerous flybys that will approach within 25 km of Europa's surface (Lam et al., 2018; Campagnola et al., 2019), less than 2% of its radius in altitude.

Understanding the magnetic fields induced from nearly spherical conductors is of particular importance in the study of moon–magnetosphere interactions. The five largest planets all have global-scale magnetic fields, and all of them except Saturn have their dipole moments misaligned with their rotation axes. This generates oscillations in their magnetospheres at rotational, synodic, and orbital periods. All of the outer planets also have large moons whose self-gravity pulls them into nearly spherical shapes, and all large moons in the solar system are tidally locked to their parent planets. Thus, they all experience asymmetric gravitational fields that perturb their shapes. Many of these moons also possess salty, global oceans of liquid water that are excellent conductors of electricity (Khurana et al., 2002) and promising candidate environments in the search for life elsewhere (Vance et al., 2018). There are, therefore, many near-spherical ocean worlds important to the study of astrobiology that are subjected to periodic magnetic fields. In fact, magnetic sounding has provided the strongest positive confirmation of an ocean of liquid water underneath Europa's icy crust (Hand and Chyba, 2007; Schilling et al., 2007). Nevertheless, all past studies of magnetic sounding for planetary bodies have assumed spherical symmetry in modeling subsurface oceans, thereby modeling only induced dipole moments (Parkinson, 1983). Although this is a sensible first-order approximation, the *Galileo* flyby MAG data for Europa are not particularly well-fit by assuming a spherical ocean (*cf.* Schilling et al. (2007), Figs. 5–9). This leaves ample room for ambiguity that may be improved upon by considering non-spherical oceans, especially with the current scarcity of satellite magnetic measurements—only five flyby datasets have been widely studied for magnetic induction of Europa.

In most cases, little is known about planetary interiors. Interpretation of spacecraft magnetic measurements requires a careful accounting of the plasma environment and ionospheric effects in

addition to planetary fields (Schilling et al., 2007). However, there remains a need for techniques capable of constraining the interior structure. As we will show in Section 2.3.3, asymmetry in subsurface oceans yields induced magnetic moments of greater than dipole order; signals from these will be much more pronounced during the close flybys planned for the *Europa Clipper* mission. Interpretation of measurements from these close flybys will require models capable of predicting higher-order magnetic moments resulting from interior structure (Soderlund, 2019; Vance et al., 2021), from plasma sources (Rubin et al., 2015) and from putative plumes (Roth et al., 2014; Jia et al., 2018; Arnold et al., 2019). Failing to account for degeneracies in the possible sources of higher-order magnetic moments will invalidate the results of such investigations.

There are strong indications that inhomogeneity in the ice shell of Europa will contribute to large-scale variance in thermal transport through the crust. In particular, cryovolcanism (Quick and Marsh, 2016) and upwelling of diapirs (Tobie et al., 2003) are expected to sustain latitudinal variation in the thickness of Europa's ice shell. A compensatory variation in the outer radius of Europa's ocean will influence the flow of electric currents generated by the excitation field applied by Jupiter. Careful examination of magnetic measurements near Europa may be able to yield information about the shape of the ice–ocean boundary, but this would be impossible without an appropriate model for the induced magnetic field.

It is important to note that the expectation of non-spherical conducting bodies within solar system moons is in contrast to the Earth. Smaller size, lower bulk densities, and proximity to parent planets apply proportionally stronger gravitational asymmetries. Patterns of tidal heating and heat escape may further distort the conductor outer boundary away from a spherical shape. In addition, strong oscillatory magnetic fields from the rapidly rotating gas giants combine with these effects to result in larger signals from non-spherical conducting bodies in satellites compared to induced fields from the Earth.

In this work, we evaluate the magnetic moments induced from a spherical conducting body whose outer surface is perturbed in terms of spherical harmonics. The induced moments are expressed in terms of the harmonic coefficients of the excitation field. Most smoothly varying, near-spherical shapes may be approximated by retaining only low-order harmonics. In Section 2.3.3,

we prove that expanding to first order in our perturbation parameter leads to simple superposition from shape harmonics to resultant magnetic moments—each harmonic appearing in the perturbed conductor's shape generates proportional magnetic moments that are independent of the other harmonics. This means that any shape whose departure from spherical symmetry may be approximated by a linear combination of spherical harmonics of degree $n = 1, 2$ has induced magnetic moments that are trivial to calculate with the results of our method, using Table 2.1. This treatment enables, for the first time, consideration of subsurface oceans that are not spherically symmetric. Applying this work to the particular case of Europa, examined through the lens of magnetic measurements from the *Galileo* mission, is a topic for future study.

2.2 Methods

We are concerned with the induced magnetic field for a configuration analogous to that of global-scale oceans of large moons in our solar system. The primary magnetic field applied to these bodies is dipolar at typical orbital distances, and neglecting contributions from magnetospheric plasma oscillations, is effectively uniform across the body (Zimmer et al., 2000). For simplicity, we therefore restrict our focus to an excitation field that is uniform across the conducting body. Similar methods may be applied to excitation fields with greater spatial variation, but the relatively simple case of a uniform field is sufficient for application to moons.

The excitation field applied to the conducting body takes the form

$$\mathbf{B}_{\text{exc}}(\mathbf{r}, t) = \mathbf{B}_o(\mathbf{r}) + \sum_j \mathbf{B}_{e,j}(\mathbf{r}) e^{-i\omega_j t}, \tag{2.1}$$

with static and dynamic components that are complex in general. The measurable magnetic field is found by taking the real part of any complex expressions. Coefficients in any expression may be complex, except where noted. Although Eq. 2.1 accounts for the possibility of multiple oscillation frequencies applied to the conducting body, we will restrict our approach to a single frequency. Superposition permits an independent handling of each excitation frequency, so our method may be applied repeatedly for a combination of frequencies.

In the absence of electric currents, the magnetic field satisfies Laplace's equation and therefore may be described by the gradient of a scalar potential ψ:

$$\nabla^2 \mathbf{B} = 0 \tag{2.2}$$

$$\mathbf{B} = -\nabla\psi. \tag{2.3}$$

These equations are valid outside the conducting body if we neglect currents in the plasma. Although the currents present in the plasma environment around the body are not generally negligible, the principle of superposition permits us to consider each contribution to the net electromagnetic response independently—the net magnetic field is then the sum from each individual contribution. In this work, we consider only the induced magnetic moments generated by the interaction of the primary excitation field with the conducting body, as this is the dominant interaction that induces magnetic fields from within solar system moons.

The near-spherical shape of the conducting body encourages our use of spherical polar coordinates $\mathbf{r} = (r, \theta, \phi)$. Solutions to Eqs. 2.2 and 2.3 are easily represented in these coordinates by the following general form (Jackson, 1999):

$$\psi(\mathbf{r}) = \sum_{n,m} a \left(B_{e,nm} \left(\frac{r}{a}\right)^n + B_{i,nm} \left(\frac{a}{r}\right)^{n+1} \right) Y_{nm}(\theta, \phi), \tag{2.4}$$

where $B_{e,nm}$ and $B_{i,nm}$ are complex coefficients for the external and induced magnetic fields, Y_{nm} are the spherical harmonics, and a is a unit of radial distance. Orthonormal expressions for spherical harmonics up to $n = 3$ are listed in Appendix 2.A. Magnetic potentials proportional to positive powers of r can only be generated from outside of the conducting body under examination; because we are assuming a uniform excitation field, we keep only the $n = 1$ terms for B_e. The B_i terms in Eq. 2.4 are those of the multipole expansion, so each $B_{i,nm}$ is proportional to, and thus represents, an induced multipole moment. We assume the magnetic potential for the excitation field oscillates sinusoidally, so time dependence is added to Eq. 2.4 by multiplication of $e^{-i\omega t}$ as in Eq. 2.1.

Within the conducting body, the dynamic excitation field induces electric fields that drive currents, so $\mathbf{B}$ cannot be represented by Eq. 2.3 in this region. Instead, we must use a diffusion equation

for **B**, derived from combining Maxwell's laws with Ohm's law:

$$\nabla^2 \mathbf{B} = \mu\sigma \frac{\partial \mathbf{B}}{\partial t}. \tag{2.5}$$

For simplicity in deriving our model, we neglect movement of conducting material within the body, which can itself induce secondary fields (Saur et al., 2010; Vance et al., 2021). Considering only the oscillatory magnetic field, taking the time derivative of **B** is equivalent to multiplication by $-i\omega$. We can thus rewrite Eq. 2.5 in terms of a diffusion constant k, and arrive at a vector Helmholtz equation:

$$\nabla^2 \mathbf{B}_{\text{osc}} = -k^2 \mathbf{B}_{\text{osc}} \tag{2.6}$$

$$k = \sqrt{i\omega\mu\sigma}. \tag{2.7}$$

In general, μ and σ are functions of position and will vary throughout the body. On planetary scales, μ is well approximated by μ_o, even for bodies containing large amounts of ferromagnetic materials (Saur et al., 2010). We further assume that σ is uniform within the conducting body. Although this may not be valid on global scales, and the conductivity will increase with depth in a well-mixed ocean (Vance et al., 2018), we will later assume that the average outer radius of the conducting body a is large. When the imaginary part of ka is large, the radial dependence of the magnetic field within the conducting body becomes an exponential function whose strength decreases with depth. When the thickness of the conducting layer τ is significantly larger than the skin depth $s = 1/\text{Im}(k) = \sqrt{2/\omega\mu\sigma}$, deeper conductivity structure will be well-screened from the oscillating excitation field, and ceases to affect the induced field (Neubauer, 1999). When this condition is satisfied, any material below the uppermost conducting layer may be safely ignored. For simplicity and clarity in our derivations, we also make the approximation that any material outside the primary conducting body has negligible conductivity. Validity of these approximations is discussed in Section 2.2.3 and Section 2.4, and a diagram of the interior structure model we apply is depicted in Figure 2.1.

General solutions to Eq. 2.6 for the configuration at hand must be consistent with a poloidal field; since they are induced by an external field, there will be no toroidal field component (Moffatt,

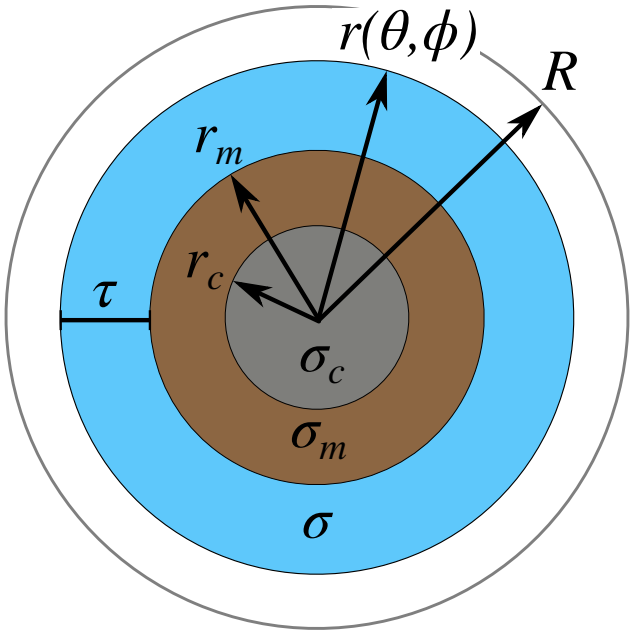

Figure 2.1: Near-spherical 3-layer model applied to calculate the induced magnetic field for a near-spherical conducting ocean. Conductivities σ and radii r are labeled for each region, as are the body radius R, average ocean layer thickness τ, and the conducting body outer radius $r(\theta, \phi)$. For the example case of Europa, an expected iron core and rocky mantle are depicted. Layers are not to scale; $r(\theta, \phi)$ is discussed in detail in Section 2.3.2.

1978). Poloidal fields take the following form:

$$\mathbf{B}_P = \nabla \times \nabla \times (P\mathbf{r}) \tag{2.8}$$

$$B_{r,P} = \frac{1}{r}\left[-\frac{1}{\sin\theta}\frac{d}{d\theta}\sin\theta\frac{d}{d\theta} - \frac{1}{\sin^2\theta}\frac{d^2}{d\phi^2}\right]P \tag{2.9}$$

$$B_{\theta,P} = \frac{1}{r}\frac{d}{d\theta}\frac{d}{dr}(Pr) \tag{2.10}$$

$$B_{\phi,P} = \frac{1}{r\sin\theta}\frac{d}{d\phi}\frac{d}{dr}(Pr), \tag{2.11}$$

where the poloidal potential P is a scalar function of position. The quantity in square brackets in Eq. 2.9 is the angular momentum operator $\hat{L}^2$, of which the spherical harmonics Y_{nm} are eigenfunctions:

$$\hat{L}^2 Y_{nm} = n(n+1)Y_{nm}. \tag{2.12}$$

If we suppose P is separable, we can expand it in spherical harmonics:

$$P(r,\theta,\phi) = \sum_{n,m} A_{nm}\mathcal{R}_n(r)\,Y_{nm}(\theta,\phi), \tag{2.13}$$

where A_{nm} are constant coefficients determined by the boundary conditions and $\mathcal{R}_n$ are functions we must determine from other relations. As we later satisfy the boundary conditions with this functional form of P, the uniqueness theorem confirms that this is *the* physically correct representation, validating the supposition that P is separable.

Inserting Eq. 2.13 into Eqs. 2.9–2.11 and utilizing Eq. 2.12 yields expressions for the components of the magnetic field within the conducting body in terms of $\mathcal{R}$:

$$B_{r,\text{int}} = \sum_{n,m}\frac{A_{nm}}{r}\mathcal{R}_n\,n(n+1)Y_{nm} \tag{2.14}$$

$$B_{\theta,\text{int}} = \sum_{n,m}\frac{A_{nm}}{r}\frac{d}{dr}(r\mathcal{R}_n)\frac{\partial Y_{nm}}{\partial\theta} \tag{2.15}$$

$$B_{\phi,\text{int}} = \sum_{n,m}\frac{A_{nm}}{r\sin\theta}\frac{d}{dr}(r\mathcal{R}_n)\frac{\partial Y_{nm}}{\partial\phi}. \tag{2.16}$$

We can now make use of these expressions along with Eq. 2.6 to find a differential equation for $\mathcal{R}_n$. Linearity of the ∇^2 operator allows us to consider only a single n, m term, as the same equations

will apply to all terms. The $\hat{r}$ component of Eq. 2.6 reads as (Arfken et al., 2012)

$$\nabla^2 B_r - \frac{2B_r}{r^2} - \frac{2}{r^2 \sin\theta}\frac{d}{d\theta}(\sin\theta B_\theta) - \frac{2}{r^2\sin\theta}\frac{\partial B_\phi}{\partial\phi} = -k^2 B_r. \tag{2.17}$$

Inserting Eqs. 2.14–2.16 and again exploiting the angular momentum operator, we arrive at a Bessel equation for $\mathcal{R}_n$:

$$\frac{1}{\mathcal{R}_n}\frac{d}{dr}\left(r^2\frac{\partial\mathcal{R}_n}{\partial r}\right) + k^2r^2 - n(n+1) = 0. \tag{2.18}$$

Solutions to this equation are linear combinations of the particular solutions, which are the spherical Bessel functions of the first and second kind, j_n and y_n:

$$\mathcal{R}_n(r) = C_n j_n(kr) + D_n y_n(kr) \tag{2.19}$$

$$j_n(kr) = (-kr)^n\left(\frac{1}{kr}\frac{d}{d(kr)}\right)^n\frac{\sin kr}{kr} \tag{2.20}$$

$$y_n(kr) = -(-kr)^n\left(\frac{1}{kr}\frac{d}{d(kr)}\right)^n\frac{\cos kr}{kr}; \tag{2.21}$$

C_n and D_n in Eq. 2.19 are constants determined from the boundary conditions. The solutions y_n diverge at the origin, so D_n must always be zero for the innermost region. As our solution for $\mathcal{R}_n$ now contains arbitrary coefficients C and D, we may absorb the coefficients A_{nm} and rename C_n and D_n to C_{nm} and D_{nm}.

For later convenience, we also require expressions for $\frac{d}{dr}(r\,j_n(kr))$ and $\frac{d}{dr}(r\,y_n(kr))$. Eqs. 2.20 and 2.21 can be manipulated to obtain

$$\frac{d}{dr}(rj_n) = j_n^\star = (n+1)j_n - kr\,j_{n+1} \tag{2.22}$$

$$\frac{d}{dr}(ry_n) = y_n^\star = (n+1)y_n - kr\,y_{n+1}, \tag{2.23}$$

which we now also define as $j_n^\star$ and $y_n^\star$, respectively.

We can now write general expressions for the magnetic field in all regions. From Eqs. 2.3 and

2.4, the external magnetic field follows

$$B_{r,\text{ext}} = \sum_{n,m} -nB_{e,nm}\delta_{1,n}\left(\frac{r}{a}\right)^{n-1} Y_{nm} + \sum_{n,m}(n+1)B_{i,nm}\left(\frac{a}{r}\right)^{n+2} Y_{nm} \tag{2.24}$$

$$B_{\theta,\text{ext}} = \sum_{n,m} -B_{e,nm}\delta_{1,n}\left(\frac{r}{a}\right)^{n-1} \frac{\partial Y_{nm}}{\partial\theta} + \sum_{n,m} -B_{i,nm}\left(\frac{a}{r}\right)^{n+2} \frac{\partial Y_{nm}}{\partial\theta} \tag{2.25}$$

$$B_{\phi,\text{ext}} = \sum_{n,m} -\frac{B_{e,nm}\delta_{1,n}}{\sin\theta}\left(\frac{r}{a}\right)^{n-1} \frac{\partial Y_{nm}}{\partial\phi} + \sum_{n,m} -\frac{B_{i,nm}}{\sin\theta}\left(\frac{a}{r}\right)^{n+2} \frac{\partial Y_{nm}}{\partial\phi}, \tag{2.26}$$

where $\delta_{1,n}$ is a Kronecker delta function, which reflects our consideration of a uniform excitation field. Inserting Eq. 2.19 into Eqs. 2.14–2.16, and absorbing A_{nm} into C and D, the internal magnetic field follows

$$B_{r,\text{int}} = \sum_{n,m} \frac{C_{nm}j_n(kr) + D_{nm}y_n(kr)}{r} n(n+1)Y_{nm} \tag{2.27}$$

$$B_{\theta,\text{int}} = \sum_{n,m} \frac{C_{nm}j_n^\star(kr) + D_{nm}y_n^\star(kr)}{r} \frac{\partial Y_{nm}}{\partial\theta} \tag{2.28}$$

$$B_{\phi,\text{int}} = \sum_{n,m} \frac{C_{nm}j_n^\star(kr) + D_{nm}y_n^\star(kr)}{r\sin\theta} \frac{\partial Y_{nm}}{\partial\phi}. \tag{2.29}$$

Y_{nm} is an eigenfunction of $\frac{d}{d\phi}$ with an eigenvalue of im, so we later replace these derivatives. The $\frac{d}{d\theta}$ operator is not conveniently replaced; we evaluate it as needed when we examine a near-spherical boundary in Section 2.3.3.

Solving for the B_i, C, and D coefficients in these equations is accomplished by applying Maxwell's laws at the common boundaries between each region. On each boundary surface, Maxwell's laws dictate that the normal component of $\mathbf{B}$ must be continuous, and the tangential components of $\mathbf{B}/\mu$ must be continuous whenever there are no surface currents confined to the boundary itself. As we assume $\mu = \mu_o$ within the body, $\mathbf{B}$ is continuous everywhere, and the components of the magnetic field for adjacent regions are equal on the boundary surface.

2.2.1 Internal boundary conditions

Boundaries interior to the outer surface must match component values according to Eqs. 2.27–2.29 at each boundary surface. In this work, we assume that interior boundary shapes are spherically

symmetric. At a radius r_l describing the outer boundary of a lower layer l with wavenumber k_l and an upper boundary u with k_u, the internal boundary conditions read

$$C^l_{nm} j_n(k_l r_l) + D^l_{nm} y_n(k_l r_l) = C^u_{nm} j_n(k_u r_l) + D^u_{nm} y_n(k_u r_l) \tag{2.30}$$

$$C^l_{nm} j_n(k_l r_l) + D^l_{nm} y_n(k_l r_l) = C^u_{nm} j_n(k_u r_l) + D^u_{nm} y_n(k_u r_l). \tag{2.31}$$

Because the interior boundary surfaces are spherically symmetric, the C and D coefficients are independent of m.

As first introduced by Srivastava (1966), a recursion relation may be obtained from the internal boundary conditions. Factoring out the C coefficients and expressing the ratio D_n/C_n as Λ_n, we can solve for Λ^u_n in terms of Λ^l_n by dividing Eq. 2.30 by Eq. 2.31. For a given interior structure model, j_n and y_n are functions of known quantities k and r, so Λ^u_n is completely determined by the structure model and Λ^l_n. In the innermost layer, which contains the origin, Λ_n are all zero so that the resultant magnetic field remains finite. The equations above may therefore be repeatedly applied to find Λ_n for each successive layer, all the way to the outer boundary. This is a necessary step to reducing the number of variables in the exterior boundary conditions to a solvable set—the outermost Λ_n is completely determined from the interior structure of the conducting body.

2.2.2 *External boundary conditions*

Combining Eqs. 2.24–2.29, we obtain the boundary conditions that apply at the outermost boundary for a conductor of any shape:

$$B_r: \quad \sum_{n,m} nB_{e,nm}\delta_{1,n}\left(\frac{r}{a}\right)^{n-1} Y_{nm} = \sum_{n,m}\left(-nC_{nm}\frac{j_n(kr)+\Lambda_n y_n(kr)}{r} + B_{i,nm}\left(\frac{a}{r}\right)^{n+2}\right)(n+1)Y_{nm} \tag{2.32}$$

$$B_\theta: \quad \sum_{n,m} B_{e,nm}\delta_{1,n}\left(\frac{r}{a}\right)^{n-1}\frac{\partial Y_{nm}}{\partial\theta} = \sum_{n,m}\left(-C_{nm}\frac{j_n^\star(kr)+\Lambda_n y_n^\star(kr)}{r} - B_{i,nm}\left(\frac{a}{r}\right)^{n+2}\right)\frac{\partial Y_{nm}}{\partial\theta} \tag{2.33}$$

$$B_\phi: \quad \sum_{n,m} B_{e,nm}\delta_{1,n}\left(\frac{r}{a}\right)^{n-1} mY_{nm} = \sum_{n,m}\left(-C_{nm}\frac{j_n^\star(kr)+\Lambda_n y_n^\star(kr)}{r} - B_{i,nm}\left(\frac{a}{r}\right)^{n+2}\right)mY_{nm}, \tag{2.34}$$

where we have omitted the $i/\sin\theta$ factor common to all B_ϕ terms. The shape of the outer boundary is defined by a function $r(\theta,\phi)$, which we insert in place of r in the above boundary condition equations. The tangential boundary conditions (Eqs. 2.33 and 2.34) provide redundant information regarding the B_i and C coefficients.

Every term in the boundary condition equations contains a spherical harmonic; these functions are all mutually independent. From the boundary condition equations, we can therefore obtain a set of equations that are linear in the B_i and C coefficients. These linear equations are sufficient to determine all coefficients analytically if we make a pair of approximations:

1. $|kr| \to \infty$, which is reasonable for very high conductivity, for very large conductors of moderate to high conductivity, or for rapidly varying magnetic fields (Parkinson, 1983). As a corollary, the skin depth s becomes small in this regime, suggesting the interior becomes screened from oscillating fields.

2. The boundary surface may be adequately represented with a few low-order spherical harmonics.

The first approximation above is discussed in detail in Section 2.2.3. The second approximation is necessary because, as we will see in Section 2.3.3, all harmonics in the boundary shape adjust either the dipole moments or quadrupole moments relative to the spherically symmetric case. However, these adjustments are proportional to the amount of representation a given harmonic has in the boundary shape, so harmonics that have comparatively small coefficients result in smaller adjustments to the induced magnetic moments. We must therefore assume the series expansion of the boundary may be truncated, *i.e.* that the boundary shape is dominated by low-order harmonics.

Finally, the induced magnetic field outside the conducting body is found by taking the real part of

$$\mathbf{B}_{\text{ind}}(r,\theta,\phi,t) = -\boldsymbol{\nabla}\left(\sum_{n,m} aB_{i,nm}\left(\frac{a}{r}\right)^{n+1} Y_{nm}\right) e^{-i\omega t}. \tag{2.35}$$

$B_{i,nm}$ will always be expressed as linear combinations of $B_{e,nm}$. The complex values $B_{e,nm}$ are determined, for planetary bodies, by measuring the excitation field from the parent planet. Although the values measured for the excitation field are purely real, the complex coefficients B_e are determined by expressing the oscillatory components of the field in terms of complex spherical harmonics Y_{nm}.

2.2.3 High-conductivity approximation

Europa has an outer radius of 1560 km and Jupiter has a synodic rotation period of 11.2 h with Europa. Supposing Europa has a nominal ice shell thickness of 30 km, this approximation requires that Europa's ocean has a conductivity of order 1 S/m or greater. For a conductivity comparable to that of Earth's ocean at 2.75 S/m (Hand and Chyba, 2007), $|kr|$ is approximately 35; next-to-leading-order terms are about a factor of 20 smaller than the leading-order term. Measurements from the *Galileo* mission confirm that the orientation and strength of the induced field is close to that of a perfect conductor (Zimmer et al., 2000), which justifies the use of this approximation. We therefore retain only leading-order terms in $1/kr$ when applying this approximation.

The radial functions take the following asymptotic forms (Marion and Heald, 1980):

$$j_n(kr) \to \frac{(-i)^n e^{ikr} - (i)^n e^{-ikr}}{2ikr}, \qquad j_n^\star(kr) \approx \frac{(-i)^n e^{ikr} + (i)^n e^{-ikr}}{2} \tag{2.36}$$

$$y_n(kr) \to \frac{-(-i)^n e^{ikr} - (i)^n e^{-ikr}}{2kr}, \qquad y_n^\star(kr) \approx \frac{(-i)^n e^{ikr} - (i)^n e^{-ikr}}{2i}. \tag{2.37}$$

With these expressions, at the bottom of the ocean Eqs. 2.30 and 2.31 become independent of the lower layers and yield a result for Λ_n:

$$\Lambda_n \approx -\frac{j_n^\star(k(a-\tau))}{y_n^\star(k(a-\tau))} = i + 2i(-1)^n e^{2ika} e^{-2ik\tau}. \tag{2.38}$$

The second term in Eq. 2.38 results in a negligible change to the imaginary part of Λ_n, but contributes a real part of order $\exp\left\{-\sqrt{2}|ka|\right\} \exp\left\{\sqrt{2}|k\tau|\right\}$. Although this is small for large $|ka|$, it multiplies an exponential that grows as $\exp\left\{|ka|/\sqrt{2}\right\}$ in both $j_n^\star$ and $y_n^\star$, so it is important to retain as part of applying the high-conductivity approximation. We can also see from Eq. 2.38 that the real part of Λ_n scales as $\exp\left\{\sqrt{2}\tau/s\right\}$, causing deeper oceans to converge more closely to an exponential form $\exp\{-ikr\}$.

For the approximate values above for Europa, the ocean skin depth s is about 60 km. Gravity measurements from the *Galileo* mission indicate that the ocean depth is likely of order 100 km (Anderson et al., 1998), somewhat larger than $s/\sqrt{2}$. As a consequence, the Bessel functions will be dominated by the growing exponentials in Eqs. 2.36 and 2.37. We can then replace the Bessel function expressions found in the external boundary conditions with simpler forms:

$$C_{nm}(j_n + \Lambda_n y_n) \to -C_{nm}^\infty \frac{e^{-ikr}}{ikr}, \quad C_{nm}(j_n^\star + \Lambda_n y_n^\star) \to C_{nm}^\infty e^{-ikr}, \tag{2.39}$$

where we have absorbed constant factors into the final coefficient C_{nm}^∞. We will also later need

$$\frac{C_{nm} \cdot (ka)^2 \left(j_n(ka) + \Lambda_n y_n(ka)\right)}{n\left(j_n(ka) + \Lambda_n y_n(ka)\right) + \left(j_n^\star(ka) + \Lambda_n y_n^\star(ka)\right)} \to C_{nm}^\infty \, ika, \tag{2.40}$$

which may be obtained using the l'Hôpital rule and recursion relations for Bessel functions.

2.3 Results

First, we examine the case of spherical symmetry to prove consistency with this well-established solution. Next, we apply our method to an arbitrary near-spherical boundary shape. Finally, we

summarize our results with a simple formula for calculating induced moments for an arbitrary near-spherical boundary.

2.3.1 *Induced magnetic field for a spherical conductor*

A boundary surface with spherical symmetry is defined by $r(\theta, \phi) = a$. Inserting this into the boundary condition equations yields an exact solution with our approximations—only $n = 1$ terms have non-zero B_i and C coefficients. Collecting terms proportional to each Y_{nm} (or $\frac{\partial Y_{nm}}{\partial \theta}$) yields equations of the form

$$\frac{B_{e,nm}\delta_{1,n}}{n+1} = -\frac{nC^o_{nm}}{a}\left(j_n(ka) + \Lambda_n y_n(ka)\right) + B^o_{i,nm} \tag{2.41}$$

$$B_{e,nm}\delta_{1,n} = -\frac{C^o_{nm}}{a}\left(j^\star_n(ka) + \Lambda_n y^\star_n(ka)\right) - B^o_{i,nm}, \tag{2.42}$$

where B^o_i indicates that this is the zeroth-order solution for B_i. The B_θ and B_ϕ equations offer redundant information. With the expressions from Section 2.2.3 we apply our $kr \to \infty$ limit. Keeping only first order terms in $1/kr$, we get:

$$B_{e,1m} \approx -2C^{o,\infty}_{1m}\frac{e^{-ika}}{ika^2} + 2B^o_{i,1m} \tag{2.43}$$

$$B_{e,1m} \approx -C^{o,\infty}_{1m}\frac{e^{-ika}}{a} - B^o_{i,1m}. \tag{2.44}$$

Solving for $C^{o,\infty}_{1m}$ in Eq. 2.44 and inserting into Eq. 2.43, we gain a term that is reduced by a factor $1/ka$ relative to the other terms. Discarding this term, we can conclude

$$B^o_{i,1m} = \frac{1}{2}B_{e,1m}, \quad C^{o,\infty}_{1m} = -\frac{3a}{2}B_{e,1m}e^{ika}. \tag{2.45}$$

Because the excitation field is uniform, containing only $n = 1$ harmonics, the induced magnetic field is a pure dipole for this boundary shape.

2.3.2 *Near-spherical boundary shape*

We must now define the surface $r(\theta, \phi)$ for a near-spherical boundary that we will insert into the boundary conditions. Because we wish to represent physical surfaces, $r(\theta, \phi)$ must be purely real.

Furthermore, we endeavor to represent subsurface oceans of solar system moons; to do so, we must limit the deviation from spherical symmetry. This ensures that the surface described by $r(\theta, \phi)$ remains at or beneath the planetary surface, when a is the average outer radius of the conducting ocean. With these considerations in mind, we choose a surface of the form

$$r(\theta, \phi) = a + \varepsilon \sum_{p,q} \chi_{pq} S_{pq}(\theta, \phi), \tag{2.46}$$

where ε, which is purely real, is the maximum deviation from spherical symmetry, χ_{pq} are purely real or purely imaginary constants, and S_{pq} are proportional to spherical harmonics of the same indices.

The harmonic functions S_{pq} are chosen such that they represent a functional dependence in accordance with the matching normalized harmonics, but have proportionality constants chosen such that they have a maximum range $|S_{pq}| \leq 1$. Shape harmonics in our chosen normalization are listed in Appendix 2.A.

The χ_{pq} coefficients must be purely real or purely imaginary because we require that linear combinations of S_{pq} be purely real to describe a physical surface. χ_{pq} represent the relative amount of each harmonic present in the boundary shape. Typically $\sum |\chi_{pq}| = 1$; this is not strictly true because the range of S_{20} is not symmetric about zero. Coefficients χ_{pq} must be chosen so that the maximum value of $r(\theta, \phi)$ is $a + \varepsilon$, or the minimum value is $a - \varepsilon$, in accordance with the physical shape to be approximated. We will later show in Section 2.3.3 that, under our approximations, the magnetic moments for any arbitrary choice of χ_{pq} may be readily calculated from Table 2.1.

Surfaces described by Eq. 2.46 are near-spherical in that we make the approximation $\varepsilon \ll a$. Equivalently, $\varepsilon/a \ll 1$, and we retain terms up to first order in ε/a only. This enables us to use a Taylor expansion in the boundary conditions that truncates quickly, adding only one term containing a product of two spherical harmonics. Products of spherical harmonics may be expressed as a linear combination of different harmonics (Condon and Shortley, 1951). This results in "mixing" of harmonics in the excitation field from $n = 1$ into other n, so a uniform excitation field induces magnetic moments of quadrupole order or higher for this shape, in addition to the original dipole moments. Table 2.1 contains the results of multiplying each $n = 1$ spherical harmonic with each

shape harmonic, up to $p = 2$. These are the products we will need in order to find linear equations for the resultant spherical harmonics that appear in the boundary conditions.

2.3.3 Induced magnetic moments for a near-spherical boundary shape

Let us now insert our near-spherical $r(\theta, \phi)$ into the boundary conditions. To first order, a Taylor expansion of a function $f(r)$ about $r(\theta, \phi)$ has terms

$$f(r(\theta,\phi)) \approx f(a) + (r(\theta,\phi) - a)\frac{\partial f(r)}{\partial r}\Big|_{r=a} = f(a) + \varepsilon \sum_{p,q} \chi_{pq} S_{pq}(\theta,\phi)\frac{\partial f(r)}{\partial r}\Big|_{r=a}. \tag{2.47}$$

The r^n power series that multiply $B_{e,nm}$ and $B_{i,nm}$ then take the form $a^n(1 + n\varepsilon/a \sum_{p,q} \chi_{pq} S_{pq})$. The interior field terms become

$$C_{nm}\frac{\left(j_n(ka) + \Lambda_n y_n(ka)\right)}{r} \approx \frac{C_{nm}}{a}\Bigg(\left(j_n(ka) + \Lambda_n y_n(ka)\right) + \frac{\varepsilon}{a}\sum_{p,q} \chi_{pq} S_{pq}\Big[\left(j_n^\star(ka) + \Lambda_n y_n^\star(ka)\right) - 2\left(j_n(ka) + \Lambda_n y_n(ka)\right) \Big]\Bigg) \tag{2.48}$$

$$C_{nm}\frac{\left(j_n^\star(ka) + \Lambda_n y_n^\star(ka)\right)}{r} \approx \frac{C_{nm}}{a}\Bigg(\left(j_n^\star(ka) + \Lambda_n y_n^\star(ka)\right) + \frac{\varepsilon}{a}\sum_{p,q} \chi_{pq} S_{pq}\Big[\left(j_n(ka) + \Lambda_n y_n(ka)\right)\left(n(n+1) - k^2a^2\right) - \left(j_n^\star(ka) + \Lambda_n y_n^\star(ka)\right) \Big]\Bigg). \tag{2.49}$$

Applying these expansions to the exterior boundary condition equations (Eqs. 2.32–2.34) results in new terms added to the n, m series:

$$\Delta B_{r,nm} = \frac{\varepsilon}{a}\Bigg[\frac{-nC_{nm}}{a}\Big(\left(j_n^\star(ka) + \Lambda_n y_n^\star(ka)\right) - 2\left(j_n(ka) + \Lambda_n y_n(ka)\right) \Big) - n(n-1)B_{e,nm}\delta_{1,n} - (n+2)B_{i,nm}\Bigg](n+1)\sum_{p,q} \chi_{pq} S_{pq} Y_{nm} \tag{2.50}$$

$$\Delta B_{\theta,nm} = \frac{\varepsilon}{a}\Bigg[\frac{-C_{nm}}{a}\Big(\left(j_n(ka) + \Lambda_n y_n(ka)\right)\left(n(n+1) - k^2a^2\right) - \left(j_n^\star(ka) + \Lambda_n y_n^\star(ka)\right) \Big) - (n-1)B_{e,nm}\delta_{1,n} + (n+2)B_{i,nm}\Bigg]\sum_{p,q} \chi_{pq} S_{pq}\frac{\partial Y_{nm}}{\partial\theta}. \tag{2.51}$$

The ΔB_ϕ terms are identical to the ΔB_θ terms with $\frac{\partial Y}{\partial\theta}$ replaced by $\frac{\partial Y}{\partial\phi}$, so for brevity we focus only on a single tangential equation. Because we assume the boundary surface is near-spherical, there

will always be at least one induced moment of degree $n = 1$ that is non-zero, with m matching the excitation field. Higher-order magnetic moments will be proportional to ε/a, so the only ΔB terms that will be non-negligible are those where $B_{i,nm}$ in Eqs. 2.50 and 2.51 have $n = 1$; all other ΔB terms will be of second order or higher in ε/a and we discard them.

We may further simplify the ΔB terms with the help of our zeroth-order solution. Using Eqs. 2.41 and 2.42 to replace C_{nm}, and using Eq. 2.40 to make the relevant substitution for the high-$|kr|$ limit we get

$$\Delta B_{r,nm} = 0 \quad \text{(exactly)} \tag{2.52}$$

$$\begin{aligned} \Delta B_{\theta,nm} &= \frac{\varepsilon}{a}\left[-\frac{2n+1}{n+1}(ika)B_{e,nm}\delta_{1,n}\right] \sum_{p,q} \chi_{pq} S_{pq} \frac{\partial Y_{nm}}{\partial \theta} \\ &= -\frac{3}{2}\frac{\varepsilon}{a}(ika)B_{e,1m} \sum_{p,q} \chi_{pq} S_{pq} \frac{\partial Y_{1m}}{\partial \theta} \end{aligned} \tag{2.53}$$

The products $S_{pq}\frac{\partial Y_{nm}}{\partial \theta}$ will be sums of $\frac{\partial Y_{n'm'}}{\partial \theta}$ of degree and order

$$n' = p + n - 2N, \quad m' = q + m, \tag{2.54}$$

where $N = 0,\ 1,\ 2,\ \ldots$ The resulting products are given by

$$S_{pq}\frac{\partial Y_{nm}}{\partial \theta} = \sum_{n',m'} \Gamma_{nmpqn'm'} \frac{\partial Y_{n'm'}}{\partial \theta}, \tag{2.55}$$

where $\Gamma_{nmpqn'm'}$ are constant coefficients, presented in Table 2.1 for $n = 1$, up to $p = 2$. The subscripts n, m represent the degree and order of the 'input' harmonic Y_{nm}; p, q represent a shape 'operator' mixing input harmonics S_{pq} to outputs according to the particular shape of the boundary; n', m' represent the degree and order of the 'output' harmonics $Y_{n'm'}$.

As terms for all n, m are added to the boundary condition equations, we can manipulate the subscripts on ΔB_θ to more easily reduce the equations later. It is convenient to now swap the n, m and n', m' subscripts in Eq. 2.55 so that the *output* harmonics match the indices for the other terms in the n, m series. The subscripts on ΔB_θ can refer to input or output harmonics, so we keep them n, m as before. With these adjustments, Eq. 2.53 results in

$$\Delta B_{\theta,nm} = -\frac{3}{2}\frac{\varepsilon}{a}(ika) \sum_{p,q,m'} B_{e,1m'} \chi_{pq} \Gamma_{1m'pqnm} \frac{\partial Y_{nm}}{\partial \theta}. \tag{2.56}$$

This operation is equivalent to collecting all series terms proportional to $\frac{\partial Y_{nm}}{\partial \theta}$. We now define a quantity Ξ_{nm} that captures the effect on the induced magnetic moment $B_{i,nm}$ based on the boundary shape for a given excitation field:

$$\Xi_{nm} = \sum_{p,q,m'} B_{e,1m'} \chi_{pq} \Gamma_{1m'pqnm}. \tag{2.57}$$

We can now evaluate how the near-spherical boundary shape will impact the induced magnetic moments. The orthogonality of the spherical harmonics may be exploited to obtain a set of 2×2 systems of equations that contain only the unknowns C_{nm} and $B_{i,nm}$ for particular values of n and m. These orthogonality conditions are detailed in Appendix 2.A. For the B_θ conditions, we now need to express $\frac{\partial Y_{nm}}{\partial \theta}$ in terms of other harmonics:

$$\frac{\partial Y_{nm}}{\partial \theta} = m \cot\theta Y_{nm} + \sqrt{(n-m)(n+m+1)} Y_{n,m+1} e^{-i\phi} \tag{2.58}$$

We can now reduce the boundary condition equations. Multiplying both sides of the B_r boundary condition equations (Eq. 2.32) by $Y^*_{n'm'}$ and integrating over a unit sphere is equivalent to replacing Y_{nm} by $\delta_{n,n'}\delta_{m,m'}$. Similarly, multiplying both sides of the B_θ boundary condition equations (Eq. 2.33) by $\left[m \cot\theta Y^*_{nm} - \sqrt{(n-m)(n+m+1)} Y^*_{n,m+1} e^{i\phi}\right]$ and integrating over a unit sphere is equivalent to[1] replacing $\frac{\partial Y_{nm}}{\partial \theta}$ by $\delta_{n,n'}\delta_{m,m'}\left[\frac{m}{2}(2n+1) - m^2 - (n-m)(n+m+1)\right]$. Because every term that survives after applying the delta functions is proportional to this quantity, which can never be zero, it divides away. In addition, all $Y_{n'm'}e^{\pm i\phi}$ terms in Table 2.1 vanish from this operation due to the orthogonality conditions. After these reductions, the external boundary conditions finally become the following set of linear equations:

$$\frac{B_{e,nm}\delta_{1,n}}{n+1} = -\frac{nC_{nm}}{a}\left(j_n(ka) + \Lambda_n y_n(ka)\right) + B_{i,nm} \tag{2.59}$$

$$B_{e,nm}\delta_{1,n} = -\frac{C_{nm}}{a}\left(j^\star_n(ka) + \Lambda_n y^\star_n(ka)\right) - B_{i,nm} - \frac{3}{2}\frac{\varepsilon}{a}(ika)\Xi_{nm}. \tag{2.60}$$

Solving Eq. 2.60 for C_{nm} and inserting into Eq. 2.59, we can solve directly for each induced moment. There is ultimately only a small change from the spherically symmetric solution in Eq. 2.45:

[1] Although this seems to be true when $p_{\max} \leq 2$, upon a more thorough examination we have found this result does not hold in general. See Chapter 4.10 for a rigorous determination of the mixing coefficients we here call $\Gamma_{n'm'pqnm}$.

Shape	$\frac{\partial Y_{1-1}}{\partial\theta}$	$\frac{\partial Y_{10}}{\partial\theta}$	$\frac{\partial Y_{11}}{\partial\theta}$
S_{1-1}	$\frac{1}{2}\sqrt{\frac{4}{5}}\frac{\partial Y_{2-2}}{\partial\theta}$	$\frac{1}{2}\sqrt{\frac{2}{5}}\frac{\partial Y_{2-1}}{\partial\theta}-\frac{\sqrt{3}}{2}Y_{00}e^{-i\phi}$	$\frac{1}{2}\sqrt{\frac{2}{15}}\frac{\partial Y_{20}}{\partial\theta}$
S_{10}	$\frac{1}{2}\sqrt{\frac{1}{5}}\frac{\partial Y_{2-1}}{\partial\theta}+\frac{1}{2}\sqrt{\frac{3}{2}}Y_{00}e^{-i\phi}$	$\frac{1}{2}\sqrt{\frac{4}{15}}\frac{\partial Y_{20}}{\partial\theta}$	$\frac{1}{2}\sqrt{\frac{1}{5}}\frac{\partial Y_{21}}{\partial\theta}-\frac{1}{2}\sqrt{\frac{3}{2}}Y_{00}e^{i\phi}$
S_{11}	$\frac{1}{2}\sqrt{\frac{2}{15}}\frac{\partial Y_{20}}{\partial\theta}$	$\frac{1}{2}\sqrt{\frac{2}{5}}\frac{\partial Y_{21}}{\partial\theta}+\frac{\sqrt{3}}{2}Y_{00}e^{i\phi}$	$\frac{1}{2}\sqrt{\frac{4}{5}}\frac{\partial Y_{22}}{\partial\theta}$
S_{2-2}	$\frac{1}{3}\sqrt{\frac{24}{35}}\frac{\partial Y_{3-3}}{\partial\theta}$	$\frac{1}{3}\sqrt{\frac{8}{35}}\frac{\partial Y_{3-2}}{\partial\theta}-\frac{\sqrt{8}}{3}Y_{1-1}e^{-i\phi}$	$\frac{1}{3}\sqrt{\frac{8}{175}}\frac{\partial Y_{3-1}}{\partial\theta}-\frac{4}{15}\frac{\partial Y_{1-1}}{\partial\theta}$
S_{2-1}	$\frac{1}{3}\sqrt{\frac{16}{35}}\frac{\partial Y_{3-2}}{\partial\theta}+\frac{2}{3}Y_{1-1}e^{-i\phi}$	$\frac{1}{3}\sqrt{\frac{64}{175}}\frac{\partial Y_{3-1}}{\partial\theta}-\frac{4}{3}\sqrt{\frac{8}{25}}\frac{\partial Y_{1-1}}{\partial\theta}$	$\frac{1}{3}\sqrt{\frac{24}{175}}\frac{\partial Y_{30}}{\partial\theta}+\frac{1}{2}\sqrt{\frac{8}{25}}\frac{\partial Y_{10}}{\partial\theta}$
S_{20}	$\frac{1}{3}\sqrt{\frac{18}{175}}\frac{\partial Y_{3-1}}{\partial\theta}+\frac{3}{5}\frac{\partial Y_{1-1}}{\partial\theta}$	$\frac{1}{3}\sqrt{\frac{27}{175}}\frac{\partial Y_{30}}{\partial\theta}-\frac{1}{5}\frac{\partial Y_{10}}{\partial\theta}$	$\frac{1}{3}\sqrt{\frac{18}{175}}\frac{\partial Y_{31}}{\partial\theta}+\frac{3}{5}\frac{\partial Y_{11}}{\partial\theta}$
S_{21}	$\frac{1}{3}\sqrt{\frac{24}{175}}\frac{\partial Y_{30}}{\partial\theta}+\frac{1}{2}\sqrt{\frac{8}{25}}\frac{\partial Y_{10}}{\partial\theta}$	$\frac{1}{3}\sqrt{\frac{64}{175}}\frac{\partial Y_{31}}{\partial\theta}-\frac{4}{3}\sqrt{\frac{8}{25}}\frac{\partial Y_{11}}{\partial\theta}$	$\frac{1}{3}\sqrt{\frac{16}{35}}\frac{\partial Y_{32}}{\partial\theta}-\frac{2}{3}Y_{11}e^{i\phi}$
S_{22}	$\frac{1}{3}\sqrt{\frac{8}{175}}\frac{\partial Y_{31}}{\partial\theta}-\frac{4}{15}\frac{\partial Y_{11}}{\partial\theta}$	$\frac{1}{3}\sqrt{\frac{8}{35}}\frac{\partial Y_{32}}{\partial\theta}+\frac{\sqrt{8}}{3}Y_{11}e^{i\phi}$	$\frac{1}{3}\sqrt{\frac{24}{35}}\frac{\partial Y_{33}}{\partial\theta}$

Table 2.1: Results of multiplying derivatives of normalized spherical harmonics $\frac{\partial Y_{1m}}{\partial\theta}$ by shape harmonics S_{pq}, calculated in terms of derivatives of other normalized spherical harmonics. The functions $Y_{nm}(\theta,\phi)$ and $S_{pq}(\theta,\phi)$ are tabulated in Appendix 2.A. Values for $\Gamma_{nmpqn'm'}$ may be read directly from the table, and are color-coded based on n' of the resulting harmonic (online only). n, m index the column, p, q match the subscripts of the shape functions S, and n', m' identify the term within the corresponding table cell. Entries are calculated by multiplying together the functions found in Appendix 2.A, then solving for the proportionality constant of the highest order resulting harmonic, then using that factor to calculate the next highest order resulting harmonic, and so on.[2] Although the selection rules are nearly identical, the values for $\Gamma_{nmpqn'm'}$ are not the same for $S_{pq}\frac{\partial Y_{nm}}{\partial\theta}$ and $S_{pq}Y_{nm}$. However, because the radial expansion terms vanish, we only tabulate the values for the tangential terms here. In this work, we tabulate only $p = 1, 2$, as magnetic moments of higher than octupole order are expected to be undetectable at spacecraft orbital distances for solar system moons.

[2] In subsequent work (Chapter 4), we have rigorously derived a general formula for calculating the values in this table. The formula we derived (Eq. 4.122) disagrees with the values here. We favor the more rigorous result, and suppose that the approach used to calculate the values here cannot be used to determine the induction response from an asymmetric layer.

$$B_{i,nm} = \frac{B_{e,nm}\delta_{1,n}}{2} - \frac{3}{2}\frac{\varepsilon}{a}\sum_{p,q,m'} B_{e,1m'}\chi_{pq}\Gamma_{1m'pqnm} \tag{2.61}$$
$$= \frac{B_{e,nm}\delta_{1,n}}{2} - \frac{3}{2}\frac{\varepsilon}{a}\Xi_{nm}.$$

It is important to note that some $B_{i,nm}$ will contain terms with excitation moments of differing m'—for example, $B_{i,1-1}$ may contain a term proportional to $B_{e,10}$, as is the case for non-zero χ_{21}. This is true for all boundary surface harmonics of non-zero q. It is immediately apparent that taking $\varepsilon \to 0$ in Eq. 2.61, equivalent to reverting to a spherically symmetric boundary surface, recovers the solution for that configuration (Eq. 2.45).

2.4 Discussion

Here we discuss some key notes regarding our results, elaborate on how they may be applied, and detail the limits of their application.

2.4.1 Superposition of shape harmonics

Eq. 2.61 is linear in all χ and Γ, which is a powerful result. Values for χ_{pq}, which remain attached to terms stemming from shapes S of the same p, q, are all mutually independent. This tells us that the changes to the induced magnetic moments driven by the non-spherical boundary are unique to each boundary harmonic. In other words, the moments induced by each harmonic in the near-spherical boundary shape obey simple superposition. Provided our χ_{pq} yield real values for $r(\theta, \phi)$ with a maximum value of $a + \varepsilon$, they are entirely arbitrary. We can therefore choose any boundary shape as a sum of harmonic functions as in Eq. 2.46 and immediately read values from Table 2.1 to write the magnetic moments induced by this shape.

2.4.2 Application of results

Although Eq. 2.61 appears complicated, its use is made rather simple by considering the entries in Table 2.1. Eq. 2.61 essentially states that induced moments of n, m differ from the spherically symmetric case by $3\varepsilon/2a$ times each value from the table that multiplies $\frac{\partial Y_{nm}}{\partial \theta}$, times $B_{e,1m'}$, with

m' determined by the column. For example, consider the $B_{i,11}$ magnetic moment. The spherically symmetric case has $B_{i,11} = B_{e,11}/2$, so we obtain our result by adding to that. There are three entries in Table 2.1 that multiply a Y_{11} harmonic: $S_{20} \times \frac{\partial Y_{11}}{\partial \theta}$, $S_{21} \times \frac{\partial Y_{10}}{\partial \theta}$, and $S_{22} \times \frac{\partial Y_{1-1}}{\partial \theta}$. The second subscript for each $\frac{\partial Y}{\partial \theta}$ is m', so we multiply the first of these by $B_{e,11}$, the second by $B_{e,10}$, and the third by $B_{e,1-1}$. Therefore, the $B_{i,11}$ induced magnetic moment for the near-spherical case is

$$B_{i,11} = \frac{B_{e,11}}{2} + \frac{3}{2}\frac{\varepsilon}{a}\left(\frac{3}{5}\chi_{20}B_{e,11} - \frac{4}{3}\sqrt{\frac{8}{25}}\chi_{21}B_{e,10} - \frac{4}{15}\chi_{22}B_{e,1-1}\right) \tag{2.62}$$

and the induced magnetic field for this moment is found by taking the real part of Eq. 2.35 with this B_i moment inserted.

We can obtain the same result by examining Eqs. 2.61 and 2.54:

1. We are seeking the contributions to the $n = 1$, $m = 1$ term.

2. $n' = 1$, from our consideration of a uniform field, so the selection rules also tell us that p can be $2, 4, 6, \ldots$ We assume that $p = 3$ and higher harmonics may be neglected in this work, so $p = 2$.

3. m must equal $q + m'$, from the selection rules (recall that Eq. 2.61 has swapped the primed quantities from Eq. 2.54). Therefore, there are contributions to this magnetic moment only for shapes S with $q = 0, 1, 2$.

4. Finally, we multiply $B_{e,1m'}$ by the coefficients for the table entries where $p = 2$, $q + m' = 1$ and insert this product in place of ΓB_e in Eq. 2.61. As before, the table cells are those for $S_{20} \times \frac{\partial Y_{11}}{\partial \theta}$, $S_{21} \times \frac{\partial Y_{10}}{\partial \theta}$, and $S_{22} \times \frac{\partial Y_{1-1}}{\partial \theta}$.

Our method can readily be applied to near-spherical shapes described by a function $r(\theta, \phi) = a + \varepsilon \sum_{p,q} \chi_{pq} S_{pq}$ with p continued to arbitrarily large degree. The values for $\Gamma_{nmpqn'm'}$ in Table 2.1 are simply derived from algorithmic algebra. Entries are calculated by multiplying together the functions in Appendix 2.A, then solving for the proportionality constant of the highest-order resulting harmonic, then using that factor to calculate the next highest-order resulting harmonic,

and so on[3]. This procedure can be used to calculate $\Gamma_{nmpqn'm'}$, which are essentially renormalized Clebsch–Gordan coefficients, for any $S_{pq}\frac{\partial Y_{nm}}{\partial\theta}$ combination. Our choice of normalization in the shape functions S_{pq}, as well as the need for combinations of large angular momenta indices, obfuscates application of standard Clebsch–Gordan tables.

We limit our table of $\Gamma_{nmpqn'm'}$ values to $p = 2$ because the intended application does not require higher-order terms—in future work, we will study the induced magnetic moments for Europa, examining a variety of shapes for the ice–ocean boundary. For planetary bodies, global deviations from spherical symmetry in terms of shape harmonics are expected to be significant only for low-order harmonics. Although more local-scale variation is expected as well, the relative amount χ_{pq} of each shape harmonic represented in the boundary surface $r(\theta, \phi)$ drops quickly with increasing degree p, and local variation is necessarily represented by large values of p. This is essentially a statement that the spectrum of shape harmonics is very red for planetary bodies—weighted toward low frequencies. That is, the power represented by high-order harmonics is negligible, provided small-scale variations are not periodic on a global scale. Induced magnetic moments resulting from each shape harmonic are proportional to χ_{pq}, so the low-order shape harmonics will dominate the contributions to the induced moments, too.

Recent work by Vance et al. (2021) explores the magnetic effects of oceanic flows in the Galilean moons, including Europa. These authors find that, under the approximation of a steady field applied by Jupiter, expected oceanic flows induce measurable signals at orbital distances; they do not attempt to solve the more complicated problem of magnetic induction from a varying jovian field applied to a circulating ocean. The application of a steady-field approximation pairs the results of Vance et al. (2021) well with our results—under the high-conductivity approximation we apply, the time-varying field is entirely excluded from the interior of the ocean, which then experiences a steady field from Jupiter. Combining these results with our model permits calculation of a global induced magnetic field for Europa that is not degenerate in conductivity and boundary shape, even for a single inducing frequency. For highly conducting oceans, no spherically symmetric induction

[3]This approach was later determined to incorrectly calculate the induced moments, due primarily to the lack of orthogonality in the $\frac{\partial Y}{\partial\theta}$ functions—see Section 4.6.5.

model is capable of breaking this degeneracy without either signals measured at multiple frequencies (Saur et al., 2010; Seufert et al., 2011) or complicated modeling of pressure- and temperature-dependence of subsurface conductivity (Vance et al., 2021). Evaluating a global induction model that accounts for induction by oceanic flows may be important to precisely determine signal provenance for future missions, and failure to include these effects increases the uncertainty of measured ocean properties. However, such a synthesis is beyond the scope of this work.

Application to a specific example

Here we consider a specific example and apply our result to planetary magnetic sounding. Computer code written in Python for the calculations in this section is provided in the Supplementary Material. For calculations relating to the *Galileo* E26 flyby, the data set GO-J-MAG-3-RDR-HIGHRES-V1.0 was obtained from the NASA Planetary Data System (PDS).

Tobie et al. (2003) considered tidal heating and heat transport through Europa's ice shell. From numerical models of thermodynamics, these authors concluded that the shell is roughly 22.5 km thick and may be as much as 5 km thicker at the sub- and anti-jovian points than at midlatitudes. The maxima in thickness can be approximated by choosing

$$\varepsilon = 2.5\,\mathrm{km}, \quad a = 1537.5\,\mathrm{km}, \quad \chi_{2-2} = \chi_{22} = \frac{1}{2} \tag{2.63}$$

in Eq. 2.46. The minima in thickness at midlatitudes require other shape harmonics, but for simplicity we consider only one real harmonic—this linear combination of shape harmonics is equivalent to choosing $r = a + \varepsilon \sin^2\theta \cos 2\phi$.

The uniform excitation field Jupiter applies to Europa can be approximated as

$$\mathbf{B}_{\mathrm{Jup}} = (B_{ex}\hat{x} + iB_{ey}\hat{y})e^{-i\omega t}, \tag{2.64}$$

where the directions are in Europacentric E$\phi\Omega$ coordinates—$\hat{x}$ is along Europa's orbital velocity vector and $\hat{y}$ is approximately toward Jupiter's center. As in the work of Schilling et al. (2007), we take the amplitudes of oscillation to be $B_{ex} = 84\,\mathrm{nT}$, $B_{ey} = -210\,\mathrm{nT}$. From these we obtain $B_{e,1-1} \approx -425\,\mathrm{nT}$, $B_{e,10} = 0$, $B_{e,11} \approx -182\,\mathrm{nT}$. We will obtain induced magnetic moments from

four cells of Table 2.1, where the $\frac{\partial Y_{1-1}}{\partial\theta}$ and $\frac{\partial Y_{11}}{\partial\theta}$ columns of the excitation field meet the S_{2-2} and S_{22} rows of the boundary shape. From Eq. 2.61, the non-zero induced magnetic moments for this configuration will be

$$B_{i,nm} = \frac{B_{e,nm}\delta_{1,n}}{2} - \frac{3}{2}\frac{\varepsilon}{a}\sum_{p,q,m'} B_{e,1m'}\chi_{pq}\Gamma_{1m'pqnm}$$

$$B_{i,1-1} = \frac{B_{e,1-1}}{2} + \frac{3\varepsilon}{2a}B_{e,11}\cdot\frac{1}{2}\cdot\frac{-4}{15} = \frac{1}{2}B_{e,1-1} - \frac{\varepsilon}{5a}B_{e,11} \tag{2.65}$$

$$B_{i,11} = \frac{B_{e,11}}{2} + \frac{3\varepsilon}{2a}B_{e,1-1}\cdot\frac{1}{2}\cdot\frac{-4}{15} = \frac{1}{2}B_{e,11} - \frac{\varepsilon}{5a}B_{e,1-1} \tag{2.66}$$

$$B_{i,3-3} = \frac{3\varepsilon}{2a}B_{e,1-1}\cdot\frac{1}{2}\cdot\frac{1}{3}\sqrt{\frac{24}{35}} = \frac{\varepsilon}{a}\sqrt{\frac{3}{70}}B_{e,1-1} \tag{2.67}$$

$$B_{i,3-1} = \frac{3\varepsilon}{2a}B_{e,11}\cdot\frac{1}{2}\cdot\frac{1}{3}\sqrt{\frac{8}{175}} = \frac{\varepsilon}{5a}\sqrt{\frac{1}{14}}B_{e,11} \tag{2.68}$$

$$B_{i,31} = \frac{3\varepsilon}{2a}B_{e,1-1}\cdot\frac{1}{2}\cdot\frac{1}{3}\sqrt{\frac{8}{175}} = \frac{\varepsilon}{5a}\sqrt{\frac{1}{14}}B_{e,1-1} \tag{2.69}$$

$$B_{i,33} = \frac{3\varepsilon}{2a}B_{e,11}\cdot\frac{1}{2}\cdot\frac{1}{3}\sqrt{\frac{24}{35}} = \frac{\varepsilon}{a}\sqrt{\frac{3}{70}}B_{e,11}. \tag{2.70}$$

Of the flybys the *Galileo* spacecraft made past Europa, the E26 flyby had perhaps the most significant magnetic measurements confirming the subsurface ocean there. Data from the E26 flyby ruled out significant intrinsic magnetic moments (Kivelson et al., 2000; Schilling et al., 2004), and the strength of the signal encountered has encouraged the interpretation that the subsurface ocean is quite saline (Hand and Chyba, 2007). The E26 flyby had a closest approach altitude of 373 km over Europa (Kivelson et al., 2000). With the induced moments we have calculated for the shape just described, at this distance the induced magnetic field accounts for about 54.25 nT of the observed signal. If we instead assume spherical symmetry in the ice–ocean boundary, at this distance the induced magnetic field accounts for a negligible difference to the expected signal, approximately 54.27 nT. The observed signal therefore differs by only about 0.02 nT in the interpretation of *Galileo* data based on this boundary shape, and Europa resides in a region where plasma fluctuations routinely force uncertainties on the order of 10 nT (Schilling et al., 2004). It is therefore apparent that the *Galileo* data are insufficient to resolve the shape suggested by Tobie et al. (2003). However, this does not imply that the *Galileo* data are incapable of resolving a non-spherical ice–ocean boundary;

in future work, we will explore what limits may be placed from the existing data. The degree of departure from spherical symmetry in the example shape we applied may be quantified by the ratio ε/a, which for this shape was $2.5\,\mathrm{km}/1537.5\,\mathrm{km} \approx 0.0016$. A boundary shape deviating more from spherical symmetry will have a proportionally greater effect on the induced magnetic field.

The upcoming *Europa Clipper* mission will have several flybys within 25 km of Europa's surface. At this low altitude, but with the same flyby orientation as *Galileo* E26, the difference in field magnitude from assuming the ice–ocean boundary shape described by Tobie et al. (2003) is instead about 0.06 nT. In order to produce a difference in the magnitude of the induced field of greater than 1.0 nT, assuming the same flyby geometry and shape harmonics in the boundary, ε must be at least 24.5 km, with a correspondingly thicker average ice shell. This unlikely scenario would result in an ice shell of vanishing thickness at the leading and trailing points that is 49 km thick at the sub- and anti-jovian points. Examining the effect on individual components of the magnetic field is more likely to produce a measurable signal—we take a naive approach here only to demonstrate how our model may be applied.

Even for the shape described in Eq. 2.63, a lander at the sub-jovian point would likely experience such a measurable signal. Our model predicts a difference of about $1/2$ nT in the vertical component ($\mathrm{E}\phi\Omega\ \hat{y}$) of the magnetic field[4] compared to the spherically symmetric case at peak times during Europa's synodic period with Jupiter, despite a negligible change in field magnitude. Figure 2.2 shows the approximate vertical component of the net magnetic field (excitation field + induced field) experienced by a lander at the sub-jovian point on Europa's surface through a synodic period with Jupiter. The vertical component experiences a larger signal because under the high-conductivity approximation, the radial component of the time-varying field is entirely canceled at the outer boundary of the conducting surface (Parkinson, 1983). At Europa's surface, the conducting boundary is 22.5 km below the lander for the spherically symmetric case, and 25 km below the lander for the non-spherical example case. The additional difference results in induced currents generating the measured magnetic fields that are farther from the measurement point, so the time-

[4]The more rigorous analysis we perform in Chapter 4.10 has resulted in a larger effect size for the considered difference. Refer to Figure 4.5 for an updated version of this plot, which shows a difference about 5 times larger.

varying radial field is not as effectively canceled. This highlights the importance of considering the overall structure of the magnetic field measured by visiting spacecraft, and other harmonics in the boundary shape may have a more pronounced response. In addition, future magnetic measurements from Europa's surface must account for possible asymmetry in the ice–ocean boundary, lest these signals be incorrectly attributed to another source.

Although our calculated values are small compared to systematic uncertainties for *Galileo* MAG due to plasma effects, we do not mean to suggest that the magnetic effects of an asymmetric ice–ocean boundary are negligible for orbiting spacecraft. *Europa Clipper* will have numerous close flybys at varying combinations of latitude, longitude, and System III (jovian) longitude that will present wider variation in magnetic conditions. Plasma measurements by the PIMS instrument (Grey et al., 2018) will also aid in far better characterization of Europa's plasma environment than was possible with the compromised *Galileo* data return, which will support better removal of plasma signals from magnetic data. Furthermore, the overall shape of the induced magnetic field varies with differing induced moments, and changes in global field will be better captured by least-squares comparison to flyby measurements than by individual locations. In this work, we endeavor only to demonstrate how our results may be applied in the study of magnetic sounding.

2.4.3 Limits of applicability

The approximations we have made in order to obtain solutions for $\boldsymbol{B}_{i,nm}$ limit the applicability of our results. We now discuss the implications for each approximation we make and necessary considerations for the application of our results to physical situations.

Chiefly, we have assumed that kr is effectively infinite; in real applications, it will be large for planetary bodies and good conductors, but not infinite. We are therefore assuming that the induced moments are sensitive only to the shape of the *outermost* boundary surface. For intended future applications of these results, examining the effects of non-uniform conductivity structures $\sigma(\mathbf{r})$ expected to be present in ocean worlds, this approximation cannot be applied. Instead, numerical values for kr, $j_n(kr)$, and $y_n(kr)$ for layers of approximately uniform conductivity must be inserted into the boundary conditions between each layer. An approach to do this for the spherically symmet-

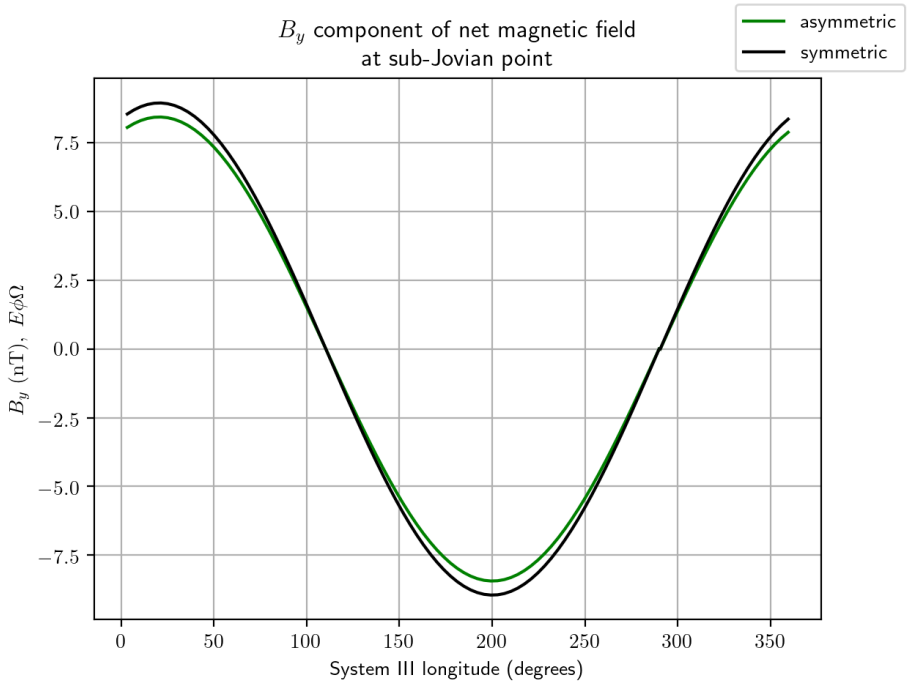

Figure 2.2: The vertical component of the net magnetic field at the sub-jovian point on Europa's surface for two cases: an asymmetric ice–ocean boundary with a shape described by Eq. 2.63, based on Tobie et al. (2003), and a spherically symmetric ice–ocean boundary with the same average ice shell thickness, 22.5 km. The maximum difference, which occurs when Jupiter's dipole moment nods directly toward or away from Europa, is approximately $1/2$ nT for this component of the magnetic field.[5] Our results demonstrate that even modest variation in ice shell thickness must be accounted for in understanding magnetic measurements by a lander on Europa's surface.

[5] The more rigorous analysis we perform in Chapter 4.10 has resulted in a larger effect size for the considered difference. Refer to Figure 4.5 for an updated version of this plot, which shows a difference about 5 times larger.

ric case was first published by Srivastava (1966), and summarized by Parkinson (1983). Concentric near-spherical shapes may be possible to combine with the technique pioneered by Srivastava, further extending the utility of our results. Whether simple superposition of boundary shapes would continue to hold for finite kr is a topic for future study.

The assumption that $\mu = \mu_o$ for the conducting body is completely overshadowed by the assumption that $kr \to \infty$, because k is proportional to $\sqrt{\mu}$, which can only be $\sqrt{\mu_o}$ or greater. In any future applications where kr is finite, non-unity μ/μ_o must be considered and incorporated, but for planetary applications the difference will still be insignificant.

Also overshadowed by assuming infinite kr is any contribution to the induced magnetic moments by buried conducting layers of much higher or lower conductivity. For example, all known ocean worlds contain rocky mantles beneath their ice and ocean layers. Except when very well hydrated, rocks are typically very poor conductors (Khurana et al., 2002). The finite depth of conducting oceans on these bodies will limit the induction response, especially for very low frequencies, where $|kr|$ takes smaller values. In addition, deep layers of high conductivity, as in the case of an iron core, which may be present within Europa, could contribute to the induced magnetic field. As described above, numerical calculations would be required to accurately represent finite-depth layers of differing conductivity, whether it grows or shrinks with depth.

We also assumed that the excitation field applied to the conducting body may be treated as uniform. This is a standard assumption, as the complexity introduced by non-uniform excitation fields is great: Magnetic moments matching the order of the spherical harmonics in the non-uniform field are induced, even for the case of a spherically symmetric boundary. For a near-spherical boundary, powers of r in the new terms for the excitation field introduce more mixing between harmonics, because they must be replaced by $r(\theta, \phi)$ in the boundary condition equations. However, deviations from uniformity encountered in physical applications are typically small, or other approximations, like considering only far-field solutions, render the higher-order terms insignificant. The boundary condition equations could be updated to reflect a non-uniform field without difficulty, but that task is left to the applications that may require it.

The assumption that we may safely neglect terms of second order or higher in ε/a is dictated by

the sensitivity of measurement equipment for the induced magnetic field. For Europa's relatively thin ice shell, which could average 30 km thick (Hand and Chyba, 2007), the maximum possible value for $\varepsilon/a = 30/(1560 - 30) \approx 0.02$ for a nominal 1,560 km planetary radius. Differences in the induced magnetic moments compared to the spherically symmetric case will be of this order of magnitude. In practice, the space around planetary bodies is far from a vacuum, and this reduces the need to consider higher-order terms in ε/a. The planets' extensive magnetospheres contain plasma flows that contribute short-period fluctuations to the measured magnetic fields. These extraneous signals are difficult to model, and even harder to extract from measurements, diminishing the precision that may be afforded in measuring the induced magnetic fields of target bodies. Incorporating higher-order terms in ε/a would be best accomplished by numerically solving the boundary conditions for $B_{i,nm}$, and would likely result in a violation of the superposition of boundary shape harmonics.

We chose to tabulate values only for shapes of harmonic order $p = 1, 2$ due to rapid decline of the magnitude of χ_{pq} with increasing p. As explained in Section 2.4.2, our methods can readily be applied to shape harmonics of higher order, but high-order shape harmonics are not expected for planetary bodies. For applications where higher-order shape harmonics are needed, the necessary $\Gamma_{nmpqn'm'}$ values can easily be calculated.

2.5 Conclusions

This work represents the first appearance in the literature of a solution to the boundary value problem of the induced magnetic moments for a near-spherical conducting body. Although the approximations we make limit the applicability of our results, the conditions under which these approximations are valid are critical areas of study. Our approximations readily apply to the many ocean worlds scattered throughout the solar system. Any planetary body with globally distributed conducting material that is subjected to a uniform oscillatory magnetic field may be described by our results. Synergy with other recent work (*e.g.* Vance et al., 2021) may even permit independent determination of conductivity and ocean shape, which are degenerate under our approximations and the standard spherically symmetric models of Zimmer et al. (2000) and Schilling et al. (2007). In

addition, near-spherical conducting bodies on a laboratory scale may be described by our results, provided they too are subjected to a uniform excitation field and are highly conducting.

Calculations using a simplified model with the results we present here demonstrate that future missions, especially those that land on Europa's surface, must account for asymmetries in the ice–ocean boundary. Our results suggest that at the surface, signals on the order of nT may be observed for even modest variations in ice shell thickness. Furthermore, these signals are likely to be resolvable at orbital distances, including for *Europa Clipper*, especially if measurement precision reaches 0.1 nT. A failure to include subsurface asymmetry will result in incorrect attribution of these signals to other processes, and increase uncertainties in valuation of subsurface properties.

This work was motivated by the lack of resources in the literature for this very problem. In future work, we aim to constrain the departure from spherical symmetry that may be present in the shape of the ice–ocean boundary beneath Europa's crust, to the extent possible with *Galileo* data. We will accomplish this by comparing the induced magnetic moments for boundary shapes representing characteristic extremes that may be expected from geological, orbital, and thermodynamic constraints to magnetic measurements from the *Galileo* mission. Calculating the induced magnetic moments using the results of this work will make that study possible.

Acknowledgments

This work was supported by NASA Headquarters under the NASA Earth and Space Science Fellowship Program — Grant 80NSSC18K1236. The authors thank S. Vance and C. Paty for insightful guidance, and D. Pickard for instrumental suggestions. The GO-J-MAG-3-RDR-HIGHRES-V1.0 data set was obtained from the Planetary Data System (PDS). The authors also thank two anonymous reviewers for their detailed comments, which improved this manuscript.

2.A Special functions

Calculation of induced magnetic moments up to $n = 3$ requires orthonormal expressions for spherical harmonics up to the same degree. In this work, we use the fully normalized spherical harmonics

to calculate our results in Table 2.1:

$n = 0$:

$$Y_{00} = \frac{1}{2}\sqrt{\frac{1}{\pi}}$$

$n = 1$:

$$Y_{1-1} = \frac{1}{2}\sqrt{\frac{3}{2\pi}}e^{-i\phi}\sin\theta$$
$$Y_{10} = \frac{1}{2}\sqrt{\frac{3}{\pi}}\cos\theta$$
$$Y_{11} = -\frac{1}{2}\sqrt{\frac{3}{2\pi}}e^{i\phi}\sin\theta$$

$n = 2$:

$$Y_{2-2} = \frac{1}{4}\sqrt{\frac{15}{2\pi}}e^{-2i\phi}\sin^2\theta$$
$$Y_{2-1} = \frac{1}{2}\sqrt{\frac{15}{2\pi}}e^{-i\phi}\sin\theta\cos\theta$$
$$Y_{20} = \frac{1}{4}\sqrt{\frac{5}{\pi}}(3\cos^2\theta - 1)$$
$$Y_{21} = -\frac{1}{2}\sqrt{\frac{15}{2\pi}}e^{i\phi}\sin\theta\cos\theta$$
$$Y_{22} = \frac{1}{4}\sqrt{\frac{15}{2\pi}}e^{2i\phi}\sin^2\theta$$

$n = 3$:

$$Y_{3-3} = \frac{1}{8}\sqrt{\frac{35}{\pi}}e^{-3i\phi}\sin^3\theta$$
$$Y_{3-2} = \frac{1}{4}\sqrt{\frac{105}{2\pi}}e^{-2i\phi}\sin^2\theta\cos\theta$$
$$Y_{3-1} = \frac{1}{8}\sqrt{\frac{21}{\pi}}e^{-i\phi}\sin\theta(5\cos^2\theta - 1)$$
$$Y_{30} = \frac{1}{4}\sqrt{\frac{7}{\pi}}(5\cos^3\theta - 3\cos\theta)$$
$$Y_{31} = -\frac{1}{8}\sqrt{\frac{21}{\pi}}e^{i\phi}\sin\theta(5\cos^2\theta - 1)$$
$$Y_{32} = \frac{1}{4}\sqrt{\frac{105}{2\pi}}e^{2i\phi}\sin^2\theta\cos\theta$$
$$Y_{33} = -\frac{1}{8}\sqrt{\frac{35}{\pi}}e^{3i\phi}\sin^3\theta.$$

In this normalization, the spherical harmonics satisfy the orthogonality conditions (Abramowitz and Stegun, 1972)

$$\int_0^{2\pi}\int_0^{\pi} Y^*_{nm}Y_{n'm'}\ \sin\theta d\theta d\phi = \delta_{n,n'}\delta_{m,m'}$$
$$\int_0^{2\pi}\int_0^{\pi} Y^*_{nm}Y_{n'm'}\ \csc\theta d\theta d\phi = \frac{2n+1}{2m}\delta_{n,n'}\delta_{m,m'},$$

where δ are Kronecker delta functions.

Deviations from spherical symmetry of the conducting body's outer surface are represented by spherical harmonics, up to degree $p = 2$ in this work. Boundary shape harmonics S_{pq} are

normalized such that the range of each function is $|S_{pq}(\theta, \phi)| \leq 1$. This ensures that the maximum radial deviation from spherical symmetry is ε when the boundary shape is described by

$$r(\theta, \phi) = a + \varepsilon \sum_{p,q} \chi_{pq} S_{pq}(\theta, \phi).$$

To represent physical boundaries, χ_{pq} will either be purely real or purely imaginary, and a and ε will be purely real. Typically $\sum |\chi_{pq}| = 1$; this is not strictly true because the range of S_{20} is not symmetric about zero. The shape harmonics we use are as follows:

$$\begin{aligned}
p = 1 :& \\
S_{1-1} &= e^{-i\phi} \sin\theta \\
S_{10} &= \cos\theta \\
S_{11} &= -e^{i\phi} \sin\theta
\end{aligned}
\qquad
\begin{aligned}
p = 2 :& \\
S_{2-2} &= e^{-2i\phi} \sin^2\theta \\
S_{2-1} &= 2e^{-i\phi} \sin\theta \cos\theta \\
S_{20} &= \frac{1}{2}(3\cos^2\theta - 1) \\
S_{21} &= -2e^{i\phi} \sin\theta \cos\theta \\
S_{22} &= e^{2i\phi} \sin^2\theta.
\end{aligned}$$

Note that we retain the Condon–Shortley phase, negating the $q = 1$ shapes.

Chapter 3

MAGNETIC INDUCTION IN THE GALILEAN MOONS WITH DEPTH-DEPENDENT PROPERTIES AND OCEAN FLOWS

This chapter consists of a peer-reviewed publication in the *Journal of Geophysical Research: Planets.* The original version is available from the publisher at https://doi.org/10.1029/2020JE006418. The main text and figures are reproduced here in their entirety with changes only to the formatting, including breaking long tables across pages; cited references appear in the Bibliography at the end of this dissertation. Computer programs contained in the Supplemental Material are available from the publisher along with the main text at the link above. A supplement containing Supporting Information follows the main text within this chapter.

Reference

"Magnetic Induction Responses of Jupiter's Ocean Moons Including Effects from Adiabatic Convection." S. D. Vance, M. J. Styczinski, B. G. Bills, C. J. Cochrane, K. M. Soderlund, N. Gómez-Pérez, and C. Paty, 2021. *Journal of Geophysical Research: Planets* **126**(2), copyright ©2021 John Wiley & Sons.

Magnetic Induction Responses of Jupiter's Ocean Moons Including Effects from Adiabatic Convection

Part 1: Main text

S. D. Vance[1], M. J. Styczinski[2], B. G. Bills[1], C. J. Cochrane[1], K. M. Soderlund[3], N. Gómez-Pérez[4], and C. Paty[5]

[1] Jet Propulsion Laboratory, California Institute of Technology

[2] Department of Physics, University of Washington

[3] Institute for Geophysics, John A. & Katherine G. Jackson School of Geosciences, The University of Texas at Austin

[4] British Geological Survey

[5] Department of Earth Sciences, University of Oregon

Abstract

Prior analyses of oceanic magnetic induction within Jupiter's large icy moons have assumed uniform electrical conductivity. However, the phase and amplitude responses of the induced fields will be influenced by the natural depth-dependence of the electrical conductivity. Here, we examine the amplitudes and phase delays for magnetic diffusion in modeled oceans of Europa, Ganymede, and Callisto. For spherically symmetric configurations, we consider thermodynamically consistent interior structures that include realistic electrical conductivity along the oceans' adiabatic temperature profiles. Conductances depend strongly on salinity, especially in the large moons. The induction responses of the adiabatic profiles differ from those of oceans with uniform conductivity set to values at the ice–ocean interface, or to the mean values of the adiabatic profile, by more than 10% for some signals. We also consider motionally induced magnetic fields generated by convective fluid motions within the oceans, which might optimistically be used to infer ocean flows or, pessimistically, act to bias the ocean conductivity inversions. Our upper-bound scaling estimates suggest this effect may be important at Europa and Ganymede, with a negligible contribution at Callisto. Based on

end-member ocean compositions, we quantify the magnetic induction signals that might be used to infer the oxidation state of Europa's ocean and to investigate stable liquids under high-pressure ices in Ganymede and Callisto. Fully exploring this parameter space for the sake of planned missions requires thermodynamic and electrical conductivity measurements in fluids at low temperature and to high salinity and pressure as well as modeling of motional induction responses.

PLAIN LANGUAGE SUMMARY: Oscillations in a planet's magnetic fields can create magnetic signals within its companion moons if those moons have salty oceans under their icy surfaces. Fluid currents within those oceans can also create magnetic fields. Spacecraft investigating those oceans can measure such fields and thereby learn about the properties of the oceans. We compute possible magnetic properties for Jupiter's ocean moons—Europa, Ganymede, and Callisto—using available chemical data and electrical conductivity. Previous work has also computed these properties, but our methods allow us to account for how the electrical properties vary with depth due to pressure and temperature. We also model ocean currents. We find that the depth-dependence of electrical conductivity affects the predicted magnetic fields more than 1 nT as compared with the typical assumption of a uniform conductivity. This is important because the planned *Europa Clipper* and *JUpiter ICy moons Explorer (JUICE)* missions are expected to measure magnetic fields at these moons with better than 1 nT precision. For Europa, we examine Seawater (mostly NaCl) and $MgSO_4$ ocean compositions linked to more hydrogen-rich or oxygen-rich scenarios. With prior constraints on ice shell and ocean thickness, magnetic measurements may be a key tool for determining the composition of Europa's ocean, and thus its chemical evolution through time.

3.1 Introduction

The jovian system is of particular interest for studying magnetic induction in icy ocean worlds. Jupiter has a strong magnetic field whose dipole axis is tilted 9.6° with respect to its rotation axis (Acuña and Ness, 1976), while the orbits of the Galilean moons lie very nearly in the equatorial plane of Jupiter. This means that Jupiter's magnetic field varies in time at the orbital positions of the satellites. Also, the outer layers of the satellites themselves are believed to consist mainly of water ice at the surface, underlain by salty oceans. Brines are good conductors, while ice is a significant

insulator.

Magnetic induction from Jupiter's diurnal signal sensed by the *Galileo* mission provides the most compelling direct observational evidence for the existence of oceans within Europa and Ganymede (Khurana et al., 1998; Saur et al., 1998; Kivelson et al., 2000; Hand and Chyba, 2007; Schilling et al., 2007; Khurana et al., 2009). The case has also been made for an induction response from an ocean in Callisto (Zimmer et al., 2000), but this interpretation may be clouded by interactions with the peak of the jovian current sheet and by ionospheric interactions (Liuzzo et al., 2015; Hartkorn and Saur, 2017).

Longer-period signals penetrate more deeply, as penetration of the magnetic field into the interior is a diffusive process. It is convenient that the skin depths at the dominant periods of variation experienced by Europa, Ganymede, and Callisto are comparable to the expected ocean depths, which makes it possible to probe the properties of their oceans using magnetic induction (Saur et al., 2010). The spectrum of frequencies driving induced magnetic responses includes not just the orbits of the Galilean satellites and the rotation of Jupiter's tilted dipole field, but also their harmonics and natural oscillations of the magnetospheric structure relative to the satellites' orbital locations (Seufert et al., 2011). Electrical conductivity structure within the subsurface oceans—for example, from convective adiabatic temperature gradients (Vance et al., 2018) and stratification (Vance and Goodman, 2009)—will affect the induction response at these frequencies.

Further variations in the magnetic fields arise from the motion of the moons about Jupiter. Perturbations to the orbits of the moons arise from multiple sources, including the oblate figure of Jupiter, gravitational interactions with the other satellites, and even from Saturn and the Sun (Lieske, 1998; Lainey et al., 2006). These subtle perturbations introduce additional frequencies of oscillation in the magnetic fields the bodies experience. These additional oscillations, in turn, induce magnetic fields that oscillate on the same time scales. A complete understanding of the dominant frequencies of oscillation is vital to a physically consistent interpretation of spacecraft measurements; for our analysis, we use the NAIF-produced SPICE kernels to obtain the most precise ephemeris data available as they include the orbital perturbations responsible for most magnetic oscillation for the bodies we study.

An additional induced magnetic response may occur in the icy Galilean satellites, arising not from Jupiter's changing magnetic field, but from motions of salty water within the oceans themselves. Such motionally induced magnetic fields are typically neglected because they are expected to be relatively weak. On Earth, ocean currents induce fields on the order of 100 nT in a background field of about 40 000 nT; these fields are observable by space-based magnetometers and have been used to monitor ocean currents (Tyler et al., 2003; Constable and Constable, 2004b). If there are motional induction signals present in the icy Galilean satellites, and if the spatial or temporal structures of these induction signals allow them to be separated from the contributions driven by variations in the jovian magnetic field, it would permit characterization of the ocean flows themselves as has been done for the oceans of Earth (*e.g.* Chave, 1983; Tyler et al., 2003; Grayver et al., 2016; Minami, 2017). Conversely, if such induced signals are present but the analysis of spacecraft magnetic field measurements does not accommodate that fact, then the recovered electrical conductivity estimates may be biased and inaccurate.

Here, we examine the amplitudes and phase delays for magnetic diffusion in modeled oceans of Europa, Ganymede, and Callisto. For Europa, we focus on whether these responses might reveal not just the ocean's thickness and electrical conductivity, but also the speciation of dissolved salts in the ocean—here either $MgSO_4$ or Seawater dominated by NaCl. We restrict our analysis to spherically symmetric configurations, treating interior structures based on self-consistent thermodynamics, which account for variations in electrical conductivity with depth in convective oceans (Vance et al., 2018).

In addition, we consider the generation of motionally induced magnetic fields due to oceanic thermal convection and estimate upper-bound field amplitudes using a scaling analysis. Based on end-member ocean compositions (Zolotov, 2008; Zolotov and Kargel, 2009), we demonstrate the possibilities for using magnetic induction to infer the oxidation state of Europa's ocean and to identify stable liquid layers under high-pressure ices in Ganymede and Callisto.

In Section 3.2, we examine the diffusive induction response of Jupiter's ocean moons. We build on the prior work of Seufert et al. (2011) by including electrical conductivity profiles that follow the adiabatic profiles of pressure and temperature within the ocean of each moon. In Section 3.3,

we describe possible ocean flows due to thermal convection (assuming the models of Soderlund, 2019) and use a scaling relationship to estimate upper bounds for motionally induced magnetic field strengths. In Section 3.4, we discuss these results and describe the prospects for detecting signals from each. The Supporting Information includes detailed derivations of the theoretical techniques we use to model the induced magnetic fields, as well as additional results for field components not covered in Sections 3.2–3.4.

3.2 Diffusive induction in Jupiter's ocean moons

The complex response to the excitation field $\mathcal{A}_1^e$ describes the frequency-dependent, normalized amplitude $A = |\mathcal{A}_n^e|$ and phase delay $\phi = -\arg(\mathcal{A}_n^e)$ for a uniform excitation field from Jupiter (degree $n = 1$). We compute the magnetic induction amplitude and phase delay for a spherically symmetric system with multiple conducting layers. This complex response function is the same as employed by *e.g.* Zimmer et al. (2000), Khurana et al. (2002), and Seufert et al. (2011), generalized to an arbitrary number of layers and any degree n in the excitation field. A derivation for this solution was first described by Srivastava (1966). Our adapted version from Eckhardt (1963) is provided in the Supporting Information, along with a description of the optimized numerical implementation used in this work. The analytical benchmark described in the supplement builds on recent work by Styczinski et al. (*submitted*—Chapter 4) examining perturbations from spherical symmetry.

3.2.1 Spectral content of the imposed magnetic field variations

Temporal variations in the magnetic field occur in the reference frames of Jupiter's satellites. Figure 3.1 shows time series spectra over the range of periods showing the strongest components for each of Europa, Ganymede, and Callisto, arising from their orbital and synodic periods, as well as beats and harmonics of these periods. Table 3.1 lists the three main periods (in hr) and the corresponding component fields (in nT). For these analyses, we use body-centric $\phi\Omega$ coordinates E$\phi\Omega$, G$\phi\Omega$, and C$\phi\Omega$ (*e.g.* "E-phi-O", Khurana et al., 2009). In these coordinate systems, $\hat{x}$ is directed

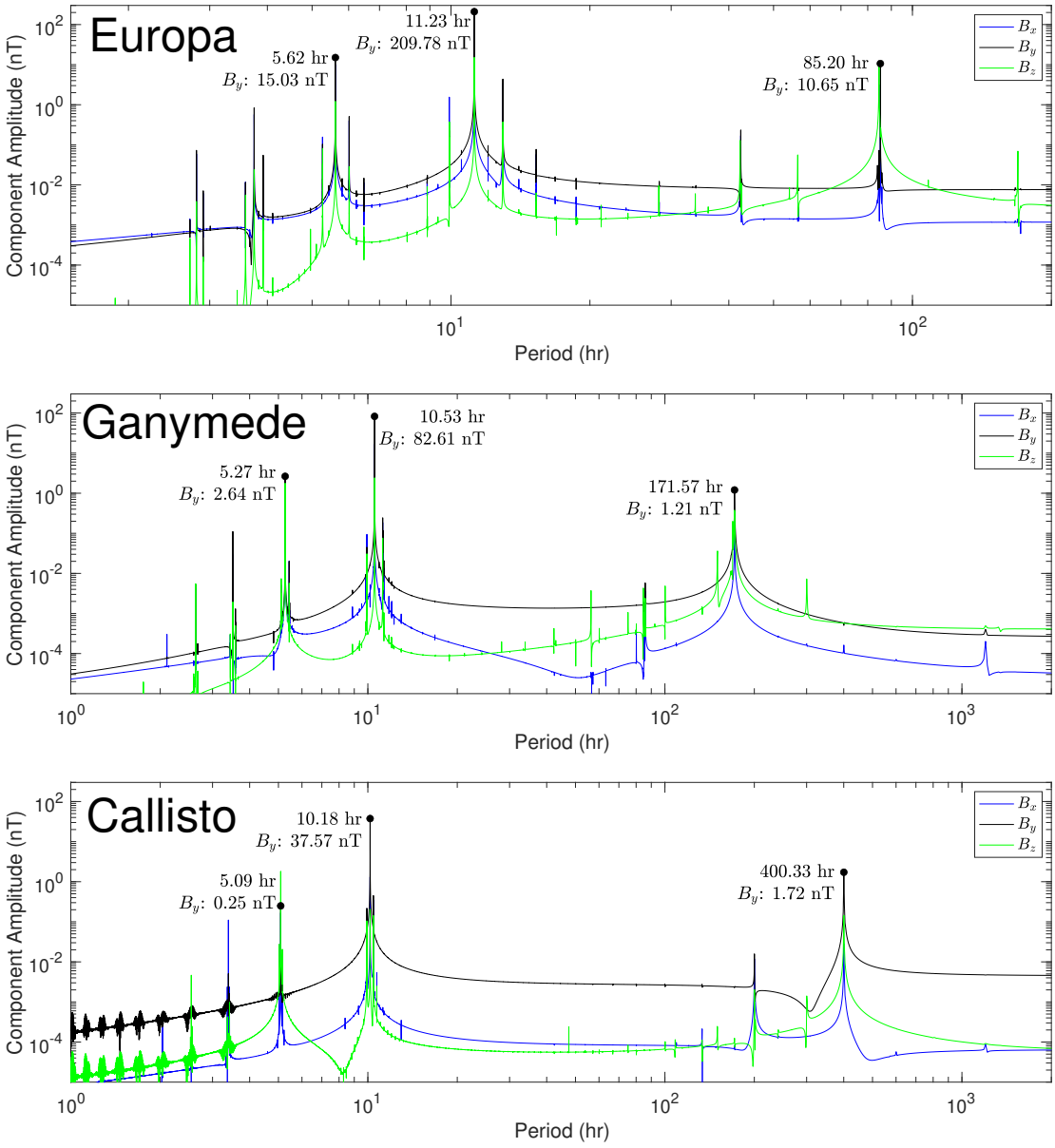

Figure 3.1: Time series spectra (in hr) for the largest magnetic field oscillations (in nT) experienced by the Galilean moons. Variations in orbital parameters over time introduce magnetic fluctuations at multiple periods in addition to Jupiter's synodic rotation and the satellites' orbits. The coordinate axes are detailed in Section 3.2.1. Peak values for the main three periods for each moon are provided in Table 3.1. The input time series is ten years long; the spectra are sampled with about 500 000 data points in uniform, ten-minute increments.

	Period (hr)		
	$B_{x,y,z}$ (nT)	$B_{x,y,z}$ (nT)	$B_{x,y,z}$ (nT)
Europa	**5.62**	**11.23**	**85.20**
	10.03 15.03 1.22	75.55 209.78 15.24	3.17 10.65 11.97
Ganymede	**5.27**	**10.53**	**171.57**
	1.76 2.64 1.78	16.64 82.61 2.42	0.14 1.21 0.38
Callisto	**5.09**	**10.18**	**400.33**
	0.17 0.25 1.82	1.31 37.57 0.20	0.03 1.72 0.14

Table 3.1: Peak periods (in hr) and component field strengths (in nT) for the time series spectra shown in Figure 3.1.

along the corotation direction, approximately along the orbital velocity vector, $\hat{y}$ is directed toward the jovian spin axis, approximately toward Jupiter's center of mass, and $\hat{z}$ is directed along the jovian spin axis in a right-handed sense. These coordinate systems are constantly rotating, and remain fixed to center of each satellite. Seufert et al. (2011) determined the time series spectra for the time-varying magnetic perturbations applied to each of the four Galilean moons based on the VIP4 model of Connerney et al. (1998) combined with the jovian current sheet model of Khurana (1997). In contrast, we use the JRM09 Jupiter field model accounting for more recent *Juno* measurements (Connerney et al., 2018). Paired with this model, we use the current sheet model of Connerney et al. (1981) because the JRM09 model is derived using this current sheet model. Together, the latter two match the *Juno* measurements well. We compute a time series of the field at the orbital positions of the moons using the NAIF SPICE kernels and ten years of data sampled at a ten-minute cadence. To determine the primary periods relevant to the diffusive interaction with the satellites, we compute the Fourier transform of the entire data set.

We note that Seufert et al. (2011) also examined the time series spectra of magnetic perturbations from dynamic migration of the jovian magnetopause based on solar wind data from the Ulysses

spacecraft, which we do not consider.

The temporal variations in imposed magnetic field at each satellite depend on the orbits of the satellites and the magnetic field of Jupiter. To find them, we compute Jupiter's magnetic field in a Jupiter-centered coordinate system from a spherical harmonic series representation of the magnetic potential (Parkinson, 1983):

$$\Phi(r,\theta,\phi,t) = R\sum_{n=1}\left(\frac{R}{r}\right)^{n+1}\sum_{m=0}^{n} S_{n,m}(\theta,\varphi)\mathrm{e}^{-i\omega t} \tag{3.1}$$

for Jupiter's rotation rate ω and R the outer radius of the body. The internally generated magnetic field vector is the negative gradient of the scalar potential

$$\mathbf{B}_{\text{int,Jup}} = -\nabla\Phi \tag{3.2}$$

The external field including the current systems is

$$\mathbf{B}_{\text{external}} = \nabla\times\mathbf{A}(\rho',z')\mathrm{e}^{-i\omega t} \tag{3.3}$$

where $\mathbf{A}(\rho',z')$ is described by the current sheet model of Connerney et al. (1981), ρ' and z' are radial and axial coordinates in the magnetic equatorial cylindrical coordinate system, and ω is again Jupiter's rotation rate. The magnetic field applied to the Galilean moons is found by taking the sum of these

$$\mathbf{B}_o = \mathbf{B}_{\text{int,Jup}} + \mathbf{B}_{\text{external}} \tag{3.4}$$

Within the conducting portion of the satellites, the net magnetic field $\mathbf{B}$ must satisfy the Helmholtz equation

$$\nabla^2\mathbf{B} = -k^2\mathbf{B} \tag{3.5}$$

which is a diffusion equation for $\mathbf{B}$. The wavenumber k is a function of the material properties and the angular frequency of oscillation of $\mathbf{B}$ within the body (see Section 3.5):

$$k = \sqrt{i\omega_p\mu_0\sigma} \tag{3.6}$$

All terms within $\mathbf{B}$ are proportional to an oscillation factor $e^{-i\omega_p t}$, where ω_p is the angular frequency of oscillation. Only the largest oscillation amplitudes induce significant diffusive responses.

The diffusive response may be expressed in terms of the normalized excitation amplitude

$$\mathcal{A}_n^e = \frac{(n+1)}{n} \frac{B_i}{B_e} \tag{3.7}$$

which is a complex quantity that has the desirable property of ranging from 0 for a nonconducting body to (1+0i) for a perfect conductor. B_i and B_e are moments for the magnetic potential for the induced and excitation fields, respectively, outside the moon (see Section 3.5.1).

The magnetic field $\mathbf{B}_o$ applied to the Galilean moons is close to uniform across the body of each satellite, so it is customary to choose $n = 1$ in the excitation field. In this case, the potential B_e is equal to the amplitude of oscillation of the applied field for a particular angular frequency ω_p and has units of nT. On the surface of the body, at the poles, the in-phase portion of the diffusive response field is directed opposite the applied field. It oscillates as

$$B_{\mathrm{dif},p}(t) = B_e \mathcal{A}_1^e e^{-i\omega_p t} \tag{3.8}$$

and it has the form of a dipole (see Section 3.5.2). The measured magnetic field is then the real part of the net field outside the moon

$$\mathbf{B}_{\mathrm{net}} = \mathbf{B}_o + \mathbf{B}_{\mathrm{dif}} \tag{3.9}$$

which includes sums over all n, m, and p. The motionally induced fields discussed in Section 3.3 add another term to Eq. 3.9. For our full mathematical derivation, see Section 3.5.

Unique among the satellites in our solar system, Ganymede has an internally generated dynamo field (Kivelson et al., 2002). In the case of this satellite, the analysis of the diffusive field is no different because this intrinsic field does not vary with time in the frame of the body. As with the mean background field applied by Jupiter, the dynamo field from Ganymede simply presents a static offset to magnetometer measurements near the body, and does not appear in the Fourier analysis. The magnitude of this net background field, around 800 nT at Ganymede's surface, is about a factor of two larger than that experienced by Europa (Zimmer et al., 2000) and thus does not present significant additional challenges to measurement precision scaling.

3.2.2 *Parameter space of the diffusive induction response*

Previous investigations have considered a continuous parameter space of ocean thickness and conductivity for three-layer models, consisting of a non-conducting mantle (and core), salty ocean, and non-conducting ice (Zimmer et al., 2000; Khurana et al., 2002). A five-layer model, adding an ionosphere and metallic core has also been studied (Schilling, 2006). More recent work by Seufert et al. (2011) has further examined the influence of a metallic core and an ionosphere. None of this prior work required the self-consistency among the ocean temperature and density, composition, ice and ocean thickness, *etc.* that are the focus of this paper. In this section, we also examine the parameter space of ocean thickness and conductivity for simple three-layer models with uniformly conducting oceans, in the interest of assessing the general range of possible responses and demonstrating consistency between our methods and those used in previous investigations.

Figures 3.2–3.4 show contours of the maximum induced magnetic field at the surface as a function of ocean thickness and mean ocean conductivity for each body. These figures show the signals for the three strongest driving periods, which are described in Section 3.2.1 and shown in Figure 3.1. Phase delays for the Jupiter synodic frequencies for Europa and Callisto match those described by Zimmer et al. (2000). An ice thickness of 20 km was set for Europa, consistent with previous calculations by Khurana et al. (2002) (K. Khurana, private communication). For both Ganymede and Callisto, 50 km ice shells were used. In each case, the fixed ice thickness means the seafloor depth varies to accommodate the range of D_{ocean}.

The amplitudes for Europa's orbital and synodic frequencies (85.23 hr and 11.23 hr) match those described by Khurana et al. (2002, 2009). However, these authors scaled the diffusive induction response to an excitation amplitude of 14 nT and 250 nT for Europa's orbital and synodic periods, respectively; in this work, each contour plot in Figures 3.2–3.4 is scaled to the largest relevant peak in the frequency spectrum in Figure 3.1. When we instead apply a matching scaling along with a 20 km ice shell, we generate matching figures.

By choosing a scaling that matches the applied excitation amplitudes, Figures 3.2–3.4 indicate the maximum magnetic field components that a magnetometer on the surface of each body would

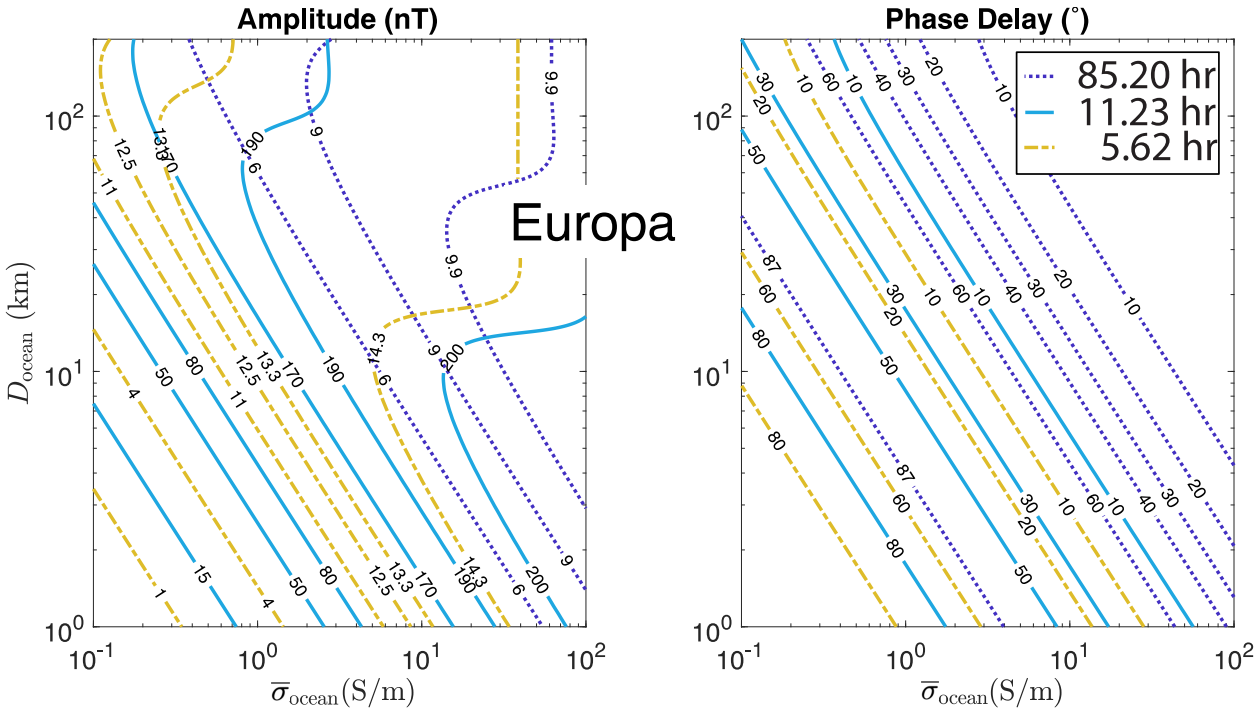

Figure 3.2: Europa: Contours of the maximum induced field B_y components (in nT) and phase delays (in °) at the strongest inducing periods—orbital (85.20 hr; dotted), Jupiter synodic (11.23 hr; solid), and 2nd synodic harmonic (5.62 hr; dot–dash)—shown in Figure 3.1. The assumed, fixed ice thickness of 20 km and variable seafloor depth yield normalized amplitudes consistent with the previous calculations by Khurana et al. (2002), and phase delays for the synodic frequency matching those described by Zimmer et al. (2000). Unlike in previous work, we scale the amplitudes to the maximum component of the magnetic oscillation the satellite actually experiences at each frequency, which are the largest peaks in Figure 3.1.

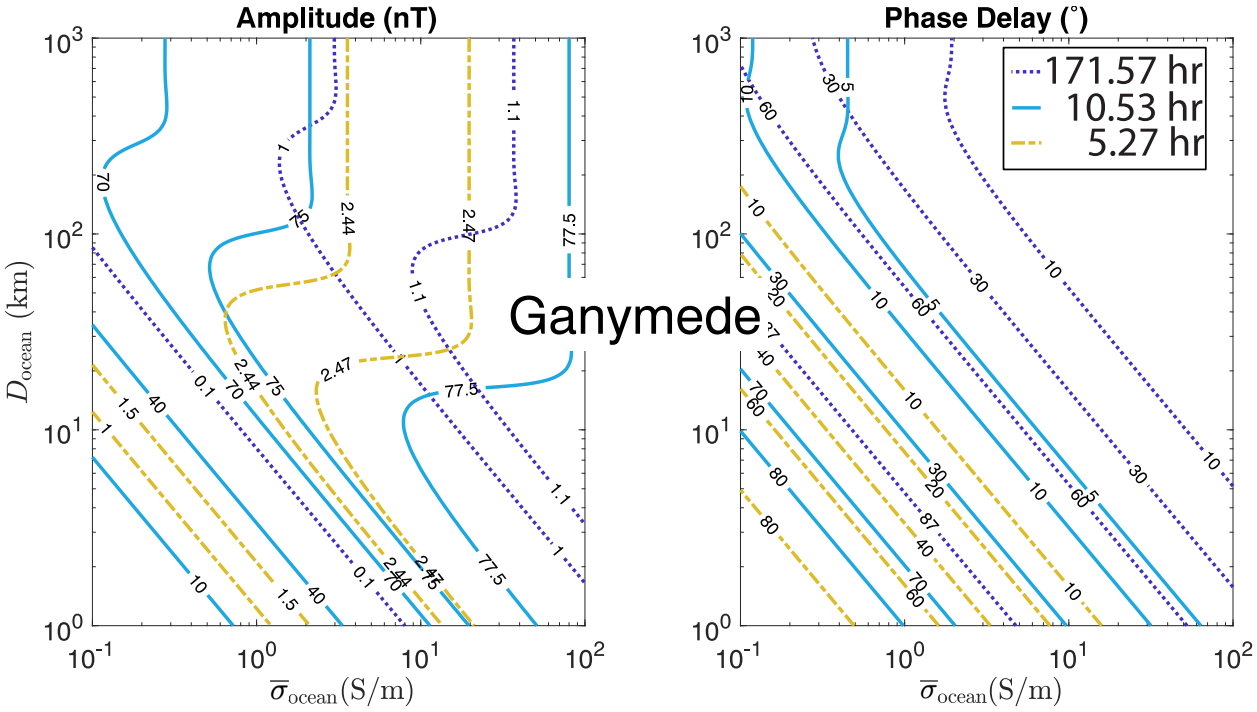

Figure 3.3: Ganymede: Contours of the maximum induced field $\boldsymbol{B}_y$ components (in nT) and phase delays (in °) at the strongest inducing periods—orbital (171.57 hr; dotted), Jupiter synodic (10.53 hr; solid), and 2nd synodic harmonic (5.27 hr; dot–dash)—shown in Figure 3.1. The amplitudes and phases for the synodic and orbital periods are comparable to those described by Seufert et al. (2011) for greater ocean conductivities and thicknesses, but these authors model a highly conducting core, which we do not consider. A 50 km ice shell is assumed at the surface, implying that the seafloor depth varies to accommodate the range of D_{ocean}.

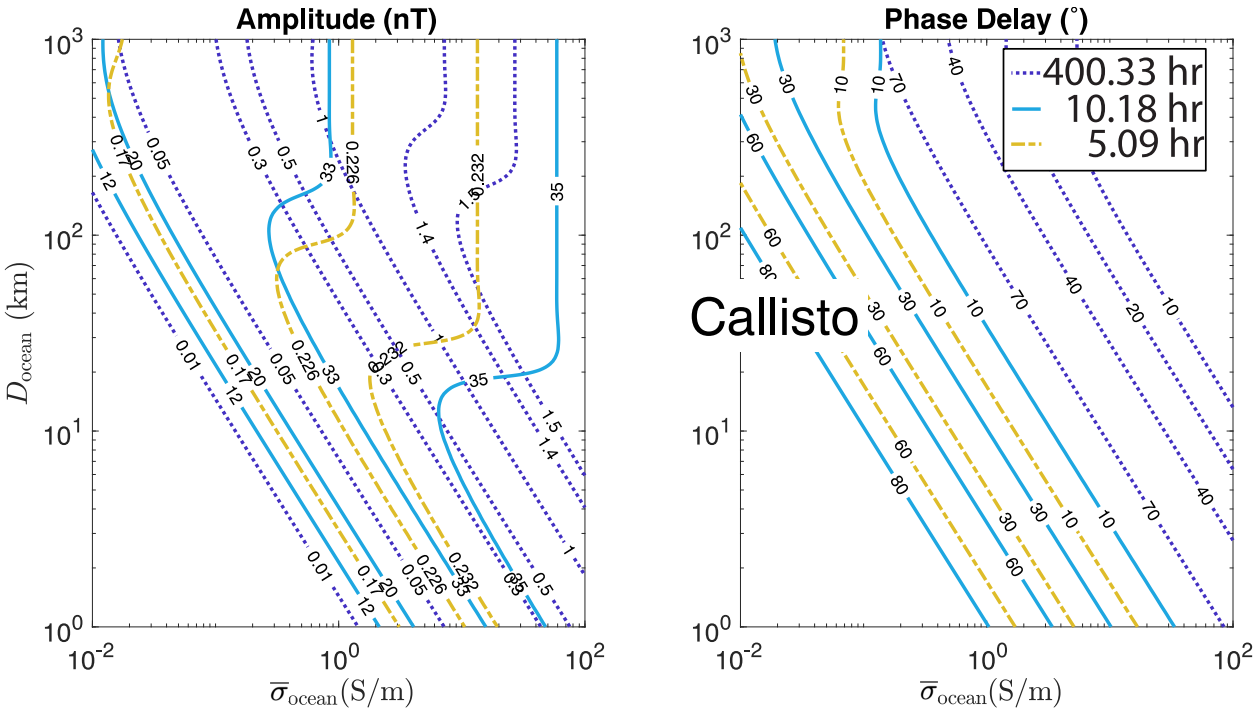

Figure 3.4: Callisto: Contours of the maximum induced field B_y components (in nT) and phase delays (in °) at the strongest inducing periods—orbital (400.33 hr; dotted), Jupiter synodic (10.18 hr; solid), and 2nd synodic harmonic (5.09 hr; dot–dash)—shown in Figure 3.1. Additional harmonic short-period components will be advantageous for investigating Callisto's interior structure. The normalized amplitudes and phases for the synodic frequencies are consistent with those described by Zimmer et al. (2000). The amplitudes and phases for the synodic and orbital periods are similar to those described by Seufert et al. (2011), but these authors model a moderately conducting silicate interior, which we do not consider. A 50 km ice shell is assumed at the surface, implying that the seafloor depth varies to accommodate the range of D_{ocean}.

measure at key locations. For example, the largest variation at Ganymede's synodic period is in its B_y component in $G\phi\Omega$ coordinates, approximately along the direction toward Jupiter. If a lander at the sub- or anti-jovian point on Ganymede's surface measures an induced field amplitude of 75 nT at that period, the matching ocean thickness D_{ocean} and mean conductivity σ_{ocean} must lie along the 75 nT contour. Ganymede's orbital period also has its largest oscillation in B_y, so including the measured amplitude at that period too determines the values for both D_{ocean} and σ_{ocean}, at the crossover point between the two contours. The phase delay for each frequency offers complementary information.

In contrast with the parameter exploration reproduced here and employed in previous work, we now allow ice thickness to vary. We consider how the ocean conductivity varies in accordance with the ice thickness: the melting temperature at the base of the ice shell sets the adiabatic temperature of the ocean, and is determined by the ocean's salinity and the pressure at the ice–ocean interface (Vance et al., 2018). Also in contrast with the parameter space exploration depicted in Figures 3.2–3.4, we examine a smaller space of σ_{ocean} and D_{ocean} consistent with previous models of Europa's ocean composition, as described in the next section and summarized in Tables 3.2–3.4.

In this work, we do not consider the effect on the diffusive induction signal from a possible highly conductive metallic core or moderately conductive, hydrated rocky mantle in any of the satellites. One past study of Europa by Schilling (2006) determined that for even modest ocean conductivities ($\gtrsim 0.06\,\mathrm{S/m}$), the presence of a core would be all but undetectable. A mantle would similarly be easily screened by a moderately conductive ocean. Seufert et al. (2011), however, found that for some combinations of D_{ocean} and σ_{ocean}, a metallic core would change the amplitude of the diffusive response by several percent and decrease the phase delay by 10° or more. A conductive core will have the most dramatic effect for the thinnest and least conductive ocean layers, at the bottom-left of Figures 3.2–3.4. For an ocean that fails to entirely screen a highly conductive core, new contours with a smaller phase delay appear in this corner of the plot. Modeling the wide parameter space of possible interior configurations that also include a core or mantle is beyond the scope of this work.

We also add to the rich set of previous analyses the exploration of a third, shorter-period signal

of intermediate strength to the orbital and synodic signals. We do not consider the longer-period solar oscillation studied by Seufert et al. (2011).

3.2.3 Depth-dependent electrical conductivity in adiabatic oceans

Here we describe the structural models that allow us to consider depth-dependent electrical conductivity in Jupiter's ocean moons. Fluid temperature, pressure, and salt content determine the electrical conductivity of an aqueous solution, and thus dictate the magnetic induction responses of the Galilean oceans. With sufficient prior knowledge of the ice thickness and the ocean's composition—for example, from geological and compositional measurements by the planned *Europa Clipper* mission (Buffington et al., 2017)—magnetic induction studies can provide information on the amounts and compositions of the salts that link to global thermal and geochemical processes.

Depth-dependence in the ocean's electrical conductivity can arise from stratification in the ocean due to melting or freezing at the ice–ocean interface, and dissolution and precipitation within the ocean or at the water–rock interface (Vance and Brown, 2005; Travis et al., 2012). Even for oceans with uniform salinity, as is typically assumed as solute diffusion will tend to enforce this, electrical conductivity will increase with depth along the ocean's convective adiabatic profile because the greater temperature and pressure affect the electrical conductivity. Figure 3.5 depicts this variation for Europa, Ganymede, and Callisto, based on the forward models of Vance et al. (2018) that use available thermodynamic and geophysical data to explore the influences of the ocean, rock layer, and any metallic core on the radial structures of known icy ocean worlds. As noted by Hand and Chyba (2007), the adiabatic gradient for Europa is rather small, albeit non-zero. A more significant influence on the ocean's temperature is the influence of pressure on the melting temperature of the ice, which in turn depends on the ocean's salinity. For Ganymede and Callisto, the adiabatic gradients are large, with temperatures at the base of the thickest Ganymede ocean reaching 290 K.

As detailed in Section 3.2.2, we examine the magnetic induction signals from a small set of self-consistent adiabatic ocean models, taken primarily from those described in detail by Vance et al. (2018). Minor changes to the *PlanetProfile* software used to generate the models (*e.g.* Section S3 of Melwani Daswani et al., 2021) do not significantly change the ocean thicknesses and electrical

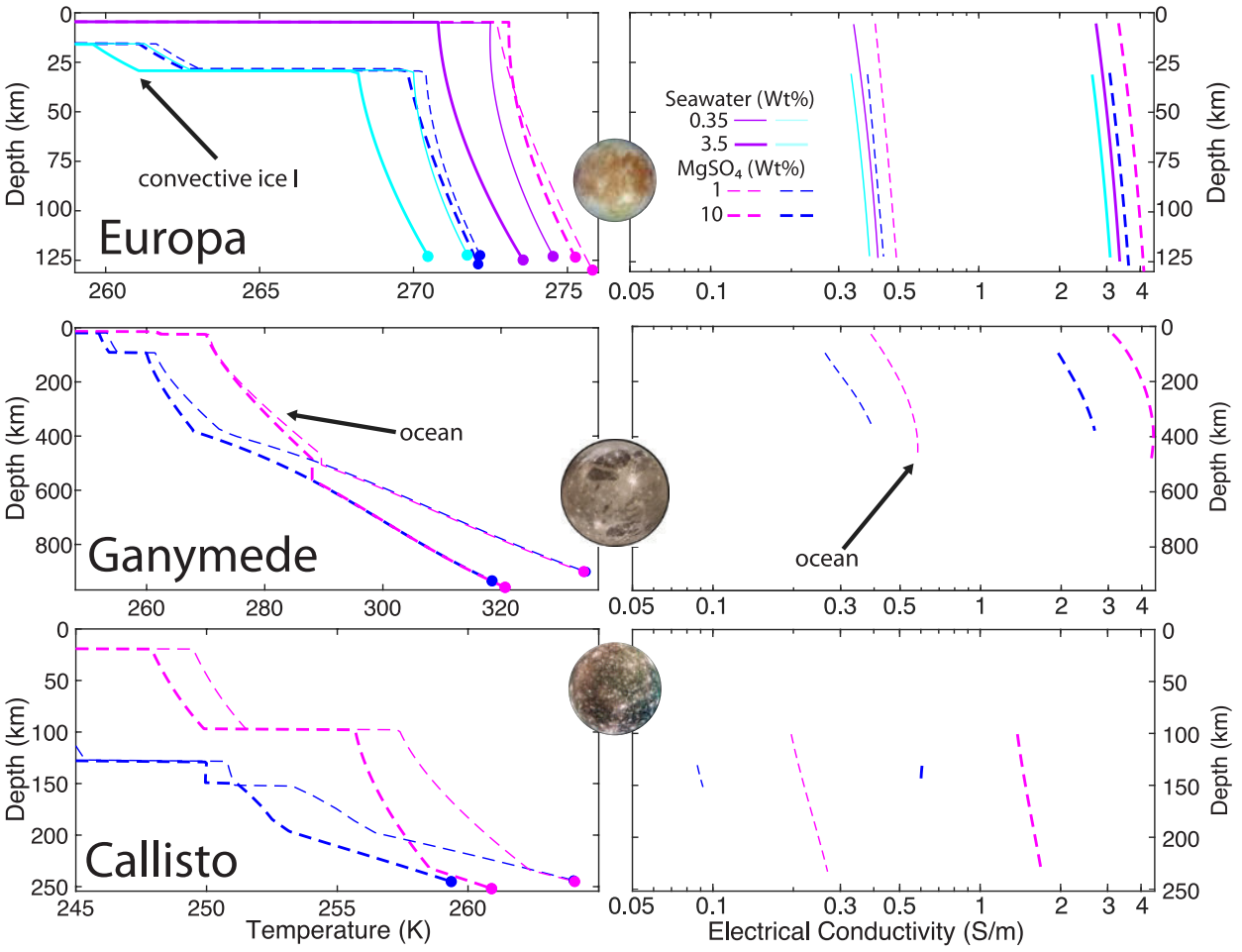

Figure 3.5: Adiabatic ocean temperature (left) and electrical conductivity (right). Convecting oceans with $MgSO_4$ (dashed lines) are warmer. Standard Seawater (mostly NaCl; dot–dashed lines) creates colder oceans and lower electrical conductivities. Thicker ice (blue), corresponds to colder adiabatic profiles in the underlying oceans, which also lowers electrical conductivity. Filled circles show the inferred depth to the upper boundary of the silicate layer for the saline and pure water oceans, respectively. Conductivities in the liquid regions are several orders of magnitude larger than in the ice and rock, the latter of which are set to zero for this study. Adapted from Vance et al. (2018).

conductivities reported in the previous work. We do not consider significant induction from rocky or metallic layers. For each ocean, we consider a nominal 10 wt% $MgSO_4$ salinity, as investigated in previous work. The published equation of state and electrical conductivity data are adequate for the pressures in the largest moon, Ganymede, up to 1.6 GPa, with the caveat that both have been extrapolated in pressure above about 0.7 GPa, and the laboratory data for electrical conductivity have been extrapolated below 298 K and above 1 wt% (Vance et al., 2018). The pressure conditions in Europa's ocean are low enough (< 200 MPa) to be in the range covered by the *TEOS-10* package (McDougall and Barker, 2011), which provides plausible values of conductivity for concentrations of Seawater equivalent to that of Earth's ocean (3.5 wt% NaCl) or less. For this work, we created additional lower-conductivity models for the same ice thickness, but with salinities reduced by a factor of 10 from the nominal cases.

On Europa, the flux of surface-generated oxygen to the ocean may have created oxidizing (acidic) conditions (Hand and Chyba, 2007; Pasek and Greenberg, 2012; Vance et al., 2016), permitting the presence of dissolved $MgSO_4$ in addition to NaCl (Zolotov, 2008; Zolotov and Kargel, 2009). The respective radial models of electrical conductivity for oceans containing seawater and $MgSO_4$ are consistent with compositions linked to the thermal evolution scenarios cited above (Zolotov and Kargel, 2009). In one scenario, Europa's ocean remains relatively reducing and high pH, with a composition dominated by NaCl. In the other, the flux of oxidants generated by radiolysis of Europa's ice into the ocean causes the ocean to become more oxidized and low pH, containing quantities of $MgSO_4$ exceeding the amount of NaCl. Thus the ocean's salinity and composition that might be constrained by magnetic induction measurements relate to the thermal history of Europa. The salinity measurement is also a key indicator of the types of life that might be able to live in the ocean because the chemical affinity—or energy in excess of equilibrium—for different metabolic reactions depends on the ocean's pH (Glein et al., 2018).

Radial conductivity profiles for Europa (Figure 3.5; top) illustrate the coupling to temperature and composition. We consider ice thicknesses of 5 and 30 km (magenta and blue curves, respectively) as representative extremes. Because we consider only the mean inferred value of the axial moment of inertia $C/MR^2 = 0.346 \pm 0.005$ (Schubert et al., 2004), the hydrosphere thickness

is fixed at about 125 km. Seawater (solid and dot–dashed lines), though less concentrated than the modeled composition of $MgSO_4$ (dashed lines), has a stronger melting point suppression, leading to an overall colder ocean for the same thickness of ice. The lower temperature for seawater combines with the different electrical conductivity for the different dissolved ions to create distinct profiles unique to ocean composition and ice thickness (upper right). As a result, our conductivity values differ from the summary predictions in Figure 1 of Hand and Chyba (2007) for $T = 0\,°C$ and 1 atm. This discrepancy from previously published values of electrical conductivity is further evident in the larger moons Ganymede and Callisto, where ocean temperatures vary farther from the freezing point at standard temperature and pressure.

Although we also fix the moments of inertia for Ganymede and Callisto to their mean published values, the depths of the ocean vary due to the presence of high pressure ices (as further discussed in Section 3.7). Because the melting of high-pressure ices also depends on pressure (*e.g.* Hogenboom et al., 1995) the presence of ices above and below the ocean increases the sensitivity of the ocean's conductance to the composition and abundance of dissolved salts.

Larger Ganymede (Figure 3.5; middle) has distinct conductivity profiles for both ice thickness and ocean composition. Although electrical conductivity generally increases with depth, it begins to decrease at the greatest depths for the warm Ganymede ocean (right-most curve). This inflection occurs because the ocean achieves GPa+ pressures, at which the packing of water molecules begins to inhibit the charge exchange of the dissolved ions (Schmidt and Manning, 2017).

Dense brines may also reside at the base of the high-pressure ices on Ganymede, and even between them (Journaux et al., 2013, 2017; Vance et al., 2014, 2018). Although more detailed modeling of the coupled geochemical and geodynamic regimes is needed, this scenario seems consistent with recent simulations of two-phase convection in high-pressure ices (Choblet et al., 2017; Kalousová et al., 2018). These simulations show that even without the effects of dissolved salts, meltwater should form at the water–rock interface as part of the geodynamic evolution of the ice. If such a stable fluid layer exists under the high-pressure ice within Ganymede, it will create an induction response at longer periods, as discussed below.

For Callisto, there is a small range of ice I thicknesses and ocean salinities for which oceans

may be present. Salty oceans considered by Vance et al. (2018) have thicknesses of 20 and 132 km. For the thinner ocean, a 96 km layer of high-pressure ice underlies the ocean. The depicted state is likely transient, as ice III is buoyant in the modeled 10 wt% $MgSO_4$ composition, and an upward snow effect should hasten the transfer of heat from the interior. Simulating a subsequent stage with ice III above the ocean awaits improved thermodynamic data that couples recently improved ice thermodynamics (Journaux et al., 2020) to the thermodynamics of aqueous phases (Bollengier et al., 2019), and is left for future work. Because of the thicker ice considered for Callisto and the consequentially lower temperature at the upper ice–ocean interface, the electrical conductivities in all Callisto models are lower than for the corresponding concentrations in Ganymede. In terms of the magnetic induction response, as shown in Section 3.2.6, these lower conductivity values compound with the lower overall conductance resulting from the thinner ocean, and also the smaller driving magnetic oscillations at more distant Callisto, to yield weak responses.

3.2.4 Accounting for the ionospheres

For each of the above models, we add an overlying ionospheric layer based on recent analyses by Hartkorn and Saur (2017). We adopt their simplified ionospheric models, while also noting that the detailed radial and asymmetric structures of the ionospheres will affect the complex induction response and should be considered in future work. For each satellite, we consider a 100 km thick layer extending from the surface, with Pedersen conductances of $\{30, 2, 800\}$ S for Europa, Ganymede, and Callisto, respectively. For Callisto, we also consider a higher value of 6850 S corresponding to a Cowling channel enhancement near the equator arising from anisotropy in the current sheet, consistent with Hartkorn and Saur (2017). We use this value as an extreme case to inform the analysis of measurements near the equator. In reality, the non-spherical character of the ionosphere will influence the induction response from the one computed here, perhaps up to the order of nT (Styczinski and Harnett, 2021). The enhancement of the Cowling effect is expected to create an effective conductance only twice that of the Pedersen value at higher latitudes. For clarity in presenting the results, the effects of the ionosphere are included only in the tabulated results (Tables 3.2–3.4). Amplitudes are normalized to the moons' surface radii R: $A_{\mathrm{surf}} = (R_{\mathrm{top}}/R)^3 A$,

where $R_{\text{top}} = R + 100\text{km}$, so they can be larger than unity.

3.2.5 Amplitude and phase delay of the diffusive response

Figure 3.6 shows the normalized surface induction responses for Europa, Ganymede, and Callisto based on the adiabatic ocean electrical conductivity profiles shown in Figure 3.5. Some general characteristics of the induction response may be discerned. Warmer and thus thicker oceans (magenta curves for $MgSO_4$ compositions) have larger amplitude responses, corresponding to overall higher values of the conductance. For longer periods, the influence of salinity on the amplitude responses dominate, while the thickness of the ocean dominates at shorter periods. Amplitudes approach zero around periods of 10^4 hr. Less saline oceans have more significant phase delays at longer periods.

For Europa, the induction characteristics for modeled oxidized (10 wt% $MgSO_4$) and reduced (Seawater) oceans are nearly identical in their amplitude responses. However, the two ocean models show a separation in phase delay of a few degrees at the orbital period of 85.20 hr. The combination of these features that constitutes the complex induction waveform will be key to separating them, as shown in Section 3.2.6.

Regional enhancements in the ocean conductivity can have a significant induction response. For Ganymede, we simulate a second ocean layer at the water–rock interface at a depth of 900 km. Lying under 530 km of ice VI (Vance et al., 2018), this layer is modeled as a 30 km thick high-conductivity region (20 S/m) corresponding to a nearly saturated $MgSO_4$ solution, consistent with (Hogenboom et al., 1995) and (Calvert et al., 1958). The influence of such a layer (dotted lines in Figure 3.6) is a $\sim$1% decrease in amplitude at the orbital period of 171.57 hr. The amplitude decrease results from mutual induction between the conducting layers at this period.

For Callisto, the present simulations illustrate the influence of the thicker and deeper oceans in terms of a higher amplitude response at lower frequencies and a phase delay curve also shifted in the direction of lower frequencies.

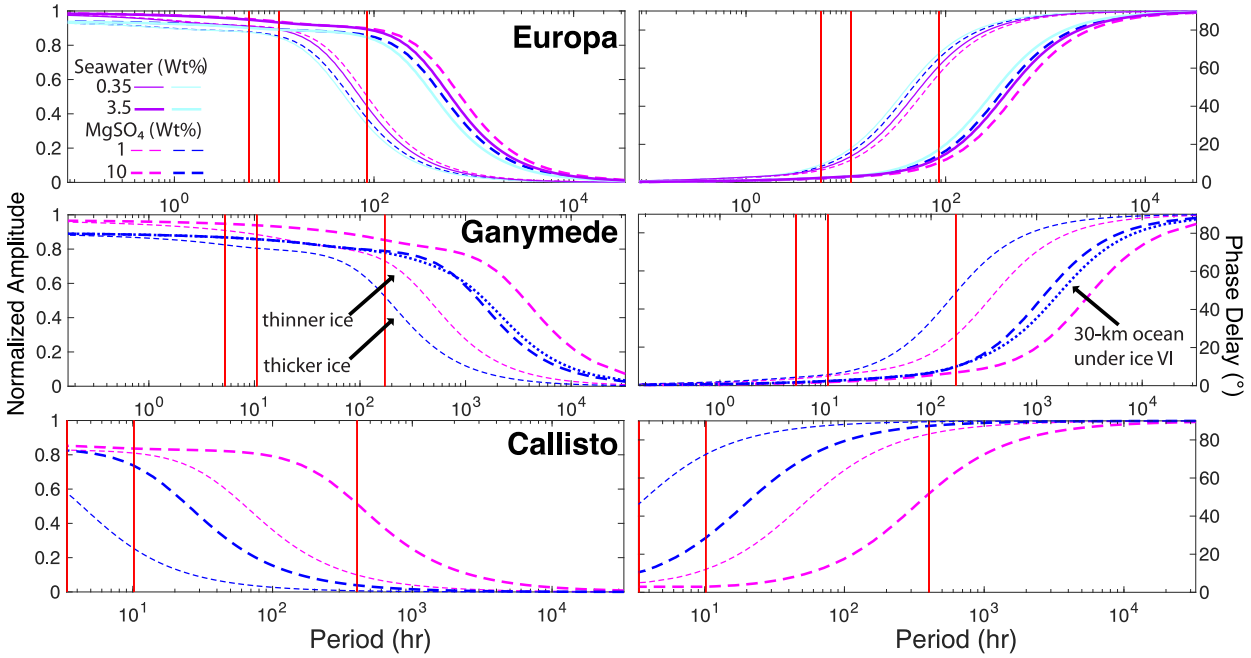

Figure 3.6: Normalized magnetic induction amplitudes ($A = |\mathcal{A}_1^e|$; left) and phase delays ($\phi = -\arg(\mathcal{A}_1^e)$; right) for Europa, Ganymede, and Callisto at periods including the induction peaks noted in Figure 3.1 (vertical red lines). As in Figure 3.5, dashed lines are for oceans containing $MgSO_4$. Solid and dot–dashed lines are for oceans containing Seawater (mostly NaCl). Thicker lines have higher concentrations of $\{10, 3.5\}$ wt%, respectively, and thinner lines correspond to oceans diluted by a factor of 10. For the $MgSO_4$-bearing oceans, thinner ice corresponding to warmer oceans is denoted with magenta and thicker ice is dark blue. The trends with ice thickness/ocean temperature are the same for Seawater oceans: larger amplitude and lower phase delay for thinner ice/warmer oceans. For Ganymede, the dotted line indicates the effect of introducing a 30 km thick, 20 S/m layer at the seafloor for the thick-ice and high-salinity ocean, which is the thicker blue dashed line.

3.2.6 *Distinguishing diffusive responses for different model oceans*

We examine the possible separability of different model oceans by plotting the real and imaginary components of the induced waveforms for the peak values of Jupiter's inducing field vectors. Figure 3.7 shows the real and imaginary parts of the complex diffusive induction response. The normalized complex response $\mathcal{A}_n^e$ is multiplied by the strength of the excitation field B_y at the driving periods shown in Figure 3.1, in accordance with Eq. 3.8. $\mathcal{A}_1^e$ is equal to $Ae^{-i\phi}$, with the normalized amplitude A and phase delay ϕ equal to those used in past studies such as Zimmer et al. (2000) (see Section 3.5). Previous authors (including Zimmer et al., 2000) have defined the complex response as $Ae^{i\phi}$, but they obtain a result equal to the complex conjugate of $\mathcal{A}_1^e$ because they rely on a derivation in Parkinson (1983) that contains an error (see Section 3.5). Relating $\mathcal{A}_1^e$ to A and ϕ as we do enables us to use the same representation as past authors in comparing the induced magnetic field to that which would result from a perfectly conducting ocean $\mathbf{B}_{\mathrm{dif},\infty}$ at an earlier time $t - \phi/\omega$:

$$\mathbf{B}_{\mathrm{dif}}(t) = A\mathbf{B}_{\mathrm{dif},\infty}(t - \phi/\omega) \tag{3.10}$$

If we were to instead define $\mathcal{A}_1^e$ as equal to $Ae^{i\phi_{\mathrm{conj}}}$, $-90° \leq \phi_{\mathrm{conj}} < 0°$ and Eq. 3.10 would then become

$$\mathbf{B}_{\mathrm{dif}}(t) = A\mathbf{B}_{\mathrm{dif},\infty}(t + \phi_{\mathrm{conj}}/\omega) \tag{3.11}$$

Both definitions represent the same physical result.

The quantities $B_y|\{\mathrm{Re}, \mathrm{Im}\}(\mathcal{A}_1^e)|$, equivalent to $B_y A\cos\phi$ and $B_y A\sin\phi$, describe the strengths of the responses that are in phase with the excitation field—an instantaneous response that opposes the external field—and the component that is exactly 90° out of phase, respectively. Thus, the two components together describe the full range of the induction response. Tables 3.2–3.4 include the corresponding data; absolute values are implied on the out-of-phase components, consistent with considering spectral information and required by the choice of positive phase delay as in Eq. 3.10. These tables also provide the computed values that include the modeled ionospheres, and the values computed for the equivalent oceans with the conductivity set to the mean of the adiabat and to the value at the top of the ocean. For convenience, Figures 3.14–3.15 and Tables 3.6–3.11 provide the

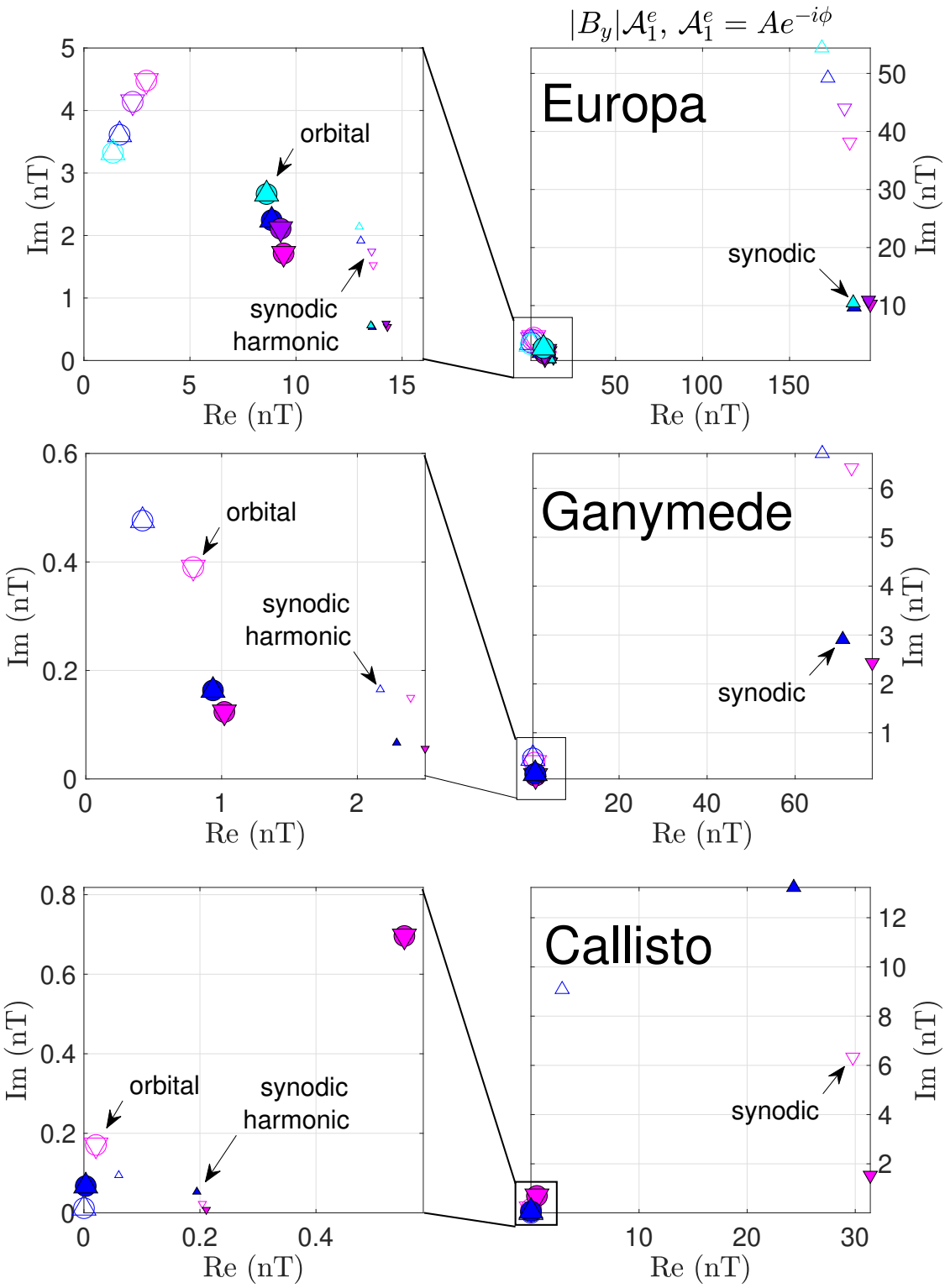

Figure 3.7: Caption appears on next page.

Figure 3.7: Real and imaginary components of the diffusive induction response to the changing B_y component of Jupiter's magnetic field at the main driving periods (Figure 3.1) for {Europa,Ganymede,Callisto}. The real component (on the x-axis) is in phase with the excitation field, and the imaginary component (on the y-axis) is 90° out of phase, as detailed in Section 3.2.6. Subpanels on the left side show the lower-magnitude signals of panels on the right. Filled symbols are for the higher concentrations. Upward and downward triangles are for thicker ice ($\{30, 95, 130\}$ km) and thinner ice ($\{5, 26, 100\}$ km), respectively. Symbol sizes scale with the period of the oscillation, denoting the orbital (largest), the synodic (intermediate), and the synodic harmonic (smallest). Circles are added to the orbital periods to guide the eye.

corresponding data for B_x and B_z; these corresponding values may also be obtained by substituting the field strengths in Table 3.1 in the data and tables for B_y.

Europa

The different phase delays and amplitudes at the orbital and synodic harmonic periods described in Section 3.2.5 create differences in the induction responses for different models of as much as 25 nT, comparing the in-phase synodic component of the more saline and thick ocean with the less-saline, thin ocean. The imaginary component of the induced field ($B_y A \sin\phi$) reveals the influence of the stronger phase delay for the lower-salinity oceans (Figure 3.7, empty symbols). The out-of-phase synodic signal in particular separates the $MgSO_4$ and Seawater models of constant ice thickness by 6 nT for the lower-salinity models. For the 5 and 30 km ice thickness models, for fixed ocean composition, the separation of the stronger in-phase synodic components is 9 and 13 nT for the nominal and lower-salinity models. The synodic harmonic components differ with salinity by as much as 1.5 nT in the out-of-phase response, and by at most 0.7 nT with ice thickness in the in-phase component.

The modeled Pedersen ionosphere has a maximum induction response of about 0.7 nT in the out-of-phase synodic component Table 3.2. This is significant relative to the numerical precision of the calculation of about 0.001% (Figure 3.10). Including the ionosphere with the modeled adiabatic ocean conductivity profiles changes $B_y\{\mathrm{Re},\mathrm{Im}\}(\mathcal{A}_n^e)$ less than 0.05 nT. Distinguishing such signal differences in spacecraft measurements of the magnetic field requires a very careful accounting of the fields generated by plasma, which is beyond the scope of this work.

Comparing the ocean with uniform conductivity set to the mean of the adiabatic profile $\overline{\sigma}$ with the adiabatic conductivity profile, the differences in the amplitude of the response field at the surface are as much as 0.7 nT (0.4%) and 0.3 nT (0.7%) for the synodic and orbital periods. For the uniform ocean using the conductivity at the ice–ocean interface σ_{top}, the orbital-period signal (85.20 hr) differs by up to 20% for the warmer and lower-salinity oceans, or about 0.5 nT.

Ganymede

The synodic component separates the modeled ice thicknesses of 25 and 90 km ($D_{\text{ocean}} \sim 450$ and 280 km) by about 7 nT in the in-phase B_y component, and for the nominal- and low-salinity models (10 and 1 wt% $MgSO_4$) by about 4 nT in both the in- and out-of-phase components. The orbital and synodic harmonic components show a similar pattern, with separations of about 0.2 nT and 0.1 nT.

Ganymede's ionospheric conductivity is smaller than Europa's. The resulting induction response is a maximum of about 0.03 nT, which adds small contributions to the oceanic fields that are comparable to the numerical resolution of the calculation. Currents and fields generated from Ganymede's magnetospheric interaction with Jupiter's local magnetic field and plasma are not considered in this calculation, although they may affect the induction signal (Paty and Winglee, 2006; Jia et al., 2009; Payan et al., 2015). Hence, this work represents an end-member induction calculation, with contributions from Ganymede's magnetospheric current system left for future studies.

The uniformly conducting ocean with conductivity set to the mean of the adiabatic profile $\overline{\sigma}$ differs from the adiabatic profile in the amplitude of the response field at the surface by up to 1.2 nT (1%) and 0.03 nT (2%) at the synodic and orbital periods (Table 3.3 and Figure 3.12). The uniform ocean using the conductivity at the outermost ice–ocean interface σ_{top} differs from the adiabatic case by up to 0.18 nT (2%) for the orbital period.

Callisto

The synodic component shows different offsets for the thick ice/thin ocean (130/20 km) and thinner ice/thicker ocean (100/130 km) for the two examined $MgSO_4$ compositions ($\{10, 1\}$ wt%). For the thinner ice (downward arrows), the in-phase synodic components differ by 1.6 nT, while the out-of-phase components differ by nearly 5 nT. Models with thicker ice (upward arrows) have larger phase delays as well as larger separations in their amplitudes at the synodic period, creating a stronger in-phase separation of 21.4 nT, and a weaker out-of-phase separation of 4.1 nT. The synodic component has a similar configuration for the amplitude and phase responses, being close in period to the synodic period, and thus shows a similar pattern of separations as the synodic signal, albeit

with smaller magnitudes on the order of 0.1 nT. The orbital component has stronger separation in both amplitude and phase for the thinner ice models, leading to proportionally larger differences in the induced field strengths, albeit for small overall magnitudes approaching zero except for the thin ice/thick ocean model that has a high salinity.

Both the Pedersen and Cowling ionospheres have strong induced field strengths and affect the induction in the presence of an ocean. For the thick ice/thin ocean case with low salinity, the presence of the modeled ionospheres creates signals of comparable or much greater magnitude than the signal of the ocean by itself. In the Cowling case the phase responses become reversed, such that the stronger field occurs for the in-phase component. Comparing these different models, the influence of the oceans creates distinct in- and out-of-phase induction responses, such that with sufficient knowledge of the properties of the ionosphere it might be possible to infer the presence of an ocean.

The uniformly conducting ocean with conductivity set to the mean of the adiabatic profile $\overline{\sigma}$ differs from the adiabatic profile in the amplitude of the response field at the surface at the orbital period (400.33 hr) by $\lesssim 2$ pT. The induction responses of the σ_{top} ocean models differ by up to 8 pT (10–20%) for the orbital period.

3.3 Motional induction due to ocean convection

We next consider motional induction driven by fluid flows within the oceans, which further complicates the interpretation of magnetic measurements. This effect is treated independently of the diffusive response considered above as a first approximation. Future work should consider the coupled induction response. Previous work by Tyler (2011) considered the possibility of magnetic remote sensing to detect resonant ocean tides on Europa in the limits of shallow water equations and thin-shell electrodynamics. Here, we focus instead on global fluid motions that may be driven by thermal convection within the oceans of Europa, Ganymede, and Callisto in the low-magnetic-Reynolds-number approximation in order to estimate upper bounds for motionally induced magnetic field amplitudes.

Europa			Period (hr):	**5.62**	**11.23**	**85.20**
			B_y (nT):	**15.03**	**209.78**	**10.65**
T_b	$\overline{T}$	D_{I}	D_{ocean}		$B_y\mathcal{A}_1^e$	
(K)	(K)	(km)	(km)		(nT)	
Ionosphere Only				**Re Im**	**Re Im**	**Re Im**
Pedersen				0.001 0.104	0.002 0.727	0.000 0.005
$MgSO_4$ 1 wt%				**Re Im**	**Re Im**	**Re Im**
273.1	273.9	5	117	13.641 1.527	184.568 38.142	2.942 4.479
Pedersen			$\Delta\mathcal{A}_1^e$ (%)	0.02 0.17	0.03 0.03	0.10 0.05
$\overline{\sigma} = 0.4533$ S/m			$\Delta\mathcal{A}_1^e$ (%)	0.36 –0.41	0.39 –0.08	0.85 0.50
$\sigma_{\mathrm{top}} = 0.4107$ S/m			$\Delta\mathcal{A}_1^e$ (%)	0.10 7.75	–0.45 8.80	–12.31 –3.57
270.4	271.1	30	91	13.054 1.917	172.021 49.195	1.680 3.611
Pedersen			$\Delta\mathcal{A}_1^e$ (%)	0.04 0.18	0.05 0.03	0.15 0.09
$\overline{\sigma} = 0.4132$ S/m			$\Delta\mathcal{A}_1^e$ (%)	0.22 –0.10	0.24 0.01	0.55 0.34
$\sigma_{\mathrm{top}} = 0.3847$ S/m			$\Delta\mathcal{A}_1^e$ (%)	–0.09 6.49	–0.88 6.09	–10.65 –4.23
$MgSO_4$ 10 wt%				**Re Im**	**Re Im**	**Re Im**
272.7	274.1	5	124	14.309 0.539	196.395 10.221	9.414 1.714
Pedersen			$\Delta\mathcal{A}_1^e$ (%)	0.01 0.38	0.00 0.16	0.00 0.01
$\overline{\sigma} = 3.7646$ S/m			$\Delta\mathcal{A}_1^e$ (%)	0.23 –3.83	0.33 –2.87	0.49 –0.10
$\sigma_{\mathrm{top}} = 3.3197$ S/m			$\Delta\mathcal{A}_1^e$ (%)	–0.01 2.28	–0.01 2.13	–0.34 11.33
269.8	270.8	30	96	13.595 0.534	187.098 9.765	8.853 2.245
Pedersen			$\Delta\mathcal{A}_1^e$ (%)	0.01 0.64	0.01 0.27	0.01 0.01
$\overline{\sigma} = 3.3661$ S/m			$\Delta\mathcal{A}_1^e$ (%)	0.18 –2.30	0.23 –1.35	0.30 0.02
$\sigma_{\mathrm{top}} = 3.0763$ S/m			$\Delta\mathcal{A}_1^e$ (%)	–0.01 1.41	0.08 2.77	–0.81 7.99

Europa			Period (hr):	**5.62**	**11.23**	**85.20**
			B_y (nT):	**15.03**	**209.78**	**10.65**
T_b	$\overline{T}$	D_{I}	D_{ocean}		$B_y\mathcal{A}_1^e$	
(K)	(K)	(km)	(km)		(nT)	
Seawater 0.35165 wt%				**Re Im**	**Re Im**	**Re Im**
272.5	273.2	5	117	13.567 1.744	181.600 44.022	2.299 4.139
Pedersen			$\Delta\mathcal{A}_1^e$ (%)	0.03 0.14	0.03 0.02	0.12 0.06
$\overline{\sigma} = 0.3855$ S/m			$\Delta\mathcal{A}_1^e$ (%)	0.43 –0.30	0.46 –0.02	1.02 0.63
$\sigma_{\mathrm{top}} = 0.3415$ S/m			$\Delta\mathcal{A}_1^e$ (%)	0.01 10.36	–0.98 10.77	–16.33 –5.92
270.0	270.7	30	91	12.983 2.139	168.558 54.379	1.368 3.324
Pedersen			$\Delta\mathcal{A}_1^e$ (%)	0.04 0.15	0.05 0.03	0.18 0.10
$\overline{\sigma} = 0.3651$ S/m			$\Delta\mathcal{A}_1^e$ (%)	0.26 –0.07	0.29 0.03	0.65 0.42
$\sigma_{\mathrm{top}} = 0.3339$ S/m			$\Delta\mathcal{A}_1^e$ (%)	–0.23 8.27	–1.49 7.33	–13.72 –5.87
Seawater 3.5165 wt%				**Re Im**	**Re Im**	**Re Im**
270.8	271.9	5	119	14.245 0.590	195.352 10.912	9.274 2.109
Pedersen			$\Delta\mathcal{A}_1^e$ (%)	0.01 0.36	0.01 0.16	0.00 0.00
$\overline{\sigma} = 3.0760$ S/m			$\Delta\mathcal{A}_1^e$ (%)	0.24 –3.32	0.33 –2.24	0.46 –0.03
$\sigma_{\mathrm{top}} = 2.7347$ S/m			$\Delta\mathcal{A}_1^e$ (%)	–0.02 2.08	0.04 2.37	–0.74 10.53
268.2	269.1	30	91	13.530 0.560	186.582 10.460	8.612 2.664
Pedersen			$\Delta\mathcal{A}_1^e$ (%)	0.01 0.63	0.01 0.26	0.01 0.00
$\overline{\sigma} = 2.8862$ S/m			$\Delta\mathcal{A}_1^e$ (%)	0.18 –1.89	0.22 –0.95	0.28 0.03
$\sigma_{\mathrm{top}} = 2.6476$ S/m			$\Delta\mathcal{A}_1^e$ (%)	0.01 1.46	0.10 3.88	–1.26 7.23

Table 3.2: Caption appears on next page.

Table 3.2: Europa: Magnetic induction field strengths $\{\mathrm{Re}, \mathrm{Im}\}(B_y \mathcal{A}_1^e)$, in nT, at the main inducing periods in Figure 3.1. For the different ocean compositions and thicknesses of the upper ice I lithosphere/ocean ($D_\mathrm{I}/D_\mathrm{ocean}$; Figure 3.5), the adiabatic response is listed first. These values are also shown in Figure 3.7. Following these are the deviations from the adiabatic response (in %) when including a 100 km ionosphere with Pedersen conductance of 30 S (Hartkorn and Saur, 2017), then for the ocean with uniform conductivity set to the mean of the adiabatic ocean ($\overline{\sigma}$), and then for the case with uniform conductivity set to the value at the ice–ocean interface (σ_top). The surface responses of the ionosphere in the absence of an ocean are listed at the top of the table.

Ganymede			Period (hr):	**5.27**	**10.53**	**171.57**
			B_y (nT):	**2.64**	**82.61**	**1.21**
T_b (K)	$\overline{T}$ (K)	D_{I} (km)	D_{ocean} (km)		$B_y\mathcal{A}_1^e$ (nT)	
Ionosphere Only				**Re Im**	**Re Im**	**Re Im**
Pedersen				0.000 0.002	0.000 0.033	0.000 0.000
$MgSO_4$ 1 wt%				**Re Im**	**Re Im**	**Re Im**
270.7	279.0	25	442	2.393 0.150	72.835 6.420	0.791 0.390
Pedersen			$\Delta\mathcal{A}_1^e$ (%)	0.00 0.03	0.00 0.01	0.00 0.00
$\overline{\sigma} = 0.5166\,\mathrm{S/m}$			$\Delta\mathcal{A}_1^e$ (%)	0.87 –8.82	1.23 –7.04	2.61 1.01
$\sigma_{\mathrm{top}} = 0.3890\,\mathrm{S/m}$			$\Delta\mathcal{A}_1^e$ (%)	–0.03 4.54	–0.14 5.86	–9.33 17.09
261.6	266.2	92	276	2.169 0.165	66.167 6.714	0.417 0.476
Pedersen			$\Delta\mathcal{A}_1^e$ (%)	0.00 0.06	0.00 0.03	0.00 0.00
$\overline{\sigma} = 0.3322\,\mathrm{S/m}$			$\Delta\mathcal{A}_1^e$ (%)	0.95 –5.29	1.18 –2.65	2.44 1.41
$\sigma_{\mathrm{top}} = 0.2623\,\mathrm{S/m}$			$\Delta\mathcal{A}_1^e$ (%)	0.08 3.83	0.45 10.74	–22.82 –3.32

Ganymede			Period (hr):	**5.27**	**10.53**	**171.57**
			B_y (nT):	**2.64**	**82.61**	**1.21**
T_b	$\overline{T}$	D_{I}	D_{ocean}		$B_y\mathcal{A}_1^e$	
(K)	(K)	(km)	(km)		(nT)	
$MgSO_4$ 10 wt%				**Re Im**	**Re Im**	**Re Im**
270.2	278.3	25	458	2.499 0.056	77.528 2.435	1.020 0.124
Pedersen			$\Delta\mathcal{A}_1^e$ (%)	0.00 0.04	0.00 0.02	0.00 0.00
$\overline{\sigma} = 4.0699$ S/m			$\Delta\mathcal{A}_1^e$ (%)	0.29 –10.57	0.41 –9.78	1.48 –3.07
$\sigma_{\mathrm{top}} = 3.1150$ S/m			$\Delta\mathcal{A}_1^e$ (%)	–0.00 2.03	–0.01 2.84	–0.18 7.55
260.0	263.5	93	282	2.290 0.067	70.816 2.910	0.936 0.163
Pedersen			$\Delta\mathcal{A}_1^e$ (%)	0.00 0.10	0.00 0.04	0.00 0.00
$\overline{\sigma} = 2.3476$ S/m			$\Delta\mathcal{A}_1^e$ (%)	0.27 –7.17	0.38 –6.43	1.01 –0.28
$\sigma_{\mathrm{top}} = 1.9483$ S/m			$\Delta\mathcal{A}_1^e$ (%)	0.00 1.71	–0.00 2.51	–0.11 15.65
brine layer: 30 km, 20 S/m			$\Delta\mathcal{A}_1^e$ (%)	0.00 –0.00	0.00 –0.00	–1.20 0.20
Pedersen			$\Delta\mathcal{A}_1^e$ (%)	0.00 0.10	0.00 0.04	–1.20 0.20

Table 3.3: Ganymede: Magnetic induction field strengths $\{\mathrm{Re}, \mathrm{Im}\}(B_y\mathcal{A}_1^e)$, in nT, at the main inducing periods in Figure 3.1. For the different ocean compositions and thicknesses of the upper ice I lithosphere (D_{I}; Figure 3.5), the adiabatic response is listed first. These values are also shown in Figure 3.7. Following these are deviations from the adiabatic response (in %) when including a 100 km ionosphere with Pedersen conductance of 2 S (Hartkorn and Saur, 2017), then for the ocean with uniform conductivity set to the mean of the adiabatic ocean ($\overline{\sigma}$), and then for the case with uniform conductivity set to the value at the ice–ocean interface (σ_{top}). The surface responses of the ionosphere in the absence of an ocean are listed at the top of the table.

Callisto			Period (hr):	**5.09**	**10.18**	**400.33**
			B_y (nT):	**0.25**	**37.57**	**1.72**
T_b	$\overline{T}$	D_{I}	D_{ocean}		$B_y\mathcal{A}_1^e$	
(K)	(K)	(km)	(km)		(nT)	
Ionosphere Only				**Re Im**	**Re Im**	**Re Im**
Pedersen				0.019 0.070	0.769 5.549	0.000 0.007
Cowling				0.230 0.097	23.854 20.120	0.002 0.056
$MgSO_4$ 1 wt%				**Re Im**	**Re Im**	**Re Im**
257.4	259.6	99	132	0.204 0.023	29.774 6.332	0.021 0.171
Pedersen				0.207 0.026	30.227 6.544	0.022 0.177
Cowling				0.231 0.036	33.248 7.167	0.033 0.225
$\overline{\sigma} = 0.2307$ S/m			$\Delta\mathcal{A}_1^e$ (%)	0.49 –0.44	0.53 –0.08	1.45 0.96
$\sigma_{\mathrm{top}} = 0.1965$ S/m			$\Delta\mathcal{A}_1^e$ (%)	0.06 14.62	–1.03 15.03	–26.08 –13.62
250.8	250.9	128	21	0.060 0.095	2.885 9.085	0.000 0.012
Pedersen				0.102 0.119	5.702 13.168	0.000 0.018
Cowling				0.238 0.083	27.259 18.811	0.003 0.068
$\overline{\sigma} = 0.0895$ S/m			$\Delta\mathcal{A}_1^e$ (%)	0.04 0.02	0.04 0.03	0.05 0.03
$\sigma_{\mathrm{top}} = 0.0874$ S/m			$\Delta\mathcal{A}_1^e$ (%)	–3.26 –0.99	–4.12 –1.87	–4.52 –2.28

Callisto			Period (hr):	**5.09**	**10.18**	**400.33**
			B_y (nT):	**0.25**	**37.57**	**1.72**
T_b	$\overline{T}$	D_{I}	D_{ocean}		$B_y\mathcal{A}_1^e$	
(K)	(K)	(km)	(km)		(nT)	
$MgSO_4$ 10 wt%				**Re Im**	**Re Im**	**Re Im**
255.7	256.9	99	130	0.211 0.008	31.391 1.533	0.552 0.696
Pedersen				0.212 0.011	31.490 1.787	0.556 0.698
Cowling				0.226 0.027	32.566 3.378	0.582 0.715
$\overline{\sigma} = 1.5256$ S/m			$\Delta\mathcal{A}_1^e$ (%)	0.20 –2.91	0.26 –1.74	0.69 0.39
$\sigma_{\mathrm{top}} = 1.3789$ S/m			$\Delta\mathcal{A}_1^e$ (%)	0.01 1.12	0.12 3.18	–10.78 –1.59
250.8	250.9	128	21	0.195 0.053	24.308 13.231	0.003 0.067
Pedersen				0.202 0.055	25.716 13.402	0.004 0.074
Cowling				0.239 0.049	32.873 12.030	0.009 0.123
$\overline{\sigma} = 0.6025$ S/m			$\Delta\mathcal{A}_1^e$ (%)	–0.00 –0.00	–0.00 –0.00	–0.00 –0.00
$\sigma_{\mathrm{top}} = 0.6062$ S/m			$\Delta\mathcal{A}_1^e$ (%)	0.08 –0.53	0.28 –0.34	1.23 0.61

Table 3.4: Callisto: Magnetic induction field strengths {Re, Im}($B_y\mathcal{A}_1^e$), in nT, at the main inducing periods in Figure 3.1. For the different ocean compositions and thicknesses of the upper ice I lithosphere/ocean ($D_{\mathrm{I}}/D_{\mathrm{ocean}}$; Figure 3.5), the adiabatic response is listed first. These values are also shown in Figure 3.7. Following these are the responses (in nT) including a 100 km ionosphere with {Pedersen,Cowling} conductance of {800, 6850} S (Hartkorn and Saur, 2017), then the deviations from the adiabatic response (in %) for the ocean with uniform conductivity set to the mean of the adiabatic ocean ($\overline{\sigma}$), and then for the case with uniform conductivity set to the value at the ice–ocean interface (σ_{top}). The surface responses of the ionosphere in the absence of an ocean are listed at the top of the table.

Thermal convection in icy satellite oceans is expected in order to efficiently transport heat from the deeper interior that arises primarily from radiogenic and tidal heating in the mantle (*e.g.* Soderlund et al., 2020). Using global convection models in combination with rotating convection theory, Soderlund et al. (2014) and Soderlund (2019) predicted the ocean of Europa to have large-scale flows organized into three zonal jets with retrograde (westward) flow at low latitudes and prograde (eastward) flow at high latitudes (Figure 3.8a). Upwelling at the equator and downwelling at mid to high latitudes effectively forms an overturning Hadley-like cell in each hemisphere (Figure 3.8b–c). Non-axisymmetric convective motions are quasi-three-dimensional, due to rotational and inertial timescales of the flow being comparable. Predictions for Ganymede are significantly more uncertain, but Soderlund (2019) argued that a similar configuration may be expected. Convection in a possible Callisto ocean may be in the double-diffusive regime (Vance and Brown, 2005; Vance and Goodman, 2009) if the ocean's salt concentration is nearly saturated (Vance et al., 2018). However, considering thermal convection as an upper bound, application of the scaling arguments in Soderlund (2019) to Callisto suggest similar ocean flows here as well. The nominal ocean model shown in Figure 3.8 will, therefore, be assumed for all three ocean worlds considered here, noting that the use of non-dimensional units permits different physical properties to be assumed for each satellite.

Because the modeled velocity field is given in units of the dimensionless Rossby number $Ro = U/\Omega D$ (the ratio of rotational to inertial timescales), the results can be scaled to the different satellites with assumptions about ocean thickness D and rotation rate Ω (Figure 3.8). A range of different ocean compositions, and therefore ocean thicknesses, are considered for velocity estimates that are given in Table 3.5. Flows are fastest for Ganymede and Europa, where the zonal jets can reach m/s speeds, the mean latitudinal flows have peak speeds of tens of cm/s, and the mean radial flows are $\sim$10 cm/s. At Callisto, flow speeds tend to be roughly an order of magnitude weaker.

Characteristic flow speeds U, in combination with the physical ocean properties σ and D, allow the ratio of magnetic induction to magnetic diffusion to be estimated via the magnetic Reynolds number: $Rm = \mu_0 \sigma U D$. Using the values of these parameters from Table 3.5, $Rm \lesssim 1$ such that the low-magnetic-Reynolds approximation may be applied (Davidson, 2002). Here, the magnetic field $\mathbf{b}$ associated with induced current $\mathbf{J} \sim \sigma \mathbf{u} \times \mathbf{B}$ (Ohm's Law) due to velocity field $\mathbf{u}$ is small

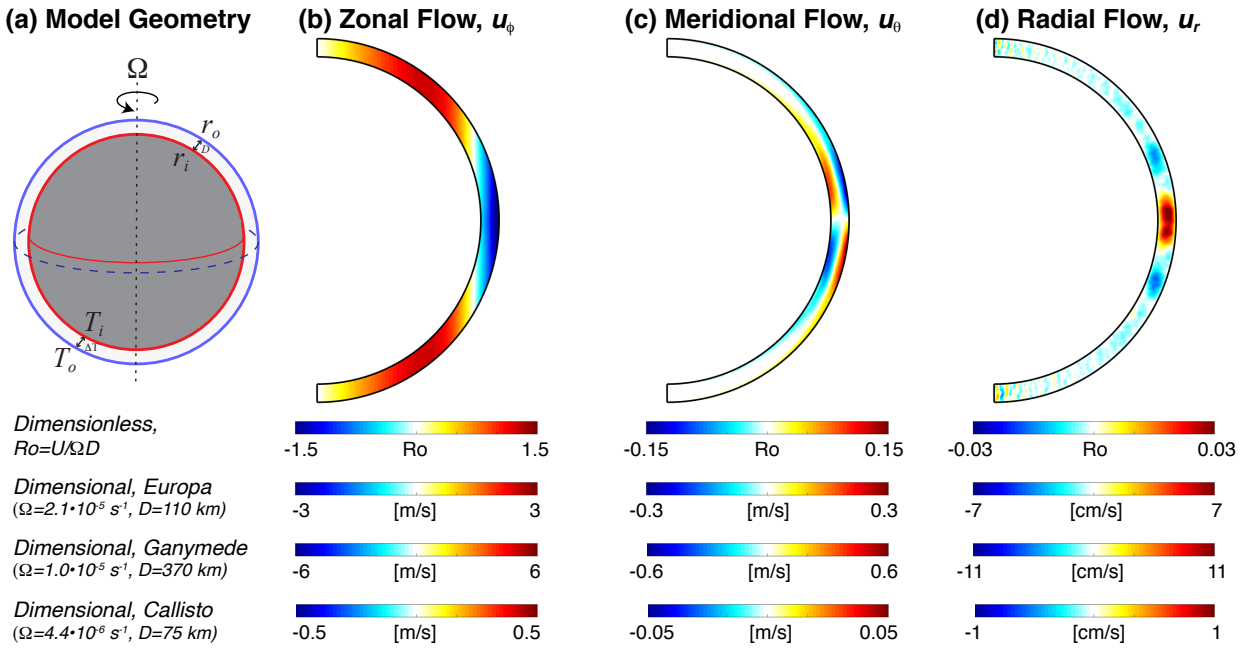

Figure 3.8: Mean flow fields in our nominal global ocean model from Soderlund (2019), averaged over 18 planetary rotations and all longitudes. To the previous work we add dimensional units for Europa, Ganymede, and Callisto assuming intermediate ocean thicknesses across the range of interior models, and a depiction of the meridional flow. **(a)** Geometry of the 3D ocean model. **(b)** Zonal (east–west) velocity field where red denotes prograde flows and blue denotes retrograde flows. **(c)** Meridional (latitudinal) velocity field where red denotes away from the north pole and blue denotes toward the north pole. **(d)** Radial velocity field where red denotes upwelling flows and blue denotes downwelling flows. The model has the following dimensionless input parameters: shell geometry $\chi = r_i/r_o = 0.9$, Prandtl number $Pr = \nu/\kappa = 1$, Ekman number $E = \nu/\Omega D^2 = 3.0 \times 10^{-4}$, and Rayleigh number $Ra = \alpha g \Delta T D^3/\nu\kappa$, where r_i and r_o are the inner and outer radii of the ocean, $D = r_o - r_i$ is ocean thickness, Ω is rotation rate, ν is kinematic viscosity, κ is thermal diffusivity, α is thermal expansivity, g is gravitational acceleration, and $\Delta T = T_i - T_o$ is the superadiabatic temperature contrast. The boundaries are impenetrable, stress-free, and isothermal.

	σ [S/m]	D [km]	U_r [m/s]	U_θ [m/s]	U_ϕ [m/s]	b_r [nT]
Europa						
$MgSO_4$ 1 wt%, Thicker ice shell	0.4	91	0.06	0.29	2.9	1
$MgSO_4$ 1 wt%, Thinner ice shell	0.5	117	0.07	0.37	3.7	2
$MgSO_4$ 10 wt%, Thicker ice shell	3.4	96	0.06	0.30	3.0	10
$MgSO_4$ 10 wt%, Thinner ice shell	3.8	124	0.08	0.39	3.9	20
Seawater 0.35 wt%, Thicker ice shell	0.4	91	0.06	0.29	2.9	1
Seawater 0.35 wt%, Thinner ice shell	0.4	117	0.07	0.37	3.7	2
Seawater 3.5 wt%, Thicker ice shell	2.9	91	0.06	0.29	2.9	8
Seawater 3.5 wt%, Thinner ice shell	3.1	119	0.07	0.37	3.7	14
Ganymede						
$MgSO_4$ 1 wt%, Thicker ice shell	0.3	276	0.08	0.41	4.1	8
$MgSO_4$ 1 wt%, Thinner ice shell	0.5	442	0.13	0.66	6.6	36
$MgSO_4$ 10 wt%, Thicker ice shell	2.3	282	0.08	0.42	4.2	65
$MgSO_4$ 10 wt%, Thinner ice shell	4.1	458	0.14	0.69	6.9	330
Callisto						
$MgSO_4$ 1 wt%, Thicker ice shell	0.09	21	0.003	0.01	0.14	$\ll 1$
$MgSO_4$ 1 wt%, Thinner ice shell	0.2	132	0.02	0.09	0.87	0.02
$MgSO_4$ 10 wt%, Thicker ice shell	0.6	21	0.002	0.01	0.12	$\ll 1$
$MgSO_4$ 10 wt%, Thinner ice shell	1.5	130	0.02	0.09	0.86	0.2

Table 3.5: Ocean characteristics and upper bound estimates of the motionally induced magnetic field strengths from Eq. (3.12) at the top of the oceans. Radial U_r, latitudinal U_θ, and zonal U_ϕ flow speeds from Figure 3.8 with $U = \Omega D Ro$; ocean thicknesses D and electrical conductivity σ from Tables 3.2–3.4.

compared to the imposed magnetic field $\mathbf{B}_o$. Using Ampere's Law, the mean motionally induced field strength in the ocean can be estimated as

$$b \sim \mu_0 \sigma D U B_o \sim Rm B_o. \tag{3.12}$$

The resulting induced magnetic fields are thus stronger for larger electrical conductivities, ocean thicknesses, flow velocities, and satellites closer to the host planet since B_o decreases with distance as $B_o = \{420, 120, 35\}$ nT for {Europa,Ganymede,Callisto} (Showman and Malhotra, 1999). Ganymede is a special case because of its intrinsic magnetic field with surface field strength of 720 nT at the equator and approximately twice that near the poles (Kivelson et al., 2002); thus, we assume here $B_o \approx 1000$ nT as a mean value. Note that a more rigorous derivation of this relationship is given in Section 3.6, which demonstrates that these b estimates should be taken as loose upper bounds and further distinguishes contributions due to radial, meridional, and azimuthal velocity fields.

Table 3.5 summarizes the assumed ocean flows at Europa, Ganymede, and Callisto as well as estimates of their induced magnetic field strengths at the top of the ocean. Field strengths at the surface will be a factor of $(r_{\text{ocean}}/r_{\text{satellite}})^{(l+2)}$ times weaker, where l is spherical harmonic degree, so the surface fields will be weaker by $\lesssim \{6\%,10\%,15\%\}$ at {Europa,Ganymede,Callisto} assuming a dipole $l = 1$ configuration for the most optimistic amplitude. Our analysis focuses on the radial $b_r \sim Rm_r B_o$ component because boundary-confined surface currents can cause discontinuities in the tangential induced magnetic components. We also assume flow speeds typical of the steady overturning cells due to their temporal persistence and large spatial scale, which we hypothesize will produce the strongest induced magnetic signatures and would be more easily discernible by spacecraft. We find that $b_r \lesssim 20$ nT for Europa, $b_r \lesssim 300$ nT for Ganymede, and $b_r \lesssim 1$ nT for Callisto. Implications of these field estimates on magnetic measurements and future work needed for their refinement are discussed in the next section.

3.4 Discussion and conclusions

The inverse problem of reconstructing the full induction response from spacecraft data is beyond the scope of this work, and is discussed in detail elsewhere (*e.g.* Khurana et al., 2009; Cochrane et al., 2021). We focus here on the significance and separability of the diffusive induction responses for the physically consistent models described above. We examine the likelihood of being able to detect and separate the signals of motional induction from the diffusive signals. We also discuss the merits of using physically consistent models as inputs to the inverse problem, the future experimental and modeling work that is needed for material properties and motional induction, and the implications for future missions.

3.4.1 Significance and separability of the diffusive and motional signals

The representative, physically consistent structures of Jupiter's ocean moons that we model have distinct magnetic induction signals when the phase delays are considered. The waveform responses at the three characteristic periods identified for each moon (Figure 3.7; Tables 3.2–3.4) illustrate the possibility for inferring key properties of the moons, possibly by planning missions (Section 3.4.3). This study demonstrates the existence of magnetic induction responses tracing to the unique melting curves of different ocean compositions, and thus to physical features arising from their coupled thermal and chemical evolution. Lower salinity oceans have larger induced responses that are out of phase with Jupiter's rotating field.

For Europa, models consistent with reducing/oxidizing ($MgSO_4$-/NaCl-dominated) oceans have distinct induction features at all three periods considered here. We find a motionally induced field of $b_r \lesssim 20$ nT for Europa, or up to 5% of the ambient jovian field. For comparison, the field strength induced by tidal motions (Rossby–Haurwitz response to obliquity tidal forcing) is ∼1 nT (Tyler, 2011) and at Jupiter's synodic period of 11.23 hr is $\lesssim$ 200 nT (Figure 3.7; Table 3.2). Schilling et al. (2004) found an upper limit for an intrinsic magnetic field at Europa to be 25 nT at the surface, implying that an observable signal from motional flows may have gone unnoticed there. A detailed analysis is required to better characterize the potential response and its implications for determining

ocean composition, salinity, and convective flows.

For Ganymede, the tabulated results (Table 3.3) show that a plausible liquid layer at the rock interface beneath the high-pressure ice would create an in-phase signal of about 0.01 nT at the orbital period. The ionosphere should not impede sensing of the induction response of the ocean. Here, $b_r \lesssim 300$ nT, which approaches half of the equatorial surface strength of the satellite's intrinsic field for the thickest, saltiest ocean considered; magnetic fields induced at Jupiter's synodic period of 10.53 hr are $\lesssim 80$ nT (Figure 3.7; Table 3.3). As a result, these motionally induced magnetic fields warrant further study as they may allow ocean flows to be inferred, bias electrical conductivity inversions, and/or complicate extraction of Ganymede's core dynamo magnetic field component.

For Callisto, strong induction responses (>10 nT) that might be used to infer the ocean's conductivity and thickness might exist at the synodic period of Jupiter's rotation, with smaller signals (>1 nT) at the other excitation periods. However, the modeled Cowling ionosphere without any ocean creates a strong induction response that is not easily distinguished from an oceanic signal. Motional inductions signals of $b_r \lesssim 1$ nT are less significant relative to the peak strength ($\lesssim$30 nT) of the field induced at Jupiter's synodic period of 10.18 hr (Figure 3.7; Table 3.4). Thus, as demonstrated and further discussed by Hartkorn and Saur (2017), magnetic induction measured by the *Galileo* spacecraft (Kivelson et al., 1999) might be explained as resulting from the response of Callisto's ionosphere and not an ocean.

Structural models of ocean worlds (*e.g.* Schubert et al., 2004) often assume a uniform ocean temperature determined by the melting temperature of the ice–ocean interface. Using this temperature as the basis for the ocean's electrical conductivity leads to large differences from the more physically consistent, adiabatic case. The greater mismatch of conductivities of the lower part of the ocean causes large differences in amplitude and phase at longer periods (*i.e.* for larger skin depths).

Prior analyses of magnetic induction in Jupiter's ocean moons have all assumed a uniform conductivity of the oceans (Kivelson et al., 2000, 2002; Khurana et al., 2002; Schilling et al., 2007; Seufert et al., 2011). For all three moons, we compared the diffusive response for a uniformly conducting ocean with conductivity set to a reference value from the adiabatic conductivity profile.

We find that the diffusive induction responses of the oceans with uniform conductivity equal to the mean of the adiabatic profile are, for many interior configurations, a reasonable approximation to the induction response for a more realistic electrical conductivity following the adiabatic profile. The response amplitudes are most distinct between the adiabatic and mean-conductivity oceans for the thin-ice, lower-salinity configurations.

For the mean-conductivity oceans ($\overline{\sigma}$), the in-phase response amplitudes are all larger than for the corresponding adiabatic profiles and the out-of-phase amplitudes mostly decrease slightly (see Tables 3.2–3.4).

For Europa, the in-phase response amplitudes range from about 0.22% to 0.46% greater for the synodic period and from 0.28% to 1.02% greater for the orbital period; the out-of-phase responses range from 2.87% less to 0.03% greater for the synodic period and from 0.10% less to 0.63% greater for the orbital period. Larger differences are observed for thinner-ice, warmer oceans in all cases.

For Ganymede, the in-phase response amplitudes range from about 0.38% to 1.23% greater for the synodic period and from 1.01% to 2.61% greater for the orbital period; the out-of-phase responses range from 9.78% to 2.65% less for the synodic period and from 3.07% less to 1.41% greater for the orbital period. These excesses/deficits in the synodic/orbital component differences arise because the mean conductivity case increases/reduces the conductance contributed by the shallower/deeper parts of the ocean (Figure 3.5) associated with smaller/larger skin depths of the diffusive response.

For Callisto, the in-phase response amplitudes range from 0.00% to 0.53% greater for the synodic period and from 0.00% to 1.45% greater for the orbital period; the out-of-phase responses range from 1.74% less to 0.03% greater for the synodic period and from 0.00% to 0.96% greater for the orbital period. For the thicker oceans, where conductivity changes with depth, the differences are similar to those for Ganymede.

We also considered the diffusive response from uniformly conducting oceans with a conduc-

tivity equal to that at the ice–ocean interface (σ_{top}) in comparison to the adiabatic profiles (see Tables 3.2–3.4). Unlike the mean-conductivity oceans, there is not a consistent pattern of larger or smaller responses when compared to the adiabatic case.

For Europa, the in-phase response amplitudes range from about 1.49% less to 0.10% greater for the synodic period and from 16.33% to 0.34% less for the orbital period; the out-of-phase responses range from 2.13% to 10.77% greater for the synodic period and from 5.92% less to 11.33% greater for the orbital period. Differences are consistently large in this comparison.

For Ganymede, the in-phase response amplitudes range from about 0.14% less to 0.45% greater for the synodic period and from 22.82% to 0.11% less for the orbital period; the out-of-phase responses range from 2.51% less to 10.74% greater for the synodic period and from 3.32% less to 17.09% greater for the orbital period. For the lower-salinity ocean we model, the marked difference in phase delay between the thin-ice, warmer profile and the thick-ice, colder profile (Figure 3.6) is evident in how the in-phase and out-of-phase components change between the two cases.

For Callisto, the in-phase response amplitudes range from about 4.12% less to 0.28% greater for the synodic period and from 26.08% less to 1.23% greater for the orbital period; the out-of-phase responses range from 1.87% less to 15.03% greater for the synodic period and from 13.62% less to 0.61% greater for the orbital period. The lower phase delay of the nominal salinity case for the thicker ocean is evident in the differences between the in-phase and out-of-phase components from the other cases.

For larger oceans, where the non-linear pressure behavior of the adiabat introduces curvature to the electrical conductivity profile, slightly larger differences can arise for thicker oceans. The presence of high-pressure ice also enhances the sensitivity of the overall ocean thickness to the ocean's salinity.

3.4.2 Future experimental and modeling work

The diffusive induction models described in Section 3.2.3 make use of thermodynamic and electrical conductivity data developed for applications to ocean worlds (Vance and Brown, 2013; Vance et al., 2018). Future work should explore a broader space of compositions. Constructing models that account for the effects of high concentration and pressure requires updated thermodynamic data (Bollengier et al., 2019; Journaux et al., 2020), as described above, matched with accurate electrical conductivity data. Recent progress in applying electrical conductivity to geochemical systems at Earth's surface (McCleskey et al., 2012) provides a starting point for considering oceanic concentrations with realistic assemblages of salts (Kargel et al., 2000; Zolotov and Shock, 2001). Extending these data to high pressures and concentrations requires further experimental work (*e.g.* Ni et al., 2014; Guo and Keppler, 2019). Future investigations should also examine a fuller parameter space of interior structures, including conductivity in the solid layers. Such future work should examine a broader range of ice and hydrosphere thicknesses, including density structures that explore the full range of constraints based on *Galileo* gravity data, not just the mean values of the moments of inertia (Schubert et al., 2004; Vance et al., 2019). Future work should also examine asymmetry in the conducting layers. Recent work by Styczinski and Harnett (2021) permits consideration of small deviations from spherical symmetry, for example due to long-wavelength variations in the thickness of Europa's ice (Nimmo et al., 2007). Ultimately, the ability to consider diffusive magnetic induction from electrically conducting regions with arbitrary geometry would enable accounting for effects such as the Cowling enhancement of Callisto's ionosphere (Hartkorn and Saur, 2017), meridional variations in salinity at Europa (Zhu et al., 2017), and brine lenses in Europa's ice (Schmidt et al., 2011).

The simplified approach to motional induction described in Sections 3.3 and 3.6 gives order-of-magnitude estimates of the maximum induced fields due to ocean convection and shows that these fields may be large enough to impact interpretations of magnetic measurements. Future work will assess the implications of the simplifying assumptions made through more detailed calculations. For example, we have assumed homogeneous and constant jovian and Ganymede background fields.

However, the temporal and spatial variation of the ambient fields and the plasma interaction fields generated by currents (especially Ganymede's magnetosphere) are expected to be significant, and the magnetic environment each satellite experiences throughout its orbit is highly dynamic (*e.g.* Bagenal et al., 2015). The influence of these variations on ocean-flow-driven magnetic field signatures also remains to be explored (*cf.* Gissinger and Petitdemange, 2019). Kinematic models that directly solve the coupled momentum and induction equations to determine the motionally induced magnetic fields are an exciting and necessary future venue to refine these estimates. The resulting predictions for field strength and spatial structure may allow the motional and diffusive components of the induced magnetic field to be separated, facilitating better electrical conductivity inversions and ocean flow hypothesis tests.

3.4.3 Implications for future missions

The *Europa Clipper* mission will conduct multiple (>40) flybys of Europa, and will investigate its magnetic induction response with the goal of constraining the ocean salinity and ice thickness, each to within 50%. With independent constraints on ice thickness obtained from the Radar for Europa Assessment and Sounding: Ocean to Near-surface (REASON) and Europa Imaging System (EIS) investigations (Steinbrügge et al., 2018), it may be possible to constrain the ocean's temperature and thus the adiabatic structure for the best-fit ocean composition inferred from compositional investigations. The analyses provided here (Figure 3.7 and Table 3.2) indicate that a sensitivity of 1.5 nT is probably sufficient to distinguish between the end-member $MgSO_4$ and NaCl oceans, and the corresponding ice thicknesses considered here.

The *JUICE* mission will execute two Europa flybys and nine Callisto flybys, and will orbit Ganymede (Grasset et al., 2013). The magnetic field investigation seeks to determine the induction response to better than 0.1 nT. The Europa flybys might aid the *Europa Clipper* investigations in constraining the composition of the ocean. We find that at Ganymede, *JUICE's* magnetic field investigation will not be sufficient to discern the modeled basal liquid layer at the ice VI–rock interface, which would require sensitivity better than 0.01 nT. Although the ability to discern between ocean compositions could not be assessed owing to insufficient thermodynamic and electrical con-

ductivity data at high pressures, it seems likely that useful constraints could be derived based on the signal strengths at Ganymede, if appropriate laboratory-derived data for relevant solutions under pressure became available. Motional induction also appears to be even more important to consider at Ganymede than Europa, with *JUICE's* orbital tour providing a continuous and detailed dataset at Ganymede, critical in investigating the interplay and relative contributions of magnetospheric interaction fields, diffusive induction fields, and motional induction fields.

At Callisto, both *Europa Clipper* and *JUICE* would be able to investigate the synodic signals that vary by more than 2 nT for the different models considered here, including models with only an ionosphere. *JUICE's* 0.1 nT sensitivity might be able to obtain useful information at the orbital and first harmonic periods as well. In contrast with Europa and Ganymede, however, good knowledge of the ionospheric structure at Callisto is required for detecting an ocean.

Acknowledgments

Work by JPL co-authors was partially supported by the Jet Propulsion Laboratory, Caltech, and by the Icy Worlds node of NASA's Astrobiology Institute (13-13NAI7_2-0024). This work was partially supported by NASA's Europa Clipper project. Work by MJS was supported by the NASA Earth and Space Science Fellowship Program — Grant 80NSSC18K1236. Work by KMS was also supported by NASA Grant NNX14AR28G.

The Matlab scripts and associated data needed to compute the results of this work are archived as a release on github (https://github.com/vancesteven/PlanetProfile) with DOI: 10.5281/zenodo.4052711.

All global ocean convection model data were first published in Soderlund (2019) and are available therein.

Magnetic Induction Responses of Jupiter's Ocean Moons Including Effects from Adiabatic Convection

Part 2: Supporting Information

3.5 Induction response model

We are interested in the magnetic fields induced within a spherically symmetric body, in which electrical conductivity is a piece-wise constant function of distance from the center. We thus assume bounding radii for N layers

$$\{r_1, r_2, r_3, \cdots, r_N\}, \tag{3.13}$$

where

$$r_N = R \tag{3.14}$$

is the outer radius of the spherical body.

The corresponding conductivity values are

$$\{\sigma_1, \sigma_2, \sigma_3, \cdots, \sigma_N\}. \tag{3.15}$$

We also assume that there is an imposed external magnetic potential, represented by a sum of terms, each of which has the form

$$\Phi_{n,m,p}(r, \theta, \varphi, t) = RB_e \left(\frac{r}{R}\right)^n S_{n,m}(\theta, \varphi) \mathrm{e}^{-i\omega_p t}, \tag{3.16}$$

where $\{r, \theta, \varphi\}$ are spherical coordinates (r is radius, θ is colatitude, and φ is longitude) of the field point, B_e is a scale factor, $S_{n,m}(\theta, \varphi)$ is a surface spherical harmonic function of degree n and order m, while t is time and ω_p is the angular frequency of oscillation of the imposed potential. The same methods apply independently to each frequency ω_p in the excitation field, and the results sum linearly by superposition. Therefore, we now drop the subscript on this quantity and simply use ω.

Within each layer, the magnetic field vector $\mathbf{B}$ must satisfy the Helmholtz equation

$$\nabla^2 \mathbf{B} = -k^2 \mathbf{B} \tag{3.17}$$

which is a diffusion equation for **B**. k is a scalar wavenumber given by

$$k^2 = i\omega\mu_0\sigma \tag{3.18}$$

where ω is angular frequency, σ is electrical conductivity, and μ_o the permeability of free space. In defining k in Eq. 3.18, we have assumed $\mu \approx \mu_0$, which holds well even for ferromagnetic materials when they are considered on a global scale (Saur et al., 2010). Note that in Eq. 3.18, we have chosen a different convention from that of Parkinson (1983) and numerous authors relying on their derivation. We make this choice in order to derive the spherical Bessel equation (Eq. 3.22) from the diffusion equation (3.17). Choosing $k^2 = -i\omega\mu_0\sigma$ results in the *modified* spherical Bessel equation, meaning the derivation in Parkinson (1983) is in error. We prefer to define k^2 as in Eq. 3.18 so that we can, in fact, reach the spherical Bessel equation and thereby compare the remaining derivation favorably to that of Parkinson (1983) and other past research using the standard spherical Bessel functions.

Independently from Eq. 3.17, the net poloidal component of the magnetic field inside the body is given by sums over n and m of terms with the forms

$$B_r(r,\theta,\varphi,t) = \frac{C}{r}\Big(F(r)\Big)n(n+1)\,S_{n,m}(\theta,\varphi)\mathrm{e}^{-i\omega t} \tag{3.19}$$

$$B_\theta(r,\theta,\varphi,t) = \frac{C}{r}\frac{d}{dr}\Big(rF(r)\Big)\,\frac{d}{d\theta}\Big(S_{n,m}(\theta,\varphi)\Big)\mathrm{e}^{-i\omega t} \tag{3.20}$$

$$B_\varphi(r,\theta,\varphi,t) = \frac{C}{r\sin\theta}\frac{d}{dr}\Big(rF(r)\Big)\,\frac{d}{d\varphi}\Big(S_{n,m}(\theta,\varphi)\Big)\mathrm{e}^{-i\omega t} \tag{3.21}$$

where C is a constant, and $F(r)$ is a function of radius, which we need to determine.

3.5.1 Analytical model based on Srivastava (1966)

For the purpose of validating our numerical model, we separately derive an analytical solution akin to that of Srivastava (1966) and summarized by Parkinson (1983). As this analytical approach is common throughout the literature, we later compare the analytical (layered) approach to our numerical (ordinary differential equation, ODE) approach in Figures 3.9 and 3.10. We find it instructive

to compare the point in the derivation where the two approaches differ, so we carry out the full derivation here, in our notation.

Applying separation of variables to the governing differential equation (Eq. 3.17), one finds that the radial factor $F(r)$ in the solution must satisfy the spherical Bessel equation

$$\frac{d^2F}{dr^2} + \left(\frac{2}{r}\right)\frac{dF}{dr} + \left(k^2 - \frac{n(n+1)}{r^2}\right)F = 0. \tag{3.22}$$

This is a second-order equation, having two solutions, $j_n(kr)$ and $y_n(kr)$, the spherical Bessel functions of the first and second kind, respectively, of degree n and argument kr.

Note that choosing to define k as we did in Eq. 3.18 was a strict requirement to obtain Eq. 3.22. If we instead chose $k^2 = -i\omega\mu_o\sigma$, we would have obtained the *modified* spherical Bessel equation

$$\frac{d^2F}{dr^2} + \left(\frac{2}{r}\right)\frac{dF}{dr} + \left(-k^2 - \frac{n(n+1)}{r^2}\right)F = 0 \tag{3.23}$$

with solutions $i_n(kr)$ and $k_n(kr)$, the *modified* spherical Bessel functions, as in Schilling et al. (2007) and Seufert et al. (2011). In effect, our choice of sign convention results in the complex response we later derive $\mathcal{A}_n^e$ (Eq. 3.57) being equal to the complex conjugate of the analogous quantity $Ae^{i\phi}$ appearing in past research (*e.g.* Zimmer et al., 2000).

It will also be convenient to define another set of related functions

$$F^\star(r) = \frac{d}{dr}\Big(rF(r)\Big) \tag{3.24}$$

with

$$\begin{aligned} j_n^\star(kr) &= \frac{d}{dr}\Big(rj_n(kr)\Big) \\ &= (n+1)j_n(kr) - kr\, j_{n+1}(kr) \end{aligned} \tag{3.25}$$

and

$$\begin{aligned} y_n^\star(kr) &= \frac{d}{dr}\Big(ry_n(kr)\Big) \\ &= (n+1)y_n(kr) - kr\, y_{n+1}(kr). \end{aligned} \tag{3.26}$$

Both y_n and $y_n^\star$ are singular at the origin $r = 0$, so in the innermost spherical layer only $j_n(kr)$ and $j_n^\star(kr)$ may describe physically consistent solutions. In other layers, we use linear combinations of j_n and y_n and linear combinations of $j_n^\star$ and $y_n^\star$.

Internal boundary conditions

The resulting piecewise-defined radial functions characterize the radial part of the magnetic field. The radial component has the form

$$F_n(r) = \begin{cases} c_1 j_n(k_1 r) & & \text{for} \quad 0 < r \le r_1 \\ c_2 j_n(k_2 r) & + d_2 y_n(k_2 r) & \text{for} \quad r_1 < r \le r_2 \\ c_3 j_n(k_3 r) & + d_3 y_n(k_3 r) & \text{for} \quad r_2 < r \le r_3 \\ \\ c_{\mathrm{j}} j_n(k_{\mathrm{j}} r) & + d_{\mathrm{j}} y_n(k_{\mathrm{j}} r) & \text{for} \quad r_{\mathrm{j}-1} < r \le r_{\mathrm{j}} \end{cases} . \tag{3.27}$$

The tangential components yield similar structure, but with all F_n, j_n, and y_n replaced by their starred counterparts.

The constants c_{j} and d_{j} are determined by continuity of radial (r) and tangential (θ, φ) components of the magnetic field across the boundaries. For each internal boundary, it must hold that

$$\begin{aligned} F_n^{\text{below}}(r_{\mathrm{j}}) &= F_n^{\text{above}}(r_{\mathrm{j}}) \\ c_{\mathrm{j}} j_n(k_{\mathrm{j}} r_{\mathrm{j}}) + d_{\mathrm{j}} y_n(k_{\mathrm{j}} r_{\mathrm{j}}) &= c_{\mathrm{j}+1} j_n(k_{\mathrm{j}+1} r_{\mathrm{j}}) + d_{\mathrm{j}+1} y_n(k_{\mathrm{j}+1} r_{\mathrm{j}}). \end{aligned} \tag{3.28}$$

Likewise for $F_n^\star$ to ensure continuity of the tangential components. These continuity constraints yield two equations at each internal boundary, from which we can determine the layer coefficients.

The internal boundary conditions are only part of the story. In a model with N layers, we have $2N - 1$ coefficients to determine ($d_1 = 0$, to avoid singular behavior at the origin), but only $N - 1$ internal boundaries, and thus only $2N - 2$ constraints. The external boundary condition provides the additional information to make the problem evenly determined.

Using notation similar to that of Parkinson (1983, Ch. 5), we can write a recursion relation that transforms the coefficients in the j$^{\text{th}}$ layer into those for the layer above it

$$\begin{bmatrix} c_{\mathrm{j}+1} \\ d_{\mathrm{j}+1} \end{bmatrix} = \boldsymbol{T}_{\mathrm{j}}(k_{\mathrm{j}}, k_{\mathrm{j}+1}, r_{\mathrm{j}}) \cdot \begin{bmatrix} c_{\mathrm{j}} \\ d_{\mathrm{j}} \end{bmatrix} \tag{3.29}$$

where the transformation matrix T_j has elements

$$T_j(k_j, k_{j+1}, r_j) = \frac{1}{\alpha_j}\begin{bmatrix} \beta_j & \gamma_j \\ \delta_j & \varepsilon_j \end{bmatrix} \tag{3.30}$$

with

$$\alpha_j = j_n(k_{j+1}r_j)\, y_n^\star(k_{j+1}r_j) - y_n(k_{j+1}r_j)\, j_n^\star(k_{j+1}r_j) = \frac{1}{k_{j+1}r_j} \tag{3.31}$$

which is a function of the conductivity in the layer above the boundary only. The other elements depend on the conductivities on both sides of the boundary:

$$\beta_j = j_n(k_j r_j)\, y_n^\star(k_{j+1}r_j) - y_n(k_{j+1}r_j)\, j_n^\star(k_j r_j) \tag{3.32}$$

$$\gamma_j = y_n(k_j r_j)\, y_n^\star(k_{j+1}r_j) - y_n(k_{j+1}r_j)\, y_n^\star(k_j r_j) \tag{3.33}$$

and

$$\delta_j = j_n(k_{j+1}r_j)\, j_n^\star(k_j r_j) - j_n(k_j r_j)\, j_n^\star(k_{j+1}r_j) \tag{3.34}$$

$$\varepsilon_j = j_n(k_{j+1}r_j)\, y_n^\star(k_j r_j) - y_n(k_j r_j)\, j_n^\star(k_{j+1}r_j). \tag{3.35}$$

For computation, it is helpful to note that Eq. 3.29 yields a convenient recursion relation if we define a quantity

$$\Lambda_j = \frac{d_j}{c_j} \tag{3.36}$$

We find that Λ_{j+1} relates to Λ_j by

$$\Lambda_{j+1} = \frac{\delta_j + \Lambda_j \varepsilon_j}{\beta_j + \Lambda_j \gamma_j}. \tag{3.37}$$

As $d_1 = 0$, $\Lambda_1 = 0$ also for that innermost layer. Note that we define this transfer coefficient differently than do Parkinson (1983). They define the reciprocal of Λ (as a quantity R) so that Eqs. 3.37 and 3.51 appear to match. Our notation allows for $\Lambda_1 = 0$, rather than leaving this quantity undefined (Styczinski et al., *submitted*—Chapter 4).

We thus start in the central spherical layer, where $\Lambda_1 = 0$, then propagate upward through the stack of layers until we have the coefficient Λ_N for the outermost (N^{th}) layer. With a piecewise model interior structure $\sigma(r)$, we compute k_j for the set of r_j. Repeated application of Eq. 3.37 then allows us to relate the interior structure to the external boundary conditions.

External boundary conditions

The final step is matching the external surface boundary condition. Outside the sphere, the magnetic field is represented by a scalar potential which is the sum of an imposed external contribution and an induced internal contribution. That sum has spatial dependence given by the form

$$\Phi(r,\theta,\varphi) = R\left(B_e\left(\frac{r}{R}\right)^n + B_i\left(\frac{R}{r}\right)^{n+1}\right)S_n(\theta,\varphi). \tag{3.38}$$

We have now dropped the subscript m from $S_{n,m}$ because for any n, a suitable choice of axes results in $m = 0$ for both external and internal fields for the case of spherical symmetry we consider here. The vector field is obtained from the potential via

$$\mathbf{B} = -\nabla\Phi. \tag{3.39}$$

The radial component of the vector field, evaluated at the surface ($r = R$), is

$$B_r = -\Big(nB_e - (n+1)B_i\Big)S_n(\theta,\varphi) \tag{3.40}$$

and the tangential components are

$$B_\theta = -\Big(B_e + B_i\Big)\frac{\partial S_n(\theta,\varphi)}{\partial\theta} \tag{3.41}$$

and

$$B_\varphi = -\Big(B_e + B_i\Big)\frac{1}{\sin\theta}\frac{\partial S_n(\theta,\varphi)}{\partial\varphi}. \tag{3.42}$$

The θ and φ equations yield redundant information, so we consider only the θ equation for the tangential components.

Matching these with the corresponding interior components, as given in Eq. 3.19–3.21, but evaluated at the top of the uppermost layer, we obtain

$$-\Big(nB_e - (n+1)B_i\Big)R = n(n+1)\Big(c_N j_n(k_N R) + d_N y_n(k_N R)\Big) \tag{3.43}$$

and

$$-\Big(B_e + B_i\Big)R = \Big(c_N j_n^\star(k_N R) + d_N y_n^\star(k_N R)\Big). \tag{3.44}$$

From these two equations, we can relate the "Q response"

$$Q = \frac{B_i}{B_e} \tag{3.45}$$

to the internal field coefficients:

$$Q = \frac{n}{n+1} \frac{c_N \beta_n + d_N \gamma_n}{c_N \delta_n + d_N \varepsilon_n}. \tag{3.46}$$

We define the parameters β_n, γ_n, δ_n, and ε_n by

$$\beta_n = j_n^\star(k_N R) - (n+1) j_n(k_N R) \tag{3.47}$$

$$\gamma_n = y_n^\star(k_N R) - (n+1) y_n(k_N R) \tag{3.48}$$

and

$$\delta_n = n j_n(k_N R) + j_n^\star(k_N R) \tag{3.49}$$

$$\varepsilon_n = n y_n(k_N R) + j_n^\star(k_N R). \tag{3.50}$$

Note that we define these quantities as above for consistency with Parkinson (1983) and for similarity between the definitions of the transfer coefficients Λ_j described above and $\mathcal{A}_n^e$ described below. Also note that although they both relate Bessel functions of argument kr, Eqs. 3.47–3.50 differ substantially from Eqs. 3.32–3.35.

Following the approach of Styczinski et al. (*submitted*—Chapter 4), we now define a final recursion quantity, the complex response to the excitation field $\mathcal{A}_n^e$ as

$$\mathcal{A}_n^e = \frac{\beta_n + \Lambda_N \gamma_n}{\delta_n + \Lambda_N \varepsilon_n}. \tag{3.51}$$

This normalized, complex amplitude has the desirable characteristic that it is asymptotic to $(1 + 0\mathrm{i})$ for a highly conducting ocean with no ice shell, for any degree n in the excitation field. Therefore, with the recursion relation from Eq. 3.37, $\mathcal{A}_n^e$ is a readily calculable measure of the effectiveness of a body at behaving as a perfect conductor, and can easily be compared to spacecraft data fit to induced magnetic moments of any order n.

For the special case of a single, uniform conducting layer representing a saline ocean, the complex response evaluates to

$$\mathcal{A}_n^e = \frac{j_{n+1}(ka)y_{n+1}(ks) - j_{n+1}(ks)y_{n+1}(ka)}{j_{n+1}(ks)y_{n-1}(ka) - j_{n-1}(ka)y_{n+1}(ks)} \tag{3.52}$$

with a the radius of the ocean outer boundary, s the radius of the ocean inner boundary, and $k = \sqrt{i\omega\mu_0\sigma}$ with σ the conductivity of the ocean layer. $a = R - h$, where h is the ice shell thickness, and $s = a - D$, where D is the ocean thickness. This result is analogous to the three-layer model of Zimmer et al. (2000). All past studies have considered a uniform excitation field, with $n = 1$; comparison with past work is made by evaluating $A = |\mathcal{A}_1^e|$ and $\phi = -\arg(\mathcal{A}_1^e)$.

3.5.2 Numerical approximation to external boundary conditions

We now detail our alternative numerical approach, based on that of Eckhardt (1963). Returning to Eq. 3.22 (the spherical Bessel equation), if instead of solving for the basis functions directly, we make the substitution

$$\frac{dF(r)}{dr} = F(r)G(r) \tag{3.53}$$

where $G(r)$ is another arbitrary function of r, we obtain a Riccati equation for G:

$$\frac{d}{dr}\left(r^2 G\right) + r^2 G^2 + k^2 r^2 - n(n+1) = 0. \tag{3.54}$$

Note that we have not made any assumptions about $k(r)$ in reaching Eq. 3.54.

We can now exploit the external boundary conditions to obtain a new equation. In Eqs. 3.43 and 3.44, on the right-hand side we insert the more general expressions from Eqs. 3.19–3.21 using the above substitution for $F(r)$. Solving for the Q response as in Eq. 3.45, we obtain

$$Q = \frac{n}{n+1}\frac{rG - n}{rG + n + 1}. \tag{3.55}$$

Taking dQ/dr and making substitutions from Eq. 3.54, we reach an ODE for Q that may be solved numerically:

$$\frac{dQ}{dr} = -\frac{k^2 r(n+1)}{(2n+1)n}\left(Q - \frac{n}{n+1}\right)^2 - \frac{2n+1}{r}Q. \tag{3.56}$$

$\mathcal{A}_n^e$ may then be found by

$$\mathcal{A}_n^e = \frac{n+1}{n} Q \tag{3.57}$$

as can be seen from comparing Eqs. 3.46 and 3.51.

3.5.3 Application of induced response functions

As applied to the Galilean moons, the primary case of interest in the magnetic induction problem is for an imposed field that is effectively uniform, where $n = 1$. The analysis contained in this work makes the approximation that the magnetic field applied to the Galilean moons is entirely spatially uniform, with $n = 1$. The higher-order components applied to the moons are small, mostly deriving from oscillations in the plasma at much higher frequencies than Jupiter's primary field (Schilling et al., 2007). In this case, expressing the complex quantity $\mathcal{A}_1^e$ in terms of a magnitude A and phase delay ϕ permits a direct comparison to work by other authors (*e.g.* Zimmer et al., 2000):

$$\mathcal{A}_1^e = Ae^{-i\phi} \tag{3.58}$$

The negative exponent in Eq. 3.58 is ultimately the result of an error in Parkinson (1983) propagated in the many past studies applying the results from that text. Our choice of sign convention for k as the complex conjugate of that chosen by Parkinson (1983), a necessary condition for deriving the spherical Bessel equation, causes our result for the complex amplitude $\mathcal{A}_1^e$ to be equal to the complex conjugate of the analogous quantity from Zimmer et al. (2000), $Ae^{i\phi}$. This merely negates the phase of this quantity, as A and ϕ are both real-valued. By defining A and ϕ as in Eq. 3.58, we can use them exactly as in past work to evaluate the internally generated, induced magnetic field outside the moon $\mathbf{B}_{\text{int,moon}}$ by

$$\mathbf{B}_{\text{int,moon}} = -Ae^{-i(\omega t-\phi)} \frac{B_e}{2} \frac{3\cos\theta\hat{r} - \hat{z}}{r^3} \tag{3.59}$$

where $\hat{z}$ is directed along the instantaneous vector of the time-varying external magnetic field $\mathbf{B}_{\text{ext,moon}}$ applied to the moon, θ is the angle between $\hat{z}$ and the measurement point at $\mathbf{r} = r\hat{r}$, the origin is centered on the body to which the excitation field is applied, and the factor of 2 in Eq. 3.59

results from inserting $n = 1$ into the factor $n/(n+1)$ in Eq. 3.46. Note that Eq. 3.59 only applies in the space outside the moon.

Figures 3.2–3.4, 3.6, and 3.7 in the main text were produced using the Eckhardt (1963)-based numerical technique. Figure 3.6 plots $A = |\mathcal{A}_1^e|$ and $\phi = -\arg(\mathcal{A}_1^e)$ for Europa, Ganymede, and Callisto. Figures 3.2–3.4 plot the same phase delay ϕ, but scale the amplitude A to the maximum induced magnetic field that would be measured at a surface point. This occurs where the time-varying external field from Jupiter is instantaneously directed vertically into or out of the surface ($\theta = 0$ or π, $r = R$, and $\hat{r} = \pm\hat{z}$ in Eq. 3.59). These conditions happen at key locations on the bodies' surfaces twice per period (once outward, once inward), and are not in general colocated for the various excitation frequencies. For example, for Europa's synodic period with Jupiter at 11.23 hr, the key points on the surface are the sub- and anti-jovian points, because the maximum oscillation is along the europacentric (E$\phi\Omega$) $\hat{y}$ direction. In contrast, at Europa's orbital period of 85.23 hr, the greatest oscillation is aligned with the E$\phi\Omega$ $\hat{z}$ direction, so the largest induced field will occur at the north and south spin poles. However, all of Figures 3.2–3.4, 3.6 scale to the B_y oscillation for ease of interpretation, and therefore describe the oscillation along the vertical at the surface at the sub- and anti-jovian points for each body.

Figures 3.9 and 3.10 show a benchmarking calculation comparing the ODE approach to the stacked layer approach. For sufficiently stringent numerical solution parameters, the two approaches yield effectively identical results. Furthermore, the ODE approach has a distinct advantage in computation time for our implementation. The stacked layer approach requires explicit calculation of many Bessel functions for the layer coefficients at closely spaced points. The results of these functions very nearly cancel, so they must be evaluated at enormously high precision. Sometimes over 200 digits of precision are required to evaluate interior models relevant to the Galilean moons, requiring special computation packages and ample computation time.

The ODE approach, in contrast, converges faster for more closely spaced layers, which create a smoother function to evaluate. Thus, in practice we evaluate a comparable result that takes a small fraction of the time to compute for a highly detailed interior structure model. Use of the ODE approach to reduce computation time for detailed interior models enables massively parallel statistical

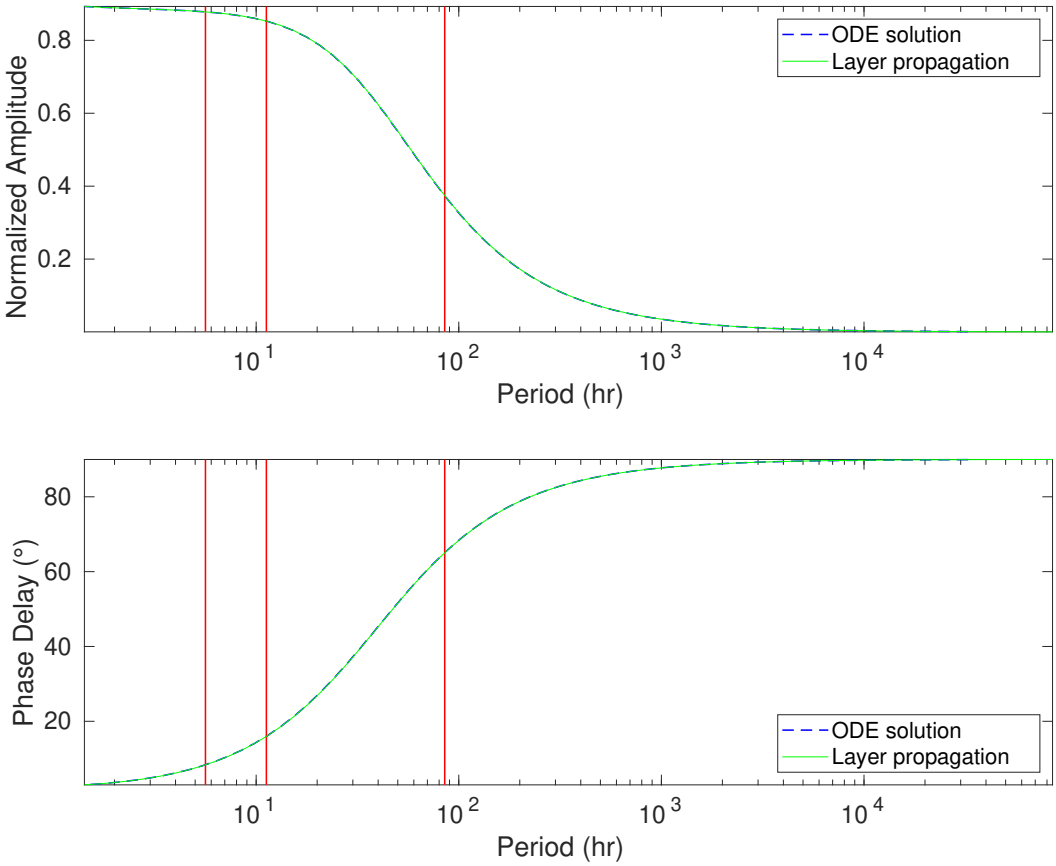

Figure 3.9: Comparison of the complex response $\mathcal{A}_1^e$ for the uniform field case, calculated by two different methods. The amplitude $A = |\mathcal{A}_1^e|$ and phase delay $\phi = -\arg(\mathcal{A}_1^e)$ are plotted separately. The Srivastava (1966) layered conductor approach common in the literature is plotted as a blue dashed line and the Eckhardt (1963) ODE approach we use in our analysis is plotted as a solid green line. For sufficiently stringent numerical solution parameters, the lines are effectively identical. A numerically challenging example case was selected for this comparison: a Europa model of approx. 150 layers and a 1 wt% $MgSO_4$ ocean.

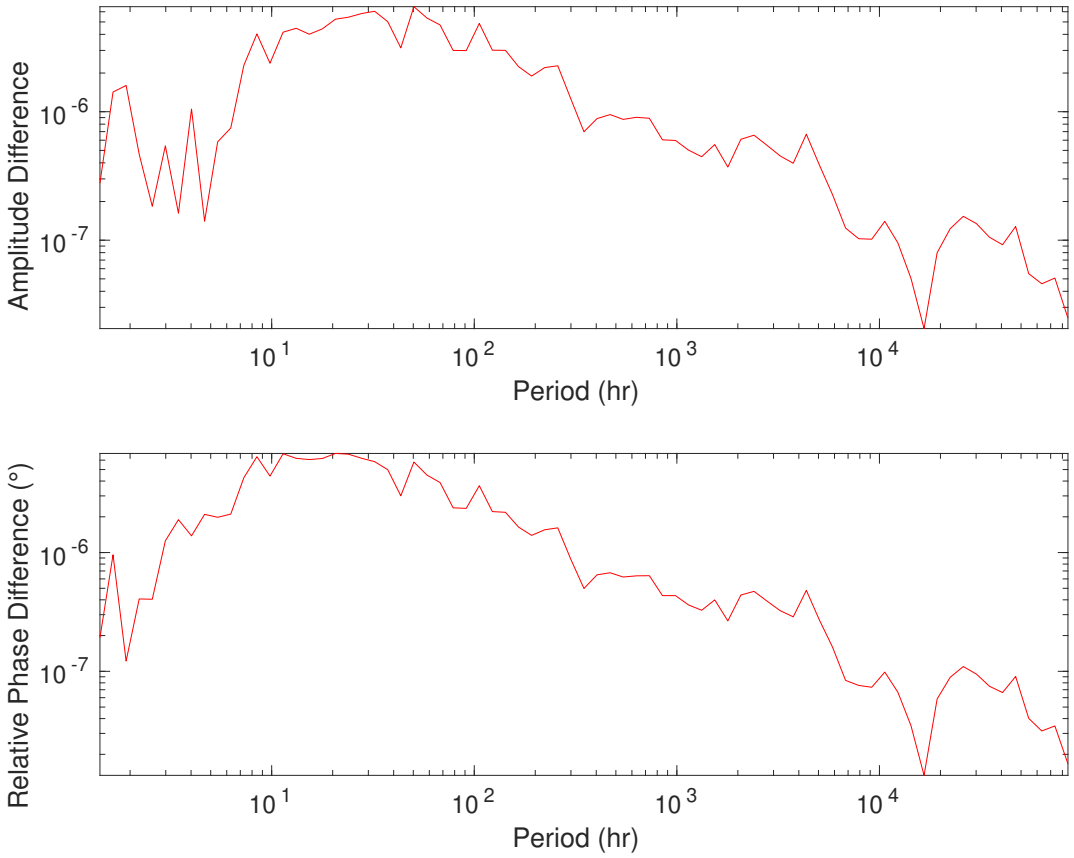

Figure 3.10: Difference of the lines in Figure 3.9. Absolute values of the difference are plotted so that a log scale may be used to display them. A normalized, relative phase difference is shown, *i.e.* normalized to a maximum of 1. The small differences belie the close overlap of the lines in Figure 3.9.

studies, such as Monte Carlo methods, to explore large parameter spaces in reasonable time frames. In future work, we intend to apply such methods to better constrain the interior structures of the Galilean moons and other moons, with current and future measurements.

3.5.4 Comparison of adiabatic ocean profiles to uniformly conducting oceans

In Section 3.2 of this work (main text), we focus on the observable signal from depth-dependent effects that shift the conductivity away from a nominal mean value. All past work studying magnetic induction of satellite oceans has assumed the ocean to be a single layer of uniform conductivity and calculated the induced field using the approach of Srivastava (1966). For comparison to this body of literature, we plot the difference in induced field from our approach to the uniform conductivity approach in Figures 3.11–3.13. In each of these figures, the top panels compare our adiabatic ocean approach to a uniform conductivity that is consistent with the mean value from the corresponding adiabatic profile; the bottom panels compare our approach against a uniform conductivity taken to be the value from our model at the uppermost ice–ocean boundary. In most cases, the differences are near a few percent for the longer periods considered (red lines).

3.6 Motional induction response model

The magnetic induction equation can be used to estimate the components of the magnetic field $\mathbf{B}$ induced by ocean currents with velocity $\mathbf{u}$ and those arising from changes in the externally imposed field:

$$\frac{\partial \mathbf{B}}{\partial t} = \nabla \times (\mathbf{u} \times \mathbf{B}) - \nabla \times (\eta \nabla \times \mathbf{B}) \tag{3.60}$$

where $\eta = (\mu_0 \sigma)^{-1}$ is the magnetic diffusivity. Here, the first term represents the evolution of the magnetic field, the second term represents magnetic induction, and the third term represents magnetic diffusion.

Neglecting variations in oceanic electrical conductivity with depth and assuming an incompressible fluid, Eq. 3.60 simplifies to

$$\frac{\partial \mathbf{B}}{\partial t} = (\mathbf{B} \cdot \nabla)\mathbf{u} - (\mathbf{u} \cdot \nabla)\mathbf{B} + \eta \nabla^2 \mathbf{B}, \tag{3.61}$$

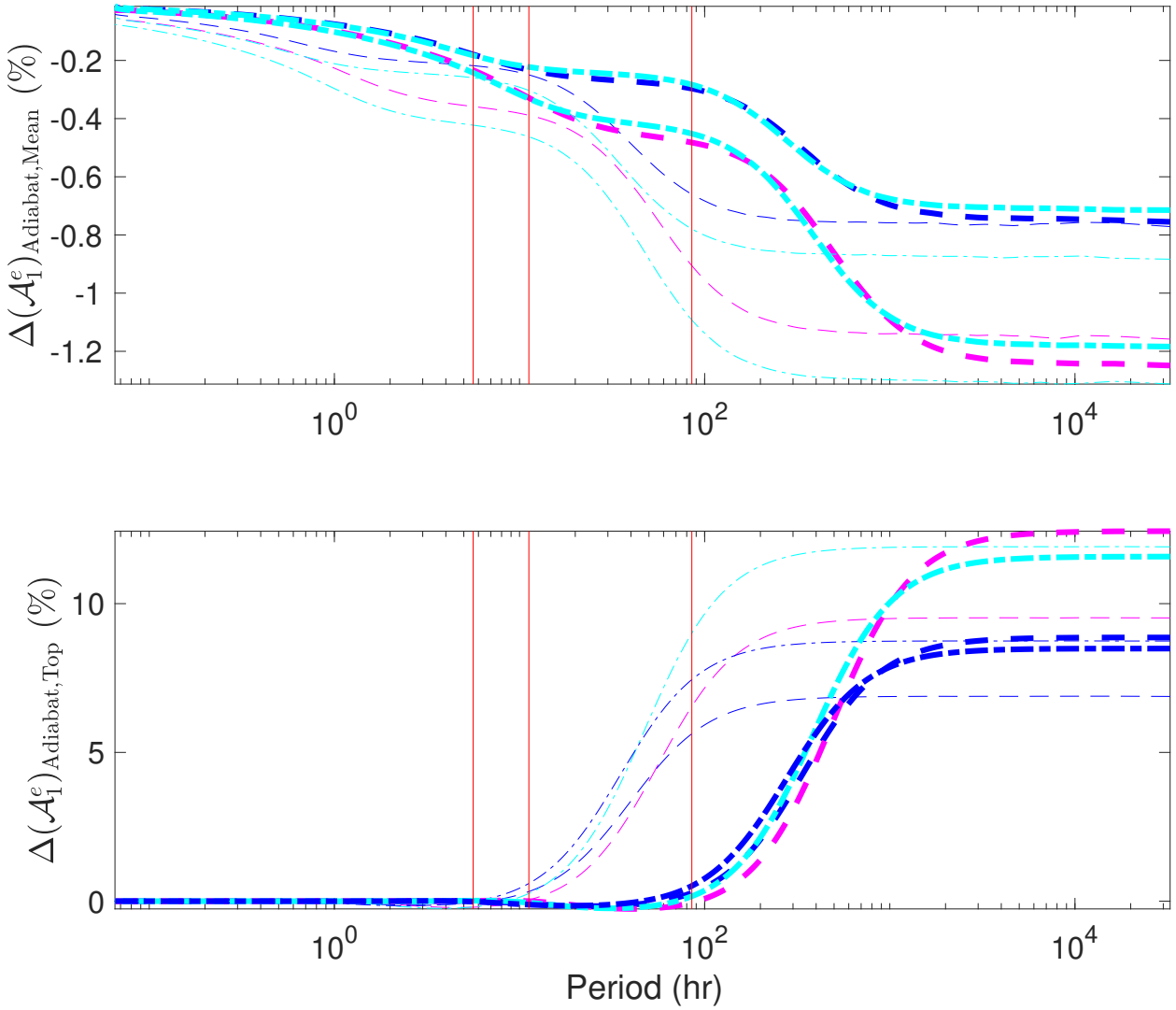

Figure 3.11: Europa: Differences (in %) from the nominal adiabatic case studied here, for uniformly conducting oceans with the equivalent mean conductivity (top panel), and for uniformly conducting oceans with the equivalent conductivity at the ice–ocean interface (bottom panel). Dashed lines (−−) are $MgSO_4$ oceans; dot–dashed lines are Seawater oceans (−·−·). Blue curves are for thicker ice (30 km), magenta curves are thinner ice (5 km) $MgSO_4$ oceans, and cyan curves are thinner ice (5 km) Seawater oceans. Thick lines are higher salinities (10 wt% and 3.5 wt%, respectively) for oceans with aqueous $MgSO_4$ and Seawater. Thinner lines are for oceans with 10% of those concentrations. Vertical lines are the strongest inducing frequencies shown in Figure 3.1.

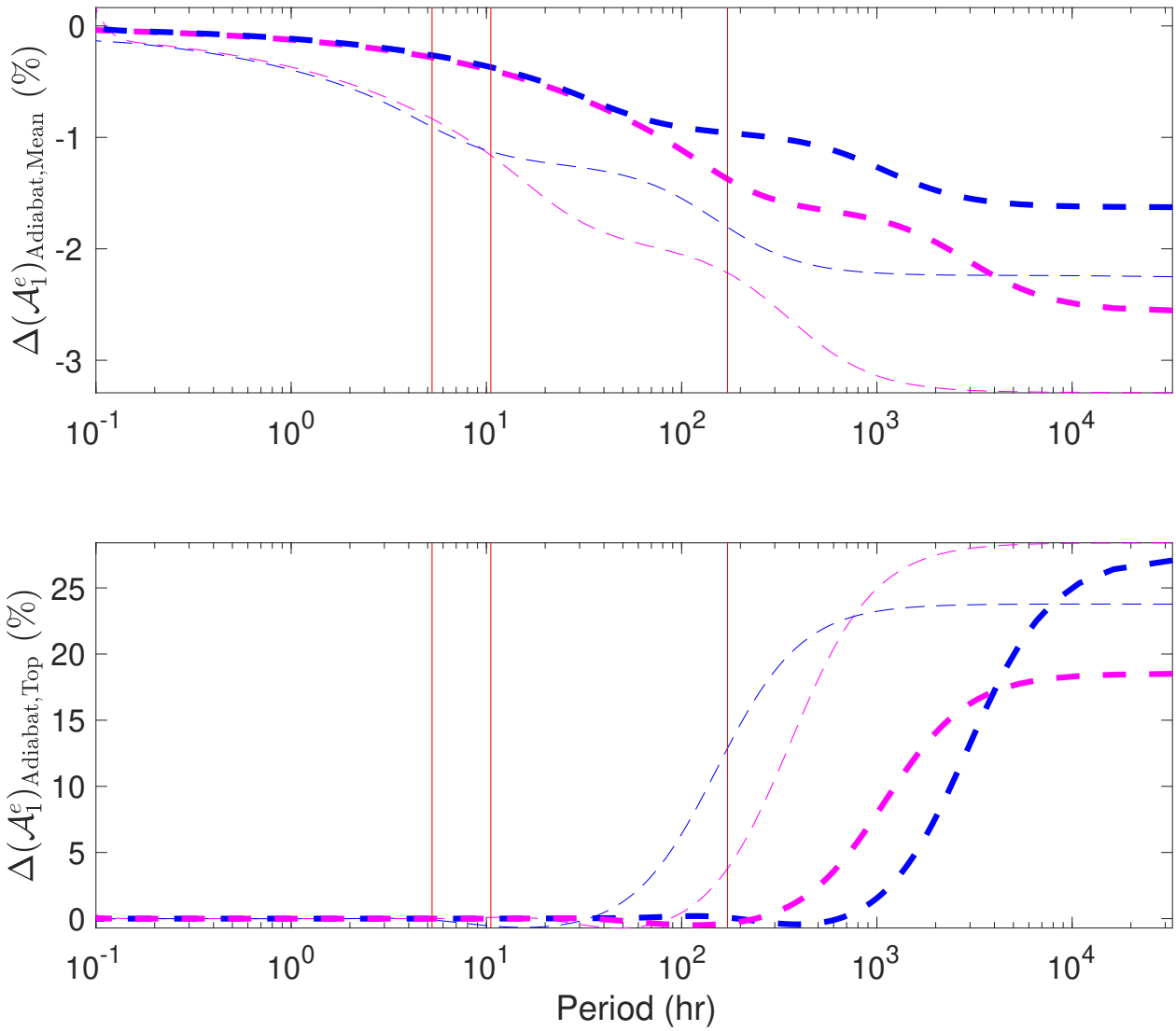

Figure 3.12: Ganymede: Differences (in %) from the nominal adiabatic case studied here for uniformly conducting oceans with the equivalent mean conductivity (top panel), and for uniformly conducting oceans with the equivalent conductivity at the ice–ocean interface (bottom panel). Magenta curves are for thinner ice (∼30 km) and blue curves are for thicker ice (∼100 km). All configurations assume an ocean with aqueous $MgSO_4$. Thick lines are higher salinity (10 wt%) and thinner lines are for oceans with 1 wt%. Vertical lines are the strongest inducing frequencies shown in Figure 3.1.

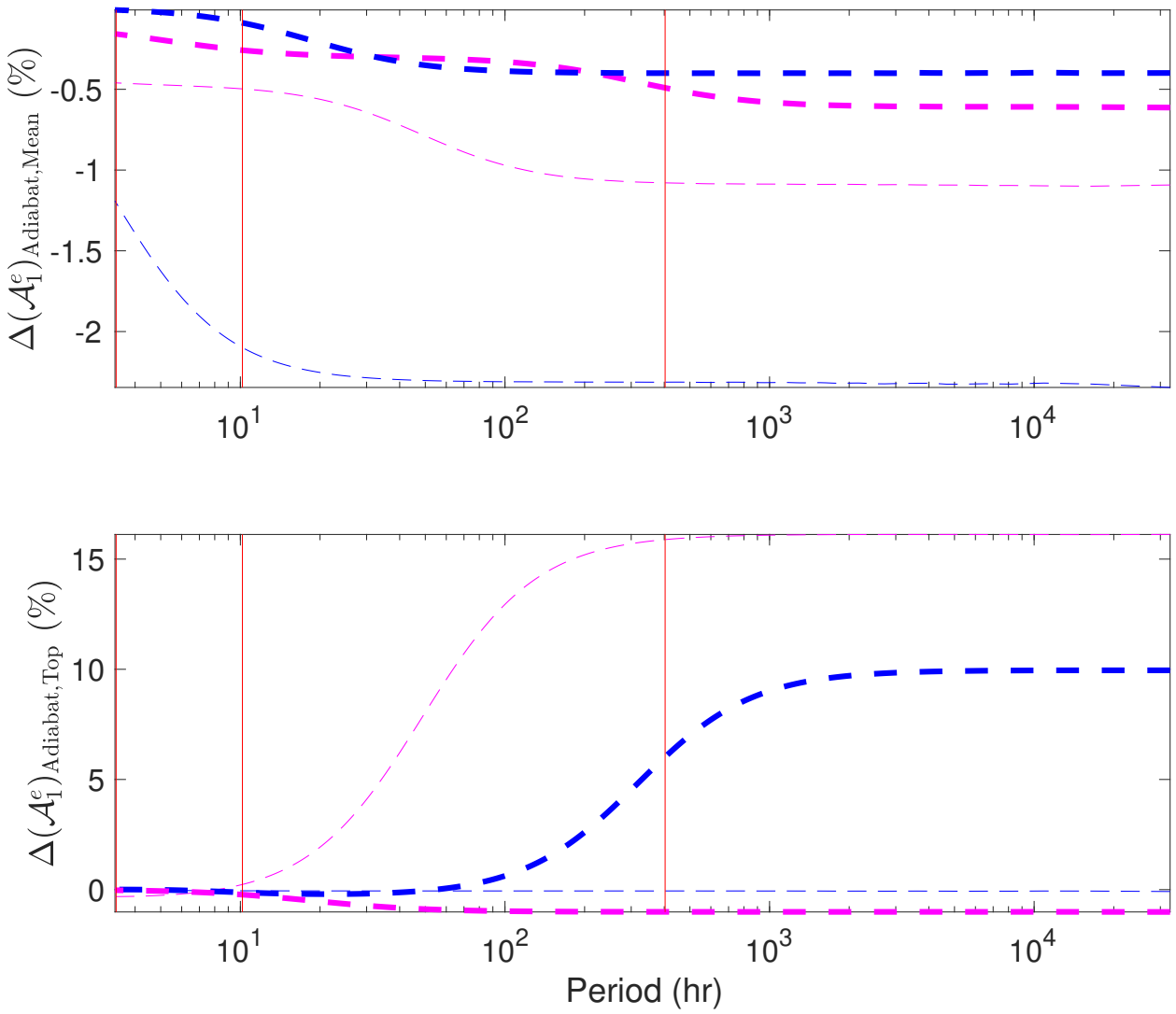

Figure 3.13: Callisto: Differences (in %) from the nominal adiabatic case studied here, for uniformly conducting oceans with the equivalent mean conductivity (top panel) and with for uniformly conducting oceans with the equivalent conductivity at the ice–ocean interface (bottom panel). Magenta curves are for thinner ice (∼30 km) and blue curves are for thicker ice (∼100 km). All configurations assume an ocean with aqueous $MgSO_4$. Thick lines are higher salinity (10 wt%) and thinner lines are for oceans with 1 wt%. Vertical lines are the strongest inducing frequencies shown in Figure 3.1.

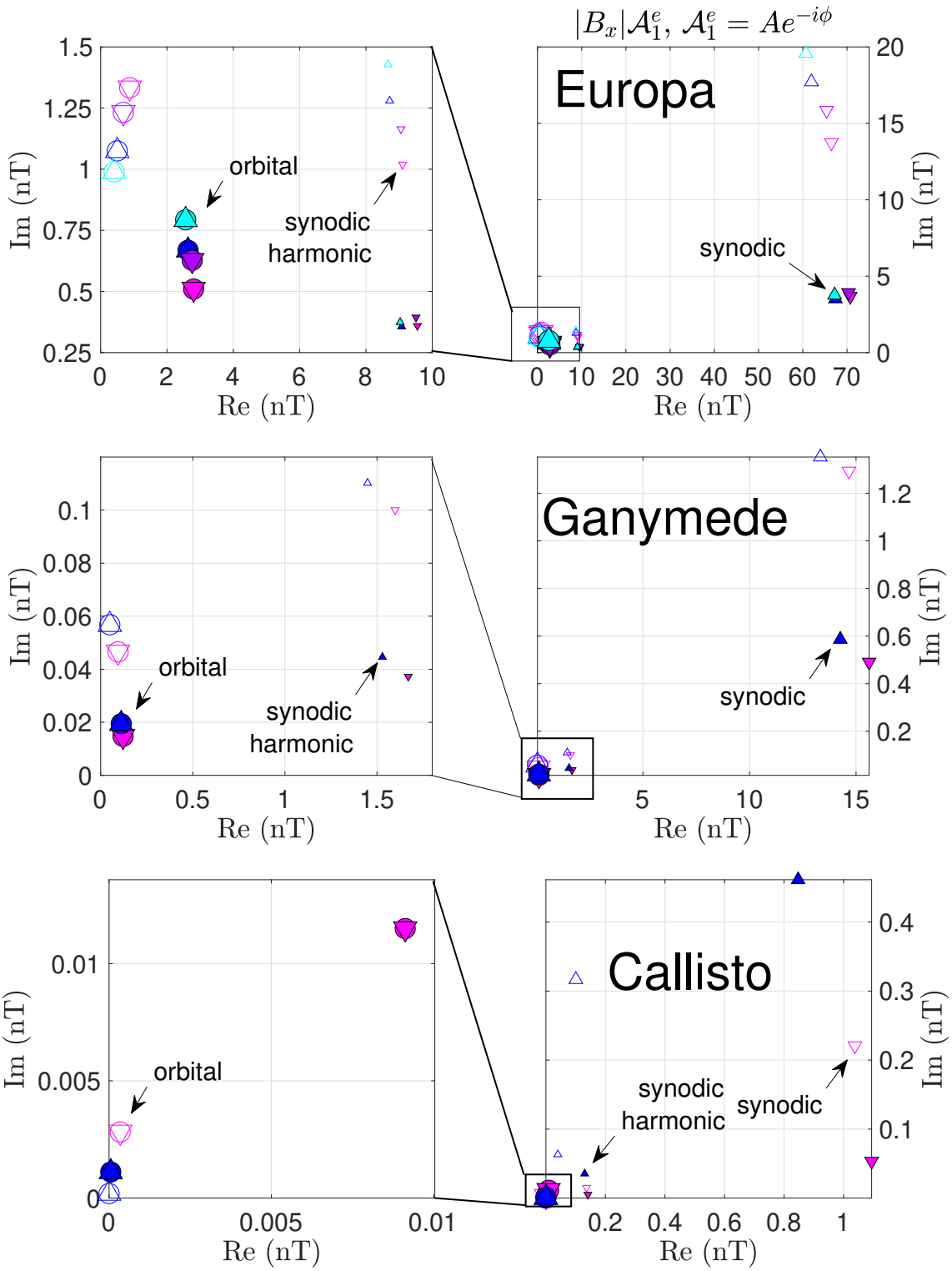

Figure 3.14: Caption appears on next page.

Figure 3.14: Real and imaginary components of the diffusive induction response to the changing B_x component of Jupiter's magnetic field at the main driving periods (Figure 3.1) for {Europa,Ganymede,Callisto}. The real part (on the x axis) is in phase with the excitation field, and the imaginary part (on the y axis) is 90° out of phase, as detailed in Section 3.2.6. Subpanels on the left side show the lower-magnitude signals of panels on the right. Filled symbols are for the higher concentrations. Upward and downward triangles are for thicker ice ($\{30, 95, 130\}$ km) and thinner ice ($\{5, 26, 100\}$ km), respectively. Symbol sizes scale with the period of the oscillation, denoting the orbital (largest), the synodic (intermediate), and the synodic harmonic (smallest). Circles are added to the orbital periods to guide the eye.

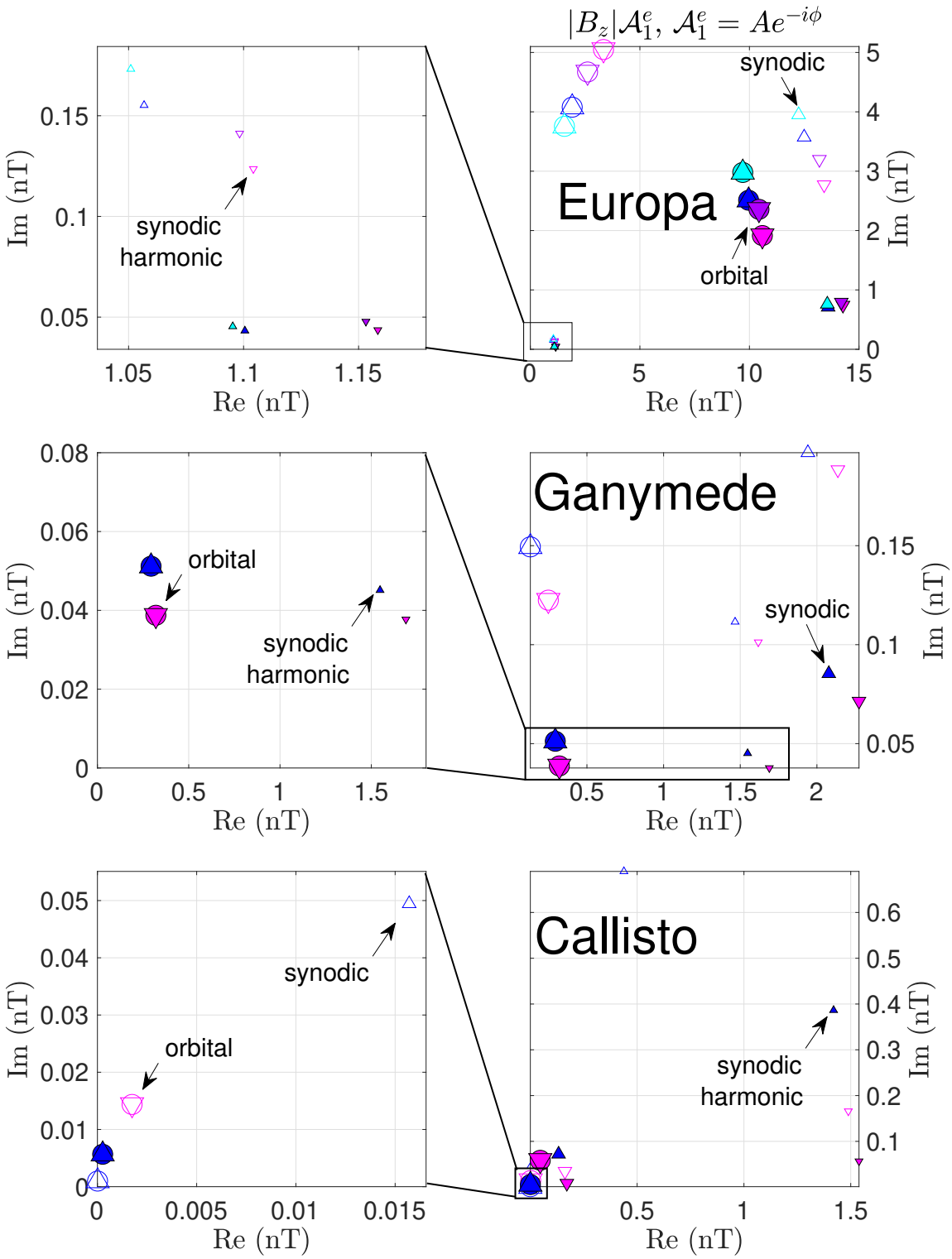

Figure 3.15: Caption appears on next page.

Figure 3.15: Real and imaginary components of the diffusive induction responses to the changing B_z component of Jupiter's magnetic field at the main driving periods (Figure 3.1) for {Europa,Ganymede,Callisto}. The real part (on the x axis) is in phase with the excitation field, and the imaginary part (on the y axis) is 90° out of phase, as detailed in Section 3.2.6. Subpanels on the left side show the lower-magnitude signals of panels on the right. Filled symbols are for the higher concentrations. Upward and downward triangles are for thicker ice ($\{30, 95, 130\}$ km) and thinner ice ($\{5, 26, 100\}$ km), respectively. Symbol sizes scale with the period of the oscillation, denoting the orbital (largest), the synodic (intermediate), and the synodic harmonic (smallest). Circles are added to the orbital periods to guide the eye.

after also expanding the induction term and utilizing $\nabla \cdot \mathbf{B} = 0$ and $\nabla \cdot \mathbf{u} = 0$. Let us decompose the total magnetic field into the background imposed field $\mathbf{B}_o$ and the satellite's induced field $\mathbf{b}$:

$$\mathbf{B} = \mathbf{B}_o + \mathbf{b} \tag{3.62}$$

with $|\mathbf{B}_o| \gg |\mathbf{b}|$. The induction equation then becomes

$$\frac{\partial \mathbf{b}}{\partial t} = -\frac{\partial \mathbf{B}_o}{\partial t} + (\mathbf{B}_o \cdot \nabla)\mathbf{u} - (\mathbf{u} \cdot \nabla)(\mathbf{B}_o + \mathbf{b}) + \eta \nabla^2 (\mathbf{B}_o + \mathbf{b}). \tag{3.63}$$

Here, the first term is the evolution of the induced magnetic field, the second term is induction due to variations in Jupiter's (or Ganymede's) intrinsic magnetic field, the third term is induction due to oceanic fluid motions, the fourth and fifth terms are advection of the fields by ocean flows, and the sixth and seventh terms are diffusion of the jovian and induced fields.

Let us next assume that the background field can be approximated by $\mathbf{B}_o = B_o \hat{z}$, where B_o is constant and homogeneous and $\hat{z}$ is aligned with the rotation axis, in which case Eq. 3.63 further simplifies to:

$$\frac{\partial \mathbf{b}}{\partial t} = B_o \frac{\partial \mathbf{u}}{\partial z} - (\mathbf{u} \cdot \nabla)\mathbf{b} + \eta \nabla^2 \mathbf{b}. \tag{3.64}$$

We will also focus on the quasi-steady induction signal generated by ocean flows rather than the rapidly varying contribution that could be difficult to distinguish from other magnetic field perturbations. Towards this end, the induced magnetic field and velocity fields are decomposed into mean and fluctuating components: $\mathbf{b} = \overline{\mathbf{b}} + \mathbf{b}'$ and $\mathbf{u} = \overline{\mathbf{u}} + \mathbf{u}'$. Inserting this into Eq. 3.64 and using Reynolds averaging yields

$$\frac{\partial \overline{\mathbf{b}}}{\partial t} = B_o \frac{\partial \overline{\mathbf{u}}}{\partial z} - (\overline{\mathbf{u}} \cdot \nabla)\overline{\mathbf{b}} - \overline{(\mathbf{u}' \cdot \nabla)\mathbf{b}'} + \eta \nabla^2 \overline{\mathbf{b}}. \tag{3.65}$$

Next, we focus on the radial and latitudinal components because the zonal flow ($\overline{u}_\phi$) is nearly invariant in the z-direction (Figure 3.8a), noting also that azimuthally oriented (toroidal) magnetic fields would not be detectable by spacecraft:

$$\frac{\partial \overline{b}_r}{\partial t} = B_o \frac{\partial \overline{u}_r}{\partial z} - (\overline{\mathbf{u}} \cdot \nabla)\overline{b}_r - \overline{(\mathbf{u}' \cdot \nabla)b'_r} + \eta \nabla^2 \overline{b}_r \tag{3.66}$$

$$\frac{\partial \overline{b}_\theta}{\partial t} = B_o \frac{\partial \overline{u}_\theta}{\partial z} - (\overline{\mathbf{u}} \cdot \nabla)\overline{b}_\theta - \overline{(\mathbf{u}' \cdot \nabla)b'_\theta} + \eta \nabla^2 \overline{b}_\theta. \tag{3.67}$$

Using simple scaling arguments, the second and third terms on the right sides are likely small compared to the first term since $|B_o| \gg |b|$ (assuming similar characteristic flow speeds and length scales), such that

$$\frac{\partial \bar{b}_r}{\partial t} \approx B_o \frac{\partial \bar{u}_r}{\partial z} + \eta \nabla^2 \bar{b}_r \tag{3.68}$$

$$\frac{\partial \bar{b}_\theta}{\partial t} \approx B_o \frac{\partial \bar{u}_\theta}{\partial z} + \eta \nabla^2 \bar{b}_\theta .. \tag{3.69}$$

Considering the poloidal flow components (Figure 3.8b-c), the induced fields would likely be strongest near the equator where large vertical gradients in the convective flows exist.

In the steady-state limit and approximating the gradient length scales as D and flow speeds as U_r and U_θ, an upper bound on magnetic fields induced by ocean currents can be estimated as:

$$\frac{B_o U_r}{D} \sim \frac{\eta b_r}{D^2}, \text{ such that } b_r \sim \frac{B_o U_r D}{\eta} = \mu_o \sigma D U_r B_o \tag{3.70}$$

$$\frac{B_o U_\theta}{D} \sim \frac{\eta b_\theta}{D^2}, \text{ such that } b_\theta \sim \frac{B_o U_\theta D}{\eta} = \mu_o \sigma D U_\theta B_o . \tag{3.71}$$

Here, we neglect the coupling between b_r and b_θ to effectively estimate maximum values for each component.

Several aspects regarding the velocity field should also be mentioned. First, the oceans are assumed to be in a convective regime that is weakly constrained by rotation following Soderlund (2019). Soderlund also notes, however, that a stronger rotational influence may be possible, which would lead to slower flow speeds and weaker induced magnetic fields. In addition, it is possible that the models overestimate the meridional circulations relative to the zonal flows compared to what might be expected in the satellites (*e.g.* Jones and Kuzanyan, 2009). Because our approach focuses on upper bound estimates, the results are still valid if meridional circulations within the oceans are weaker than those modeled. Finally, flows due to libration, precession, tides, and electromagnetic pumping (*e.g.* Le Bars et al., 2015; Gissinger and Petitdemange, 2019; Soderlund et al., 2020) are neglected here but may interact with the convective flows to change their configurations and/or speeds.

3.7 Interior structure models

The interior structures and associated electrical conductivities used in this work are computed with the *PlanetProfile* framework described by Vance et al. (2018). *PlanetProfile* employs self-consistent thermodynamics for the properties of ice, fluids, rock, and metals to compute the radial structure of an ocean world. Inputs are the surface temperature and bottom melting temperature of the ice, T_o and T_b; density of the rocky interior and any metallic core, ρ_{mantle} and ρ_{core}; salinity of the ocean, w; and gravitational moment of inertia, C/MR^2. For this work, the values for these properties are substantially the same as those used by Vance et al. (2018), with a few minor changes that do not significantly change the ocean thickness and electrical conductivity that are central to this work.

Properties of ice are now computed using the *SeaFreeze* package (Journaux et al., 2020), which provides substantial improvements in accuracy for conditions relevant to icy moon interiors. Solid-state convection in the surface ice I layer has been corrected from Vance et al. (2018) to use the thermal upper boundary layer thickness, e_{th}, from Deschamps and Sotin (2001) rather than the mechanical thickness, e_{mech}. Properties of the rocky mantle and metallic core for Europa are based on updated mineralogies described by Vance and Melwani Daswani (2020). The silicate mantle composition is that of the *MC-Scale* model, an aggregate of type CM and CI chondrite compositions, and the composition of comet 67P. The core composition is a Fe–FeS mixture containing 5 wt% sulfur. Sulfur is appropriately partitioned between the mantle and core to preserve bulk planetary distribution of sulfur in the *MC-Scale* model. This approach does not account for the addition of sulfur to the ocean, which makes up 2.6% of the ocean's mass for the 10 wt% $MgSO_4$ case. The effect of this minor inconsistency on the thickness of the ocean is smaller than the few-km variation in ocean thicknesses between the different ocean compositions (Table 3.1).

Using the moment of inertia along with supposed core and mantle densities to inform the construction of interior models effectively fixes the hydrosphere thickness. For example, for Europa we use the mean value from Anderson et al. (1998) of $C/MR^2 = 0.346 \pm 0.005$. The uncertainty in this result, combined with the assumed densities of the different radial layers, provide the canonical range of hydrosphere thicknesses of 80–170 km. Our choice of the fixed value of 0.346, and the

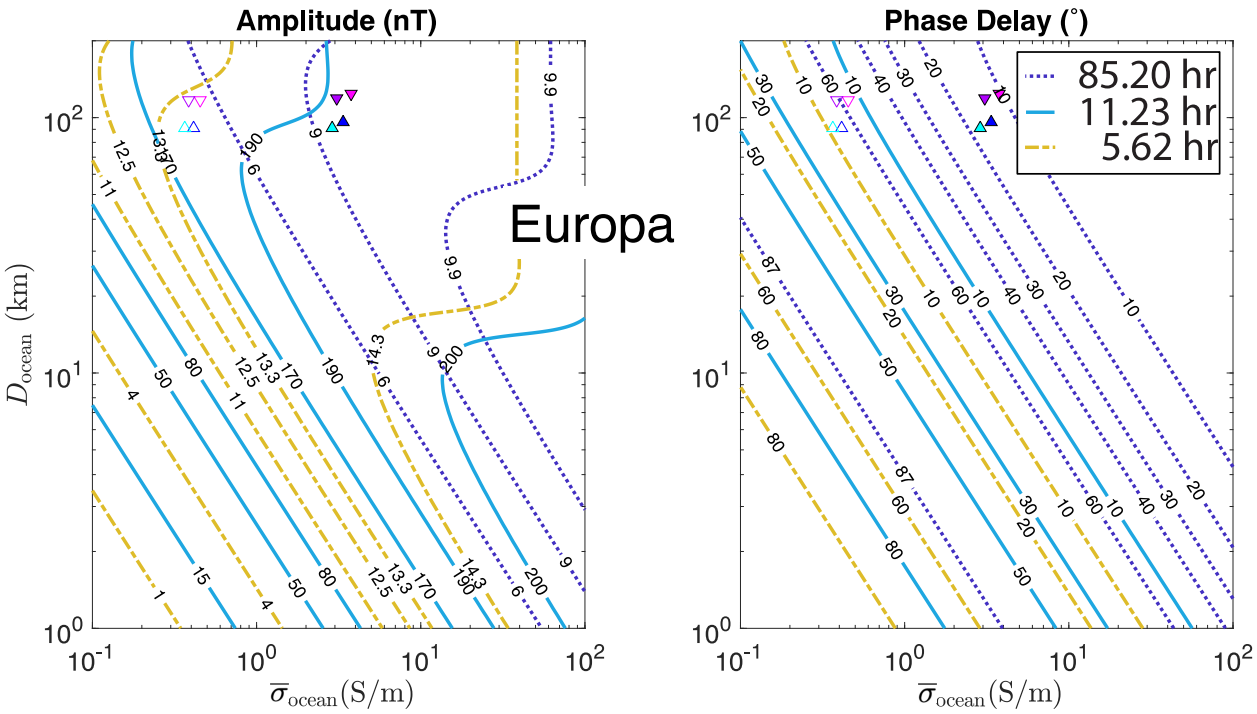

Figure 3.16: Europa: Reproduction of main text Figure 3.2, with points showing the coordinates of the studied models. The marked points match the identification scheme described in Figure 3.7.

fixed core and mantle density, create the ocean+ice hydrosphere thickness of about 125 km. This applies to all interior structures considered for this body. The near-fixed hydrosphere thicknesses are evident in the positions of the filled circles in Figure 3.5. Note that the interior structures we infer from moments of inertia restrict the realistic parameter space in Figures 3.2–3.4 to be a narrow region near the top of each contour plot. This is demonstrated in Figures 3.16–3.18, wherein the studied models are marked on the contours from Figures 3.2–3.4.

The discrete layers in *PlanetProfile* are sufficient in number to provide step transitions between layers that are smaller than 1 km in the hydrospheres and smaller than a few km in the deeper interior. For example, the Europa models used here employ 200 steps in the ice, 350 steps in the ocean, 500 steps in the silicate layer, and 10 steps in the core. Similar scalings are used for Ganymede and Callisto in proportion to their thicker oceans and ice layers.

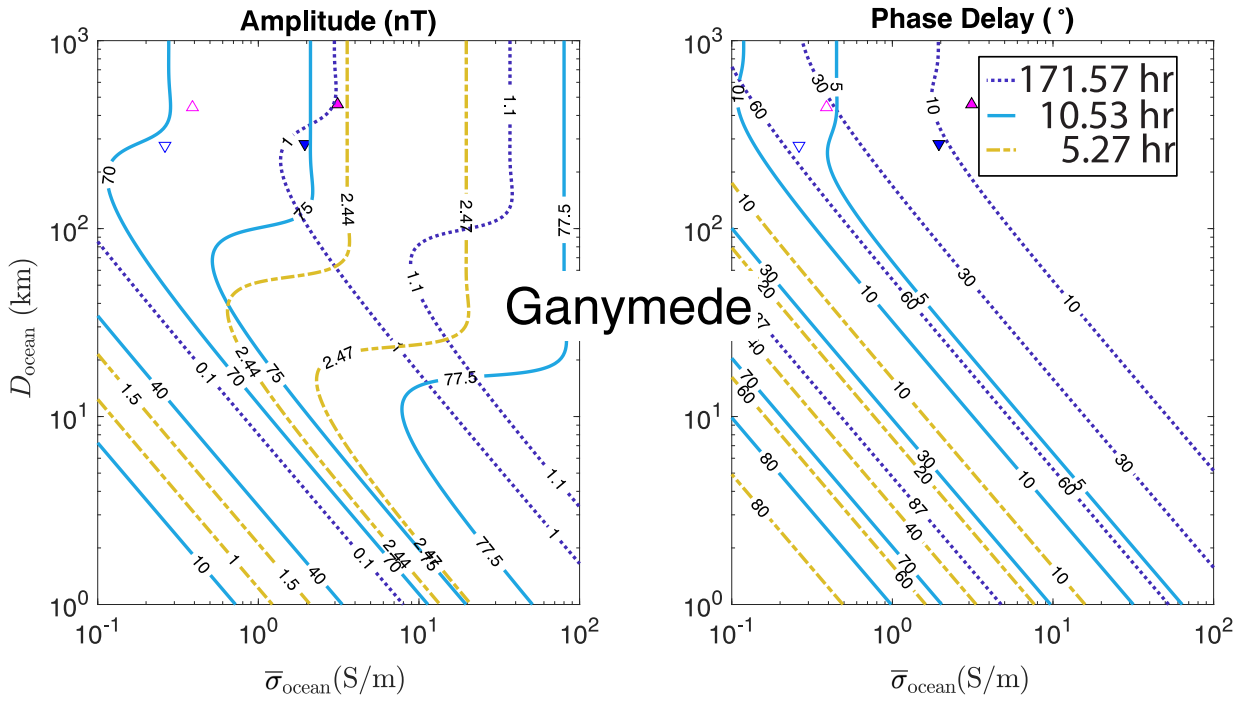

Figure 3.17: Ganymede: Reproduction of main text Figure 3.3, with points showing the coordinates of the studied models. The marked points match the identification scheme described in Figure 3.7.

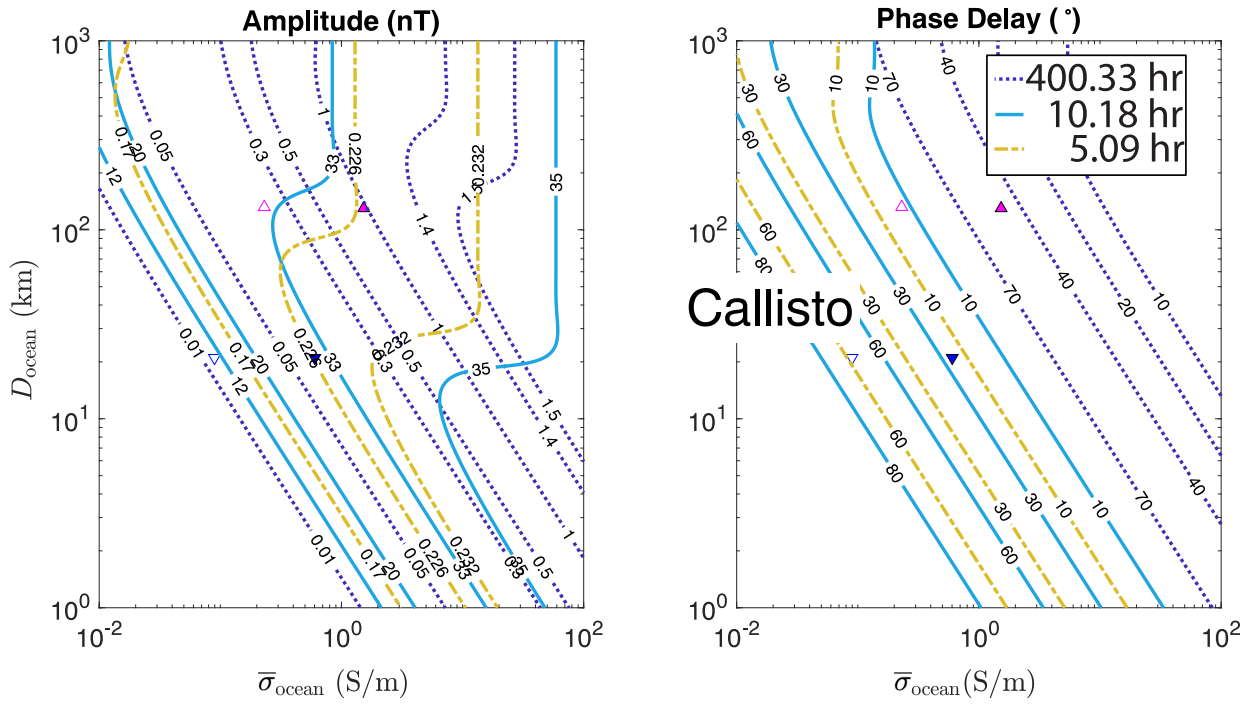

Figure 3.18: Callisto: Reproduction of main text Figure 3.4, with points showing the coordinates of the studied models. The marked points match the identification scheme described in Figure 3.7.

Europa ($\hat{x}$)			Period (hr):	**5.62**	**11.23**	**85.20**
			B_x (nT):	**10.03**	**75.55**	**3.17**
T_b	$\overline{T}$	D_{I}	D_{ocean}		$B_x \mathcal{A}_1^e$	
(K)	(K)	(km)	(km)		(nT)	
Ionosphere Only				**Re Im**	**Re Im**	**Re Im**
Pedersen				0.000 0.069	0.001 0.262	0.000 0.001
$MgSO_4$ 1 wt%				**Re Im**	**Re Im**	**Re Im**
273.1	273.9	5	117	9.106 1.019	66.471 13.737	0.876 1.333
Pedersen				9.108 1.021	66.488 13.741	0.877 1.334
$\overline{\sigma} = 0.4533$ S/m			$\Delta\mathcal{A}_1^e$ (%)	0.36 –0.41	0.39 –0.08	0.85 0.50
$\sigma_{\mathrm{top}} = 0.4107$ S/m			$\Delta\mathcal{A}_1^e$ (%)	0.10 7.75	–0.45 8.80	–12.31 –3.57
270.4	271.1	30	91	8.714 1.280	61.952 17.717	0.500 1.075
Pedersen				8.718 1.282	61.980 17.723	0.501 1.076
$\overline{\sigma} = 0.4132$ S/m			$\Delta\mathcal{A}_1^e$ (%)	0.22 –0.10	0.24 0.01	0.55 0.34
$\sigma_{\mathrm{top}} = 0.3847$ S/m			$\Delta\mathcal{A}_1^e$ (%)	–0.09 6.49	–0.88 6.09	–10.65 –4.23
$MgSO_4$ 10 wt%				**Re Im**	**Re Im**	**Re Im**
272.7	274.1	5	124	9.552 0.359	70.730 3.681	2.803 0.510
Pedersen				9.553 0.361	70.733 3.687	2.803 0.510
$\overline{\sigma} = 3.7646$ S/m			$\Delta\mathcal{A}_1^e$ (%)	0.23 –3.83	0.33 –2.87	0.49 –0.10
$\sigma_{\mathrm{top}} = 3.3197$ S/m			$\Delta\mathcal{A}_1^e$ (%)	–0.01 2.28	–0.01 2.13	–0.34 11.33
269.8	270.8	30	96	9.075 0.357	67.382 3.517	2.635 0.668
Pedersen				9.076 0.359	67.386 3.526	2.636 0.669
$\overline{\sigma} = 3.3661$ S/m			$\Delta\mathcal{A}_1^e$ (%)	0.18 –2.30	0.23 –1.35	0.30 0.02
$\sigma_{\mathrm{top}} = 3.0763$ S/m			$\Delta\mathcal{A}_1^e$ (%)	–0.01 1.41	0.08 2.77	–0.81 7.99

Europa ($\hat{x}$)			Period (hr):	**5.62**	**11.23**	**85.20**
			B_x (nT):	**10.03**	**75.55**	**3.17**
T_b	$\overline{T}$	$D_{\rm I}$	$D_{\rm ocean}$		$B_x \mathcal{A}_1^e$	
(K)	(K)	(km)	(km)		(nT)	
Seawater 0.35165 wt%				**Re Im**	**Re Im**	**Re Im**
274.9	275.7	5	117	9.076 1.102	65.860 14.958	0.758 1.275
Pedersen				9.078 1.103	65.879 14.961	0.759 1.276
$\overline{\sigma} = 0.4124$ S/m			$\Delta\mathcal{A}_1^e$ (%)	0.41 –0.33	0.44 –0.04	0.96 0.58
$\sigma_{\rm top} = 0.3670$ S/m			$\Delta\mathcal{A}_1^e$ (%)	0.05 9.74	–0.77 10.45	–15.30 –5.17
270.0	270.7	30	91	8.667 1.428	60.705 19.584	0.407 0.990
Pedersen				8.670 1.430	60.738 19.589	0.408 0.991
$\overline{\sigma} = 0.3651$ S/m			$\Delta\mathcal{A}_1^e$ (%)	0.26 –0.07	0.29 0.03	0.65 0.42
$\sigma_{\rm top} = 0.3339$ S/m			$\Delta\mathcal{A}_1^e$ (%)	–0.23 8.27	–1.49 7.33	–13.72 –5.87
Seawater 3.5165 wt%				**Re Im**	**Re Im**	**Re Im**
270.8	271.9	5	119	9.509 0.394	70.355 3.930	2.761 0.628
Pedersen				9.510 0.396	70.358 3.936	2.761 0.628
$\overline{\sigma} = 3.0760$ S/m			$\Delta\mathcal{A}_1^e$ (%)	0.24 –3.32	0.33 –2.24	0.46 –0.03
$\sigma_{\rm top} = 2.7347$ S/m			$\Delta\mathcal{A}_1^e$ (%)	–0.02 2.08	0.04 2.37	–0.74 10.53
268.2	269.1	30	91	9.032 0.374	67.196 3.767	2.564 0.793
Pedersen				9.033 0.376	67.201 3.777	2.564 0.793
$\overline{\sigma} = 2.8862$ S/m			$\Delta\mathcal{A}_1^e$ (%)	0.18 –1.89	0.22 –0.95	0.28 0.03
$\sigma_{\rm top} = 2.6476$ S/m			$\Delta\mathcal{A}_1^e$ (%)	0.01 1.46	0.10 3.88	–1.26 7.23

Table 3.6: Europa: magnetic induction field strengths for B_x, under the same assumptions as described for B_y in main text Table 3.2. The corresponding values for the main models are shown in Figure 3.14.

Ganymede ($\hat{x}$)			Period (hr):	**5.27**	**10.53**	**171.57**
			B_x (nT):	**1.76**	**16.64**	**0.14**
T_b	$\overline{T}$	D_{I}	D_{ocean}		$B_x \mathcal{A}_1^e$	
(K)	(K)	(km)	(km)		(nT)	
Ionosphere Only				**Re Im**	**Re Im**	**Re Im**
Pedersen				0.000 0.001	0.000 0.007	0.000 0.000
$MgSO_4$ 1 wt%				**Re Im**	**Re Im**	**Re Im**
270.7	279.0	25	442	1.598 0.100	14.669 1.293	0.094 0.047
Pedersen				1.598 0.100	14.669 1.293	0.094 0.047
$\overline{\sigma} = 0.5166\,\mathrm{S/m}$			$\Delta\mathcal{A}_1^e$ (%)	0.87 –8.82	1.23 –7.04	2.61 1.01
$\sigma_{\mathrm{top}} = 0.3890\,\mathrm{S/m}$			$\Delta\mathcal{A}_1^e$ (%)	–0.03 4.54	–0.14 5.86	–9.33 17.09
261.6	266.2	92	276	1.449 0.110	13.326 1.352	0.050 0.057
Pedersen				1.449 0.110	13.326 1.353	0.050 0.057
$\overline{\sigma} = 0.3322\,\mathrm{S/m}$			$\Delta\mathcal{A}_1^e$ (%)	0.95 –5.29	1.18 –2.65	2.44 1.41
$\sigma_{\mathrm{top}} = 0.2623\,\mathrm{S/m}$			$\Delta\mathcal{A}_1^e$ (%)	0.08 3.83	0.45 10.74	–22.82 –3.32

Ganymede ($\hat{x}$)			Period (hr):	**5.27**	**10.53**	**171.57**
			B_x (nT):	**1.76**	**16.64**	**0.14**
T_b	$\overline{T}$	D_{I}	D_{ocean}		$B_x \mathcal{A}_1^e$	
(K)	(K)	(km)	(km)		(nT)	
$MgSO_4$ 10 wt%				**Re Im**	**Re Im**	**Re Im**
270.2	278.3	25	458	1.670 0.037	15.614 0.490	0.122 0.015
Pedersen				1.670 0.037	15.614 0.491	0.122 0.015
$\overline{\sigma} = 4.0699$ S/m			$\Delta\mathcal{A}_1^e$ (%)	0.29 –10.57	0.41 –9.78	1.48 –3.07
$\sigma_{\mathrm{top}} = 3.1150$ S/m			$\Delta\mathcal{A}_1^e$ (%)	–0.00 2.03	–0.01 2.84	–0.18 7.55
260.0	263.5	93	282	1.530 0.045	14.262 0.586	0.112 0.019
Pedersen				1.530 0.045	14.262 0.586	0.112 0.019
$\overline{\sigma} = 2.3476$ S/m			$\Delta\mathcal{A}_1^e$ (%)	0.27 –7.17	0.38 –6.43	1.01 –0.28
$\sigma_{\mathrm{top}} = 1.9483$ S/m			$\Delta\mathcal{A}_1^e$ (%)	0.00 1.71	–0.00 2.51	–0.11 15.65
brine layer: 30 km, 20 S/m			$\Delta\mathcal{A}_1^e$ (%)	0.00 –0.00	0.00 –0.00	–1.20 0.20
Pedersen			$\Delta\mathcal{A}_1^e$ (%)	0.00 0.10	0.00 0.04	–1.20 0.20

Table 3.7: Ganymede: magnetic induction field strengths for B_x, under the same assumptions as described for B_y in main text Table 3.3. The corresponding values for the main models are shown in Figure 3.14.

Callisto ($\hat{x}$)			Period (hr):	**5.09**	**10.18**	**400.33**
			B_x (nT):	**0.17**	**1.31**	**0.03**
T_b	$\overline{T}$	D_{I}	D_{ocean}		$B_x\mathcal{A}_1^e$	
(K)	(K)	(km)	(km)		(nT)	
Ionosphere Only				**Re Im**	**Re Im**	**Re Im**
Pedersen				0.013 0.047	0.027 0.193	0.000 0.000
Cowling				0.154 0.065	0.832 0.701	0.000 0.001
$MgSO_4$ 1 wt%				**Re Im**	**Re Im**	**Re Im**
257.4	259.6	99	132	0.137 0.015	1.038 0.221	0.000 0.003
Pedersen				0.139 0.017	1.054 0.228	0.000 0.003
Cowling				0.154 0.024	1.159 0.250	0.001 0.004
$\overline{\sigma} = 0.2307\,\mathrm{S/m}$			$\Delta\mathcal{A}_1^e$ (%)	0.49 –0.44	0.53 –0.08	1.45 0.96
$\sigma_{\mathrm{top}} = 0.1965\,\mathrm{S/m}$			$\Delta\mathcal{A}_1^e$ (%)	0.06 14.62	–1.03 15.03	–26.08 –13.62
250.8	250.9	128	21	0.040 0.063	0.101 0.317	0.000 0.000
Pedersen				0.068 0.079	0.199 0.459	0.000 0.000
Cowling				0.159 0.055	0.950 0.656	0.000 0.001
$\overline{\sigma} = 0.0895\,\mathrm{S/m}$			$\Delta\mathcal{A}_1^e$ (%)	0.04 0.02	0.04 0.03	0.05 0.03
$\sigma_{\mathrm{top}} = 0.0874\,\mathrm{S/m}$			$\Delta\mathcal{A}_1^e$ (%)	–3.26 –0.99	–4.12 –1.87	–4.52 –2.28

Callisto ($\hat{x}$)			Period (hr):	**5.09**	**10.18**	**400.33**
			B_x (nT):	**0.17**	**1.31**	**0.03**
T_b	$\overline{T}$	D_{I}	D_{ocean}		$B_x \mathcal{A}_1^e$	
(K)	(K)	(km)	(km)		(nT)	
$MgSO_4$ 10 wt%				**Re Im**	**Re Im**	**Re Im**
255.7	256.9	99	130	0.141 0.005	1.094 0.053	0.009 0.011
Pedersen				0.142 0.007	1.098 0.062	0.009 0.012
Cowling				0.151 0.018	1.135 0.118	0.010 0.012
$\overline{\sigma} = 1.5256\,\mathrm{S/m}$			$\Delta\mathcal{A}_1^e$ (%)	0.20 –2.91	0.26 –1.74	0.69 0.39
$\sigma_{\mathrm{top}} = 1.3789\,\mathrm{S/m}$			$\Delta\mathcal{A}_1^e$ (%)	0.01 1.12	0.12 3.18	–10.78 –1.59
250.8	250.9	128	21	0.130 0.035	0.847 0.461	0.000 0.001
Pedersen				0.135 0.037	0.897 0.467	0.000 0.001
Cowling				0.160 0.033	1.146 0.419	0.000 0.002
$\overline{\sigma} = 0.6025\,\mathrm{S/m}$			$\Delta\mathcal{A}_1^e$ (%)	–0.00 –0.00	–0.00 –0.00	–0.00 –0.00
$\sigma_{\mathrm{top}} = 0.6062\,\mathrm{S/m}$			$\Delta\mathcal{A}_1^e$ (%)	0.08 –0.53	0.28 –0.34	1.23 0.61

Table 3.8: Callisto: magnetic induction field strengths for B_x, under the same assumptions as described for B_y in main text Table 3.4. The corresponding values for the main models are shown in Figure 3.14.

Europa ($\hat{z}$)			Period (hr):	**5.62**	**11.23**	**84.63**
			B_z (nT):	**1.22**	**15.24**	**11.97**
T_b	$\overline{T}$	D_{I}	D_{ocean}		$B_z\mathcal{A}_1^e$	
(K)	(K)	(km)	(km)		(nT)	
Ionosphere Only				**Re Im**	**Re Im**	**Re Im**
Pedersen				0.000 0.008	0.000 0.053	0.000 0.006
$MgSO_4$ 1 wt%				**Re Im**	**Re Im**	**Re Im**
273.1	273.9	5	117	1.104 0.124	13.409 2.771	3.339 5.049
Pedersen				1.105 0.124	13.412 2.772	3.342 5.052
$\overline{\sigma} = 0.4533$ S/m			$\Delta\mathcal{A}_1^e$ (%)	0.36 –0.41	0.39 –0.08	0.85 0.50
$\sigma_{\mathrm{top}} = 0.4107$ S/m			$\Delta\mathcal{A}_1^e$ (%)	0.10 7.75	–0.45 8.80	–12.31 –3.57
270.4	271.1	30	91	1.057 0.155	12.497 3.574	1.910 4.078
Pedersen				1.057 0.155	12.503 3.575	1.913 4.082
$\overline{\sigma} = 0.4132$ S/m			$\Delta\mathcal{A}_1^e$ (%)	0.22 –0.10	0.24 0.01	0.55 0.34
$\sigma_{\mathrm{top}} = 0.3847$ S/m			$\Delta\mathcal{A}_1^e$ (%)	–0.09 6.49	–0.88 6.09	–10.65 –4.23
$MgSO_4$ 10 wt%				**Re Im**	**Re Im**	**Re Im**
272.7	274.1	5	124	1.158 0.044	14.268 0.743	10.590 1.916
Pedersen				1.158 0.044	14.268 0.744	10.591 1.916
$\overline{\sigma} = 3.7646$ S/m			$\Delta\mathcal{A}_1^e$ (%)	0.23 –3.83	0.33 –2.87	0.49 –0.10
$\sigma_{\mathrm{top}} = 3.3197$ S/m			$\Delta\mathcal{A}_1^e$ (%)	–0.01 2.28	–0.01 2.13	–0.34 11.33
269.8	270.8	30	96	1.101 0.043	13.592 0.709	9.962 2.510
Pedersen				1.101 0.044	13.593 0.711	9.963 2.510
$\overline{\sigma} = 3.3661$ S/m			$\Delta\mathcal{A}_1^e$ (%)	0.18 –2.30	0.23 –1.35	0.30 0.02
$\sigma_{\mathrm{top}} = 3.0763$ S/m			$\Delta\mathcal{A}_1^e$ (%)	–0.01 1.41	0.08 2.77	–0.81 7.99

Europa ($\hat{z}$)			Period (hr):	**5.62**	**11.23**	**84.63**
			B_z (nT):	**1.22**	**15.24**	**11.97**
T_b	$\overline{T}$	D_{I}	D_{ocean}		$B_z\mathcal{A}_1^e$	
(K)	(K)	(km)	(km)		(nT)	
Seawater 0.35165 wt%				**Re Im**	**Re Im**	**Re Im**
274.9	275.7	5	117	1.101 0.134	13.285 3.017	2.893 4.833
Pedersen				1.101 0.134	13.289 3.018	2.896 4.836
$\overline{\sigma} = 0.4124\,\mathrm{S/m}$			$\Delta\mathcal{A}_1^e$ (%)	0.41 –0.33	0.44 –0.04	0.96 0.58
$\sigma_{\mathrm{top}} = 0.3670\,\mathrm{S/m}$			$\Delta\mathcal{A}_1^e$ (%)	0.05 9.74	–0.77 10.45	–15.30 –5.17
270.0	270.7	30	91	1.051 0.173	12.245 3.951	1.556 3.755
Pedersen				1.051 0.173	12.252 3.952	1.559 3.759
$\overline{\sigma} = 0.3651\,\mathrm{S/m}$			$\Delta\mathcal{A}_1^e$ (%)	0.26 –0.07	0.29 0.03	0.65 0.42
$\sigma_{\mathrm{top}} = 0.3339\,\mathrm{S/m}$			$\Delta\mathcal{A}_1^e$ (%)	–0.23 8.27	–1.49 7.33	–13.72 –5.87
Seawater 3.5165 wt%				**Re Im**	**Re Im**	**Re Im**
270.8	271.9	5	119	1.153 0.048	14.192 0.793	10.435 2.358
Pedersen				1.153 0.048	14.193 0.794	10.435 2.358
$\overline{\sigma} = 3.0760\,\mathrm{S/m}$			$\Delta\mathcal{A}_1^e$ (%)	0.24 –3.32	0.33 –2.24	0.46 –0.03
$\sigma_{\mathrm{top}} = 2.7347\,\mathrm{S/m}$			$\Delta\mathcal{A}_1^e$ (%)	–0.02 2.08	0.04 2.37	–0.74 10.53
268.2	269.1	30	91	1.095 0.045	13.555 0.760	9.695 2.979
Pedersen				1.095 0.046	13.556 0.762	9.696 2.979
$\overline{\sigma} = 2.8862\,\mathrm{S/m}$			$\Delta\mathcal{A}_1^e$ (%)	0.18 –1.89	0.22 –0.95	0.28 0.03
$\sigma_{\mathrm{top}} = 2.6476\,\mathrm{S/m}$			$\Delta\mathcal{A}_1^e$ (%)	0.01 1.46	0.10 3.88	–1.26 7.23

Table 3.9: Europa: magnetic induction field strengths for B_z, under the same assumptions as described for B_y in main text Table 3.2. The corresponding values for the main models are shown in Figure 3.15.

Ganymede ($\hat{z}$)			Period (hr):	**5.27**	**10.53**	**171.57**
			B_z (nT):	**1.78**	**2.42**	**0.38**
T_b (K)	$\overline{T}$ (K)	D_{I} (km)	D_{ocean} (km)		$B_z\mathcal{A}_1^e$ (nT)	
Ionosphere Only				**Re Im**	**Re Im**	**Re Im**
Pedersen				0.000 0.001	0.000 0.001	0.000 0.000
$MgSO_4$ 1 wt%				**Re Im**	**Re Im**	**Re Im**
270.7	279.0	25	442	1.618 0.101	2.137 0.188	0.248 0.122
Pedersen				1.618 0.101	2.137 0.188	0.248 0.122
$\overline{\sigma} = 0.5166\,\mathrm{S/m}$			$\Delta\mathcal{A}_1^e$ (%)	0.87 –8.82	1.23 –7.04	2.61 1.01
$\sigma_{\mathrm{top}} = 0.3890\,\mathrm{S/m}$			$\Delta\mathcal{A}_1^e$ (%)	–0.03 4.54	–0.14 5.86	–9.33 17.09
261.6	266.2	92	276	1.466 0.112	1.941 0.197	0.131 0.149
Pedersen				1.466 0.112	1.941 0.197	0.131 0.149
$\overline{\sigma} = 0.3322\,\mathrm{S/m}$			$\Delta\mathcal{A}_1^e$ (%)	0.95 –5.29	1.18 –2.65	2.44 1.41
$\sigma_{\mathrm{top}} = 0.2623\,\mathrm{S/m}$			$\Delta\mathcal{A}_1^e$ (%)	0.08 3.83	0.45 10.74	–22.82 –3.32

Ganymede ($\hat{z}$)			Period (hr):	**5.27**	**10.53**	**171.57**
			B_z (nT):	**1.78**	**2.42**	**0.38**
T_b	$\overline{T}$	D_{I}	D_{ocean}		$B_z \mathcal{A}_1^e$	
(K)	(K)	(km)	(km)		(nT)	
$MgSO_4$ 10 wt%				**Re Im**	**Re Im**	**Re Im**
270.2	278.3	25	458	1.690 0.038	2.274 0.071	0.320 0.039
Pedersen				1.690 0.038	2.274 0.071	0.320 0.039
$\overline{\sigma} = 4.0699\,\mathrm{S/m}$			$\Delta\mathcal{A}_1^e$ (%)	0.29 –10.57	0.41 –9.78	1.48 –3.07
$\sigma_{\mathrm{top}} = 3.1150\,\mathrm{S/m}$			$\Delta\mathcal{A}_1^e$ (%)	–0.00 2.03	–0.01 2.84	–0.18 7.55
260.0	263.5	93	282	1.548 0.045	2.077 0.085	0.294 0.051
Pedersen				1.548 0.045	2.077 0.085	0.294 0.051
$\overline{\sigma} = 2.3476\,\mathrm{S/m}$			$\Delta\mathcal{A}_1^e$ (%)	0.27 –7.17	0.38 –6.43	1.01 –0.28
$\sigma_{\mathrm{top}} = 1.9483\,\mathrm{S/m}$			$\Delta\mathcal{A}_1^e$ (%)	0.00 1.71	–0.00 2.51	–0.11 15.65
brine layer: 30 km, 20 S/m			$\Delta\mathcal{A}_1^e$ (%)	0.00 –0.00	0.00 –0.00	–1.20 0.20
Pedersen			$\Delta\mathcal{A}_1^e$ (%)	0.00 0.10	0.00 0.04	–1.20 0.20

Table 3.10: Ganymede: magnetic induction field strengths for B_z, under the same assumptions as described for B_y in main text Table 3.3. The corresponding values for the main models are shown in Figure 3.15.

Callisto ($\hat{z}$)			Period (hr):	**5.09**	**10.18**	**400.33**
			B_z (nT):	**1.82**	**0.20**	**0.14**
T_b	$\overline{T}$	D_{I}	D_{ocean}		$B_z\mathcal{A}_1^e$	
(K)	(K)	(km)	(km)		(nT)	
Ionosphere Only				**Re Im**	**Re Im**	**Re Im**
Pedersen				0.141 0.508	0.004 0.030	0.000 0.001
Cowling				1.677 0.708	0.130 0.110	0.000 0.005
$MgSO_4$ 1 wt%				**Re Im**	**Re Im**	**Re Im**
257.4	259.6	99	132	1.489 0.166	0.162 0.034	0.002 0.014
Pedersen				1.511 0.190	0.165 0.036	0.002 0.015
Cowling				1.683 0.265	0.181 0.039	0.003 0.019
$\overline{\sigma} = 0.2307$ S/m			$\Delta\mathcal{A}_1^e$ (%)	0.49 –0.44	0.53 –0.08	1.45 0.96
$\sigma_{\mathrm{top}} = 0.1965$ S/m			$\Delta\mathcal{A}_1^e$ (%)	0.06 14.62	–1.03 15.03	–26.08 –13.62
250.8	250.9	128	21	0.438 0.690	0.016 0.049	0.000 0.001
Pedersen				0.746 0.865	0.031 0.072	0.000 0.002
Cowling				1.738 0.603	0.148 0.102	0.000 0.006
$\overline{\sigma} = 0.0895$ S/m			$\Delta\mathcal{A}_1^e$ (%)	0.04 0.02	0.04 0.03	0.05 0.03
$\sigma_{\mathrm{top}} = 0.0874$ S/m			$\Delta\mathcal{A}_1^e$ (%)	–3.26 –0.99	–4.12 –1.87	–4.52 –2.28

Callisto ($\hat{z}$)			Period (hr):	**5.09**	**10.18**	**400.33**
			B_z (nT):	**1.82**	**0.20**	**0.14**
T_b	$\overline{T}$	D_{I}	D_{ocean}		$B_z\mathcal{A}_1^e$	
(K)	(K)	(km)	(km)		(nT)	
$MgSO_4$ 10 wt%				**Re Im**	**Re Im**	**Re Im**
255.7	256.9	99	130	1.539 0.057	0.171 0.008	0.046 0.059
Pedersen				1.546 0.079	0.171 0.010	0.047 0.059
Cowling				1.648 0.195	0.177 0.018	0.049 0.060
$\overline{\sigma} = 1.5256$ S/m			$\Delta\mathcal{A}_1^e$ (%)	0.20 –2.91	0.26 –1.74	0.69 0.39
$\sigma_{\mathrm{top}} = 1.3789$ S/m			$\Delta\mathcal{A}_1^e$ (%)	0.01 1.12	0.12 3.18	–10.78 –1.59
250.8	250.9	128	21	1.420 0.386	0.132 0.072	0.000 0.006
Pedersen				1.476 0.399	0.140 0.073	0.000 0.006
Cowling				1.743 0.358	0.179 0.065	0.001 0.010
$\overline{\sigma} = 0.6025$ S/m			$\Delta\mathcal{A}_1^e$ (%)	–0.00 –0.00	–0.00 –0.00	–0.00 –0.00
$\sigma_{\mathrm{top}} = 0.6062$ S/m			$\Delta\mathcal{A}_1^e$ (%)	0.08 –0.53	0.28 –0.34	1.23 0.61

Table 3.11: Callisto: magnetic induction field strengths for B_z, under the same assumptions as described for B_y in main text Table 3.4. The corresponding values for the main models are shown in Figure 3.15.

Chapter 4

AN ANALYTIC SOLUTION FOR EVALUATING THE MAGNETIC FIELD INDUCED FROM AN ARBITRARY, ASYMMETRIC OCEAN WORLD

This chapter consists of a manuscript that has been submitted for peer review to the planetary science journal *Icarus*. An arXiv preprint is available at https://arxiv.org/abs/2106.10878. The main text and figures are reproduced here in their entirety with changes only to the formatting; cited references appear in the Bibliography at the end of this dissertation. The Supplemental Material described in the text is available as two Zenodo archives: https://zenodo.org/record/5002956 (computer programs) and https://zenodo.org/record/5004369 (animations). The Supplemental Text follows the main text within this chapter.

An analytic solution for evaluating the magnetic field induced from an arbitrary, asymmetric ocean world

Part 1: Main text

M. J. Styczinski[1,2], S. D. Vance[3], E. M. Harnett[2,4], and C. J. Cochrane[3]

[1] Department of Physics, University of Washington

[2] UW Astrobiology Program, University of Washington

[3] Jet Propulsion Laboratory, California Institute of Technology

[4] Department of Earth and Space Sciences, University of Washington

Abstract

Magnetic investigations of icy moons have provided some of the most compelling evidence available that confirms the presence of subsurface, liquid water oceans. In the exploration of ocean moons, especially Europa, there is a need for mathematical models capable of predicting the magnetic fields induced under a variety of conditions, including in the case of asymmetric oceans. Existing models are limited to either spherical symmetry or assume an ocean with infinite conductivity. In this work, we derive an analytic result capable of determining the induced magnetic moments for an arbitrary, layered body. Crucially, we find that degree-2 tidal deformation results in changes to the induced dipole moments. We demonstrate application of our results to models of plausible asymmetry from the literature within the oceans of Europa and Miranda and the ionospheres of Callisto and Triton. For the models we consider, we find that in the asymmetric case, the induced magnetic field differs by more than 2 nT near the surface of Europa, 0.25–0.5 nT at 1 R above Miranda and Triton, and is essentially unchanged for Callisto. For Miranda and Triton, this difference is as much as 20–30% of the induced field magnitude. If measurements near the moons can be made precisely to better than a few tenths of a nT, these values may be used by future spacecraft investigations to characterize asymmetry within the interior of icy moons.

4.1 Introduction

Any moon subjected to an oscillating magnetic field is a candidate for magnetic sounding—the determination of subsurface properties from magnetic measurements. Liquid water oceans containing dissolved salts conduct electricity, causing them to respond to oscillating fields that may be applied by their parent planet. This concept has proven especially useful in the study of icy moons in the outer solar system, as the induced magnetic fields that result from this interaction have been measured by orbiting spacecraft.

Induced magnetic fields observed by analysis of *Galileo* magnetometer data have provided the most compelling direct detection of oceans within Jupiter's moons Europa, Ganymede, and Callisto (Kivelson et al., 2000; Zimmer et al., 2000; Kivelson et al., 2002). This demonstrated methodology will be deployed by the planned *Europa Clipper* and *JUICE* missions to characterize the oceans of these bodies. The same technique also shows promise for the investigation of the large moons of Uranus and Neptune (Khurana and the *Trident* Team, 2019; Weiss et al., 2020; Arridge and Eggington, 2021; Cochrane et al., 2021); magnetometer investigations are likely to play a central role in future missions to these moons, too.

Magnetic sounding of moons requires a method for calculating the *expected* induced field that would result from a particular model of the interior conductivity structure, based on the measured oscillations of the parent planet's magnetosphere far from the moon. Forward models of planetary magnetic induction typically assume a spherically symmetric body for simplicity, as in the oft-cited Parkinson (1983, Ch. 5). Various interior models can then be supposed, the results calculated, and induced fields compared against spacecraft measurements near the moon to determine which model best fits the measurements. However, to date there has been no solution that analytically determines the induced magnetic field resulting from excitation of a planetary ocean that is not spherically symmetric.

The ability to suppose an asymmetric model for the conductivity structure of a moon is critical to an interpretation of measurements from upcoming missions, especially *Europa Clipper,* which plans flybys of Europa just 25 km above the surface—$0.02\,R_E$ in altitude (Campagnola et al., 2019).

Close to the moon, induced magnetic moments of quadrupole and higher order will have their largest effect relative to the dominant dipole moments. However, a spherically symmetric solution would predict only dipole moments are induced.

Further, asymmetries in the shape of subsurface oceans are fully expected, especially in the degree-2 shapes (*e.g.* the J_2 and C_{22} gravitational moments). The moons are expected to be oblate spheroids because they spin as they orbit, and the asymmetric gravity field applied by their parent planet will introduce an elongated, bulging pattern. These shapes can even impact the induced dipole moments, by affecting where electric currents can flow within the body. Interpretation of magnetic measurements near icy moons will require an understanding of the effects asymmetry may have on the induced field. Sufficient measurements may even permit a detailed characterization of the asymmetric interior shape.

In this work, we refine our previously derived solution for highly conducting oceans (Styczinski and Harnett, 2021). Here, we generalize the approach to apply to cases of arbitrary conductivity, described by uniformly conducting layers with boundaries of arbitrary, but near-spherical shape[1]. Then, we apply our mathematical result to plausible models of asymmetry within the conductivity structure of the moons Europa, Miranda, Callisto, and Triton, informed by the literature and calculated using the geophysical modeling framework *PlanetProfile* (Vance et al., 2018, 2021). A summary of the results from the example cases studied is in Section 4.3.2; a full collection of the model results is contained in the Supplemental Text, Section 4.9.

The excitation field applied by the parent planet typically has complicated interactions with the asymmetric boundary shape, resulting in changes to the magnetic field that vary with latitude, longitude, and time. To simplify the analysis of the examples we study, we choose to evaluate the magnetic fields at the J2000 reference epoch, approximately noon UTC on January 1, 2000. Plots showing the differences in all vector components of the induced field are included in the Supplemental Text (Figures 4.10–4.15). We include animations of the differences in induced magnetic

[1]The meaning of "near-spherical" is clarified in Section 4.2.4—in short, this assumption should hold well in considering asymmetric oceans for most solar system moons. The consequences of our assumptions are elaborated in Section 4.4.1.

field throughout the synodic period for some components as Supplemental Material[2]. The Supplemental Material also contains Python code[3] for evaluating our model, including creation of all plots in this manuscript.

4.2 Methods

At core, we apply Maxwell's laws at boundaries between regions and find the induced magnetic moments that satisfy the resulting equations. The same is true of the spherically symmetric, recursive solution developed by Srivastava (1966) and prominently applied by Zimmer et al. (2000), Seufert et al. (2011), and others. However, in our application, we describe the boundaries between regions of varying electrical conductivity by an arbitrary shape, rather than by a constant radius. The shape of the boundary has important consequences, and determines which magnetic moments are induced by a given excitation field applied by the parent planet. Here, we summarize the key points in our derivation and the final result for determining the induced magnetic field for an asymmetric conducting ocean.

A derivation of the Srivastava recursive method is recounted in more modern notation by the oft-cited Parkinson (1983). The Parkinson derivation has formed the basis for several influential studies of magnetic sounding of Europa, notably Zimmer et al. (2000), Khurana et al. (2002), and Hand and Chyba (2007). The Parkinson derivation contains several errors and inconsistencies that were repeated by the aforementioned studies, so we cover each step in our derivation from first principles and in fine detail in the Supplemental Text (Section 4.6). Despite the errors, the Parkinson derivation still gives the physically correct result for a spherically symmetric conductor. The consequences on the comparison to prior work that result from these errors are described in Section 4.2.1.

The key steps in our approach are:

1. Define a radial electrical conductivity structure within the body.

[2]Animations are available as a Zenodo archive at https://zenodo.org/record/5004369.

[3]Computer programs also available as a Zenodo archive: https://zenodo.org/record/5002956.

2. Apply Maxwell's laws at the boundaries between uniformly conducting regions.

3. Expand the boundary radii in a first-order Taylor expansion in terms of spherical harmonics.

4. Solve the resulting linear system of equations for the induced magnetic moments.

Two main approximations are required for this approach to adequately describe a physical system.

First, we must assume that the electrical conductivity is uniform within each layer within the planetary body. This assumption holds approximately for any planetary body with layers that are global in extent, although geophysical conditions changing with depth require a greater number of radial layers in order to be adequately represented (Vance et al., 2021). The consequence of this assumption is that our model is not expected to be capable of predicting the induced field of a body containing localized melt lenses (Schmidt et al., 2011), sills (Michaut and Manga, 2014), *etc.* within an ice shell. However, it may still be possible to do so using extensive spherical harmonic representations of the boundaries between layers.

Second, we assume that the boundaries are *near-spherical,* in that we may retain only the first term in a Taylor expansion about the boundary radius. This approximation is valid if the differences expected from the second-order terms are negligible, *i.e.* smaller than the expected measurement precision. Second-order terms are expected to be negligible for all icy moons in the solar system. The validity of this approximation is discussed further in Section 4.2.4.

4.2.1 Basic physics of magnetic induction

In the presence of an electrical conductor, an oscillating magnetic field will induce a secondary, induced magnetic field in accordance with Maxwell's laws. The strength of the induced field depends on the angular frequency ω of the oscillating applied field (called the *excitation* field) and the material properties everywhere within the conducting body: the electrical conductivity σ and the magnetic permittivity μ. It is customary to assume $\mu = \mu_o$, as this approximation holds very well on planetary scales (Saur et al., 2010). The faster the oscillation and the greater the electrical conductivity, the stronger the induced magnetic field, up to a maximum such that the radial component

of the excitation field is exactly cancelled at the outer boundary of a perfect conductor.

For simplicity in deriving our model, we neglect movement of conducting material within the body (as in the case of ocean currents), which can itself induce secondary fields (Saur et al., 2010; Vance et al., 2021). We also neglect electric currents outside the body. Although currents in the plasma environment around the body are not generally negligible, the principle of superposition permits us to consider each contribution to the net electromagnetic response independently—the net magnetic field is then the sum from each individual contribution. In this work, we consider only the induced magnetic moments generated by the interaction of the primary excitation field with the conducting body, as this is the dominant interaction that induces magnetic fields from within solar system moons.

Inside the conducting body, the net magnetic field $\mathbf{B}$ obeys a diffusion equation:

$$\nabla^2 \mathbf{B} = \mu\sigma \frac{\partial \mathbf{B}}{\partial t}, \tag{4.1}$$

where μ is magnetic permeability and σ is electrical conductivity, both functions of position. For a sinusoidal time dependence $e^{-i\omega t}$ with angular frequency ω,

$$\nabla^2 \mathbf{B} = -i\omega\mu\sigma \mathbf{B}, \tag{4.2}$$

or alternatively

$$\nabla^2 \mathbf{B} = -k^2 \mathbf{B}, \tag{4.3}$$

where k is known as the wavenumber. Eq. 4.3 is a vector Helmholtz equation, with

$$k = \sqrt{i\omega\mu\sigma}. \tag{4.4}$$

Outside the body, both the excitation field and the induced field, as well as their sum, obey the Laplace equation:

$$\nabla^2 \mathbf{B} = 0. \tag{4.5}$$

In this outer region, the magnetic field can be determined from (Jackson, 1999)

$$\mathbf{B}_{\text{net}} = -\nabla \left[\sum_{n,m} R \left(B^e_{nm} \left(\frac{r}{R} \right)^n + B^i_{nm} \left(\frac{R}{r} \right)^{n+1} \right) Y_{nm}(\theta, \phi) \right], \tag{4.6}$$

where the excitation moments B^e_{nm} are determined by measuring the oscillating field far from the body, B^i_{nm} are the induced magnetic moments, R is a unit of radial distance (typically the outer radius of the conducting body), and Y_{nm} are the spherical harmonics.

As the induced field can only be as strong as the excitation field, and that only happens in the limit of high conductivity, it is often convenient to consider the ratio of the induced and excitation moments, B^i_{nm}/B^e_{nm}, sometimes called the "Q-response." In the case of spherical symmetry and in the high-conductivity limit, this ratio approaches $n/(n+1)$. Because B^i_{nm}/B^e_{nm} can be complex, we define the complex amplitude $\mathcal{A}^e_n$ such that

$$B^i_{nm} = \frac{n}{n+1}\mathcal{A}^e_n B^e_{nm}. \tag{4.7}$$

Comparison to derivations used in prior work

In the commonly studied case of a uniform excitation field, with $n = 1$, $\mathcal{A}^e_n$ may be expressed in terms of the real amplitude A and phase delay ϕ (*e.g.* as defined by Zimmer et al., 2000):

$$\mathcal{A}^e_1 = Ae^{-i\phi}, \tag{4.8}$$

allowing for ready comparison with prior work.

Note that the negative exponent in Eq. 4.8 results from our definition of k in Eq. 4.4, with $+i$ under the square root, and the contrasting choice of Parkinson (1983)—and several authors of prior work who have relied on the Parkinson derivation, notably Zimmer et al. (2000), Khurana et al. (2002), Hand and Chyba (2007), and Arridge and Eggington (2021). The Parkinson derivation contains an error, in that choosing $-i$ in the definition of k results in the *modified* spherical Bessel equation, with the *modified* spherical Bessel functions $i_n(kr)$ and $k_n(kr)$ as solutions, as detailed in Schilling et al. (2007) and Seufert et al. (2011). Parkinson (1983) incorrectly arrives at the standard spherical Bessel equation (Eq. 4.37). In effect, both our input wavenumber k and our result for the complex response amplitude $\mathcal{A}$ are equal to the complex conjugate of the analogous quantities from prior work, hence the negative exponent in Eq. 4.8. See Section 4.6.1 for more information. We define the relationship between $\mathcal{A}^e_1$, A, and ϕ as in Eq. 4.8 to facilitate comparison with the rich set of prior work related to this topic.

4.2.2 *Radial conductivity structure*

Within the planetary body, we must suppose a radial conductivity structure $\sigma(r)$. Solution of the vector Helmholtz equation (Eq. 4.3) in spherical coordinates is made a tractable problem by our assumption that each layer has uniform conductivity. In this work, we use the *PlanetProfile* framework (Vance et al., 2018, 2021) to model the electrical conductivity of ocean waters under geophysical conditions likely found within icy moons. The conductivity within ice and rock are typically small ($<10^{-2}$ S/m, Glover, 2015). The conductivity of an iron core may be much higher ($>10^{6}$ S/m, Khurana et al., 2002), but its contribution to the induction response is likely a few percent at most (Seufert et al., 2011) due to its smaller size and screening of the excitation field by the ocean. We neglect the conductivity of ice, rock, and a possible iron core, but these are easily inserted into our model.

We require a spherically symmetric conductivity model as a starting point for our derivation because we assume only the boundaries between the conducting regions are asymmetric. This is a requirement for an analytic solution of the boundary condition equations. Although the conductivity within each asymmetric layer is likely to differ with a change in depth, our near-spherical approximation ensures that this difference is small compared to the global effect of the asymmetric boundary. This approximation is most valid when there are sharp contrasts in conductivity between the layers, *e.g.* between the ocean and nonconducting ice shell, because the depth-dependence of the conductivity in the ocean has a much smaller effect on conductivity than the layer transition.

4.2.3 *Applying Maxwell's laws at the boundaries*

In spherical coordinates, the vector components of general solutions to Eqs. 4.1 and 4.5 are spherical harmonics and their θ derivatives, multiplied by either spherical Bessel functions and their r derivatives (inside) or a power series in r (outside) (Moffatt, 1978; Jackson, 1999). As we have assumed $\mu = \mu_o$ everywhere, and currents are not confined to the boundary surfaces, Maxwell's laws dictate that the vector components of $\mathbf{B}$ must be continuous at every boundary. This continuity gives us equalities that relate coefficients for the general solutions that describe each region, and

ultimately will yield a solvable set of linear equations.

In this work, we use the fully normalized, complex spherical harmonics:

$$Y_{nm} = \sqrt{\frac{2n+1}{4\pi}\frac{(n-m)!}{(n+m)!}}\, P_n^m(\cos\theta)\, e^{im\phi}, \tag{4.9}$$

$$Y_{n,-m} = (-1)^m Y_{nm}^* \tag{4.10}$$

for degree n and order m, where P_n^m are the associated Legendre functions with the Condon–Shortley phase (Condon and Shortley, 1951) and $*$ denotes a complex conjugate. In contrast, much of the geomagnetism and geodetics communities use real-valued spherical harmonics, in terms of $\sin\phi$ and $\cos\phi$, in the Schmidt normalization, and omit the Condon–Shortley phase. We choose our convention out of necessity to match that common in quantum physics, so that we may use results from historic works (Wigner, 1931; Brink and Satchler, 1968; Edmonds, 1996) involving the products of spherical harmonics. See Section 4.6 for more details.

For the spherical harmonics, we define

$$Y_{nm}^\star \equiv \frac{\partial Y_{nm}}{\partial\theta} = \frac{1}{\sin\theta}\left(-w_{nm}^- Y_{n-1,m} + w_{nm}^+ Y_{n+1,m}\right) \quad \text{for } m \geq 0, \tag{4.11}$$

$$w_{nm}^- = (n+1)\sqrt{\frac{n^2-m^2}{(2n-1)(2n+1)}}, \quad w_{nm}^+ = n\sqrt{\frac{(n+1)^2-m^2}{(2n+1)(2n+3)}}, \tag{4.12}$$

$$Y_{n,-m}^\star = (-1)^m Y_{nm}^{\star *}. \tag{4.13}$$

For spherical Bessel functions of the first and second kind $j_n(kr)$ and $y_n(kr)$, we define

$$j_n^\star \equiv \frac{d}{dr}(rj_n) = (n+1)j_n - kr\, j_{n+1}, \quad y_n^\star \equiv \frac{d}{dr}(ry_n) = (n+1)y_n - kr\, y_{n+1}. \tag{4.14}$$

The starred functions appear in the tangential boundary condition equations and the overall solutions.

4.2.4 Near-spherical boundary shapes

We must define surfaces $r_l(\theta,\phi)$ for arbitrary boundaries that we will insert into the internal and external boundary condition equations. We choose boundary surfaces of the form

$$r_l(\theta,\phi) = \bar{r}_l + \varepsilon_l \sum_{p,q} \chi_{pq}^l Y_{pq}(\theta,\phi) \tag{4.15}$$

because expanding in spherical harmonics will allow us to make use of well-known relations from the mathematics of quantum mechanics. Here, $\bar{r}_l$ is the mean radius of boundary l, ε_l is the amplitude of deviation from spherical symmetry, χ^l_{pq} is a dimensionless constant that indicates the relative amount of each harmonic represented in the boundary surface, and Y_{pq} are fully normalized spherical harmonics of degree p and order q. We use the index l to indicate that this surface describes the outer boundary of the lower region. Care must be taken to select values for χ that prevent boundary surfaces from overlapping, so as to describe physically possible interior structures. Contour maps plotting the difference between layers are instructive for this purpose, as in Figures 4.6 and 4.1, which were created with the analysis software in the Supplemental Material.

As we wish to describe physical surfaces, Eq. 4.15 must be real-valued. The spherical harmonics we use are complex in general; so too must χ^l_{pq} be. Topographical descriptions in the literature against which we wish to compare are often described in terms of coefficients for real-valued, Schmidt semi-normalized spherical harmonics. The provided software includes a tool for converting this format into the coefficients χ^l_{pq}, as we have used in our analysis. In Eq. 4.15, for $\bar{r}_l$ in meters, ε_l is also in meters. For a perturbation represented by a pure harmonic of degree p and order q, ε_l is the maximum radial displacement from a perfect sphere, and χ^l_{pq} is $1/\max(Y_{pq})$.

Surfaces described by Eq. 4.15 are near-spherical in that we make the approximation $\varepsilon_l \ll \bar{r}_l$ for all l. Equivalently, $\varepsilon_l/\bar{r}_l \ll 1$, and we retain terms up to first order in $\varepsilon_l/\bar{r}_l$ only. This enables us to use a Taylor expansion in the boundary conditions that truncates quickly, adding only one term containing a product of two spherical harmonics. Products of spherical harmonics may be expressed as a linear combination of different harmonics (Wigner, 1931; Condon and Shortley, 1951). This results in "mixing" of harmonics in the excitation field from $n = 1$ into other n, so a uniform excitation field induces magnetic moments of quadrupole order or higher for this shape, in addition to altering the original dipole moments.

Taylor expansion of boundary shapes

We account for asymmetry in the conductivity structure of the body by expanding the boundary surfaces about their average radii. To first order, a Taylor expansion of a function $f(r)$ about r_l has

terms

$$f(r_l) \approx f(\bar{r}_l) + (r_l - \bar{r}_l)\frac{\partial f(r)}{\partial r}\Big|_{r=\bar{r}_l} = f(\bar{r}_l) + \varepsilon_l\Big[\sum_{p,q} \chi^l_{pq} Y_{pq}(\theta,\phi)\Big]\frac{\partial f(r)}{\partial r}\Big|_{r=\bar{r}_l}. \tag{4.16}$$

We evaluate these terms, then insert the result in place of the boundary radius in the general expressions for the field within each region (Eqs. 4.47–4.52) in order to match the components of the field at the boundaries.

The next term in the expansion (the second-order term) will be proportional to ε_l^2 and the second derivative of $f(r)$. Each derivative will contribute a division by r (from the Bessel functions, Marion and Heald, 1980), so each successive term gains another power of $\varepsilon_l/\bar{r}_l$, the ratio of the maximum deviation from spherical symmetry to the average radius of the boundary surface. We assume the boundaries are near-spherical, as $\varepsilon_l/\bar{r}_l$ is small—for Enceladus, for example, the maximum possible value is about $21\,\mathrm{km}/231\,\mathrm{km} \approx 0.09$ (Hemingway and Mittal, 2019). For Europa, the maximum ratio is even smaller, at about $30\,\mathrm{km}/1530\,\mathrm{km} \approx 0.02$ (Billings and Kattenhorn, 2005). The excitation moments experienced by icy moons in the solar system range from 7 nT for Triton up to about 300 nT for Miranda (Cochrane et al., 2021). The largest differences in magnetic field at the surface of these bodies from the first-order term can be about 10% for highly conducting, maximally asymmetric oceans. The second-order term can then only be about 1% of the maximum, up to a few nT on the surface. A lander on a highly asymmetric moon may need to account for second-order effects. However, at orbital/flyby altitudes and with realistic ocean shapes and conditions, we find that second-order effects are likely to be under 1 nT, and thus insignificant in a dynamic space environment.

4.3 Results

4.3.1 Analytic solution for the induced magnetic moments

Through application of the methods described above, for B^i_{nm} of a body containing N conducting layers and an average outer radius R, we obtain a solution

$$B^i_{nm} = \frac{n}{n+1}\mathcal{A}^e_n B^e_{nm} + n\sum_{\mathrm{i}=1}^{N} \mathcal{A}^{t,\mathrm{i}}_n K^{\mathrm{i}}_n \Delta^{\mathrm{i}}_{nm}, \tag{4.17}$$

with

$$\Delta^{\mathrm{i}}_{nm} \equiv \begin{cases} \displaystyle\sum_{n',m',p,q} \frac{\varepsilon_{\mathrm{i}} \chi^{\mathrm{i}}_{pq}}{\bar{r}_{\mathrm{i}}} \Xi^{\star\, nm}_{n'm'pq} \frac{\bar{a}^{\mathrm{i}}_{nm}}{R} \left(j^{\mathrm{i,i}}_{n'} + \Lambda^{\mathrm{i}}_{n'} y^{\mathrm{i,i}}_{n'} \right) \left(k^2_{\mathrm{i}} \bar{r}^{-2}_{\mathrm{i}} - k^2_{\mathrm{i}+1} \bar{r}^{-2}_{\mathrm{i}} \right) & \text{for i} < N, \\ \displaystyle\sum_{n',m',p,q} \frac{\varepsilon_N \chi^N_{pq}}{R} \Xi^{\star\, nm}_{n'm'pq} \frac{2n'+1}{n'+1} \mathcal{A}^{\star}_{n'} B^{e}_{n'm'} & \text{for i} = N. \end{cases} \tag{4.18}$$

Each quantity is fully determined by the interior structure model and the excitation moments, so the induced magnetic field can be directly calculated. $\mathcal{A}^e_n$ is the complex amplitude for the zeroth-order (spherically symmetric) excitation, $\mathcal{A}^{t,\mathrm{i}}_n$ is the complex amplitude from the "output" harmonic n, m for the tangential component from the i$^{\text{th}}$ layer, and $\mathcal{A}^{\star}_{n'}$ is the complex amplitude from the "input" harmonic that mixes into the output harmonic. As with $\mathcal{A}^e_n$, the product $\mathcal{A}^{t,N}_n \mathcal{A}^{\star}_{n'}$ is asymptotic to $(1 + 0i)$ in the limit $|k_N R| \to \infty$. The radial first-order term that would multiply a quantity $\mathcal{A}^r$ analogous to $\mathcal{A}^t$ is identically zero, so it does not appear. Δ^{i}_{nm} represents the strength of the induced magnetic field from each asymmetric boundary that "mixes" into the output harmonic n, m from the known excitation field. K^{i}_n is a propagation factor that determines how the induced magnetic field resulting from a buried asymmetric boundary gets attenuated by the conducting layers above it. $\Xi^{\star\, nm}_{n'm'pq}$ is a complicated function of Clebsch–Gordan coefficients that determines the strength of coupling between the given excitation moment n', m', a given boundary shape harmonic p, q, and the induced moment n, m. Please refer to the full derivation in Section 4.6 for more details, including definitions of every quantity.

Eq. 4.17 is our final result. Along with a suitable conductivity model and excitation moments from a magnetospheric model of the parent planet, this result may be applied to determine the induced magnetic field for a non-spherical ocean or ionosphere or both.

4.3.2 Application to ocean worlds in our solar system

We now apply our model to several examples of icy moons in our solar system that are expected to contain asymmetry in their conductivity structure. We provide computer programs written in Python for evaluating our model as Supplemental Material, including the code for generating the plots in this Section. A full detailing of the results for each example, including contour maps of

the asymmetry model and differences in the induced magnetic field arising from asymmetry, are contained in the Supplemental Text (Section 4.9). Here, we focus on the reasoning for the modeled asymmetry and the key findings from each application.

Conductivities within the ocean layers are determined using the *PlanetProfile* geophysical modeling framework (Vance et al., 2018, 2021). Several bulk parameters are used as inputs, such as surface temperature and moment of inertia, which are typically determined from spacecraft measurements; Table 4.1 lists each of the parameters we used. Ice shell thicknesses are assumed for each body. The interior structure is then determined self-consistently, accounting for solid-state convection in ice and adiabatic convection in the ocean, and using recently developed Gibbs-energy-based thermodynamics of solids and liquids. The ocean is assumed to be well-mixed, with a specified salt composition and concentration that is constant throughout the ocean. Depth-dependent pressures and temperatures are then combined with the salinity to determine ocean conductivities using the Gibbs Seawater model (McDougall and Barker, 2011) for Seawater or extrapolation from the measurements of Larionov and Kryukov (1984) for $MgSO_4$ oceans (Vance et al., 2018). Oceans are then reduced to three radial conducting layers before inserting them into our model, to reduce computational load. A greater number of layers may impact detailed analyses of spacecraft data, but the impact is expected to be small compared to other effects if ocean composition is uniform with depth (Vance et al., 2021). Asymmetry is then applied by describing the boundaries between radial layers as in Eq. 4.15. Ocean layers in our examples are assumed to be concentric, in that they each have the same asymmetric shape but scaled proportionally to the radius of the boundary.

Contour maps for Europa and Miranda show the asymmetry we model in the outermost ocean boundary, the ice–ocean interface for these bodies. The interiors for Callisto and Triton are assumed spherically symmetric; asymmetry is applied to their ionospheres based on a day–night dichotomy in ionization rate. Interior contour maps may appear similar to those seen in the literature showing tidal flexure, but the similarity is only because they are each global maps portraying low-degree spherical harmonics. The difference from diurnal tides is relatively small (about 30 m for Europa, Moore and Schubert, 2000) so we assume static asymmetry in the layer boundaries. As the ionospheric asymmetry we assume for Callisto and Triton is due to day–night differences, the

asymmetric shapes for these bodies will oscillate throughout their orbital periods (all the moons we study rotate synchronously). However, the strongest excitations applied to Callisto and Triton occur at their synodic periods with the parent planet's rotation, 10–40 times more rapid than their orbital periods. For simplicity, we assume a fixed asymmetry in their ionospheres and consider our results an order-of-magnitude estimate for these bodies.

In all cases, the excitation moments applied to the moon are determined by taking a Fourier transform of the magnetic field at the position of the moon, evaluated over a 10-year time series. Body positions are determined using SPICE kernels available from NAIF[4,5]. The magnetic field of the parent planet is calculated using a magnetosphere model from the literature: JRM09 + the Connerney current sheet model for Jupiter (Connerney et al., 1981, 2018), AH_5 for Uranus (Herbert, 2009), and that of Connerney et al. (1991) for Neptune. Although we determine excitation moments for all significant periods, in this work we consider only the largest excitation, at the synodic period.

Europa

To model plausible asymmetry in the interior of Europa, we suppose a shape approximating the results of Tobie et al. (2003) for the ice shell thickness. In addition, we suppose a tidally deformed shape consistent with the static gravity coefficients J_2 and C_{22} inferred from radio Doppler shifts due to acceleration of the *Galileo* spacecraft (Anderson et al., 1998)—see Section 4.8 for more details. Tobie et al. (2003) studied the dynamics of tidal heating and convection in Europa's ice shell with numerical simulations, concluding that the shell is likely thickest at the sub- and anti-jovian points and thinnest at mid-latitudes on the leading and trailing hemispheres. Figure 4.1 shows the shape model we use to approximate this ice shell, which we have selected based on Figure 12a of Tobie et al. (2003). We model the ocean using 3 concentric layers with the same boundary shape between layers, scaled to the radius of each boundary. A Seawater ocean is assumed; interior structure, including electrical conductivity, is evaluated using *PlanetProfile* as described above (Section 4.3.2).

[4]Generic SPICE kernels are hosted by NAIF at `https://naif.jpl.nasa.gov/naif/data_generic.html`.

[5]The specific kernels we used are `pck00010.tpc` and `gm_de431.tpc` for planetary constants, `naif0012.tls` for leap seconds, and `jup310.bsp`, `ura111.bsp`, and `nep081.bsp` for ephemerides.

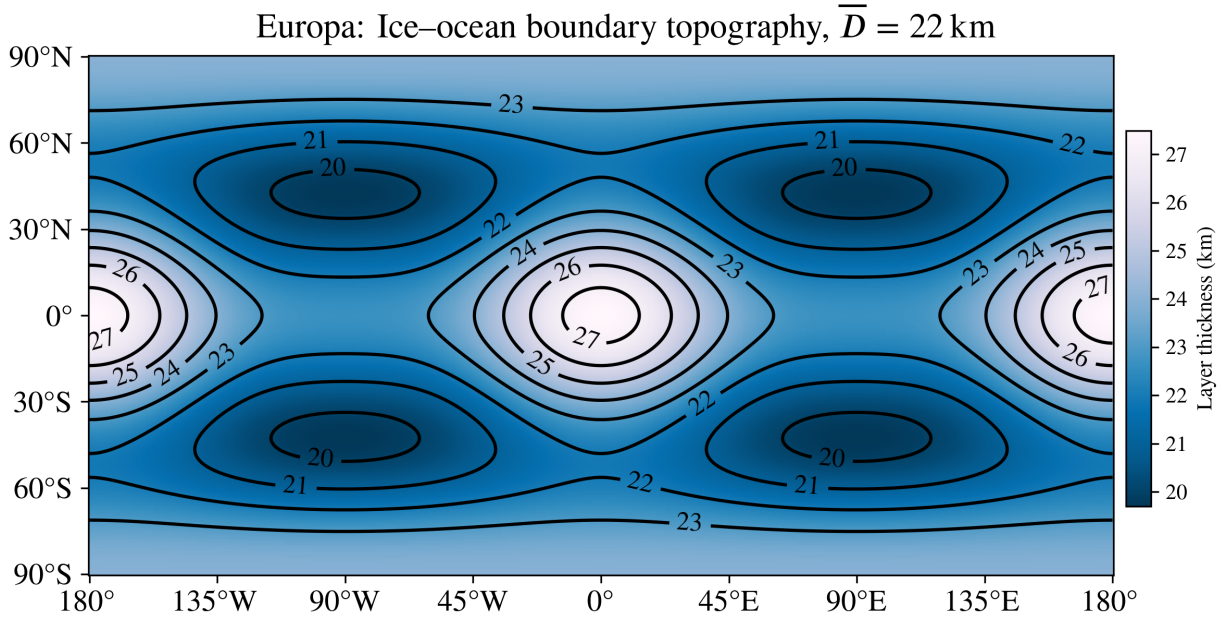

Figure 4.1: Asymmetry model for Europa, showing the thickness of the ice shell as a function of latitude and longitude in IAU coordinates, where $(0°, 0°)$ is the sub-jovian point. The outer surface of Europa is assumed to be a perfect sphere and the ice–ocean boundary is perturbed. Then, both surfaces have tidal deformation added in accordance with J_2 and C_{22} values reported by Anderson et al. (1998). We have supposed an ice shell asymmetry model approximating the results of Tobie et al. (2003); compare to Figure 12a of that work. Ice thickness is 22.5 km on average and ranges from 20–27 km.

Conduction in the core is ignored for simplicity.

Figure 4.2 shows the difference in the B_x component (in IAU coordinates) of the induced magnetic field that results from the asymmetric structure at an altitude of 25 km. This altitude is chosen to assess the possible impact of our results on the *Europa Clipper* mission, which plans several flybys with closest approaches at this altitude or less (Campagnola et al., 2019). The displayed vector component is aligned with the strongest excitation applied by Jupiter; analogous maps for all components are shown in the Supplemental Text (Figure 4.10). Differences of over 1.8 nT are observed in several locations at this time, the J2000 reference epoch. Tidal deformation is responsible for about 1/3 of the difference in the B_x component (Figure 4.2) and about half of the difference in the B_z component (Figure 4.10f), which can be as much as 2.4 nT. Although the background field of Jupiter is around 500 nT (Connerney et al., 2018), features of order 1 nT are routinely considered measurable in the analysis of spacecraft data (Horbury et al., 2020).

The J2000 epoch is at an arbitrary point in time during Europa's synodic period. At about 0.7 hr after J2000, the difference in B_x resulting from asymmetry is maximized. As seen in Figure 4.2, the difference is also maximized near 30°N, 0°E. To form an initial estimate of how this asymmetric ocean model will impact spacecraft measurements at a variety of altitudes, we evaluated the induced field in a straight line normal to the surface above this location. Figure 4.3 shows the difference resulting from asymmetry along this line. Near the surface, the difference is about 2.2 nT. The difference drops to 0.2 nT, likely small enough to ignore, only above an altitude of about 1500 km. Note also that the differences are sometimes small nearly everywhere—for example, the differences are below 0.6 nT at all points 25 km above the surface around $t = 3.4$ hr past J2000 (see Figure 4.17).

We also evaluated a near-copy of this model, only with a salinity 10% that of Seawater, to examine the influence of asymmetry at other concentrations considered in the literature (*e.g.* Vance et al., 2021). The difference in the B_x component of the induced magnetic field resulting from asymmetry for this lower-salinity model is shown in Figure 4.4. In this case, the differences are smaller by 10–40% and a slight phase shift is observed. However, compared to the spherically symmetric analog, the differences are still as much as 2 nT. Europa's relatively large size causes it to behave as a strong conductor and reject penetration by the time-varying excitation field with

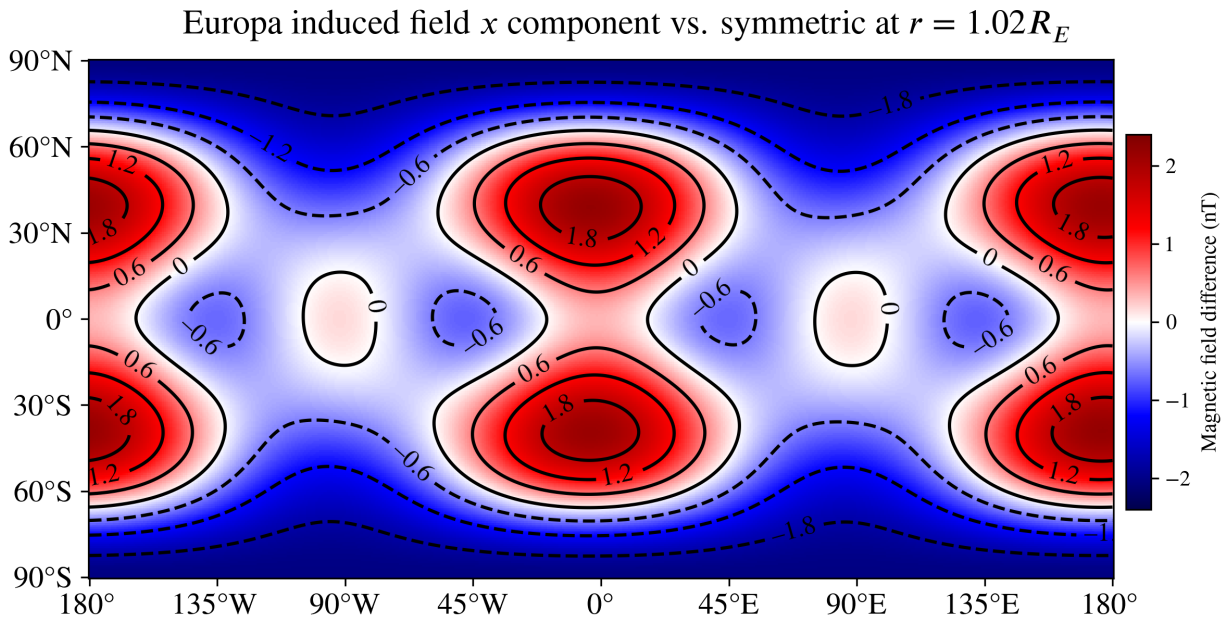

Figure 4.2: Difference in the B_x component (in IAU coordinates) of the induced magnetic field of Europa resulting from asymmetry in the ice–ocean boundary corresponding to the shape displayed in Figure 4.1 and static gravity inferred by Anderson et al. (1998). A Seawater ocean composition is assumed. The magnetic fields are evaluated at the J2000 reference epoch and at 25 km altitude, consistent with the closest approach of several flybys planned by the *Europa Clipper* mission. This component of the induced field is changed by more than 1 nT in many locations, demonstrating that expected asymmetry in Europa's ice shell is likely to have measurable effects in the nearest flybys by *Europa Clipper*. These closest flybys may help constrain the shape of Europa's ice shell from magnetic measurements if precision reaches a few tenths of a nT. Tidal deformation is responsible for about 1/3 of the difference in this component. This global map of differences resulting from asymmetry changes throughout the synodic period; an animation showing the same map as it varies during the 11.2-hour period is included in the Supplemental Material.

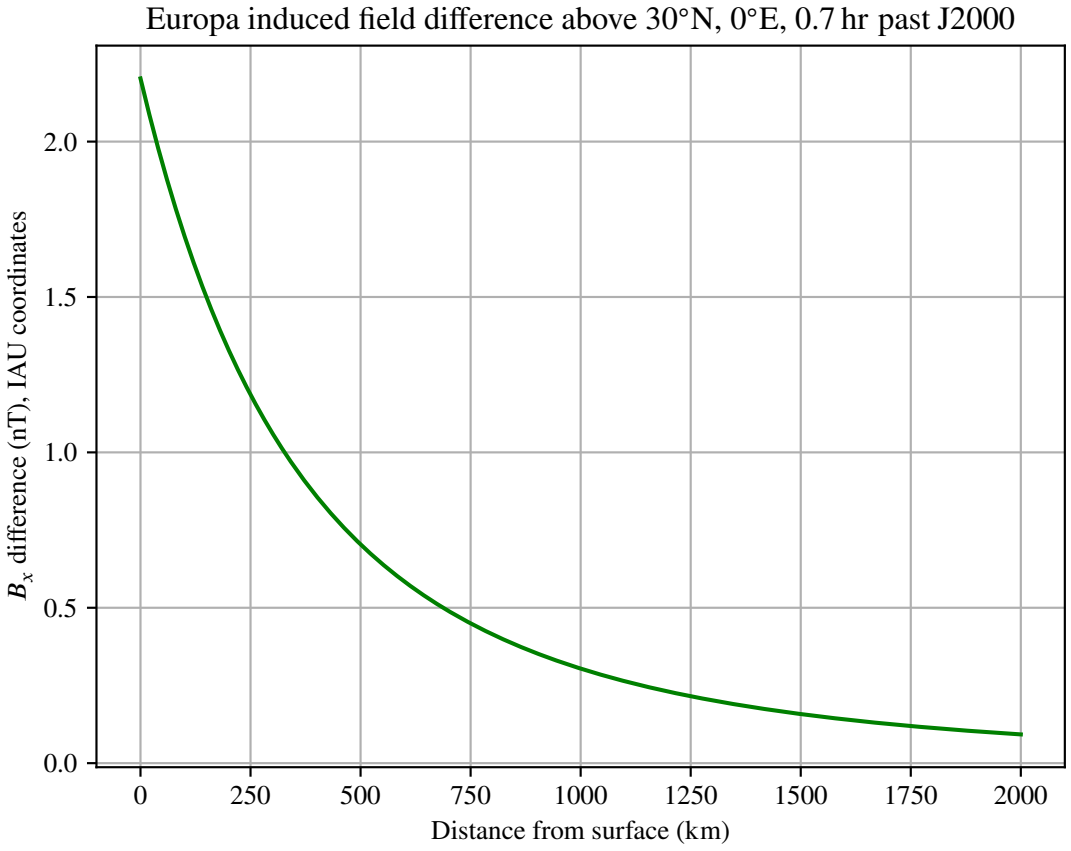

Figure 4.3: Difference in induced field B_x component for our Europa Seawater model as a function of altitude for a fixed point in time. The selected surface location (30°N, 0°E) and time (0.7 hr past J2000) maximize the observed difference relative to the spherically symmetric case for this interior model and component—see Figure 4.2. Beyond about 1500 km altitude, the difference is around 0.2 nT and likely negligible.

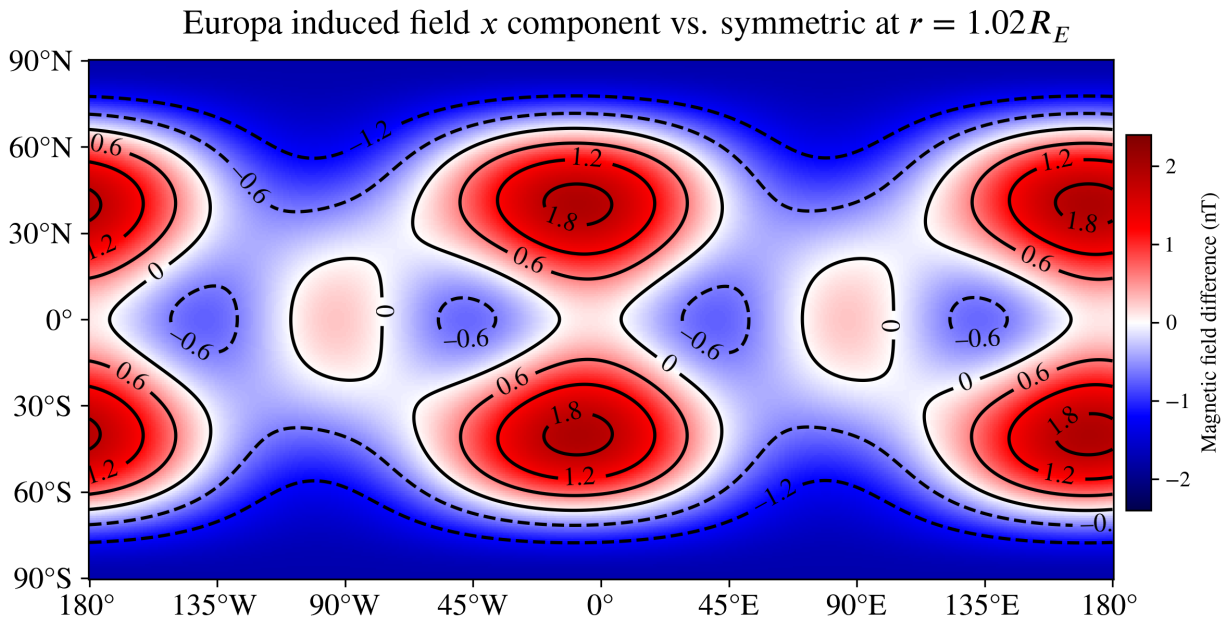

Figure 4.4: Difference in the B_x component of the induced magnetic field of Europa resulting from the asymmetry model shown in Figure 4.1, as in Figure 4.2, but with a salinity 10% that of Seawater. Comparison between the two cases shows these differences to be smaller for this component (60–90% as great), as well as having a slight phase shift relative to the Seawater ocean. The colormap and contours for this plot are fixed to match those of Figure 4.2.

a strong induced field; this effect has a much stronger dependence on size than on conductivity or oscillation frequency (through an exponential dependence on $(r\sqrt{i\omega\mu\sigma})$ in Bessel functions $j_n(kr)$; see Eq. 4.4).

Comparison with prior work

In prior work (Styczinski and Harnett, 2021), we derived an approximation for evaluating the effects of asymmetry on induced fields, but in the limit of high conductivity in the conducting region ($|kr| \to \infty$). In this approximation, only the shape of the outermost boundary matters, because the time-varying excitation field is rapidly attenuated within the conducting material by the induced currents that generate the induced field. For comparison with that work, we now consider the exact same boundary shape studied in that work for Europa, *i.e.* by setting

$$\varepsilon_l = 2.5\,\text{km}, \quad r_l = 1537.5\,\text{km}, \quad \chi^l_{2,-2} = \chi^l_{2,2} = \frac{1}{2}\cdot 4\sqrt{\frac{2\pi}{15}} \tag{4.19}$$

in Eq. 4.15 (note the difference in normalization of χ^l_{pq} in the earlier work, see Appendix 2.A). Figure 4.5 shows the vertical component of the net magnetic field a lander at the sub-jovian point would measure throughout a synodic period, considering only that excitation period, analogous to Figure 2 of Styczinski and Harnett (2021) (Figure 2.2 in this dissertation). In that work, the greatest difference was near the same points in time, though only about 0.5 nT.

Armed now with a rigorously derived, explicit formula for evaluating the mixing coefficients $\Xi^{\star\,nm}_{n'm'pq}$ (Section 4.10), we find that the reason for the greater effect size compared to our previous work is that we had underestimated these coefficients. Our previous method for determining the values of $\Xi^{\star\,nm}_{n'm'pq}$ did not account for non-orthogonality of the $Y^\star_{nm}$ (see Section 4.6.5), and so scaled incorrectly when multiple excitation harmonics or multiple shape harmonics are represented. We now estimate a maximum difference of about 2.5 nT for this extreme limiting case, absent tidal deformation.

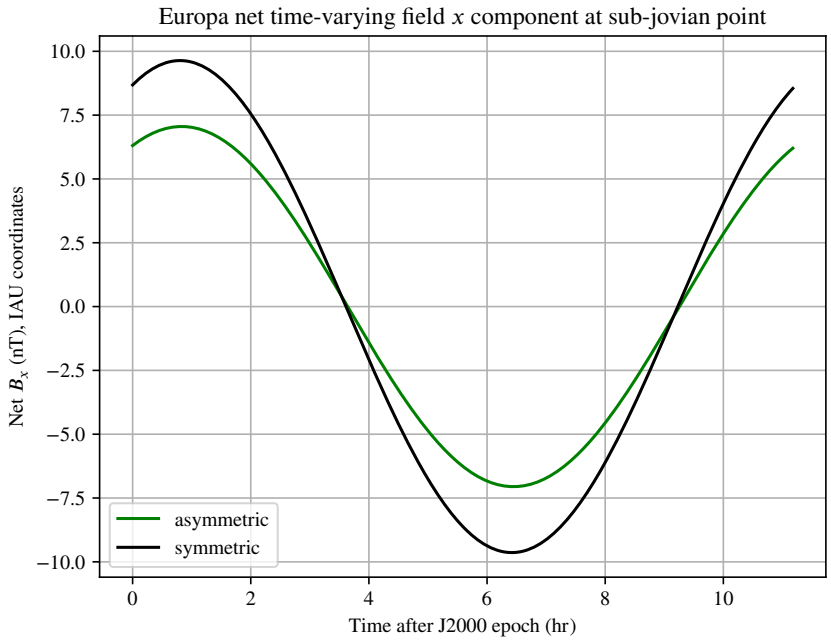

Figure 4.5: Vertical component of the net magnetic field a lander located at the sub-jovian point would measure on Europa for the asymmetric ice–ocean boundary studied in our previous work (Styczinski and Harnett, 2021), along with that of an analogous, spherically symmetric model. The ocean is treated as having effectively infinite conductivity, as in prior work. The effects of an ionosphere are neglected. The difference between the asymmetric and symmetric cases predicted by our complete model in this work is several times larger than the estimate from our previous work, about 2.5 nT at most. This model does not include tidal deformation, for a consistent comparison with prior work (Figure 2.2).

Miranda

Miranda is the innermost large moon of Uranus. The orbital configuration of the large uranian moons implies past orbital resonances that likely caused tidal heating (Ćuk et al., 2020), and Miranda's surface shows possible signs of past geologic activity (Beddingfield and Cartwright, 2020) that might have been provoked by this heating. The presence of ammonia-bearing compounds on the surface of nearby Ariel (Cartwright et al., 2020) implies lowered melting temperatures for the oceans on these moons (Croft et al., 1988), so liquid oceans may persist to the present even in this far-out system. With a radius of 235.8 km, Miranda is also comparable in size to Enceladus (radius 252.1 km). Enceladus has been found to have a marked asymmetry in its ice shell, with a notably thinner portion around the south pole (where plume activity is concentrated, Iess et al., 2014; Hemingway and Mittal, 2019). Together, these factors encourage a comparison between Miranda and Enceladus.

To model possible Enceladus-like asymmetry in the interior of Miranda, we scale the asymmetric topography of the ice–ocean boundary for Enceladus favored by Hemingway and Mittal (2019) based on isostatic compensation combined with gravity measurements and models of tidal heating in the ice shell. To account for the colder surface temperature of Miranda, which receives about 10% the insolation as Enceladus, we assume a 50 km thick ice shell, and scale the asymmetry model of Hemingway and Mittal (2019) from a 20 km average thickness to match. We consider this an upper estimate of asymmetry that may be possible within Miranda's interior, as viscous relaxation is likely to smooth out the exaggerated features somewhat. The shape of the ice–ocean boundary model we have supposed for Miranda is shown in Figure 4.6—compare to Figure 11d of Hemingway and Mittal (2019). We assume an ocean composition of Seawater with 10% the salinity of Earth's oceans, approximating the salinity of Enceladus inferred from *Cassini* Dust Analyzer sampling of the plumes (Postberg et al., 2009).

Miranda's small size and proximity to Uranus prevent it from retaining a significant ionosphere. Comparison of the plasma environment (Mauk et al., 1987) to that near Callisto has led us to suppose a simple, uniformly conducting ionosphere that extends from the surface to 100 km altitude and has

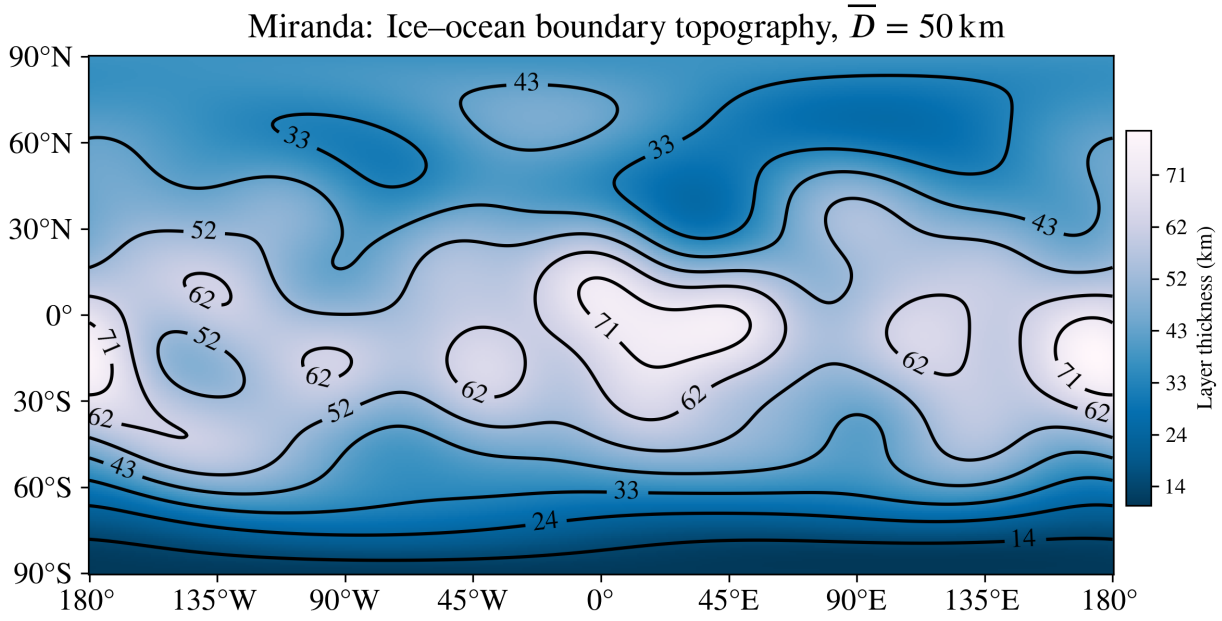

Figure 4.6: Possible "Enceladus-like" asymmetry in the ice shell of Miranda used in this study. The topography of the ice–ocean boundary for this body is scaled up from a model for Enceladus by Hemingway and Mittal (2019) inferred from isostatic compensation and spacecraft measurements. Compare to Figure 11d from that work.

a total height-integrated conductivity of 800 S (Hartkorn et al., 2017) to serve as an upper limit. We assume a spherically symmetric ionosphere for Miranda; conduction in the ionosphere will serve only to attenuate the differences resulting from asymmetry as measured outside the body.

Figure 4.7 shows the difference in the magnitude of the induced magnetic field resulting from the asymmetry model we have applied. The magnetic fields are again evaluated at the J2000 reference epoch, but this time at a distance $r = 2R_M$, a plausible range around closest approach for flybys by a future Uranus orbiter. In this case, the differences are a significant fraction of the total induced field—over 20% in most places. As in other examples, all vector components are shown in the Supplemental Text (Figure 4.13). Greater salinity in the ocean will result in larger differences resulting from asymmetry, though typically a smaller fraction of the total induced field. A closer approach will also increase the differences substantially, especially because of the quadrupole and octupole moments represented in the induced field, whose field strengths decrease faster than those of the dipole moments.

Callisto and Triton

For both Callisto and Triton, we model spherically symmetric interiors and suppose asymmetry in their ionospheric structure based on a day–night dichotomy. This day–night difference occurs when the ionization rate is heavily influenced by EUV flux from the Sun, as is the expected case for Callisto (Hartkorn et al., 2017) and Triton (Krasnopolsky and Cruikshank, 1995). To approximate the asymmetric conductivity structure introduced by the day–night dichotomy, we apply a single degree-1 real harmonic for each moon, such that the uniformly conducting ionosphere bulges outward at local noon and inward at local midnight. Contour maps for these simple shapes are included in the Supplemental Text (Figures 4.14a and 4.15a). Note that the asymmetric shape of the ionosphere will rotate in the frame of reference of the satellite on the same time scale as the orbital period. However, we aim to estimate the order of magnitude for the signal from asymmetry and demonstrate application of our model, so for simplicity we assume the asymmetric structure is fixed and consider only the synodic period for excitations.

The ionosphere of Callisto is assumed to extend from the surface to 100 km altitude and to have

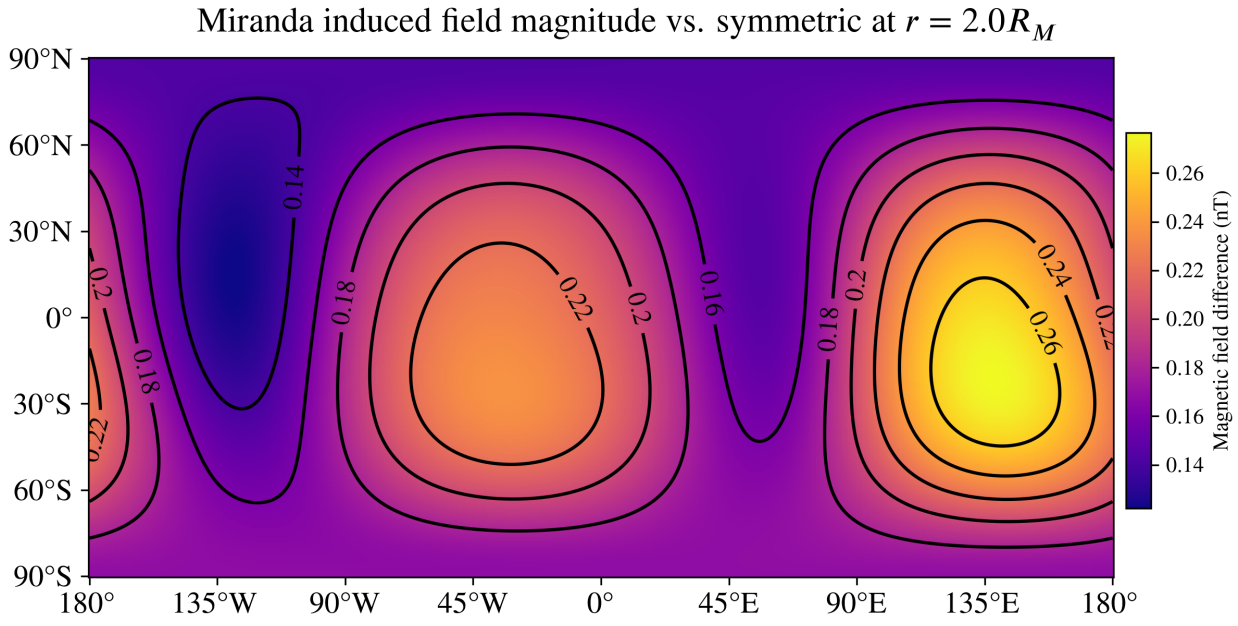

Figure 4.7: Difference in the magnitude of the induced magnetic field of Miranda resulting from the interior model shown in Figure 4.6. Magnetic fields are evaluated at the J2000 reference epoch and at $r = 2R_M$, a plausible flyby distance for a future mission. The simple geometry of the differences shown here reflects the fact that the change is dominated by increases in the dipole moments. This happens because the asymmetry model results in more conducting material residing closer to the surface, increasing the overall response to the excitation field. Unlike for Europa, the signal from asymmetry is over 20% of the total induced field in most places (compare to Figure 4.13b). An animation showing the same map as it varies throughout the 35-hour synodic period is included in the Supplemental Material.

a total height-integrated conductivity of 800 S, consistent with the estimate of Pedersen conductivity concluded by Hartkorn and Saur (2017). The upper boundary of this shape is then perturbed as described above. *Voyager 2* radio measurements revealed Triton to have a highly conductive ionosphere, with an ion density peaking well above the surface (Tyler et al., 1989). To model Triton's ionosphere, we assume a uniformly conducting shell beginning at 250 km altitude and extending upward for 200 km. The upper boundary of this shape is then perturbed as described above, and the neutral atmosphere below is assumed to be nonconducting. In the highly conducting ionosphere of Triton, convection electric fields will tend to transport plasma from areas of high ion density to areas with lower density, smoothing out the asymmetry somewhat (Schunk and Nagy, 2009). To account for this, we decrease the amplitude of asymmetry compared to Callisto (to ±60 km rather than ±100 km).

Our conductivity models for both moons also contain conducting oceans in their interiors. For the interior of Callisto, we have assumed parameters consistent with previous studies of magnetic induction at this moon (*e.g.* Vance et al., 2021), namely a 100 km thick ice shell atop an ocean of 10 wt% $MgSO_4$(aq). Magnetic induction at Triton has not yet been studied in detail; we have chosen the same composition for Triton's ocean as for Callisto, and a slightly thicker ice shell of 112 km. Our Triton interior model is based on the moment of inertia and surface temperatures assumed for Pluto by Hussmann et al. (2006).

Figures 4.8 and 4.9 show the differences in the B_x component of the induced magnetic field resulting from asymmetry in the ionospheres of Callisto and Triton, respectively. The magnetic fields are evaluated at the J2000 epoch and at $r = 2R$, where R is the body radius; as with Miranda, this distance is selected as a plausible flyby distance for past or future missions. Differences in the magnetic field from asymmetry in the Callisto ionosphere appear to be negligible, due primarily to the small ionospheric conductivity there. However, for Triton the high conductivity supports large differences, with the asymmetry accounting for as much as 1/3 of the total induced field (compare to Figure 4.15b). For both moons, the degree-1 shape we use to perturb the upper ionospheric boundary is not capable of changing the induced dipole moment, so all differences will decay faster with distance than the main induction field from the spherically symmetric layers. Any asymmetry rep-

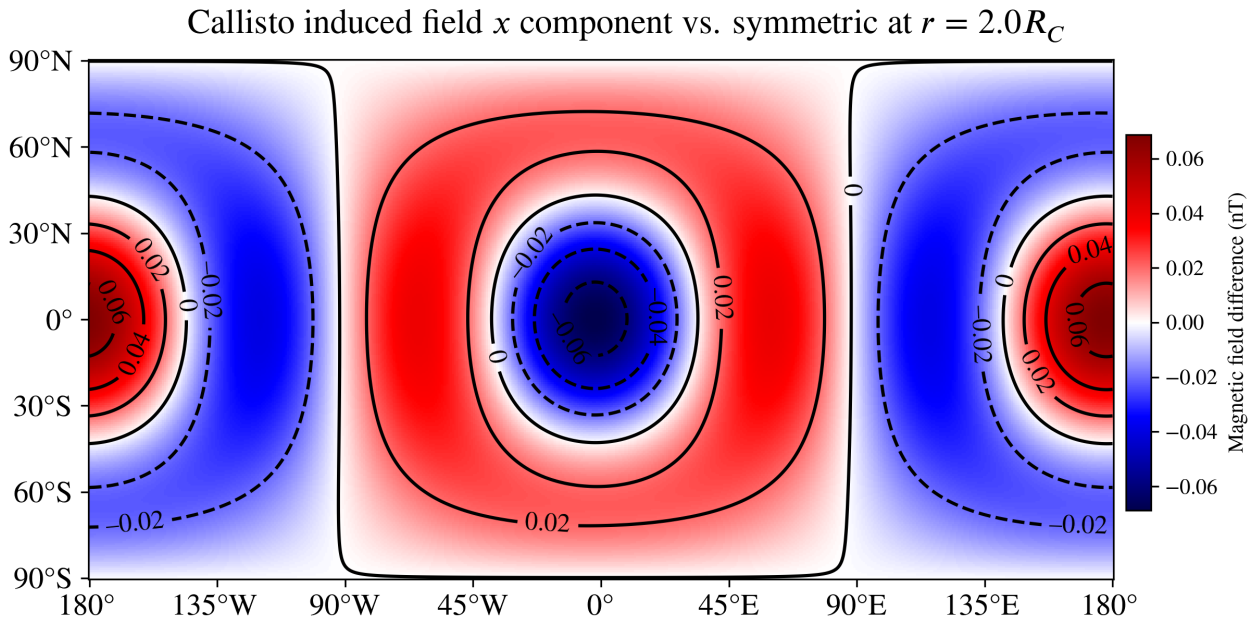

Figure 4.8: Difference in the B_x component of the induced magnetic field of Callisto resulting from asymmetry in the ionosphere representing a day–night dichotomy. Magnetic fields are evaluated at $r = 2R_C$, consistent with a spacecraft flyby. The induced field is nearly unaffected by the large asymmetry in the ionosphere because of the small ionospheric conductivity (Hartkorn and Saur, 2017) and because the odd-degree shape harmonic we used does not cause any change to the dominant induced dipole moment.

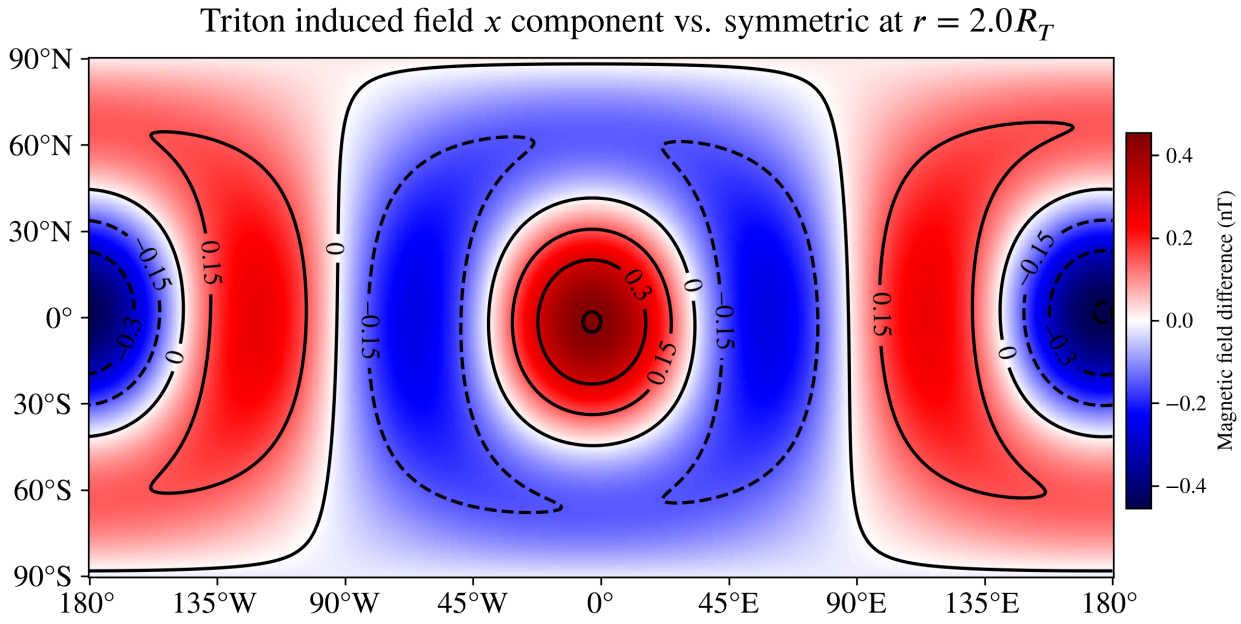

Figure 4.9: Difference in the B_x component of the induced magnetic field of Triton resulting from asymmetry in the ionosphere representing a day–night dichotomy. Magnetic fields are evaluated at $r = 2R_T$, consistent with a flyby as part of a possible future mission. The high-altitude, highly conducting, asymmetric ionosphere we model introduces a significant difference relative to a spherically symmetric analog (about 1/3 of the total induced field, see Figure 4.15b). This suggests ionospheric asymmetry is likely to play an important role in future magnetic investigations of Triton. However, the observed differences are limited to induced moments of quadrupole order and larger, as the asymmetric shape we use to represent the day–night dichotomy cannot change the induced dipole moments.

resenting a day–night dichotomy will be dominated by odd-degree shapes describing the boundary due to their symmetry properties, so a more detailed asymmetric shape is unlikely to significantly change this result.

4.4 Discussion

The model we have developed is versatile in how it can be used to calculate induced magnetic fields. Our final result (Eq. 4.17) is a direct generalization of the recursive method presented by Parkinson (1983) that is often used in magnetic sounding studies of icy moons (*e.g.* Hand and Chyba, 2007; Schilling et al., 2007; Seufert et al., 2011). Describing asymmetric boundaries between regions in terms of spherical harmonics, as in Eq. 4.15, permits a wide array of reasonable shapes to be supposed, allowing for forward models of the induced magnetic field of realistic, asymmetric oceans for the first time.

Our model takes only seconds to run, supporting Monte Carlo/Bayesian statistical methods that require a vast array of possible configurations in order to constrain interior properties. Such "big data" approaches are simply not possible with numerical solutions that require hours or days to evaluate. Furthermore, as our model determines the complex induced magnetic moments at a particular epoch, explicit time dependence is added simply with a factor $e^{-i\omega t}$ for each period of excitation. This allows our model to immediately be applied to evaluate the magnetic field at any date and time. Such functionality is already a part of the Python code we used to calculate results and create all figures, included as Supplemental Material.

4.4.1 Limitations of the analytic model

The necessary assumptions we have made in order to obtain an analytic result create some limitations to the applicability of the solution. The primary limiting assumptions are that of uniform conductivity within each conducting layer and that asymmetric boundaries are near-spherical.

Uniform conductivity layers

Assuming uniform conductivity within each layer in the conducting body restricts our result to applications where the sequence of conducting layers along a line outward from the center is independent of latitude and longitude. In principle, it is possible to represent any closed surface containing the body center using a spherical harmonic expansion with high enough degree p. However, the advantages of taking such an approach with our model, *e.g.* to represent a melt lens within an ice shell, are likely outweighed by the additional complexity and computation time required. Higher-degree harmonics in such an expansion will have a much decreased weighting compared to low-degree harmonics, so the improved accuracy in the representation of the boundary will result in more modest gains in accuracy of representing the induced magnetic field. For these reasons, we recommend forming a low-degree ($p_{\max} \leq 8$) approximation for non-spherical boundaries to use with our model.

This condition requires that our solution is only approximate in cases where a rapid lateral change in conductivity is expected—for example, at the terminator line in Callisto's ionosphere (Hartkorn et al., 2017). Far from the rapid lateral cutoff, our approach may still yield valid results, especially if the induced currents travel mostly parallel to the discontinuity. In the example of Callisto's ionosphere, photoionization from solar EUV photons is the primary source of plasma, so a sharp dropoff in charge carriers, and hence conductivity, is expected behind the terminator line. To completely account for an abrupt lateral discontinuity in conductivity, a numerical solution is required. However, approximating a dichotomy like that in Callisto's ionosphere with our approach still captures significant first-order effects of asymmetry and yields insights not possible to obtain with a spherically symmetric conductivity model.

Near-spherical boundary shape

The second major assumption that limits applicability of our solution is that the boundaries between conducting regions are near-spherical. This assumption is required in order to limit our solution to a solvable set of equations describing a first-order change in the induced magnetic field. In

other words, we are assuming that the second-order effects, *i.e.* the induced moments that result from the interaction of asymmetric boundaries with the new moments induced by the first-order expansion, are negligible. Each successive term in the Taylor expansion that determines the order of the solution (Eq. 4.16) gains a new factor $\varepsilon_l/\overline{r}_l$ compared to the previous term. All other factors keep the same order of magnitude, although some mixing coefficients may grow or shrink slightly depending on the particular first-order induced moment and boundary shape considered. $\varepsilon_l/\overline{r}_l$ will generally be quite small for bodies large enough to differentiate, as their self-gravity is already sufficient to pull them into a near-spherical shape.

The value of the boundary deviation parameter $\varepsilon_l/\overline{r}_l$ for the bodies we studied ranges from 0.016 for Europa (Tobie et al., 2003, model) to 0.056 for the large Triton ionosphere, with the value for Miranda an outlier at 0.210. The asymmetry model for Enceladus (after Hemingway and Mittal, 2019) has a value of 0.071. We accounted for the thicker Miranda ice shell essentially by scaling up this parameter; our Miranda model serves to quantify an upper limit to the resulting differences from the spherically symmetric case for the assumed bulk properties. We found in Section 4.3.2 that the differences caused by this asymmetry were a significant fraction of the total induced field, but the total induced field was only on the order of 1 nT, so second-order effects would still be negligible in this case. If we had supposed a more saline ocean for Miranda, the induced field would grow substantially, and second-order effects could potentially become measurable. This may become a concern for future missions to the Uranus system, but we leave investigation of such second-order effects for future work.

4.4.2 Summary of example applications

Applying our analytic result to example moons as in Section 4.3.2, we provide evidence that the expected asymmetries are likely to result in measurable signals that will impact future magnetometer investigations. With the possible exception of Callisto, the conditions we studied resulted in significant differences compared to analogous, spherically symmetric models: we find changes to the induced field of up to about 2.4 nT for Europa, 0.5 nT for Triton, and 0.25 nT for Miranda at plausible distances for orbiting spacecraft, and with marked variation in latitude, longitude, and

time. In the case of asymmetric oceans, where degree-2 shape harmonics will be strongly represented, a significant amount of the change arises from alteration of the induced dipole moment. The size of this signal is likely to be significant for the upcoming *Europa Clipper* mission, which plans several near flybys of under 25 km. For the Europa Seawater model we studied, our initial estimates (Figure 4.3) show that these effects will have measurable effects for a variety of flyby altitudes, but will also vary throughout the excitation period. However, we only considered this behavior for a single plausible model of asymmetry in Europa's interior. It is not yet clear whether the effects of plausible asymmetry may be disregarded under some general condition, *e.g.* flybys above some threshold altitude. We recommend this as a topic for future work.

For Europa, we studied the same asymmetric shape under assumptions of two different compositions, end-member Seawater oceans with salinities previously considered in the literature (*e.g.* Vance et al., 2021). From comparing these results (Figures 4.2, 4.4), we can conclude that lowering the ocean solute concentration had a relatively small impact on the signal arising from asymmetry. However, ocean composition is likely to play a bigger role at smaller moons such as Miranda and Enceladus than at Europa because the asymmetry there may be a significant fraction of the radius. In addition, the smaller radii of the conducting boundaries render the predicted induced moments more sensitive to the electrical conductivity for the same reason Europa is less sensitive—an exponential dependence on $(r\sqrt{i\omega\mu\sigma})$ in the Bessel functions $j_n(kr)$. The radii are large enough for Europa that ratios of these functions are close to unity, but the same does not apply to Miranda or Enceladus, thus causing changes in σ to have a greater effect on the induced field. The strong dependence on radius in these functions also causes asymmetric oceans that rise nearer to the surface to have outsize effects on the induced moments. This is evident in the differences in the magnitude of the induced field for Miranda in Figure 4.7, which are universally positive for all latitudes and longitudes.

We did not consider magnetic fields arising due to currents in the plasma environment outside the bodies beyond the current sheet models used to determine the excitation moments. Such plasma fields will be critical to any future analysis of spacecraft measurements, but to include them in induction modeling is beyond the scope of this work.

4.5 Conclusions

With the mathematical methods described in this work, we have derived an analytic model capable of calculating the induced magnetic field for any arbitrary planetary body to first order, provided it is near-spherical. This capability is an essential step forward in considering and accounting for the expected global asymmetries in ocean worlds. We have demonstrated that these asymmetries will produce measurable effects on the induced fields used in magnetic sounding investigations. These effects will introduce a source of systematic noise in measurements of order 2 nT near the surface of Europa, and will have some impact on characterization studies using flyby data at all altitudes because the largest differences result from changes to the induced dipole moments. Future spacecraft investigations may be able to characterize asymmetry within the interiors of icy moons if they are able to achieve measurement precision on the order of a few tenths of a nT. Our analytic model and the software we provide for its evaluation support study of the interior structure of icy moons with an unprecedented level of detail.

Acknowledgments

This work was supported by NASA Headquarters under the NASA Earth and Space Science Fellowship Program — Grant 80NSSC18K1236. Part of the research was carried out at the Jet Propulsion Laboratory, California Institute of Technology, under a contract with the National Aeronautics and Space Administration (80NM0018D0004). Data used in this work were generated using the open source *PlanetProfile* software hosted on GitHub. The authors acknowledge that portions of this work have been carried out on the traditional lands of the Coast Salish and Tongva peoples. The authors are indebted to D. Hemingway for data required to reproduce their interior model for Enceladus. The authors also thank H. Hay for helpful discussion on tidal deformation and P. Jandir for feedback regarding notation.

An analytic solution for evaluating the magnetic field induced from an arbitrary, asymmetric ocean world

Part 2: Supplemental Material

The final result from our derivation is complicated. To clarify the source of each piece of the result, we present each step of the derivation from first principles in Section 4.6. Python code for evaluating our model is provided as Supplemental Material[6]. Next, we present a table of values given as inputs to the *PlanetProfile* framework in Section 4.7 (Table 4.1). In Section 4.8, we give a detailed derivation of our method for translating J_2 and C_{22} gravity coefficients into geometric perturbations of boundary shapes. The full results from our example models applying our results for magnetic induction of asymmetric conducting layers in icy moons are presented in Section 4.9. Therein, we include figures showing the asymmetric layer topography, induced field magnitude at the considered altitude for the asymmetric model, and differences in the induced field components and magnitude that result from the asymmetry in the conductivity structure. Section 4.10 compiles explicit formulas for the Wigner $3j$-symbols and the mixing coefficients $\Xi^{nm}_{n'm'pq}$ and $\Xi^{\star\,nm}_{n'm'pq}$. Finally, in Section 4.11, we describe strategies for mitigating numerical difficulties with applying the layer method that result from the need to evaluate ratios of differences of very large, complex numbers.

4.6 Derivation from first principles

Our goal is to apply Maxwell's laws at boundaries between regions and find the induced magnetic moments that satisfy the resulting equations. The same is true of the spherically symmetric, recursive solution developed by Srivastava (1966) and prominently applied by Zimmer et al. (2000), Seufert et al. (2011), and others. However, in our application, we describe the boundaries between regions of varying electrical conductivity by an arbitrary shape, rather than by a constant radius. The shape of the boundary has important consequences, and determines which magnetic moments are induced by a given excitation field applied by the parent planet. A derivation of the Srivastava

[6]Also available as a Zenodo archive: https://zenodo.org/record/5002956.

recursive method is presented in more modern notation by the oft-cited Parkinson (1983). The Parkinson derivation contains several errors and inconsistencies, so we include here a full detailing of our solution from first principles so that we may best identify the consequences of those errors.

The excitation field applied to the conducting body has the form

$$\mathbf{B}_{\text{exc}}(\mathbf{r}, t) = \mathbf{B}_o(\mathbf{r}) + \sum_{\text{j}} \mathbf{B}_{e,\text{j}}(\mathbf{r}) e^{-i\omega_{\text{j}} t}, \tag{4.20}$$

with static ($\mathbf{B}_o$) and dynamic ($\mathbf{B}_{e,\text{j}}$) components that are complex in general. The measurable magnetic field is found by taking the real part of any complex expressions for the vector components. Superposition permits an independent handling of each excitation frequency, so we will focus on a single excitation frequency in our derivation. Our method may then be applied repeatedly for a combination of frequencies, and the results summed together.

In regions free of electric currents, the magnetic field satisfies Laplace's equation and therefore may be described by the gradient of a scalar potential ψ:

$$\nabla^2 \mathbf{B} = 0 \tag{4.21}$$

$$\mathbf{B} = -\nabla \psi. \tag{4.22}$$

These equations are valid outside the conducting body (and outside any ionosphere) if we neglect currents in the magnetized plasma. Although currents in the plasma environment around the body are not generally negligible, the principle of superposition permits us to consider each contribution to the net electromagnetic response independently—the net magnetic field is then the sum from each individual contribution. In this work, we consider only the induced magnetic moments generated by the interaction of the primary excitation field with the conducting body, as this is the dominant interaction that induces magnetic fields from within solar system moons.

In spherical polar coordinates $\mathbf{r} = (r, \theta, \phi)$, general solutions to Eqs. 4.21 and 4.22 have the form (Jackson, 1999)

$$\psi(\mathbf{r}) = \sum_{n,m} R \left(B^e_{nm} \left(\frac{r}{R} \right)^n + B^i_{nm} \left(\frac{R}{r} \right)^{n+1} \right) Y_{nm}(\theta, \phi), \tag{4.23}$$

where B^e_{nm} and B^i_{nm} are complex coefficients for the excitation and induced magnetic fields, Y_{nm} are spherical harmonics of degree n and order m, and R is a unit of radial distance, typically the outer radius of the conducting body. The B^e potentials, proportional to positive powers of r, can only be generated from outside of the conducting body under examination. The B^i terms in Eq. 4.23 are those of the multipole expansion, so each B^i_{nm} is proportional to, and thus represents, an induced multipole moment. We assume the magnetic potential for the excitation field oscillates sinusoidally, so time dependence is added to Eq. 4.23 by multiplication of $e^{-i\omega t}$ as in Eq. 4.20.

Within the conducting body, the dynamic excitation field induces electric fields that drive currents, so $\mathbf{B}$ cannot be represented by Eq. 4.22 in this region. Instead, we must use a diffusion equation for $\mathbf{B}$, derived from combining Maxwell's laws with Ohm's law:

$$\nabla^2 \mathbf{B} = \mu\sigma \frac{\partial \mathbf{B}}{\partial t}. \tag{4.24}$$

For simplicity in deriving our model, we neglect movement of conducting material within the body (as in the case of ocean currents), which can itself induce secondary fields (Saur et al., 2010; Vance et al., 2021). As we are considering only the oscillatory magnetic field, taking the time derivative of $\mathbf{B}$ is equivalent to multiplication by $-i\omega$. We can thus rewrite Eq. 4.24 in terms of a diffusion constant k, and arrive at a vector Helmholtz equation:

$$\nabla^2 \mathbf{B}_{\text{osc}} = -k^2 \mathbf{B}_{\text{osc}} \tag{4.25}$$

$$k = \sqrt{i\omega\mu\sigma}. \tag{4.26}$$

The definition of k includes an arbitrary phase—we may also have chosen to include the $(-)$ underneath the square root, as in Parkinson (1983). This choice of phase will ultimately determine which differential equation we find for the radial dependence of the internal magnetic field (Eq. 4.37).

In general, μ and σ are functions of position and will vary throughout the body. On planetary scales, μ is well approximated by μ_o, even for bodies containing large amounts of ferromagnetic materials (Saur et al., 2010); we assume $\mu = \mu_o$ everywhere in this work. We further assume that σ is uniform within each conducting region, and that each region is global in extent, *i.e.* any path outwards from the center must pass through each region sequentially.

General solutions to Eq. 4.25 for the configuration at hand must be consistent with a poloidal field; since they are induced by an external field, there will be no toroidal field component (Moffatt, 1978). Poloidal fields take the following form:

$$\mathbf{B}_\Psi = \nabla \times \nabla \times (\Psi \mathbf{r}) \tag{4.27}$$

$$B_{r,\Psi} = \frac{1}{r}\left[-\frac{1}{\sin\theta}\frac{d}{d\theta}\sin\theta\frac{d}{d\theta} - \frac{1}{\sin^2\theta}\frac{d^2}{d\phi^2}\right]\Psi \tag{4.28}$$

$$B_{\theta,\Psi} = \frac{1}{r}\frac{d}{d\theta}\frac{d}{dr}(\Psi r) \tag{4.29}$$

$$B_{\phi,\Psi} = \frac{1}{r\sin\theta}\frac{d}{d\phi}\frac{d}{dr}(\Psi r), \tag{4.30}$$

where the poloidal potential Ψ is a scalar function of position. Note that the expressions for the poloidal potential vector components given by Parkinson (1983, Eq. 158) contain a sign error in the $\hat{r}$ component.

The quantity in square brackets in Eq. 4.28 is the angular momentum operator $\hat{L}^2$, of which the spherical harmonics Y_{nm} are eigenfunctions (Edmonds, 1996; Jackson, 1999):

$$\hat{L}^2 Y_{nm} = n(n+1)Y_{nm}. \tag{4.31}$$

Note that Moffatt (1978, Eq. 2.26) presents Eq. 4.31 with a sign error based on their definition of the angular momentum operator. If we suppose Ψ is separable, we can expand it in spherical harmonics:

$$\Psi(r,\theta,\phi) = \sum_{n,m} c_{nm}\mathcal{R}_{nm}(r)\,Y_{nm}(\theta,\phi), \tag{4.32}$$

where c_{nm} are constant coefficients determined by the boundary conditions and $\mathcal{R}_{nm}$ are functions we must determine from other relations. As we later satisfy the boundary conditions with this functional form of Ψ, the uniqueness theorem confirms that this is *the* physically correct representation (Dennery and Krzywicki, 2012), validating the supposition that Ψ is separable.

Inserting Eq. 4.32 into Eqs. 4.28–4.30 and utilizing Eq. 4.31 yields expressions for the compo-

nents of the magnetic field within the conducting body in terms of $\mathcal{R}$:

$$B_{r,\text{int}} = \sum_{n,m} \frac{c_{nm}}{r} \mathcal{R}_{nm}\, n(n+1) Y_{nm} \tag{4.33}$$

$$B_{\theta,\text{int}} = \sum_{n,m} \frac{c_{nm}}{r} \frac{d}{dr}(r\mathcal{R}_{nm}) \frac{\partial Y_{nm}}{\partial \theta} \tag{4.34}$$

$$B_{\phi,\text{int}} = \sum_{n,m} \frac{c_{nm}}{r \sin\theta} \frac{d}{dr}(r\mathcal{R}_{nm}) \frac{\partial Y_{nm}}{\partial \phi}. \tag{4.35}$$

We can now make use of these expressions along with Eq. 4.25 to find a differential equation for $\mathcal{R}_{nm}$. Linearity of the ∇^2 operator allows us to consider only a single n, m term, as the same equations will apply to all terms. The $\hat{r}$ component of Eq. 4.25 reads as (Arfken et al., 2012)

$$\nabla^2 B_r - \frac{2B_r}{r^2} - \frac{2}{r^2 \sin\theta} \frac{d}{d\theta}(\sin\theta B_\theta) - \frac{2}{r^2 \sin\theta} \frac{\partial B_\phi}{\partial \phi} = -k^2 B_r. \tag{4.36}$$

Inserting Eqs. 4.33–4.35 and again exploiting the angular momentum operator, we arrive at a Bessel equation for $\mathcal{R}_{nm}$:

$$\frac{1}{\mathcal{R}_{nm}} \frac{d}{dr}\left(r^2 \frac{\partial \mathcal{R}_{nm}}{\partial r}\right) + k^2 r^2 - n(n+1) = 0. \tag{4.37}$$

Solutions to this equation are linear combinations of the particular solutions, which are the spherical Bessel functions of the first and second kind, j_n and y_n:

$$\mathcal{R}_{nm}(r) = a_{nm} j_n(kr) + b_{nm} y_n(kr) \quad \text{or} \quad \mathcal{R}_{nm}(r) = a_{nm}\left(j_n(kr) + \Lambda_{nm} y_n(kr)\right) \text{ with } \Lambda_{nm} \equiv b_{nm}/a_{nm}, \tag{4.38}$$

$$j_n(kr) = (-kr)^n \left(\frac{1}{kr}\frac{d}{d(kr)}\right)^n \frac{\sin kr}{kr}, \tag{4.39}$$

$$y_n(kr) = -(-kr)^n \left(\frac{1}{kr}\frac{d}{d(kr)}\right)^n \frac{\cos kr}{kr}. \tag{4.40}$$

a_{nm} and b_{nm} (or a_{nm} and Λ_{nm}) in Eq. 4.38 are constants determined from the boundary conditions; they will play a critical role in determining the induced magnetic field. The second format for $\mathcal{R}_{nm}$ presented in Eq. 4.38 is useful for expressing recursion relations for spherically symmetric bodies, but the first format must be used in solving the full boundary conditions for the asymmetric case. We will use both formats in our derivation.

4.6.1 *Consequences of the choice of phase for k*

If, in defining the diffusion constant k in Eq. 4.26, we had chosen the alternate phase $k = \sqrt{-i\omega\mu\sigma}$, the first term in Eq. 4.37 would be negated. In that case, the resulting differential equation would be the *modified* spherical Bessel equation, with solutions $i_n(kr)$ and $k_n(kr)$, the *modified* spherical Bessel functions of the first and second kinds, respectively. These are similar to the spherical Bessel functions j_n and y_n and have similar properties; they are functions of sinh kr and cosh kr rather than sin kr and cos kr. In the commonly cited derivation by Parkinson (1983, Ch. 5), this choice of phase for k should yield the modified spherical Bessel functions for the radial dependence of the internal magnetic field, but Parkinson incorrectly arrives at Eq. 4.37. Several authors (Zimmer et al., 2000; Khurana et al., 2002; Hand and Chyba, 2007; Arridge and Eggington, 2021) have repeated this error and applied a phase for k inconsistent with use of the standard Bessel functions. This error leaves the real part of the argument kr unchanged, while negating the imaginary part, equivalent to taking the complex conjugate.

The real part of kr determines the (real) exponential dependence of the Bessel functions, so the scale of the result is the same. The complex part determines the oscillation phase of the Bessel functions, and it becomes negated. In effect, the error described above causes the resulting solution for the induced magnetic field to *lead* the excitation field by the amount of the phase delay ϕ, rather than lagging (as it must lag behind the excitation to preserve causality). Overall, the conclusions of the authors repeating this error are unaffected, but the expressions they apply all include a sign change in connecting the phase delay to the equations describing the induced magnetic field. For consistent comparisons to these important prior studies, we note by Eq. 4.8 that the phase delay ϕ is the *negative* of the phase of the complex amplitude $\mathcal{A}_1^e$ we later derive.

4.6.2 *General expressions for the magnetic field in each region*

We must now use the expressions we have obtained to relate the magnetic field components at boundaries, as needed to solve for the induced moments. First, we note some considerations for the general radial dependence $\mathcal{R}_{nm}$ inside the conducting body: The solutions y_n diverge at the origin,

so b_{nm} (or Λ_{nm}) must always be zero for the innermost region. As our solution for $\mathcal{R}_{nm}$ now contains arbitrary coefficients, we absorb the coefficients c_{nm} into a_{nm} and b_{nm}.

For later convenience, we also require expressions for $\frac{d}{dr}(r\, j_n(kr))$ and $\frac{d}{dr}(r\, y_n(kr))$. Eqs. 4.39 and 4.40 can be manipulated to obtain

$$j_n^\star \equiv \frac{d}{dr}(rj_n) = (n+1)j_n - kr\, j_{n+1}, \quad y_n^\star \equiv \frac{d}{dr}(ry_n) = (n+1)y_n - kr\, y_{n+1}, \tag{4.41}$$

which we now also define as $j_n^\star$ and $y_n^\star$, respectively.

The details and formulation of the spherical harmonics are of central importance to this work. We use the fully normalized, complex spherical harmonics:

$$Y_{nm} = \sqrt{\frac{2n+1}{4\pi}\frac{(n-m)!}{(n+m)!}}\, P_n^m(\cos\theta)\, e^{im\phi}, \tag{4.42}$$

$$Y_{n,-m} = (-1)^m Y_{nm}^*, \tag{4.43}$$

where P_n^m are the associated Legendre functions with the Condon–Shortley phase. Although in the geomagnetics literature, the spherical harmonics are often expressed using real harmonics, in the Schmidt normalization, and without the Condon–Shortley phase, we have chosen a convention ubiquitous throughout the literature on angular momentum in quantum mechanics. From this literature we draw many helpful results, especially regarding the Clebsch–Gordan coefficients in Section 4.6.5.

We will also later need expressions for θ derivatives of Y_{nm}:

$$Y_{nm}^\star \equiv \frac{\partial Y_{nm}}{\partial\theta} = \frac{1}{\sin\theta}\left(-w_{nm}^- Y_{n-1,m} + w_{nm}^+ Y_{n+1,m}\right) \quad \text{for } m \geq 0, \tag{4.44}$$

$$w_{nm}^- = (n+1)\sqrt{\frac{n^2-m^2}{(2n-1)(2n+1)}}, \quad w_{nm}^+ = n\sqrt{\frac{(n+1)^2-m^2}{(2n+1)(2n+3)}}, \tag{4.45}$$

$$Y_{n,-m}^\star = (-1)^m Y_{nm}^{\star *}. \tag{4.46}$$

We thereby define $Y_{nm}^\star$ similar to $j_n^\star$ and $y_n^\star$, as they all pertain to the tangential components; we will not need the ϕ derivatives in our derivation. The format of Eq. 4.44, obtained using recurrence relations for the associated Legendre functions (*e.g.* Abramowitz and Stegun, 1972), has been selected for optimal use of orthogonality relations to solve the boundary conditions later.

We can now write general expressions for the magnetic field in all regions. From Eqs. 4.22 and 4.23, the external magnetic field follows

$$B_{r,\text{ext}} = \sum_{n,m} \left[-n \left(\frac{r}{R} \right)^{n-1} B^e_{nm} + (n+1) \left(\frac{R}{r} \right)^{n+2} B^i_{nm} \right] Y_{nm} \tag{4.47}$$

$$B_{\theta,\text{ext}} = \sum_{n,m} \left[- \left(\frac{r}{R} \right)^{n-1} B^e_{nm} - \left(\frac{R}{r} \right)^{n+2} B^i_{nm} \right] Y^\star_{nm} \tag{4.48}$$

$$B_{\phi,\text{ext}} = \sum_{n,m} \left[- \left(\frac{r}{R} \right)^{n-1} B^e_{nm} - \left(\frac{R}{r} \right)^{n+2} B^i_{nm} \right] \frac{1}{\sin\theta} \frac{\partial Y_{nm}}{\partial \phi}. \tag{4.49}$$

From Eqs. 4.33–4.35, the internal magnetic field follows

$$B_{r,\text{int}} = \sum_{n,m} \frac{a_{nm} j_n(kr) + b_{nm} y_n(kr)}{r} n(n+1) Y_{nm} \tag{4.50}$$

$$B_{\theta,\text{int}} = \sum_{n,m} \frac{a_{nm} j^\star_n(kr) + b_{nm} y^\star_n(kr)}{r} Y^\star_{nm} \tag{4.51}$$

$$B_{\phi,\text{int}} = \sum_{n,m} \frac{a_{nm} j^\star_n(kr) + b_{nm} y^\star_n(kr)}{r} \frac{1}{\sin\theta} \frac{\partial Y_{nm}}{\partial \phi}. \tag{4.52}$$

The tangential components B_θ and B_ϕ offer redundant information in matching the solutions across the boundaries, so we will restrict our focus to the B_θ component because it contains terms for all n and m.

Solving for the a_{nm}, b_{nm}, and B^i_{nm} coefficients in these equations is accomplished by applying Maxwell's laws at the common boundaries between each region. On each boundary surface, Maxwell's laws dictate that the normal component of $\mathbf{B}$ must be continuous, and the tangential components of $\mathbf{B}/\mu$ must be continuous whenever there are no surface currents confined to the boundary itself (Jackson, 1999). As we assume $\mu = \mu_o$ within the body, $\mathbf{B}$ is continuous everywhere, and the components of the magnetic field for adjacent regions are equal on the boundary surface.

4.6.3 Internal boundary conditions

At each boundary interior to the outer surface, the vector components of the magnetic field must match according to Eqs. 4.50–4.52. At a distance from the body center $r_l(\theta, \phi)$ describing the outer

boundary surface of a lower layer l with wavenumber k_l and an upper boundary u with wavenumber k_u, the internal boundary conditions read

$$B_r: \quad \sum_{n,m} n(n+1)\frac{j_n(k_l r_l)+\Lambda^l_{nm} y_n(k_l r_l)}{r_l} a^l_{nm} Y_{nm} = \sum_{n,m} \frac{j_n(k_u r_l)+\Lambda^u_{nm} y_n(k_u r_l)}{r_l} a^u_{nm} Y_{nm} n(n+1) \tag{4.53}$$

$$B_\theta: \quad \sum_{n,m} \frac{j_n(k_l r_l)+\Lambda^l_{nm} y_n(k_l r_l)}{r_l} a^l_{nm} Y^\star_{nm} = \sum_{n,m} \frac{j_n(k_u r_l)+\Lambda^u_{nm} y_n(k_u r_l)}{r_l} a^u_{nm} Y^\star_{nm}. \tag{4.54}$$

In general, r_l may be a function of θ and ϕ; this is the major focus of the present work. Formatting the linear combinations of j_n and y_n as we have done will, in the case of spherical symmetry, allow us to solve Eqs. 4.53 and 4.54 for Λ^u_{nm} in terms of Λ^l_{nm}, resulting in a recursion relation.

Mutual orthogonality of the spherical harmonics may be exploited to extract terms in Eq. 4.53 proportional to a desired harmonic $Y_{n'm'}$. Multiplying both sides by the complex conjugate of the desired harmonic $Y^*_{n'm'}$ and integrating over a unit sphere is equivalent to replacing $Y_{n'm'}$ with $\delta_{n,n'}\delta_{m,m'}$ (Kronecker delta functions), effectively discarding all other terms. A similar operation, multiplying both sides of Eq. 4.54 by $Y^{\star *}_{n'm'}\sin^2\theta$ and integrating over a unit sphere, yields somewhat different results but may be used to reach an analogous equation, as we now describe.

Linear combinations of orthogonal functions are not, in general, mutually orthogonal. From Eq. 4.44, we can determine that $Y^\star_{nm}\sin\theta$ may not be orthogonal to $Y^\star_{n'm'}\sin\theta$ when $m = m'$ and $n' = n+2$ or $n' = n-2$. One such example is $Y^\star_{31}$ and $Y^\star_{11}$: integrating $Y^{\star *}_{31} Y^\star_{11}\sin^2\theta$ over a unit sphere gives a non-zero result. This results from the overlap of the $Y_{n+1,m}$ term in Eq. 4.44 for $n = 1$ and the $Y_{n-1,m}$ term for $n = 3$. When this operation is applied in the sums over n and m in the boundary conditions, coupled linear equations result for these overlapping values of n. Ultimately, the equations are separable because of the following factors:

- For all terms, $n \geq 1$ because $\frac{\partial Y_{00}}{\partial\theta} = 0$.

- We can determine which a_{nm} are zero from the radial boundary condition equations, which has terms proportional to mutually orthogonal functions.

- The result of the overlap integral is the same in each conducting region, and so appears on both sides of each boundary condition equation.

The first two items above bound the number of equations. The final item may be used to scale and sum the equations so as to eliminate the terms proportional to $n' + 2$ or $n' - 2$, where the terms proportional to $Y^{\star}_{n'm'}$ are desired. The coefficient of the remaining n' term is altered by the overlap terms, but all terms are multiplied by the same coefficient (combinations of $w^{-}_{n'm'}$ and $w^{+}_{n'm'}$), so it divides away. Therefore, analogous to the radial equation, we finally obtain a result equivalent to replacing $Y^{\star}_{nm}$ by $\delta_{n,n'}\delta_{m,m'}$. These operations will be critical in collecting the new terms that arise from expanding the boundary radii in spherical harmonics.

Spherically symmetric case

If we assume spherical symmetry in the boundary surface at r_l, Λ_{nm} in Eqs. 4.53 and 4.54 is independent of m and can be reduced using the orthogonality relations discussed above. Each value of m yields equations identical to other m, so we set $m = 0$ and drop that subscript on Λ. Multiplying both sides of Eq. 4.53 by $Y^{*}_{n'm'}$ and integrating over a unit sphere yields

$$a^{l}_{nm}\left(j_n(k_l r_l) + \Lambda^{l}_{n} y_n(k_l r_l)\right) = a^{u}_{nm}\left(j_n(k_u r_l) + \Lambda^{u}_{n} y_n(k_u r_l)\right). \tag{4.55}$$

with $n = n'$. Multiplying both sides of Eq. 4.54 by $Y^{\star *}_{n'm'}\sin^2\theta$ and integrating over a unit sphere similarly yields

$$a^{l}_{nm}\left(j_n(k_l r_l) + \Lambda^{l}_{n} y_n(k_l r_l)\right) = a^{u}_{nm}\left(j_n(k_u r_l) + \Lambda^{u}_{n} y_n(k_u r_l)\right). \tag{4.56}$$

Dividing these equations (4.55 and 4.56) by each other, we can now solve for Λ^{u}_{n} in terms of Λ^{l}_{n} to obtain the desired recursion relations. The solution is

$$\Lambda^{u}_{n} = \frac{(j^{u,l}_{n} j^{\star l,l}_{n} - j^{l,l}_{n} j^{\star u,l}_{n}) + \Lambda^{l}_{n}(j^{u,l}_{n} y^{\star l,l}_{n} - y^{l,l}_{n} j^{\star u,l}_{n})}{(j^{l,l}_{n} y^{\star u,l}_{n} - y^{u,l}_{n} j^{\star l,l}_{n}) + \Lambda^{l}_{n}(y^{l,l}_{n} y^{\star u,l}_{n} - y^{u,l}_{n} y^{\star l,l}_{n})}, \tag{4.57}$$

or

$$\Lambda^{u}_{n} = \frac{\delta^{u,l}_{n} + \Lambda^{l}_{n}\epsilon^{u,l}_{n}}{\beta^{u,l}_{n} + \Lambda^{l}_{n}\gamma^{u,l}_{n}} \tag{4.58}$$

with

$$\alpha_n^{u,l} \equiv j_n^{u,l} y_n^{\star u,l} - y_n^{u,l} j_n^{\star u,l} = \frac{1}{k_u r_l} \tag{4.59}$$

$$\beta_n^{u,l} \equiv j_n^{l,l} y_n^{\star u,l} - y_n^{u,l} j_n^{\star l,l} \tag{4.60}$$

$$\gamma_n^{u,l} \equiv y_n^{l,l} y_n^{\star u,l} - y_n^{u,l} y_n^{\star l,l} \tag{4.61}$$

$$\delta_n^{u,l} \equiv j_n^{u,l} j_n^{\star l,l} - j_n^{l,l} j_n^{\star u,l} \tag{4.62}$$

$$\epsilon_n^{u,l} \equiv j_n^{u,l} y_n^{\star l,l} - y_n^{l,l} j_n^{\star u,l}, \tag{4.63}$$

$$j_n^{l,l} \equiv j_n(k_l r_l), \quad y_n^{\star u,l} \equiv y_n(k_u r_l), \quad etc. \tag{4.64}$$

Although $\alpha_n^{u,l}$ does not appear in Eq. 4.58, it will later appear in the asymmetric solutions.

For N layers within the body, there are $N-1$ internal boundaries, so Eq. 4.58 must be applied $N-1$ times to obtain Λ_n^N. Recall that for the innermost layer, $\Lambda_n^1 = 0$, so the next layer above has $\Lambda_n^2 = \delta_n^{2,1}/\beta_n^{2,1}$. The notation in Eqs. 4.58–4.63 is selected to be directly comparable to the recursion relations presented by Parkinson (1983) for the spherically symmetric case. However, Eq. 4.58 appears inverted because we have chosen Λ_n to be a coefficient for y_n instead of j_n. In Section 4.6.6, we will expand these results to first order about the boundary radius r_l to obtain our results for asymmetric boundaries.

4.6.4 External boundary conditions

Combining Eqs. 4.47–4.52, we obtain the boundary conditions that apply at the outermost $\left(N^{\text{th}}\right)$ conducting boundary of any shape:

$$B_r : \sum_{n,m} n(n+1) a_{nm}^N \frac{j_n(kr_N) + \Lambda_{nm}^N y_n(kr_N)}{r_N} Y_{nm} = \tag{4.65}$$

$$\sum_{n,m} \left[-n \left(\frac{r_N}{R}\right)^{n-1} B_{nm}^e + (n+1) \left(\frac{R}{r_N}\right)^{n+2} B_{nm}^i \right] Y_{nm}$$

$$B_\theta : \sum_{n,m} a_{nm}^N \frac{j_n^\star(kr_N) + \Lambda_{nm}^N y_n^\star(kr_N)}{r_N} Y_{nm}^\star = \sum_{n,m} \left[-\left(\frac{r_N}{R}\right)^{n-1} B_{nm}^e - \left(\frac{R}{r_N}\right)^{n+2} B_{nm}^i \right] Y_{nm}^\star, \tag{4.66}$$

where $r_N(\theta, \phi)$ is the distance from the center of the body to the outermost conducting surface, with a nominal mean value of R. $k = k_N$ is that of the outermost conducting layer in the ocean. As with the internal boundary conditions, the only tangential component we consider is B_θ, as B_ϕ offers redundant information.

Spherically symmetric case

In the case of spherical symmetry in the outer boundary surface, $r_N = R$. We can again exploit the orthogonality of the spherical harmonics to extract terms proportional to each individual Y_{nm} or $Y^\star_{nm}$. As described in Section 4.6.3, spherical symmetry in the interior layers results in all Λ_{nm} independent of m, but the same does not apply to the external coefficients if we wish to describe a general excitation field. Multiplying Eq. 4.65 by $Y^*_{n'm'}$ and inserting $r_N = R$, then integrating over a unit sphere we obtain

$$n(n+1)\frac{a^N_{nm}}{R}\left(j_n(kR) + \Lambda^N_n y_n(kR)\right) = -nB^e_{nm} + (n+1)B^i_{nm} \tag{4.67}$$

with $n = n'$. Multiplying Eq. 4.66 by $Y^{\star *}_{n'm'} \sin^2\theta$ and inserting $r_N = R$, then integrating over a unit sphere we obtain

$$\frac{a^N_{nm}}{R}\left(j^\star_n(kR) + \Lambda^N_n y^\star_n(kR)\right) = -B^e_{nm} - B^i_{nm}, \tag{4.68}$$

again with $n = n'$. If the interior boundaries are all spherically symmetric as well, Λ^N_n may be derived from the recursion relation (Eq. 4.58) using the desired interior layer model.

Eliminating a^N_{nm} as in the internal boundary conditions, we can solve for the unknown B^i_{nm} in terms of B^e_{nm}. In this spherically symmetric case, the solution is

$$B^i_{nm} = \frac{n}{n+1}\frac{\beta^N_n + \Lambda^N_n \gamma^N_n}{\delta^N_n + \Lambda^N_n \epsilon^N_n} B^e_{nm} \tag{4.69}$$

with

$$\beta_n^N \equiv j_n^{\star N} - (n+1) j_n^N \qquad = -kRj_{n+1}(kR) \tag{4.70}$$

$$\gamma_n^N \equiv y_n^{\star N} - (n+1) y_n^N \qquad = -kRy_{n+1}(kR) \tag{4.71}$$

$$\delta_n^N \equiv n j_n^N + j_n^{\star N} \qquad = kRj_{n-1}(kR) \tag{4.72}$$

$$\epsilon_n^N \equiv n y_n^N + y_n^{\star N} \qquad = kRy_{n-1}(kR), \tag{4.73}$$

$$j_n^N \equiv j_n(kR), \quad etc. \tag{4.74}$$

Our notation here differs slightly from that of Parkinson (1983), in that we factor out $n/(n+1)$ from the other terms in Eq. 4.69. This change allows us to readily make comparisons to the response of a perfectly conducting ocean. We collect the remaining parameters into another quantity, the complex response amplitude $\mathcal{A}_n^e$:

$$\mathcal{A}_n^e \equiv \frac{\beta_n^N + \Lambda_n^N \gamma_n^N}{\delta_n^N + \Lambda_n^N \epsilon_n^N} \qquad = -\frac{j_{n+1}(kR) + \Lambda_n^N y_{n+1}(kR)}{j_{n-1}(kR) + \Lambda_n^N y_{n-1}(kR)}, \tag{4.75}$$

so that

$$B_{nm}^i = \frac{n}{n+1} \mathcal{A}_n^e B_{nm}^e \tag{4.76}$$

describes the magnetic field induced by the body. Eq. 4.76 gives the primary response to the excitation field. The results of this work all represent perturbations to the spherically symmetric case; as a consequence, the complex response amplitude $\mathcal{A}_n^e$ appears in each result. At large $|kr|$, $\mathcal{A}_n^e$ is asymptotic to $(1+0i)$ for all n. $\mathcal{A}_n^e$ is independent of m, a result that will also hold in the asymmetric case, though the form of Eq. 4.76 will change.

In the commonly studied case of a uniform excitation field, with $n = 1$, $\mathcal{A}_n^e$ may be expressed in terms of the real amplitude A and phase delay ϕ (*e.g.* as defined by Zimmer et al., 2000):

$$\mathcal{A}_1^e = Ae^{-i\phi}, \tag{4.77}$$

allowing for ready comparison with prior work. Eq. 4.75 may therefore be used with a proposed layered structure model to easily calculate the response amplitude and phase delay in the case of

spherical symmetry. Python programs we created for this purpose are provided as Supplemental Material.

Note that the negative exponent in Eq. 4.77 results from our definition of k in Eq. 4.26, as described further in Section 4.6.1. As a consequence of the error in the Parkinson (1983) derivation, both our input wavenumber k and our result for the complex response amplitude $\mathcal{A}$ are equal to the complex conjugate of the analogous quantities from prior work, hence the negative exponent in Eq. 4.77. We define the relationship between $\mathcal{A}_1^e$, A, and ϕ as in Eq. 4.77 to facilitate comparison with the rich set of prior work related to this topic.

4.6.5 Near-spherical boundary shapes

We must now define surfaces $r_l(\theta, \phi)$ for near-spherical boundaries that we will insert into the internal and external boundary condition equations. Expanding each surface in spherical harmonics allows us to make use of relations well-known from problems involving addition of angular momenta from quantum mechanics, which we need because we will be multiplying harmonics together. We therefore choose boundary surfaces of the form

$$r_l(\theta, \phi) = \bar{r}_l + \varepsilon_l \sum_{p,q} \chi_{pq}^l Y_{pq}(\theta, \phi). \tag{4.78}$$

$\bar{r}_l$ is the mean radius of boundary l, ε_l is the amplitude of deviation from spherical symmetry, χ_{pq}^l is a dimensionless constant that indicates the relative amount of each harmonic represented in the boundary surface, and Y_{pq} are fully normalized spherical harmonics of degree p and order q. We use the index l to indicate that this surface describes the outer boundary of the lower region.

Surfaces described by Eq. 4.78 are near-spherical in that we make the approximation $\varepsilon_l \ll \bar{r}_l$ for all l. Equivalently, $\varepsilon_l / \bar{r}_l \ll 1$, and we retain terms up to first order in $\varepsilon_l / \bar{r}_l$ only. This approximation enables us to use a Taylor expansion in the boundary conditions that truncates quickly, adding only one term containing a product of two spherical harmonics. A product of spherical harmonics may be expressed as a linear combination of different harmonics (Wigner, 1931; Condon and Shortley, 1951). The multiplication of harmonics therefore results in "mixing" of harmonics in the excitation

field from $n = 1$ into other n, so a uniform excitation field induces magnetic moments of quadrupole order or higher for this shape, in addition to altering the original dipole moments.

Taylor expansion of boundary shapes

Let us now insert our near-spherical r_l into the expressions for the magnetic field in Eqs. 4.47–4.52. To first order, a Taylor expansion of a function $f(r)$ about r_l has terms

$$f(r_l) \approx f(\bar{r}_l) + (r_l - \bar{r}_l)\frac{\partial f(r)}{\partial r}\Big|_{r=\bar{r}_l} = f(\bar{r}_l) + \varepsilon_l\Big[\sum_{p,q}\chi^l_{pq}Y_{pq}(\theta,\phi)\Big]\frac{\partial f(r)}{\partial r}\Big|_{r=\bar{r}_l}. \tag{4.79}$$

The r^n power series that multiply B^e_{nm} and B^i_{nm} in Eqs. 4.47–4.49 then have the form

$$r_l^n \approx \bar{r}_l^n\left(1 + n\frac{\varepsilon_l}{\bar{r}_l}\sum_{p,q}\chi^l_{pq}Y_{pq}\right). \tag{4.80}$$

The interior field terms in Eqs. 4.50–4.52 become

$$\begin{aligned}\frac{j_n(kr_l) + \Lambda^l_{nm}y_n(kr_l)}{r_l} \approx \frac{1}{\bar{r}_l}\Bigg(&j_n(k\bar{r}_l) + \Lambda^l_{nm}y_n(k\bar{r}_l) \\ &+\frac{\varepsilon_l}{\bar{r}_l}\Big[\sum_{p,q}\chi^l_{pq}Y_{pq}\Big]\Big[j_n^\star(k\bar{r}_l) + \Lambda^l_{nm}y_n^\star(k\bar{r}_l) - 2\big(j_n(k\bar{r}_l) + \Lambda^l_{nm}y_n(k\bar{r}_l)\big)\Big]\Bigg)\end{aligned} \tag{4.81}$$

and

$$\begin{aligned}\frac{j_n^\star(kr_l) + \Lambda^l_{nm}y_n^\star(kr_l)}{r_l} \approx \frac{1}{\bar{r}_l}\Bigg(&j_n^\star(k\bar{r}_l) + \Lambda^l_{nm}y_n^\star(k\bar{r}_l) \\ &+\frac{\varepsilon_l}{\bar{r}_l}\Big[\sum_{p,q}\chi^l_{pq}Y_{pq}\Big]\Big[\big(j_n(k\bar{r}_l) + \Lambda^l_{nm}y_n(k\bar{r}_l)\big)\big(n(n+1) - k^2\bar{r}_l^2\big) - \big(j_n^\star(k\bar{r}_l) + \Lambda^l_{nm}y_n^\star(k\bar{r}_l)\big)\Big]\Bigg),\end{aligned} \tag{4.82}$$

where k may correspond to that above or below the boundary (consistent throughout the expression), except at the outer boundary where all k take the value of the top conducting layer k_N. With the above expressions, we can now evaluate both the internal and external boundary conditions at the perturbed, near-spherical boundaries between layers.

Products of spherical harmonics

The final piece required to express the internal and external boundary conditions in our method is to convert the products of spherical harmonics that result from the Taylor expansion into sums of

other harmonics. We wish to express

$$Y_{nm}Y_{pq} = \sum_{n',m'} \Xi^{n'm'}_{nmpq} Y_{n'm'}, \tag{4.83}$$

allowing us to replace these products where they appear so that we may retrieve the resulting magnetic moments through orthogonality of the spherical harmonics. Ξ are constant coefficients with subscripts indicating the input excitation harmonic n, m, the boundary shape harmonic p, q, and the output expansion harmonic n', m'. We also desire a similar expression for the analogous $\Xi^\star$ that will allow us to replace $Y^\star_{nm}Y_{pq}$, but it cannot be expressed as simply (see Section 4.6.5). Using fully normalized spherical harmonics Y that incorporate the Condon–Shortley phase, $\Xi^{n'm'}_{nmpq}$ are the Clebsch–Gordan coefficients. Ultimately, we will multiply by $Y^*_{n'm'}$ or $Y^{\star *}_{n'm'} \sin^2\theta$ and integrate over a unit sphere; with this intent in mind, we will express Ξ in terms of the Wigner $3j$-symbols $\begin{pmatrix} j & \ell & J \\ m & n & M \end{pmatrix}$, which are proportional to the Clebsch–Gordan coefficients. The $3j$-symbols satisfy the useful identity

$$\int_0^{2\pi}\int_0^{\pi} Y_{nm}Y_{pq}Y_{n'm'} \sin\theta d\theta d\phi = \sqrt{\frac{(2n+1)(2p+1)(2n'+1)}{4\pi}} \begin{pmatrix} n & p & n' \\ 0 & 0 & 0 \end{pmatrix} \begin{pmatrix} n & p & n' \\ m & q & -m' \end{pmatrix}, \tag{4.84}$$

which follows from a related identity from Brink and Satchler (1968):

$$\int_0^{2\pi}\int_0^{\pi} (-1)^{m\delta_{m|m|}} P_{nm} e^{im\phi} \, (-1)^{m\delta_{q|q|}} P_{pq} e^{iq\phi} \, (-1)^{m\delta_{m'|m'|}} P_{n'm'} e^{im'\phi} \sin\theta d\theta d\phi = 4\pi \begin{pmatrix} n & p & n' \\ 0 & 0 & 0 \end{pmatrix} \begin{pmatrix} n & p & n' \\ m & q & m' \end{pmatrix}, \tag{4.85}$$

where P_{nm} are associated Legendre functions in the Schmidt normalization, without the Condon–Shortley phase. The general expression for the Wigner $3j$-symbols is given in Section 4.10. The selection rules, which dictate the combinations of harmonics yielding non-zero terms, are summarized as follows (Brink and Satchler, 1968):

- $|n - p| \leq n' \leq n + p$, often called the "triangular condition."
- $m' = -(m + q)$. The general expression for the $3j$-symbols is unchanged under $m' \to -m'$ (see Eq. 4.116). From Eq. 4.43, we see that Eq. 4.84 is unchanged if we replace $Y_{n'm'}$ with

$(-1)^{m'} Y^*_{n',-m'}$. We therefore use the selection rule $m' = m + q$ for clarity in our derivation and negate m' in the final $3j$-symbol, as we have done in Eq. 4.84.

- When $m = q = m' = 0$, the $3j$-symbols are non-zero only if $n + p + n'$ is even. Therefore, only $n' = n + p,\ n + p - 2,\ n + p - 4,\ \ldots\ |n - p|$ give nonzero terms.

The results of the integration in each of Eqs. 4.84 and 4.85 are proportional to $\begin{pmatrix} n & p & n' \\ 0 & 0 & 0 \end{pmatrix}$, so all products are subject to all of these conditions.

Finally, we now obtain a direct expression for the product coefficients $\Xi^{n'm'}_{nmpq}$ to replace the products $Y_{nm} Y_{pq}$ in the radial boundary conditions. Multiplying both sides of Eq. 4.83 by $Y^*_{n'm'}$ and integrating over a unit sphere, we obtain

$$\Xi^{n'm'}_{nmpq} = (-1)^{m'} \sqrt{\frac{(2n+1)(2p+1)(2n'+1)}{4\pi}} \begin{pmatrix} n & p & n' \\ 0 & 0 & 0 \end{pmatrix} \begin{pmatrix} n & p & n' \\ m & q & -m' \end{pmatrix} \tag{4.86}$$

$$\text{for} \quad |n-p| \le n' \le n+p, \quad n+p+n' \text{ is even}, \quad \text{and} \quad m' = m+q,$$

$$\Xi^{n'm'}_{nmpq} = 0 \quad \text{otherwise.} \tag{4.87}$$

Using the selection rules and the expressions in Eqs. 4.116 and 4.117, we can derive an explicit formula for the nonzero terms in $\Xi^{n'm'}_{nmpq}$ (see Eq. 4.120):

$$\Xi^{n'm'}_{nmpq} = (-1)^{\nu} \sqrt{\frac{(2n+1)(2p+1)(2n'+1)\,(n'+m')!(n'-m')!}{4\pi\,(n+m)!(n-m)!(p+q)!(p-q)!}} \quad \times \tag{4.88}$$

$$\frac{(n+p-\nu)!}{\nu!(n-\nu)!(p-\nu)!} \, \frac{(2n-2\nu)!(2p-2\nu)!}{(2n'+1+2\nu)!} \quad \times$$

$$\sum_{\kappa=\kappa^-}^{\kappa^+} \frac{(-1)^{\kappa}(2\nu)!}{\kappa!(2\nu-\kappa)!} \, \frac{(n+m)!(n-m)!(p+q)!(p-q)!}{\big(n+m-(2\nu-\kappa)\big)!\big(n-m-\kappa\big)!\big(p+q-\kappa\big)!\big(p-q-(2\nu-\kappa)\big)!}$$

for $\nu = \frac{1}{2}(n+p-n')$, $\kappa^- = \max(0,\ 2\nu - (n+m),\ 2\nu - (p-q))$, and $\kappa^+ = \min(2\nu,\ n-m,\ p+q)$. These expressions allow us to use the replacement rule $Y_{nm} Y_{pq} \to \sum_{n',m',p,q} \Xi^{n'm'}_{nmpq}$.

We also require a similar expression that allows us to make the same replacement for the products $Y^\star_{nm} Y_{pq}$ in the tangential boundary conditions. Although we are able to make this replacement owing to separability of the linear equations, lack of orthogonality in $Y^\star_{nm}$ results in an extremely

complicated expression for $\Xi^{\star\, n'm'}_{nmpq}$. A finite expression may nevertheless be obtained under the condition that we assume a maximum n in the excitation field $n_{\max}$ and a maximum p in the boundary shape $p_{\max}$. For $n > n_{\max}$, $B^e_{nm} = 0$ and for $p > p_{\max}$, $\chi^l_{pq} = 0$, so the sums over these indices truncate.

From Eqs. 4.44, 4.84, and 4.86, we obtain

$$\int_0^{2\pi}\int_0^{\pi} Y^{\star}_{nm} Y_{pq} Y^{\star *}_{n'm'} \sin^3\theta d\theta d\phi = \Xi^{w}_{n'} \tag{4.89}$$

$$\Xi^{w}_{n'} \equiv w^{-}_{nm} w^{-}_{n'm'} \Xi^{n'-1\, m'}_{n-1\, mpq} + w^{+}_{nm} w^{+}_{n'm'} \Xi^{n'+1\, m'}_{n+1\, mpq} - w^{-}_{nm} w^{+}_{n'm'} \Xi^{n'+1\, m'}_{n-1\, mpq} - w^{+}_{nm} w^{-}_{n'm'} \Xi^{n'-1\, m'}_{n+1\, mpq}, \tag{4.90}$$

where $w^{\pm}_{nm}$ are defined in Eq. 4.45. We have defined $\Xi^{w}_{n'}$ for compactness of notation; n' is the only index which varies for this quantity in subsequent expressions, although all other indices n, m, p, q, m' are implied and required to evaluate it. This quantity roughly represents the amount of overlap between the product $Y^{\star}_{nm} Y_{pq}$ and the desired harmonic $Y^{\star}_{n'm'}$.

To next express $\Xi^{\star\, n'm'}_{nmpq}$ compactly, we must also define the following quantities, which are continued fractions:

$$F^{\pm}_{n,2\kappa} \equiv \frac{w^{\pm}_{n\pm 2\kappa} w^{\mp}_{n\pm(2\kappa+2)}}{\left(w^{-}_{n\pm(2\kappa+2)}\right)^2 + \left(w^{+}_{n\pm(2\kappa+2)}\right)^2 - w^{\pm}_{n\pm(2\kappa+2)} w^{\mp}_{n\pm(2\kappa+4)} F^{\pm}_{n,2\kappa+2}}, \tag{4.91}$$

where $2\kappa = 0, 2, 4, \ldots$ and a subscript m is implied on all w. The recursion in $F^{-}_{n,2\kappa}$ continues until 2κ exceeds $n - |m| - 2$ and the recursion in $F^{+}_{n,2\kappa}$ continues until 2κ exceeds $n_{\max} + p_{\max} - n$. When 2κ exceeds these respective values, $F^{\pm}_{n,2\kappa} = 0$. $F^{-}_{n,2\kappa}$ is also zero for $n < 3$ because there are no $Y^{\star}_{n'm'}$ below $n = 2$ that can mix into $n = 2$, and the same is true for $n = 1$. These bounding values result from non-orthogonality of the $Y^{\star}_{nm}$. For a term of degree n'' below the considered value n', non-orthogonality is possible only for $n'' = n' - 2, n' - 4$, *etc.*, but $Y^{\star}_{n''m''}$ is defined and non-zero only for $n'' > 0$ and $n'' \geq m''$. This constraint limits the non-zero values of $F^{-}_{n',0}$ to $n' \geq 3$ and $n' \geq m' + 2$. The n'' above the considered n' that yield non-orthogonal terms are similarly limited by the selection rules for $\Xi^{n'm'}_{nmpq}$, *i.e.* n'' cannot exceed $n_{\max} + p_{\max}$ because no combination of $Y^{\star}_{nm} Y_{pq} \rightarrow \Xi^{\star\, n'm'}_{nmpq} Y^{\star}_{n'm'}$ results in $n' > n_{\max} + p_{\max}$ and we have assumed the series in n' may be truncated at $n'_{\max} = n_{\max} + p_{\max}$.

We obtain solvable linear equations by multiplying both sides of the tangential boundary condition equations (Eqs. 4.54 and 4.66) by $Y^{\star *}_{n'm'} \sin^2\theta$, then integrating over a unit sphere. Solving the resulting equations for the terms initially proportional to $Y^{\star}_{n'm'}$, we finally obtain the replacement rule $Y^{\star}_{nm} Y_{pq} \rightarrow \sum_{n',m',p,q} \Xi^{\star\, n'm'}_{nmpq}$, with

$$\Xi^{\star\, n'm'}_{nmpq} = \frac{\Xi^{w}_{n'} + \sum_{\nu=1}^{g^{-}_{\max}} \Xi^{w}_{n'-2\nu} \prod_{\kappa=0}^{\nu-1} F^{-}_{n',2\kappa} + \sum_{\nu=1}^{g^{+}_{\max}} \Xi^{w}_{n'+2\nu} \prod_{\kappa=0}^{\nu-1} F^{+}_{n',2\kappa}}{\left(w^{-}_{n'}\right)^2 + \left(w^{+}_{n'}\right)^2 - w^{-}_{n'} w^{+}_{n'-2} F^{-}_{n',0} - w^{+}_{n'} w^{-}_{n'+2} F^{+}_{n',0}}, \tag{4.92}$$

$$g^{-}_{\max} \equiv \begin{cases} \mathrm{floor}\left(\frac{1}{2}\left(n' - |m'|\right)\right) & \text{if } n' \geq 3 \\ 0 & \text{otherwise} \end{cases}, \quad g^{+}_{\max} \equiv \mathrm{floor}\left(\frac{1}{2}\left(n_{\max} + p_{\max} - n'\right)\right), \tag{4.93}$$

where $\mathrm{floor}(a)$ is the nearest integer less than or equal to a.

Consequences of non-orthogonality of $Y^{\star}_{nm}$

In our previous work (Styczinski and Harnett, 2021), based on several considered cases we assumed that certain linear combinations of the $Y^{\star}_{nm}$ could be made mutually orthogonal. Although this assumption seems to be true when the shape harmonics Y_{pq} are limited to $p_{\max} = 2$, in this work we have endeavored to find a more general solution that may be applied to all $Y^{\star}_{nm}$ and for any $p_{\max}$. The primary consequence of non-orthogonality of the $Y^{\star}_{nm}$ is coupling between the boundary condition equations. This coupling is why $\Xi^{\star\, n'm'}_{nmpq}$ is not equal to $\Xi^{w}_{n'}$, and may be non-zero for any allowed n' and m' that differ from $(n + p)$ by an even integer. The end result is that some harmonics in the near-spherical boundaries can produce induced moments with high degree n'. For example, for a boundary surface containing harmonics up to degree $p_{\max} = 8$, as we consider in our Miranda model in Section 4.3.2, the Y_{21} boundary harmonic combines with the Y_{11} excitation harmonic to produce induced moments of degree $n' = 1$, 3, 5, 7, and 9. In this work, though we calculate all of the induced magnetic moments, we only plot the magnetic fields for n' up to 4, as the induced moments are already negligible at that degree, and the fields from these moments also shrink faster with distance from the body. Although the induced fields from the high-degree moments are likely to be small at spacecraft distances, they are nevertheless predicted by our model, a direct result from the non-orthogonality of the $Y^{\star}_{nm}$.

4.6.6 *Boundary conditions with a near-spherical boundary shape*

Solving all the boundary conditions with near-spherical boundaries relies on simultaneous Taylor expansions of each boundary. For clarity in the end solution, we will now exchange the arbitrary indices n and n', so that n' refers to the "input" harmonics pertaining to the excitation field and n refers to the "output" harmonics that index the induced magnetic moments. We must also now use $b_{nm} = a_{nm}\Lambda_{nm}$ for the asymmetric layer coefficients, as a solution cannot be obtained otherwise. The procedures described in Section 4.6.5 result in the following boundary conditions for asymmetric bodies:

$$
\begin{aligned}
&B_{r,\text{int}}: \\
&\quad n(n+1)\left(a^l_{nm} j^{l,l}_n + b^l_{nm} y^{l,l}_n\right) + \\
&\qquad \sum_{n',m',p,q} \frac{\varepsilon_l \chi^l_{pq}}{\bar{r}_l} \Xi^{nm}_{n'm'pq}\, n'(n'+1) a^l_{n'm'} \left((j^{\star l,l}_{n'} + \Lambda^l_{n'} y^{\star l,l}_{n'}) - 2(j^{l,l}_{n'} + \Lambda^l_{n'} y^{l,l}_{n'})\right) = \\
&\quad n(n+1)\left(a^u_{nm} j^{u,l}_n + b^u_{nm} y^{u,l}_n\right) + \\
&\qquad \sum_{n',m',p,q} \frac{\varepsilon_l \chi^l_{pq}}{\bar{r}_l} \Xi^{nm}_{n'm'pq}\, n'(n'+1) a^u_{n'm'} \left((j^{\star u,l}_{n'} + \Lambda^u_{n'} y^{\star u,l}_{n'}) - 2(j^{u,l}_{n'} + \Lambda^u_{n'} y^{u,l}_{n'})\right)
\end{aligned}
\tag{4.94}
$$

$$
\begin{aligned}
&B_{\theta,\text{int}}: \\
&\quad a^l_{nm} j^{\star l,l}_n + b^l_{nm} y^{\star l,l}_n + \\
&\qquad \sum_{n',m',p,q} \frac{\varepsilon_l \chi^l_{pq}}{\bar{r}_l} \Xi^{\star\, nm}_{n'm'pq}\, a^l_{n'm'} \left((n'(n'+1) - k^2_l \bar{r}^2_l)(j^{l,l}_{n'} + \Lambda^l_{n'} y^{l,l}_{n'}) - (j^{\star l,l}_{n'} + \Lambda^l_{n'} y^{\star l,l}_{n'})\right) = \\
&\quad a^u_{nm} j^{\star u,l}_n + b^u_{nm} y^{\star u,l}_n + \\
&\qquad \sum_{n',m',p,q} \frac{\varepsilon_l \chi^l_{pq}}{\bar{r}_l} \Xi^{\star\, nm}_{n'm'pq}\, a^u_{n'm'} \left((n'(n'+1) - k^2_u \bar{r}^2_l)(j^{u,l}_{n'} + \Lambda^u_{n'} y^{u,l}_{n'}) - (j^{\star u,l}_{n'} + \Lambda^u_{n'} y^{\star u,l}_{n'})\right)
\end{aligned}
\tag{4.95}
$$

$B_{r,\text{ext}}$: (4.96)

$$\frac{n(n+1)}{R}\left(a^N_{nm}j^N_n + b^N_{nm}y^N_n\right) + \sum_{n',m',p,q}\frac{\varepsilon_N\chi^N_{pq}}{R}\Xi^{nm}_{n'm'pq}\frac{n'(n'+1)}{R}a^N_{n'm'}\left((j^{\star N}_{n'} + \Lambda^N_{n'}y^{\star N}_{n'}) - 2(j^N_{n'} + \Lambda^N_{n'}y^N_{n'})\right) =$$

$$-nB^e_{nm} + (n+1)B^i_{nm} + \sum_{n',m',p,q}\frac{\varepsilon_N\chi^N_{pq}}{R}\Xi^{nm}_{n'm'pq}\left(-n'(n'-1)B^e_{n'm'} - (n'+1)(n'+2)B^i_{n'm'}\right)$$

$B_{\theta,\text{ext}}$: (4.97)

$$\frac{1}{R}\left(a^N_{nm}j^{\star N}_n + b^N_{nm}y^{\star N}_n\right) + \sum_{n',m',p,q}\frac{\varepsilon_N\chi^N_{pq}}{R}\Xi^{\star\,nm}_{n'm'pq}\frac{a^N_{n'm'}}{R}\left((n'(n'+1) - k^2R^2)(j^N_{n'} + \Lambda^N_{n'}y^N_{n'}) - (j^{\star N}_{n'} + \Lambda^N_{n'}y^{\star N}_{n'})\right) =$$

$$-B^e_{nm} - B^i_{nm} + \sum_{n',m',p,q}\frac{\varepsilon_N\chi^N_{pq}}{R}\Xi^{\star\,nm}_{n'm'pq}\left(-(n'-1)B^e_{n'm'} + (n'+2)B^i_{n'm'}\right).$$

The new terms are all contained within the series in each equation. Because these terms are all multiplied by a factor ε_l/r_l, we can insert the spherically symmetric solutions for every constant within the series, since we assume terms to second order in ε_l/r_l are negligible. Inserting expressions from Eqs. 4.55 and 4.69, we find that every single term within the series in the radial boundary conditions has a matching term on both sides, and so they all cancel. In the tangential equations, the only terms that survive are those that multiply an additional factor of k because it is different above and below the boundary. Thus, the boundary condition equations reduce to:

$$a^l_{nm}j^{l,l}_n + b^l_{nm}y^{l,l}_n = a^u_{nm}j^{u,l}_n + b^u_{nm}y^{u,l}_n \tag{4.98}$$

$$a^l_{nm}j^{\star l,l}_n + b^l_{nm}y^{\star l,l}_n = a^u_{nm}j^{\star u,l}_n + b^u_{nm}y^{\star u,l}_n + \sum_{n',m',p,q}\frac{\varepsilon_l\chi^l_{pq}}{\bar{r}_l}\Xi^{\star\,nm}_{n'm'pq}\,\bar{a}^l_{n'm'}\left(j^{l,l}_{n'} + \Lambda^l_{n'}y^{l,l}_{n'}\right)\left(k^2_l r^2_l - k^2_u r^2_l\right) \tag{4.99}$$

$$\frac{n(n+1)}{R}\left(a^N_{nm}j^N_n + b^N_{nm}y^N_n\right) = -nB^e_{nm} + (n+1)B^i_{nm} \tag{4.100}$$

$$\frac{1}{R}\left(a^N_{nm}j^{\star N}_n + b^N_{nm}y^{\star N}_n\right) = -B^e_{nm} - B^i_{nm} + \sum_{n',m',p,q}\frac{\varepsilon_N\chi^N_{pq}}{R}\Xi^{\star\,nm}_{n'm'pq}\,\frac{2n'+1}{n'+1}B^e_{n'm'}\,\frac{\xi^N_{n'} + \Lambda^N_{n'}\rho^N_{n'}}{\delta^N_{n'} + \Lambda^N_n\epsilon^N_{n'}}, \tag{4.101}$$

with

$$\xi^N_{n'} \equiv -(kR)^2 j_n(kR) \tag{4.102}$$

$$\rho^N_{n'} \equiv -(kR)^2 y_n(kR), \tag{4.103}$$

and the bar over $\overline{a}^l_{n'm'}$ to indicate that it is identically the solution from the spherically symmetric case. The symmetric boundary condition equations give us

$$\overline{a}^{\mathrm{i}}_{nm} \equiv -\frac{2n+1}{n+1}\frac{RB^e_{nm}}{\delta^N_n + \Lambda^N_n \epsilon^N_n}\prod_{\mathrm{j=i+1}}^{N}\frac{j^{\mathrm{j,j-1}}_n + \Lambda^{\mathrm{j}}_n y^{\mathrm{j,j-1}}_n}{j^{\mathrm{j-1,j-1}}_n + \Lambda^{\mathrm{j-1}}_n y^{\mathrm{j-1,j-1}}_n}. \tag{4.104}$$

With these expressions, and recalling that $b^1_{nm} = 0$ for all n and m, Eqs. 4.98–4.101 are at last a solvable linear system of equations. Ultimately, for B^i_{nm} we obtain a solution

$$B^i_{nm} = \frac{n}{n+1}\mathcal{A}^e_n B^e_{nm} + n\sum_{\mathrm{i=1}}^{N}\mathcal{A}^{t,\mathrm{i}}_n K^{\mathrm{i}}_n \Delta^{\mathrm{i}}_{nm}, \tag{4.105}$$

where we have defined

$$\mathcal{A}^{t,\mathrm{i}}_n \equiv \frac{j^{\mathrm{i,i}}_n + \Lambda^{\mathrm{i}}_n y^{\mathrm{i,i}}_n}{\delta^N_n + \Lambda^N_n \epsilon^N_n}, \tag{4.106}$$

$$K^{\mathrm{i}}_n \equiv \prod_{\mathrm{j=i+1}}^{N}\frac{\alpha^{\mathrm{j,j}}_n}{\beta^{\mathrm{j,j-1}}_n + \Lambda^{\mathrm{j-1}}_n \gamma^{\mathrm{j,j-1}}_n}, \qquad K^N_n = 1, \tag{4.107}$$

$$\Delta^{\mathrm{i}}_{nm} \equiv \begin{cases} \displaystyle\sum_{n',m',p,q}\frac{\varepsilon_{\mathrm{i}}\chi^{\mathrm{i}}_{pq}}{\overline{r}_{\mathrm{i}}}\Xi^{\star\,nm}_{n'm'pq}\frac{\overline{a}^{\mathrm{i}}_{nm}}{R}\left(j^{\mathrm{i,i}}_{n'} + \Lambda^{\mathrm{i}}_{n'} y^{\mathrm{i,i}}_{n'}\right)\left(k^2_{\mathrm{i}}\overline{r}^2_{\mathrm{i}} - k^2_{\mathrm{i+1}}\overline{r}^2_{\mathrm{i}}\right) & \text{for i} < N, \\ \displaystyle\sum_{n',m',p,q}\frac{\varepsilon_N\chi^N_{pq}}{R}\Xi^{\star\,nm}_{n'm'pq}\frac{2n'+1}{n'+1}\mathcal{A}^\star_{n'}B^e_{n'm'} & \text{for i} = N, \end{cases} \tag{4.108}$$

$$\mathcal{A}^\star_{n'} \equiv \frac{\xi^N_{n'} + \Lambda^N_{n'}\rho^N_{n'}}{\delta^N_{n'} + \Lambda^N_{n'}\epsilon^N_{n'}}. \tag{4.109}$$

As with $\mathcal{A}^e_n$, the product $\mathcal{A}^{t,N}_n \mathcal{A}^\star_{n'}$ is asymptotic to $(1{+}0i)$ in the limit $|kR| \to \infty$ for all n and n'. Each of these complex amplitude quantities is labeled with a superscript to indicate their relationship to other relevant quantities: $\mathcal{A}^e$ multiplies the excitation field, $\mathcal{A}^t$ multiplies the tangential first-order term in the non-spherical expansion, and $\mathcal{A}^\star$ multiplies the mixing coefficients $\Xi^\star$. The radial first-order term that would multiply a quantity $\mathcal{A}^r$ analogous to $\mathcal{A}^t$ is identically zero, so it does not

appear. Eq. 4.105 is our final result, and may be used to evaluate the induced magnetic field for any arbitrary layered conducting body, so long as the near-spherical approximation holds for each boundary.

4.7 Table of interior structure parameters

In Table 4.1, we list the chosen bulk properties for the four satellites investigated here. The base PlanetProfile models assume spherical symmetry. The entire set of assumed parameters can be found in the Matlab files for the individual models, which can also be used to reproduce the models themselves.

Body	T_s (K)	R (km)	M (kg)	C/MR^2	Reference
Europa	110	1561.0	4.7991×10^{22}	0.346 ± 0.005	Anderson et al. (1998)
Callisto	110	2410.3	1.4819×10^{23}	0.3549 ± 0.0042	Anderson et al. (2001)
Miranda	60	235.8	6.4×10^{19}	0.346	Hussmann et al. (2006)
Triton	38	1353.4	2.14×10^{22}	0.315	Hussmann et al. (2006)

Table 4.1: Model parameters used to determine interior conductivity profiles using *PlanetProfile*. T_s: surface temperature; R: radius of body surface; M: total body mass; C/MR^2: axial coefficient of moment of inertia. Moments of inertia for Miranda and Triton are assumed for consistency with prior models, as no measurements are available. For Triton the value was increased by 0.005 for consistency with the model study of Cochrane et al. (2021).

4.8 Gravitational deformation in satellites; application to Europa

Tidal forces applied by gravity from the parent planet and centrifugal acceleration from spin rotation will deform satellites, primarily in the $p = 2$ spherical harmonic shapes (Rambaux and Castillo-Rogez, 2013). Anderson et al. (1998) used Doppler shifts available from precise radio tracking of *Galileo* by the Deep Space Network to infer the $p = 2$ gravity coefficients for Europa. These authors

favored best-fit values of $C_{20} = -435.5 \times 10^{-6}$, $C_{22} = 131.0 \times 10^{-6}$ from their analysis. Assuming the body is in hydrostatic equilibrium, these authors also found the axial moment of inertia for Europa to be approximately $C/MR^2 = 0.346$.

Under the assumption of hydrostatic equilibrium, the Radau–Darwin approximation allows us to relate the axial moment of inertia to the secular (non-time-varying) Love number k_f (Rambaux and Castillo-Rogez, 2013):

$$\frac{C}{MR^2} = \frac{2}{3}\left[1 - \frac{2}{5}\sqrt{\frac{4-k_f}{1+k_f}}\right]. \tag{4.110}$$

The fluid Love number $h_f = k_f + 1$. This quantity relates the gravitational tides to the geometric deformation of the body by (Rambaux and Castillo-Rogez, 2013; Hemingway and Mittal, 2019)

$$r_{\text{surf}}(\theta, \phi) = h_f \frac{V(\theta, \phi)}{g_{\text{surf}}}, \tag{4.111}$$

where r_{surf} is the shape of the body surface, V is the gravitational potential, and $g_{\text{surf}} = GM/R^2$ is the mean gravitational acceleration at the surface. At the surface of the body, the gravitational moments V_{pq} are proportional to the coefficients C_{pq} with a proportionality factor of GM/R (Rambaux and Castillo-Rogez, 2013). Inserting gravitational terms into Eq. 4.111, we arrive at the simple conversion

$$H_{pq} = h_f C_{pq} R, \tag{4.112}$$

where H are Schmidt semi-normalized spherical harmonic coefficients for the body surface shape—analogous to χ^N_{pq} (Eq. 4.78), but in a different normalization that matches the one in which the gravity coefficients are given. Eq. 4.112 will allow us to find the shape of the body surface as perturbed by tidal forces.

We can now determine the values to apply to Europa. Solving Eq. 4.110 for k_f and replacing with h_f, we obtain

$$h_f = 1 + \frac{4-u}{1+u}, \quad u \equiv \left[\frac{5}{2}\left(1 - \frac{3}{2}\frac{C}{MR^2}\right)\right]^2, \tag{4.113}$$

with $h_f = 2.044$ for Europa from $C/MR^2 = 0.346$ as determined by Anderson et al. (1998). Combining these results with Eq. 4.112 and the C_{20}, C_{22} gravity coefficients from Anderson et al.

(1998), we obtain Schmidt semi-normalized shape coefficients of

$$H_{20} = -1.390\,\mathrm{km}, \tag{4.114}$$

$$H_{22} = 0.418\,\mathrm{km}. \tag{4.115}$$

These values describe the equilibrium shape of the icy surface of Europa as perturbed by tides. In order to preserve the ice shell thickness estimates we model after Tobie et al. (2003), we apply the same gravitational shape perturbation to the surface and ocean layers, without scaling.

Although Enceladus also has a triaxial ellipsoid shape perturbed by gravity (Iess et al., 2014), we choose not to apply this analysis to our Enceladus-like interior for Miranda because gravity data are not yet available for Miranda. Thus, we limit our Miranda models to the asymmetry in the ice–ocean boundary.

4.9 Supplemental figures for example applications

In Figures 4.10–4.15, we include a full detailing of analysis products from example applications of our model to several ocean worlds in the solar system (described in Section 4.3). Blue–white contour maps show the asymmetry models applied for all example cases studied: asymmetric ice–ocean boundaries for Europa and Miranda and asymmetric ionospheres for Triton and Callisto. Heat maps show the magnitude of the induced magnetic field predicted for the asymmetric models. Some maps are repeated from the main text for completeness. Symmetric analog models have the same layer structure as the asymmetric models, and are evaluated using the standard recursion method of Srivastava (1966). Please refer to the main text (Section 4.3) for further details regarding the reasoning behind each model.

Red–blue and other colormaps show the difference in induced magnetic field between our model predictions for the asymmetric cases as compared to spherically symmetric analogs, for all magnetic field vector components and the magnitude. Vector components are in IAU coordinates, such that at 0° latitude, 0° longitude, the parent planet is directly overhead; this is a right-handed coordinate system, with east longitudes positive. This coordinate system is rotated approximately 90° from the $\phi\Omega$ ("Phi-O," *e.g.* E-Phi-O for Europa) coordinates sometimes used in analysis of spacecraft

data. All induced fields are evaluated at the J2000 reference epoch, 12:00 pm Jan 1, 2000 TDB and consider only the synodic period. Animations of the differences in magnitude and the B_x component throughout a synodic period are included for each model as Supplemental Material.

4.9.1 Europa — effect size with distance

It may be advantageous for future investigations to pursue modeling efforts that neglect asymmetry, or at least limit studied cases to only include known shapes (*i.e.* tidal deformation). To facilitate these efforts, we have evaluated the difference in the induced magnetic field resulting from asymmetry as a function of distance from Europa. Figure 4.16 shows the difference in induced field caused by asymmetry from our Europa Seawater model (Figure 4.10) from the surface upward to 2000 km altitude. We selected a time (0.7 hr after J2000) and surface point (see Figure 4.10c) at which the effect size is approximately maximized, with a difference at the surface of about 2.2 nT. The difference resulting from asymmetry drops to 0.2 nT at about 1 R_E in altitude, around 1500 km.

It may also be noted that the effect of asymmetry on the induced field can become small at key points in time during the considered excitation period. In Figure 4.17, we have extracted a single frame from our animation of the B_x difference for the Europa Seawater model available in the Supplemental Material. At the time shown—3.4 hr past J2000—only the 0 nT contour is plotted, meaning the difference is everywhere less than 0.6 nT. This condition lasts for about 4% of the synodic period, or about 30 minutes. If a spacecraft reaches its closest approach near this time, at a distance at or above 25 km, the difference contributed by the asymmetric ocean will be small. This implies that there may be some conditions (including particular asymmetry models) under which the induced field measured by the spacecraft is essentially the same as that predicted by a spherically symmetric model.

(a) Europa Seawater ice thickness (km), $\overline{D} = 22\,\mathrm{km}$

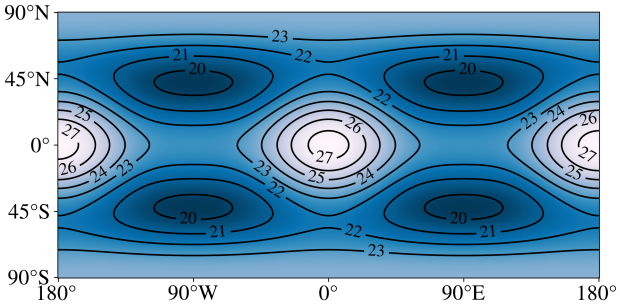

(b) Asymmetric model $|\mathbf{B}_{\mathrm{ind}}|$ (nT) at $r = 1.02R_E$

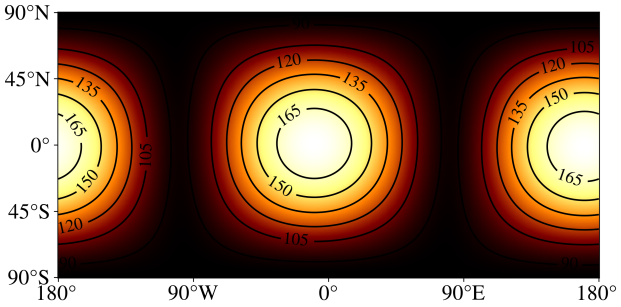

(c) B_x difference (nT) vs. symmetric at $r = 1.02R_E$

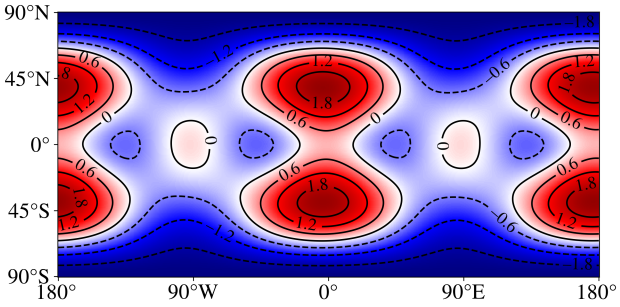

(d) $|\mathbf{B}_{\mathrm{ind}}|$ difference (nT) vs. symmetric at $r = 1.02R_E$

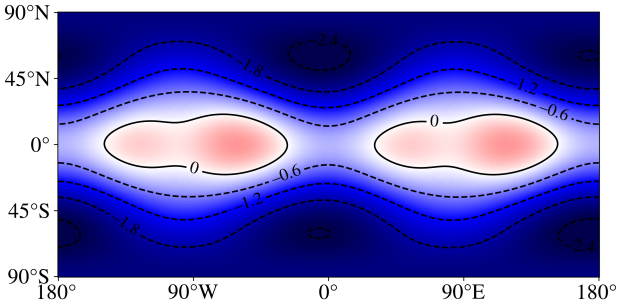

(e) B_y difference (nT) vs. symmetric at $r = 1.02R_E$

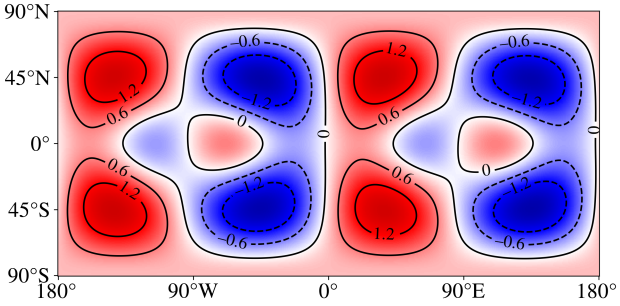

(f) B_z difference (nT) vs. symmetric at $r = 1.02R_E$

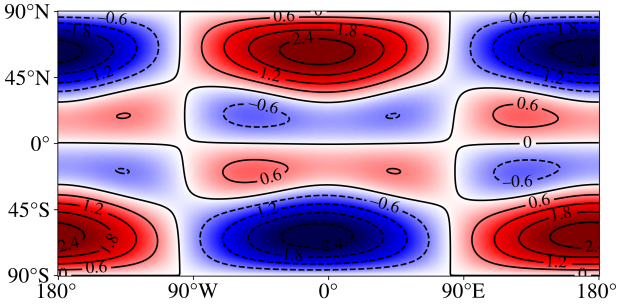

Figure 4.10: Caption appears on next page.

Figure 4.10: Europa model with an asymmetric ice–ocean boundary approximating the results of Tobie et al. (2003), whose analysis was based on modeling tidal heating and thermodynamics, and static gravity inferred by Anderson et al. (1998). Compare Figure 4.10a to Figure 12a of Tobie et al. (2003). Average ice shell thickness is 22.5 km. In this model, a Seawater composition is assumed for the ocean; conduction in the ionosphere is ignored. Electrical conductivities are calculated using the *PlanetProfile* geophysical modeling framework (Vance et al., 2021). Magnetic fields are evaluated at the J2000 epoch and at 25 km altitude, as the upcoming *Europa Clipper* mission plans several flybys of 25 km or less at closest approach. Only the synodic period is modeled here for simplicity. The difference in the magnetic field resulting from asymmetry is over 2 nT in some locations, and is likely to have a measurable influence on *Europa Clipper* investigations using data from these near flybys. The differences in induced field are not static but move and oscillate throughout the synodic period. Animations for the difference in x component and magnitude are included as Supplemental Material.

(a) Europa 10% Seawater ice thickness (km), $\overline{D}$ = 22 km

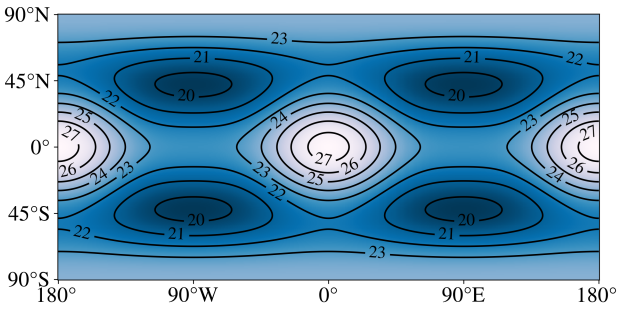

(b) Asymmetric model $|\mathbf{B}_{\text{ind}}|$ (nT) at $r = 1.02R_E$

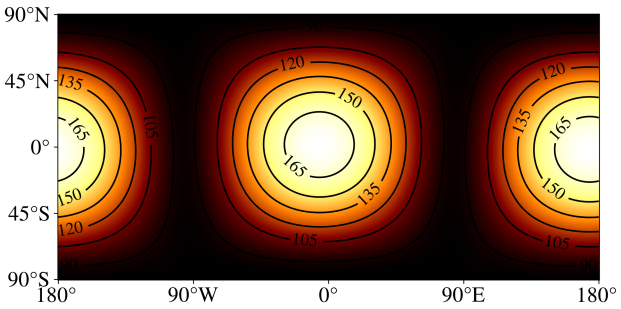

(c) B_x difference (nT) vs. symmetric at $r = 1.02R_E$

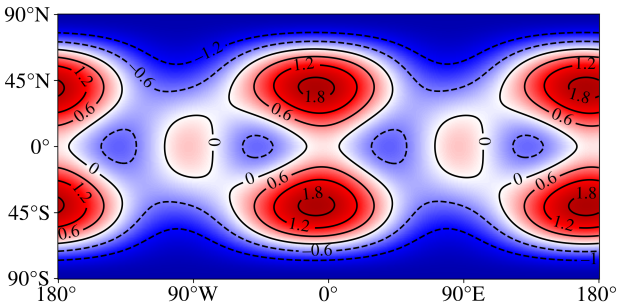

(d) $|\mathbf{B}_{\text{ind}}|$ difference (nT) vs. symmetric at $r = 1.02R_E$

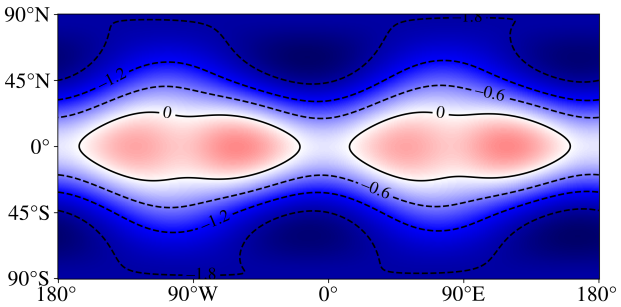

(e) B_y difference (nT) vs. symmetric at $r = 1.02R_E$

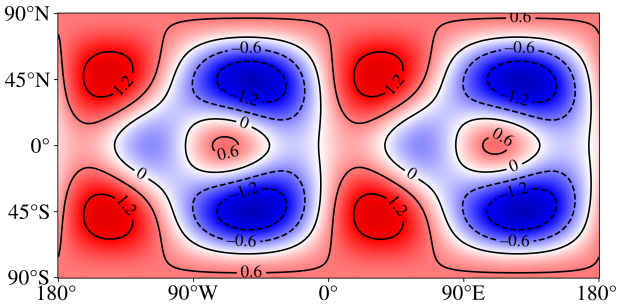

(f) B_z difference (nT) vs. symmetric at $r = 1.02R_E$

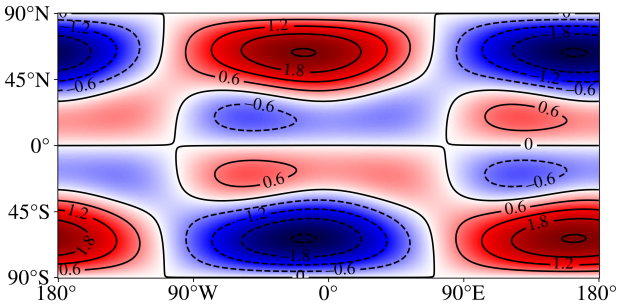

Figure 4.11: Caption appears on next page.

Figure 4.11: Europa model very similar to that in Figure 4.10 but with an ocean composition $1/10$ the salinity of Seawater. Magnetic fields are again evaluated at the J2000 epoch and at 25 km altitude. Comparison to Figure 4.10 shows smaller differences and a slight phase difference. However, the differences in the magnetic field resulting from asymmetry are still well over 1 nT in some places even in this lower-salinity case, a consequence of Europa's relatively large size. The colormaps and contours for the difference plots are fixed to match those of Figure 4.10. Animations for the difference in x component and magnitude as they vary throughout the synodic period are included as Supplemental Material.

(a) Europa comparison ice thickness (km), $\overline{D} = 22\,\mathrm{km}$

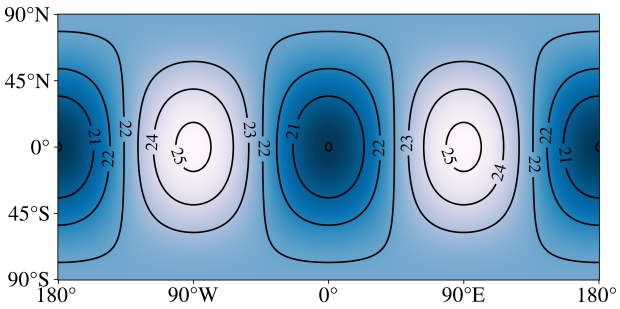

(b) Asymmetric model $|\mathbf{B}_{\mathrm{ind}}|$ (nT) at $r = R_E$

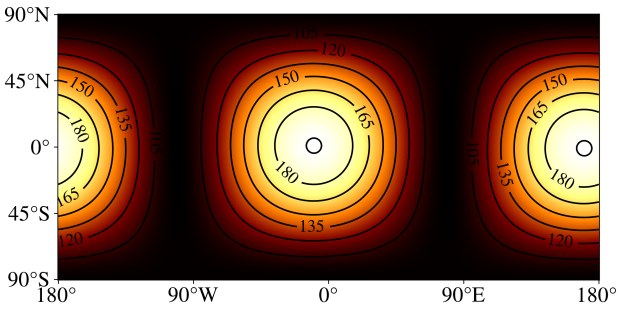

(c) B_x difference (nT) vs. symmetric at $r = R_E$

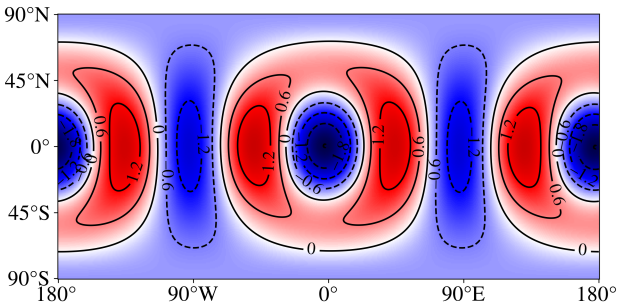

(d) $|\mathbf{B}_{\mathrm{ind}}|$ difference (nT) vs. symmetric at $r = R_E$

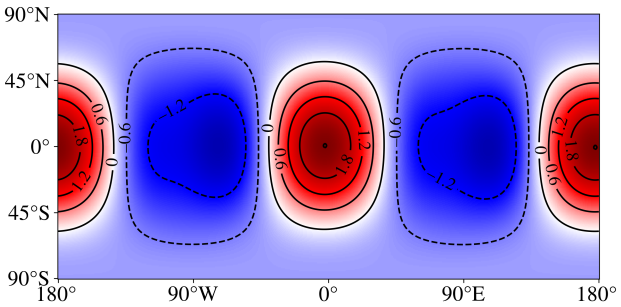

(e) B_y difference (nT) vs. symmetric at $r = R_E$

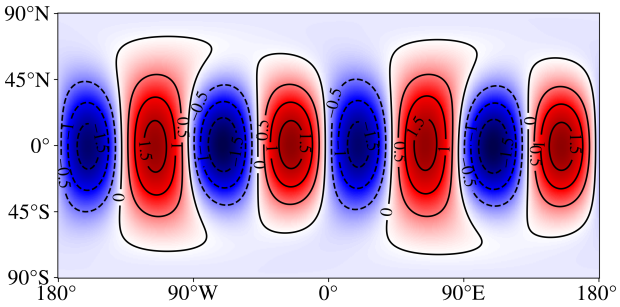

(f) B_z difference (nT) vs. symmetric at $r = R_E$

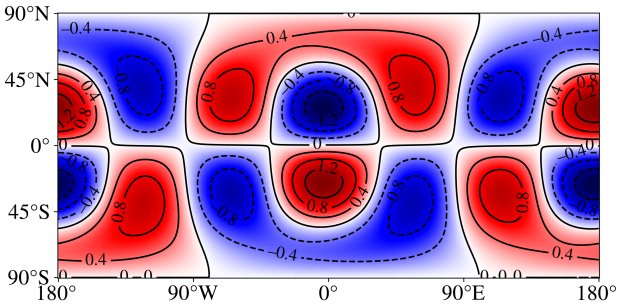

Figure 4.12: Caption appears on next page.

Figure 4.12: Simplified Europa model also based on the results of Tobie et al. (2003), but with only a single real harmonic represented in the boundary shape and with very high ocean conductivity. The asymmetry model is identical to that considered in our previous work (Styczinski and Harnett, 2021); in this case, the conductivity is very high ($2,750\,\mathrm{S/m}$) so that the result can be compared to the high-conductivity limit previously studied. Conduction in the ionosphere is ignored. Magnetic fields are evaluated at the J2000 epoch on the surface of Europa. For simplicity, only the synodic period is modeled here. As can be seen in the time series for $\boldsymbol{B}_x$ at the sub-jovian point plotted in Figure 4.5 (main text), the more rigorous model derived in this work predicts a larger difference compared to the spherically symmetric case, several times larger than our previous estimates. Animations for the difference in x component and magnitude as they vary throughout the synodic period are included as Supplemental Material.

(a) Miranda ice shell thickness (km), $\overline{D} = 50\,\mathrm{km}$

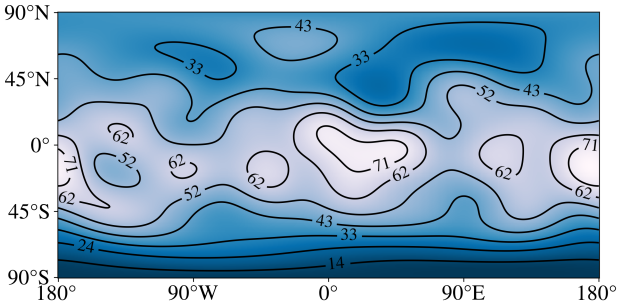

(b) Asymmetric model $|\mathbf{B}_{\mathrm{ind}}|$ (nT) at $r = 2R_M$

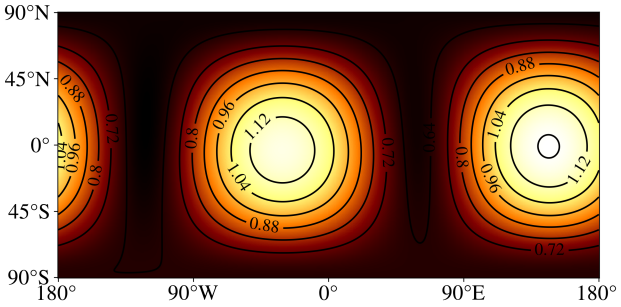

(c) B_x difference (nT) vs. symmetric at $r = 2R_M$

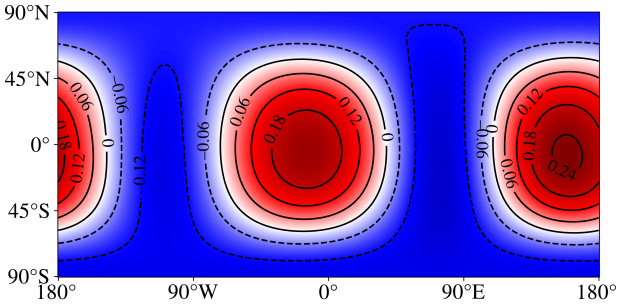

(d) $|\mathbf{B}_{\mathrm{ind}}|$ difference (nT) vs. symmetric at $r = 2R_M$

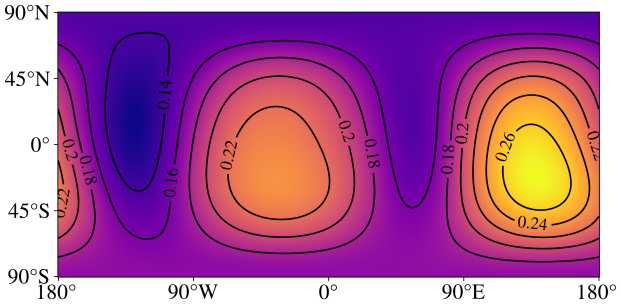

(e) B_y difference (nT) vs. symmetric at $r = 2R_M$

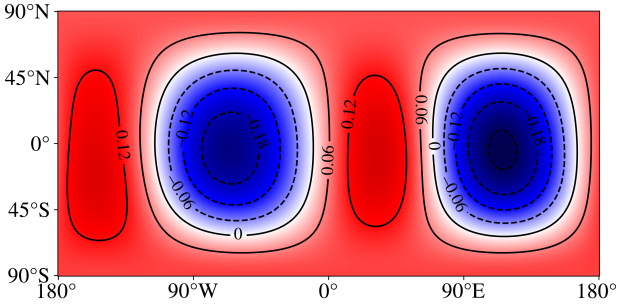

(f) B_z difference (nT) vs. symmetric at $r = 2R_M$

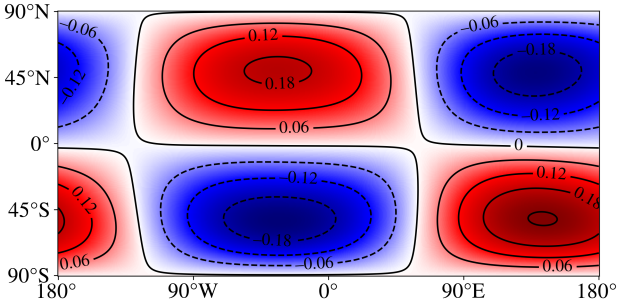

Figure 4.13: Caption appears on next page.

Figure 4.13: Miranda model with an ice–ocean boundary shape based on the asymmetric Enceladus ice shell inferred by Hemingway and Mittal (2019) from isostatic compensation and gravity measurements. The asymmetry in the ice shell has been scaled up from the 21 km average thickness model of Enceladus to the 50 km average thickness ice shell we suppose for Miranda, to serve as an upper limit of expected asymmetry in demonstrating application of our results. Enceladus model data are courtesy D. Hemingway; compare Figure 4.13a to Figure 11d of Hemingway and Mittal (2019). The difference in induced field magnitude relative to spherically symmetric is always positive because the largest change to the induced magnetic moments is in the dipole moment. More conducting ocean material is closer to the surface in the asymmetric model, enhancing the largest moments. Magnetic fields are evaluated at the J2000 epoch, this time at $r = 2R_M$, a plausible flyby altitude for a future mission to the Uranus system. A Seawater composition is assumed for the ocean, and a 100 km uniform ionosphere is assumed, with a total ionospheric conductance of 800 S based on comparison with the plasma environment of Callisto (Hartkorn and Saur, 2017). Electrical conductivities in the ocean are calculated using the *PlanetProfile* geophysical modeling framework (Vance et al., 2021). For simplicity, only the synodic period is modeled here. Animations for the difference in x component and magnitude as they vary throughout the synodic period are included as Supplemental Material.

(a) Callisto ionosphere thickness (km), $\overline{D} = 100\,\mathrm{km}$

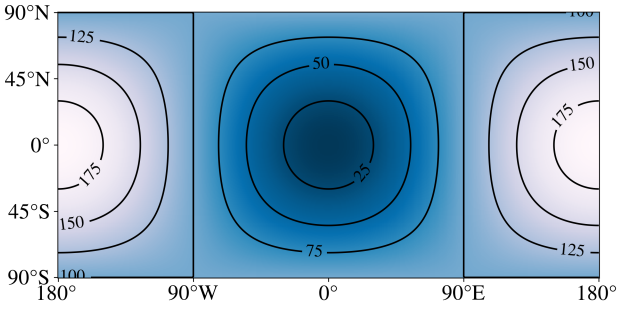

(b) Asymmetric model $|\mathbf{B}_{\mathrm{ind}}|$ (nT) at $r = 2R_C$

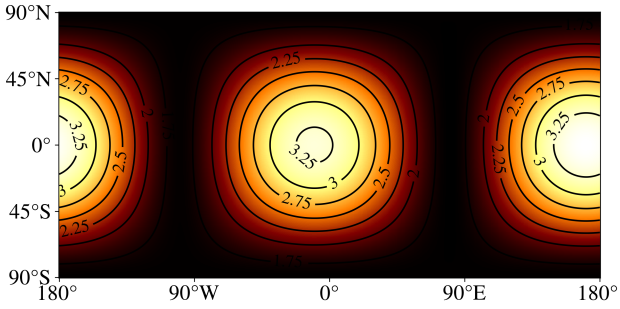

(c) B_x difference (nT) vs. symmetric at $r = 2R_C$

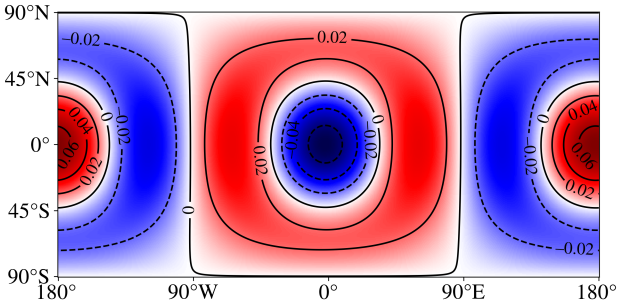

(d) $|\mathbf{B}_{\mathrm{ind}}|$ difference (nT) vs. symmetric at $r = 2R_C$

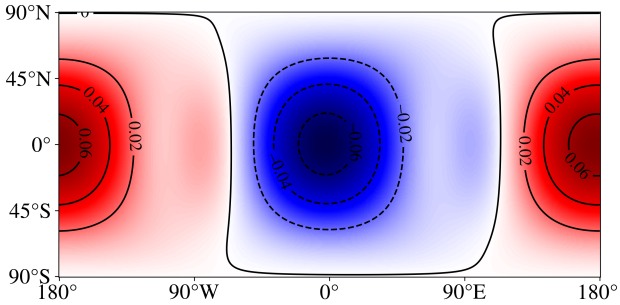

(e) B_y difference (nT) vs. symmetric at $r = 2R_C$

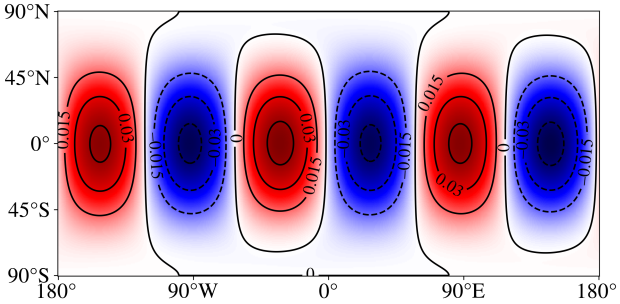

(f) B_z difference (nT) vs. symmetric at $r = 2R_C$

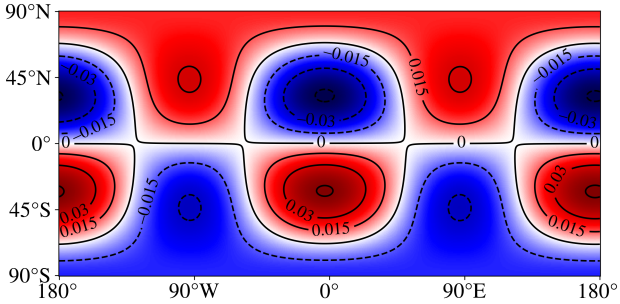

Figure 4.14: Caption appears on next page.

Figure 4.14: Callisto model with an asymmetric ionosphere modeled after Hartkorn et al. (2017). Uniform conductivity, an average ionospheric thickness of 100 km, and a total height-integrated conductivity of 800 S are assumed, as a rough approximation of the day–night dichotomy inferred by Hartkorn et al. An ocean with dissolved $MgSO_4$ and a 100 km thick ice shell are assumed. The magnetic field is evaluated at the J2000 epoch and at $r = 2R_C$, a plausible distance for a spacecraft flyby. In this case, the differences due to asymmetry are negligible, owing to the relatively low ionospheric conductivity where the considered asymmetry is present. Electrical conductivities in the ocean are calculated using the *PlanetProfile* geophysical modeling framework (Vance et al., 2021). For simplicity, only the synodic period is modeled here. Animations for the difference in x component and magnitude as they vary throughout the synodic period are included as Supplemental Material.

(a) Triton ionosphere thickness (km), $\overline{D} = 200\,\mathrm{km}$

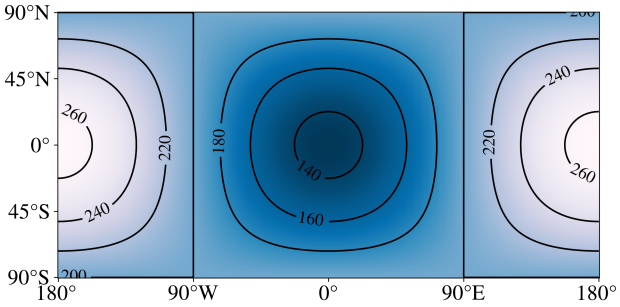

(b) Asymmetric model $|\mathbf{B}_{\mathrm{ind}}|$ (nT) at $r = 2R_T$

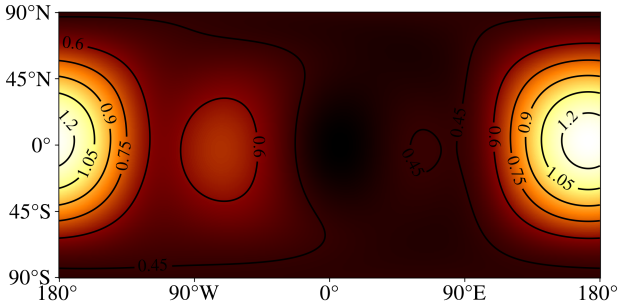

(c) B_x difference (nT) vs. symmetric at $r = 2R_T$

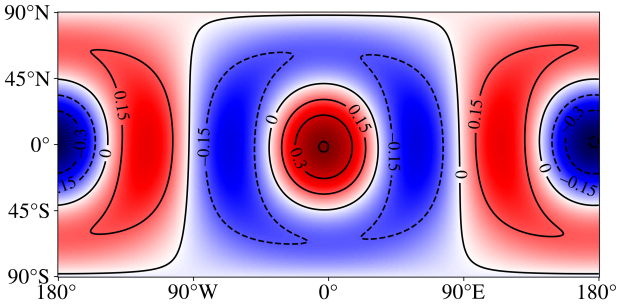

(d) $|\mathbf{B}_{\mathrm{ind}}|$ difference (nT) vs. symmetric at $r = 2R_T$

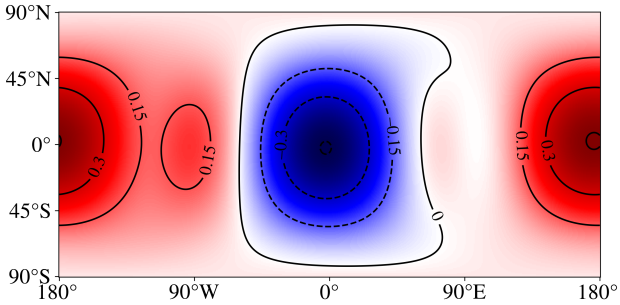

(e) B_y difference (nT) vs. symmetric at $r = 2R_T$

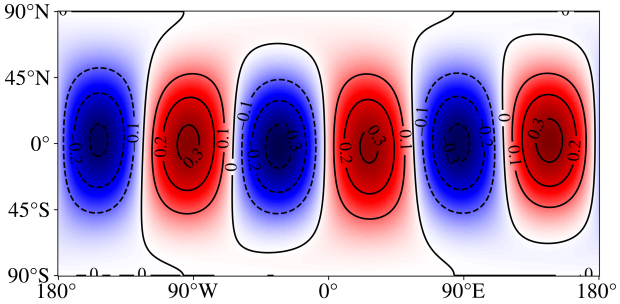

(f) B_z difference (nT) vs. symmetric at $r = 2R_T$

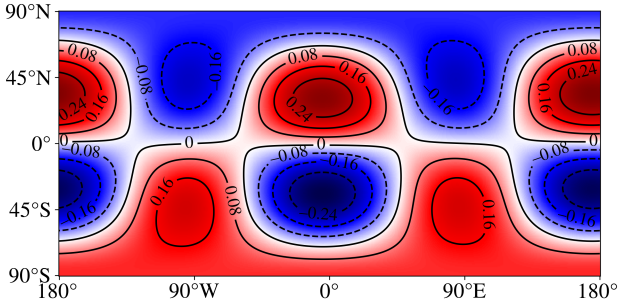

Figure 4.15: Caption appears on next page.

Figure 4.15: Triton model with an asymmetric ionosphere similar to that supposed for Callisto, an approximation of a day–night dichotomy. Uniform conductivity, an average ionospheric thickness of 200 km, a lower bound for the ionosphere of 250 km altitude, and a total height-integrated conductivity of 20 kS are assumed, based on the structure inferred by Tyler et al. (1989) from *Voyager* measurements. The interior structure we suppose for Triton is based on a moment of inertia inferred for Pluto by Hussmann et al. (2006) and geophysical modeling using the *PlanetProfile* framework. An ocean with dissolved $MgSO_4$ and a 112 km thick ice shell are assumed. The magnetic field is evaluated at the J2000 epoch and at $r = 2R_T$, a plausible distance for a spacecraft flyby. Unlike for Callisto, the differences due to asymmetry are a substantial fraction of the overall magnitude of the induced field (compare Figures 4.15c–4.15f to 4.15b), owing to the high conductivity and pronounced asymmetry we suppose for the ionosphere. Electrical conductivities in the ocean are determined using the *PlanetProfile* geophysical modeling framework (Vance et al., 2021). For simplicity, only the synodic period is modeled here. Animations for the difference in x component and magnitude as they vary throughout the synodic period are included as Supplemental Material.

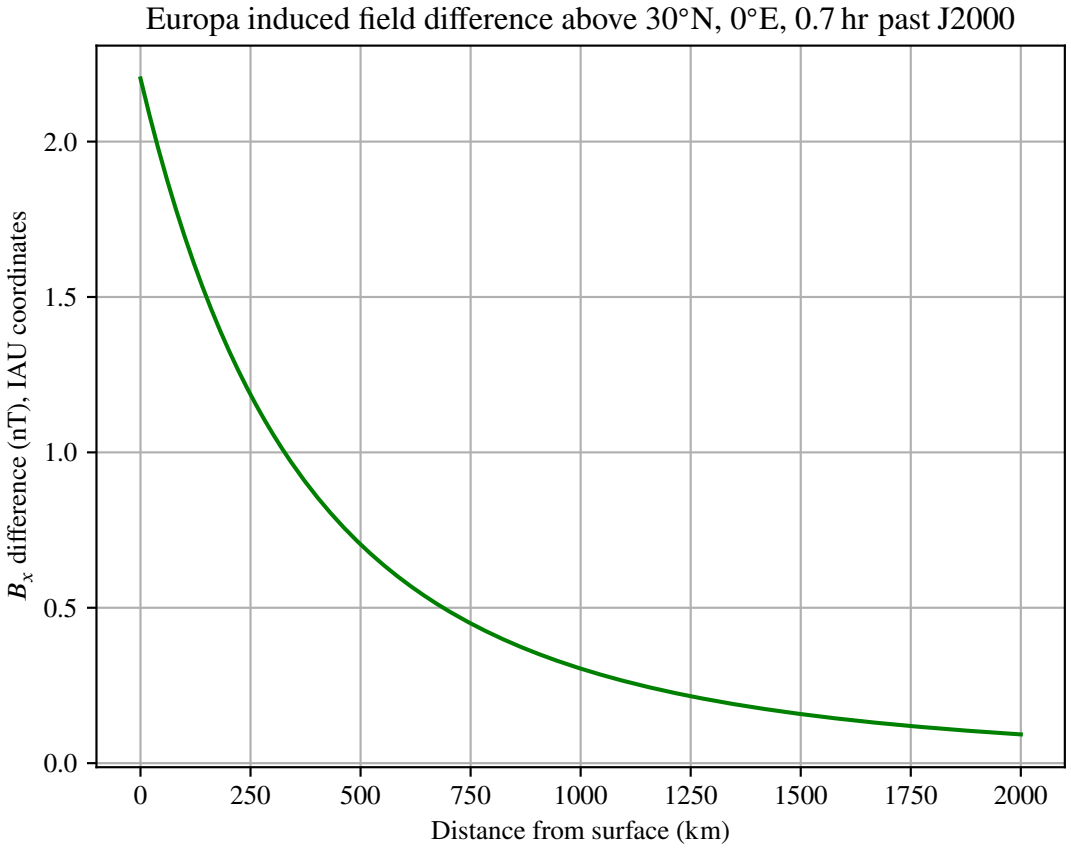

Figure 4.16: Difference in induced field B_x component for our Europa Seawater model as a function of altitude for a fixed point in time. The selected surface location (30°N, 0°E) and time (0.7 hr past J2000) maximize the observed difference relative to the spherically symmetric case for this interior model and component—see Figure 4.2. Beyond about 1500 km altitude, the difference is around 0.2 nT and likely negligible. Repeated from the main text (Figure 4.3).

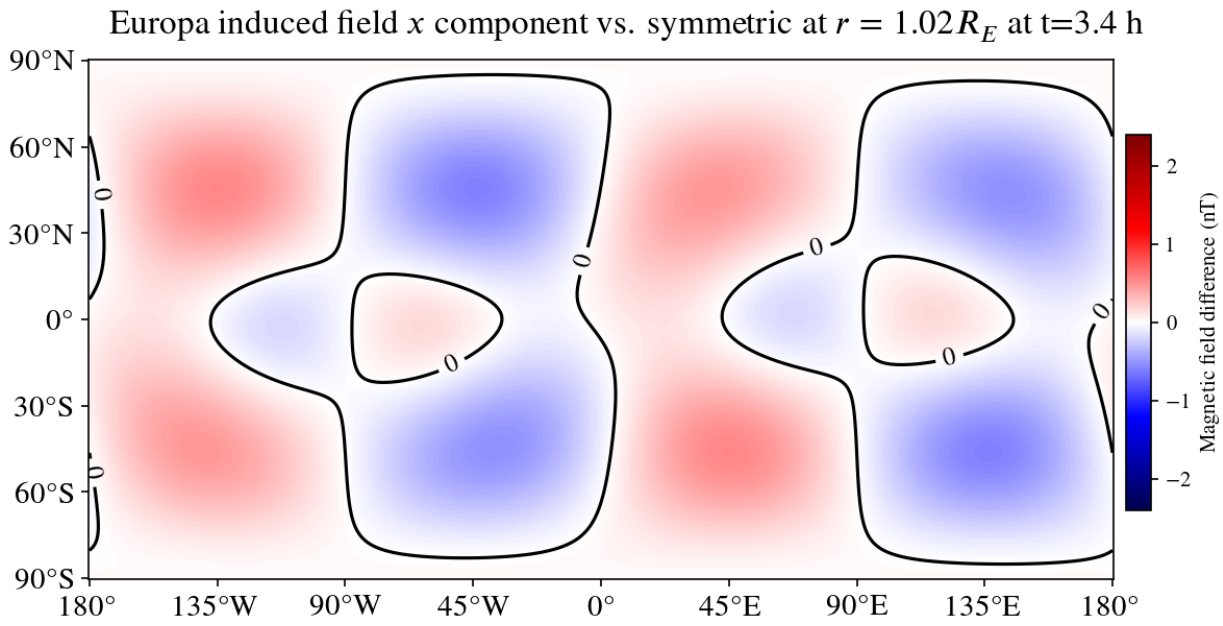

Figure 4.17: Single frame from the animated version of Figure 4.10c, at $t = 3.4$ hr past J2000. At this time, the difference resulting from asymmetry is much smaller than at J2000, and is less than 0.6 nT everywhere. This state lasts for around 30 min. A spacecraft reaching its closest approach altitude above 25 km during a flyby at times such as this may be able to ignore the influence of asymmetry under certain conditions.

4.10 Direct expressions for $3j$*-symbols and harmonic product coefficients*

Products of spherical harmonics are often expressed in terms of the Wigner $3j$-symbols. A general expression for the $3j$-symbols is presented by several authors (*e.g.* Brink and Satchler, 1968; Edmonds, 1996):

$$\begin{pmatrix} j & \ell & J \\ m & n & M \end{pmatrix} = (-1)^{j-\ell-M} \sqrt{\frac{(j+\ell-J)!(j-\ell+J)!(-j+\ell+J)!}{(j+\ell+J+1)!}} \quad \times \tag{4.116}$$

$$\sqrt{(j+m)!(j-m)!(\ell+n)!(\ell-n)!(J+M)!(J-M)!} \quad \times$$

$$\sum_{\kappa} \left[(-1)^{\kappa} \Big(\kappa!(j+\ell-J-\kappa)!(j-m-\kappa)!(\ell+n-\kappa)!(J-\ell+m+\kappa)!(J-j-n+\kappa)! \Big)^{-1} \right]$$

$$\text{for} \quad |j-\ell| \le J \le j+\ell \quad \text{and} \quad M = -(m+n),$$

$$\begin{pmatrix} j & \ell & J \\ m & n & M \end{pmatrix} = 0 \quad \text{otherwise.}$$

The sum in Eq. 4.116 is over each integer value of κ for which *all* factorials in the sum are non-negative. For many of the low-degree combinations of spherical harmonics with which we are concerned, the series has only a single term with $\kappa = 0$.

When $m = n = M = 0$, the $3j$-symbols are non-zero only if $j+\ell+J$ is even (Brink and Satchler, 1968). Another way to express this is that J takes values of $j+\ell,\ j+\ell-2,\ j+\ell-4,\ \ldots\ |j-\ell|$. Eq. 4.116 simplifies under many conditions. The results of products of spherical harmonics are always proportional to $\left(\begin{smallmatrix} j & \ell & J \\ 0 & 0 & 0 \end{smallmatrix}\right)$. In this case, Eq. 4.116 becomes (Edmonds, 1996)

$$\begin{pmatrix} j & \ell & J \\ 0 & 0 & 0 \end{pmatrix} = (-1)^{(j+\ell+J)/2} \sqrt{\frac{(j+\ell-J)!(j-\ell+J)!(-j+\ell+J)!}{(j+\ell+J+1)!}} \quad \times \tag{4.117}$$

$$\frac{\left(\frac{1}{2}(j+\ell+J)\right)!}{\left(\frac{1}{2}(j+\ell-J)\right)!\left(\frac{1}{2}(j-\ell+J)\right)!\left(\frac{1}{2}(-j+\ell+J)\right)!}$$

Using Eqs. 4.116 and 4.117, we may obtain explicit expressions for the products $Y_{nm}Y_{pq}$ and $Y^{\star}_{nm}Y_{pq}$. The selection rules for both mixing coefficients are similar, but not identical. For $\Xi^{n'm'}_{nmpq}$, the

conditions are

$$|n-p| \le n' \le n+p, \quad n+p+n' \text{ is even}, \quad \text{and} \quad m' = m+q. \tag{4.118}$$

For $\Xi^{\star\, n'm'}_{nmpq}$, the conditions are instead

$$0 < n' \le n+p, \quad n+p+n' \text{ is even}, \quad \text{and} \quad m' = m+q. \tag{4.119}$$

For $\Xi^{\star\, n'm'}_{nmpq}$, the triangular condition is modified because it relates products involving $Y^{\star}_{nm}$, which are linear combinations of $Y_{n+1,m}/\sin\theta$ and $Y_{n-1,m}/\sin\theta$, linking each (n,m) to both $(n+2,m)$ and $(n-2,m)$. The net result is that either $n' = 1$ or 2 will have non-zero mixing coefficients for all combinations of n and p, and even large p can still impact induced moments of degree 1 (the dipole moments).

If the selection rules are satisfied, the following expressions apply. Otherwise, the coefficient is zero. In the radial boundary conditions, the coefficients are

$$\begin{aligned} Y_{nm}Y_{pq} &= \sum_{n'} \Xi^{n'm'}_{nmpq} Y_{n'm'} \\ \Xi^{n'm'}_{nmpq} &= (-1)^{\nu}\sqrt{\frac{(2n+1)(2p+1)(2n'+1)}{4\pi}}\frac{(2\nu)!}{\nu!}\frac{(2n-2\nu)!}{(n-\nu)!}\frac{(2p-2\nu)!}{(p-\nu)!}\frac{(n'+\nu)!}{(2n'+1+2\nu)!} \quad \times \\ &\qquad \sqrt{(n+m)!(n-m)!(p+q)!(p-q)!(n'+m')!(n'-m')!} \quad \times \\ &\sum_{\kappa=\kappa^-}^{\kappa^+}\left[(-1)^{\kappa}\Big(\kappa!(2\nu-\kappa)!(n-m-\kappa)!(n+m-(2\nu-\kappa))!(p+q-\kappa)!(p-q-(2\nu-\kappa))!\Big)^{-1}\right], \\ &\qquad \text{with} \;\; \nu \equiv \frac{1}{2}(n+p-n'). \end{aligned} \tag{4.120}$$

The sum over κ is again limited to those integer values of κ for which all factorials have nonnegative arguments. This limits possible values of κ to lie between 0 and 2ν, but does not necessarily include those values. For example, in the case of $q = p$ with $\nu = 1$, $\kappa = 0$ yields a negative value for $p-q-(2\nu-\kappa)$, the final factorial in the series expression. This occurs for $n, m = 1, -1$, $p, q = 2, 2$, $n', m' = 1, 1$, a case of interest for application of our methods because it relates $p = 2$ boundary harmonics to the induced dipole moment from a uniform excitation field. This condition dictates

that the minimum value for κ is the greatest value among $[0,\ 2\nu-(n+m),\ 2\nu-(p-q)]$ and the maximum value for κ is the least value among $[2\nu,\ n-m,\ p+q]$. In summary:

$$\begin{aligned}\kappa^- &= \max(0,\ 2\nu-(n+m),\ 2\nu-(p-q)) \\ \kappa^+ &= \min(2\nu,\ n-m,\ p+q).\end{aligned} \tag{4.121}$$

In the tangential boundary conditions, the products $Y^\star_{nm}Y_{pq}$ proportional to a desired $Y^\star_{n'm'}$ may be replaced by $\Xi^{\star\,n'm'}_{nmpq}$:

$$\Xi^{\star\,n'm'}_{nmpq} = \frac{\Xi^w_{n'} + \sum_{g=1}^{g^-_{\max}} \Xi^w_{n'-2g} \prod_{\kappa=0}^{g-1} F^-_{n',2\kappa} + \sum_{g=1}^{g^+_{\max}} \Xi^w_{n'+2g} \prod_{\kappa=0}^{g-1} F^+_{n',2\kappa}}{\left(w^-_{n'}\right)^2 + \left(w^+_{n'}\right)^2 - w^-_{n'}w^+_{n'-2}F^-_{n',0} - w^+_{n'}w^-_{n'+2}F^+_{n',0}}, \tag{4.122}$$

$$g^-_{\max} \equiv \begin{cases} \mathrm{floor}\left(\frac{1}{2}\left(n'-|m'|\right)\right) & \text{if } n' \geq 3 \\ 0 & \text{otherwise} \end{cases}, \quad g^+_{\max} \equiv \mathrm{floor}\left(\frac{1}{2}\left(n_{\max}+p_{\max}-n'\right)\right), \tag{4.123}$$

$$F^\pm_{n,2\kappa} \equiv \frac{w^\pm_{n\pm 2\kappa} w^\mp_{n\pm(2\kappa+2)}}{\left(w^-_{n\pm(2\kappa+2)}\right)^2 + \left(w^+_{n\pm(2\kappa+2)}\right)^2 - w^\pm_{n\pm(2\kappa+2)} w^\mp_{n\pm(2\kappa+4)} F^\pm_{n,2\kappa+2}}, \tag{4.124}$$

$$\Xi^w_{n'} \equiv w^-_{nm}w^-_{n'm'}\Xi^{n'-1\,m'}_{n-1\,mpq} + w^+_{nm}w^+_{n'm'}\Xi^{n'+1\,m'}_{n+1\,mpq} - w^-_{nm}w^+_{n'm'}\Xi^{n'+1\,m'}_{n-1\,mpq} - w^+_{nm}w^-_{n'm'}\Xi^{n'-1\,m'}_{n+1\,mpq}, \tag{4.125}$$

$$w^-_{nm} = (n+1)\sqrt{\frac{n^2-m^2}{(2n-1)(2n+1)}}, \quad w^+_{nm} = n\sqrt{\frac{(n+1)^2-m^2}{(2n+1)(2n+3)}}, \tag{4.126}$$

where $\kappa = 0, 1, 2, \ldots$, $\mathrm{floor}(a)$ rounds a down to the nearest integer, and a subscript m is implied on all w in all equations where it is omitted, corresponding to the subscript n. The recursion in $F^+_{n,2\kappa}$ continues until 2κ exceeds $n_{\max}+p_{\max}-n$, and the recursion in $F^-_{n,2\kappa}$ continues until 2κ exceeds $n-|m|-2$. When 2κ exceeds these respective values, $F^\pm_{n,2\kappa}=0$. $F^-_{n,2\kappa}$ is also zero for $n<3$. The sums in the numerator of Eq. 4.122 result from isolating the desired terms of degree n' and order m'; the denominator results from solving the isolated term for $\Xi^{\star\,n'm'}_{nmpq}$.

These bounding values result from non-orthogonality of the $Y^\star_{nm}$. For a term of degree n'' below the considered value n', non-orthogonality is possible only for $n''=n'-2$, $n'-4$, etc., but $Y^\star_{n''m''}$ is defined and non-zero only for $n''>0$ and $n''\geq m''$. This constraint limits the non-zero values of $F^-_{n',0}$ to $n'\geq 3$ and $n'\geq m'+2$. The n'' above the considered n' that yield non-orthogonal terms

are similarly limited by the selection rules for $\Xi^{n'm'}_{nmpq}$, *i.e.* n'' cannot exceed $n_{\max} + p_{\max}$ because no combination of $Y^{\star}_{nm} Y_{pq} \to \Xi^{\star\, n'm'}_{nmpq} Y^{\star}_{n'm'}$ results in $n' > n_{\max} + p_{\max}$ and we have assumed the series in n' may be truncated at $n' = n_{\max} + p_{\max}$.

4.11 Sharp transitions in layer conductivities

As a matter of practical consideration, here we highlight important challenges for application of the layer method (and thus our results) and strategies for their mitigation. The content of this section has also proven useful for validating the functional dependence of the quantities we derive in our solutions. In this section, we assume spherical symmetry.

The Bessel functions j_n and y_n always contain complex exponentials with complex arguments kr. For large $|kr|$, the functions are all asymptotic to a growing exponential divided by kr; when kr is close to zero, they are asymptotic to power laws in kr (Marion and Heald, 1980). On planetary scales, kr often takes extreme values in various layers. For example, in metallic cores, the conductivity σ may be over 10^6 S/m (Khurana et al., 2002), providing a strong response for all periods of excitation and for any value of r. $|kr|$ can be large for even moderately conducting oceans on large scales—$|kr| \sim 100$ for a spherical Earth-size ocean for a 1-day period of oscillation. In contrast, in insulating materials such as ice and rock, conductivity values can be extremely low: $10^{-12} \lesssim \sigma \lesssim 10^{-2}$, depending on hydration state, porosity, and presence of contaminants (Glover, 2015). Additionally, for all materials, conductivity is pressure- and temperature-dependent. Because $|kr|$ can span many orders of magnitude across boundaries, especially at an ice–ocean interface or a core–mantle boundary, application of the recursion relations in Section 4.6.3 often results in differences of very large terms that are very close together in value, requiring great numerical precision in computation to reliably evaluate. With some realistic planetary values, numerical overflow or underflow are assured even for specialized, high-precision libraries such as mpmath[7] in Python and MPFUN[8] in Fortran.

---

[7] http://mpmath.org/

[8] MPFUN is available for Unix-based systems on author D. Bailey's personal website: https://www.davidhbailey.com/dhbsoftware/

In handling these challenges, we have found it essential to account for sharp conductivity boundaries by using approximations appropriate to the type of boundary transition. Under limiting conditions, the spherical Bessel functions take the following asymptotic forms, derived from Marion and Heald (1980):

$$\begin{aligned} j_n(kr) &\approx \tfrac{(-i)^n e^{ikr} - (i)^n e^{-ikr}}{2ikr}, \quad & y_n(kr) &\approx \tfrac{-(-i)^n e^{ikr} - (i)^n e^{-ikr}}{2kr}, \\ j_n^\star(kr) &\approx \tfrac{(-i)^n e^{ikr} + (i)^n e^{-ikr}}{2}, \quad & y_n^\star(kr) &\approx \tfrac{(-i)^n e^{ikr} - (i)^n e^{-ikr}}{2i} \end{aligned} \qquad \text{for } |kr| \gg n, \tag{4.127}$$

$$\begin{aligned} j_n(kr) &\approx \tfrac{(kr)^n}{(2n+1)!!}, & y_n(kr) &\approx -\tfrac{(2n-1)!!}{(kr)^{n+1}}, \\ j_n^\star(kr) &\approx (n+1)\tfrac{(kr)^n}{(2n+1)!!}, & y_n^\star(kr) &\approx n\tfrac{(2n-1)!!}{(kr)^{n+1}} \end{aligned} \qquad \text{for } |kr| \ll n. \tag{4.128}$$

These expressions may then be used to identify replacement rules for the spherical Bessel functions as they appear in Eq. 4.57 for extreme layers:

$$\begin{aligned} &j_n^\star(kr) \to -kr\, y_n(kr), \quad y_n^\star(kr) \to kr\, j_n(kr), \\ &|j_n^\star(kr)| \gg |j_n(kr)|, \qquad |y_n^\star(kr)| \gg |y_n(kr)| \end{aligned} \qquad \text{for } |kr| \gg n, \tag{4.129}$$

$$\begin{aligned} &j_n^\star(kr) \to (n+1)\, j_n(kr), \quad y_n^\star(kr) \to -n\, y_n(kr), \\ &|y_n(kr)| \gg |j_n(kr)|, \qquad |y_n^\star(kr)| \gg |j_n^\star(kr)| \end{aligned} \qquad \text{for } |kr| \ll n. \tag{4.130}$$

Using this information, we can reduce Eqs. 4.57 and 4.75 to account for extreme transitions. For the innermost boundary, Eq. 4.57 becomes

$$\Lambda_{nm}^2 \to -\frac{j_n^{2,1} + \frac{j_n^{\star 2,1}}{ik_1 r_1}}{y_n^{2,1} + \frac{y_n^{\star 2,1}}{ik_1 r_1}} \qquad \text{for } |k_1 r_1| \gg n, \tag{4.131}$$

$$\Lambda_{nm}^2 \to -\frac{j_{n+1}^{2,1}}{y_{n+1}^{2,1}} \qquad \text{for } |k_1 r_1| \ll n. \tag{4.132}$$

Note that the superscripts in the expressions above are all indices, not exponents—these relate the quantity Λ for the second-innermost layer to k_1, k_2, and r_1 when the innermost layer is a very strong or very poor conductor.

For intermediate layers, when $|kr|$ is large, if we keep only first-order terms in $1/kr$ we obtain the same result as Eq. 4.131. Consequently, if $|kr|$ is large enough to cause numerical overflows, currents flowing in this layer entirely screen every layer beneath it from oscillations in the magnetic field. The behavior is more complicated for an interstitial nonconducting layer, however.

For a j$^{\text{th}}$ (middle) layer with wavenumber k_{j}, lower bounding radius $r_l = r_{\text{j}-1}$, upper bounding radius $r_u = r_{\text{j}}$, and wavenumbers $k_l = k_{\text{j}-1}$, $k_u = k_{\text{j}+1}$ pertaining to the lower and upper layers respectively, Λ^u_{nm} for the upper layer takes the form

$$\Lambda^u_{nm} \to -\frac{j^{u,u}_n + \frac{j^{\star u,u}_n}{ik_{\text{j}}r_{\text{j}}}}{y^{u,u}_n + \frac{y^{\star u,u}_n}{ik_{\text{j}}r_{\text{j}}}} \qquad \text{for } |k_{\text{j}}r_{\text{j}}| \gg n, \tag{4.133}$$

$$\Lambda^u_{nm} \to \frac{\beta^U_n + \mathcal{A}^L_{nm}\delta^U_n \left(\frac{r_l}{r_u}\right)^{2n+1}}{\gamma^U_n + \mathcal{A}^L_{nm}\epsilon^U_n \left(\frac{r_l}{r_u}\right)^{2n+1}} = -\frac{j_{n+1}(k_u r_u) - \mathcal{A}^L_{nm} j_{n-1}(k_u r_u)\left(\frac{r_l}{r_u}\right)^{2n+1}}{y_{n+1}(k_u r_u) - \mathcal{A}^L_{nm} y_{n-1}(k_u r_u)\left(\frac{r_l}{r_u}\right)^{2n+1}} \qquad \text{for } |k_{\text{j}}r_{\text{j}}| \ll n. \tag{4.134}$$

In Eq. 4.134 we have defined the following quantities based on their similarity to those that appear in Eqs. 4.70–4.73 and 4.58:

$$\beta^U_n = j^\star_n(k_u r_u) - (n+1)j_n(k_u r_u) = -k_u r_u j_{n+1}(k_u r_u) \tag{4.135}$$

$$\gamma^U_n = y^\star_n(k_u r_u) - (n+1)y_n(k_u r_u) = -k_u r_u y_{n+1}(k_u r_u) \tag{4.136}$$

$$\delta^U_n = j^\star_n(k_u r_u) + n j_n(k_u r_u) = k_u r_u j_{n-1}(k_u r_u) \tag{4.137}$$

$$\epsilon^U_n = y^\star_n(k_u r_u) + n y_n(k_u r_u) = k_u r_u y_{n-1}(k_u r_u) \tag{4.138}$$

$$\mathcal{A}^L_{nm} = \frac{\beta^l_n + \Lambda^l_{nm}\gamma^l_n}{\delta^l_n + \Lambda^l_{nm}\epsilon^l_n} = -\frac{j_{n+1}(k_l r_l) + \Lambda^l_{nm} y_{n+1}(k_l r_l)}{j_{n-1}(k_l r_l) + \Lambda^l_{nm} y_{n-1}(k_l r_l)}, \tag{4.139}$$

where β^l_n–ϵ^l_n in Eq. 4.139 are defined as in Eqs. 4.70–4.73—the lower boundary acts as an "outer" boundary, as Laplace's equation applies in the space where $k \to 0$. Eq. 4.134 is the only layer recursion relation that contains more than one radius value, because it propagates from the lower

boundary to the upper across the "gap" nonconducting layer. Finally, at the outermost boundary:

$$\mathcal{A}_n^e \to 1 \qquad |kR| \gg n, \tag{4.140}$$

$$\mathcal{A}_n^e \to \left(\frac{r_{N-1}}{R}\right)^{2n+1} \frac{\beta_n^{N-1} + \Lambda_n^{N-1}\gamma_n^{N-1}}{\delta_n^{N-1} + \Lambda_n^{N-1}\epsilon_n^{N-1}} \qquad |kR| \ll n. \tag{4.141}$$

For a highly conducting outermost layer, all interior layers are screened and the entire body acts as a perfect conductor. For an insulating outer layer, Eq. 4.141 tells us the net effect is that the outer boundary moves one layer down and the final value for $\mathcal{A}_n^e$ is scaled down as if the outer layer were not present.

Eqs. 4.131–4.141 have been constructed such that numerical overflow is avoided in computation. In this formulation, when underflow occurs, a valid approximate result is still successfully computed. These expressions are physically valid when the skin depth $s_j = 1/\mathrm{Im}(k_j)$ is much less or much greater than the layer thickness $D_j = r_j - r_{j-1}$ (Styczinski and Harnett, 2021).

Chapter 5

CONCLUSIONS

Magnetic sounding is a complicated enterprise. In some ways, the technique stands emblematic of modern science itself—both require extensive input from a vast array of complementary disciplines. Both synthesize detailed laboratory studies and sparse measurements by spacecraft. Both hinge on the power of modern computing and simulation techniques. In spite of all this complexity, or perhaps because of it, prior to the present work interior conductivity models for magnetic sounding have been as simple as possible.

As an initial measure, using the simplest model is a sensible approach. However, the present work marks a shift in perspective: We have presented evidence that variation in geophysical properties and boundary shapes, which both *do* happen in planetary interiors, affect the induced magnetic fields by measurable amounts. We have modeled depth-dependent ocean conductivities (Chapter 3) and asymmetric ocean layers (Chapter 4) and we have shown that both will affect spacecraft measurements with signals on the order of nT, accounting for 1–30% of the overall induced field. The tools now exist to account for these effects, and we have made them publicly available. They must now become a part, in some form, of a more complete analysis that attempts to characterize interior structure using such measurements.

Thus far, a detailed characterization of the interior of an icy moon by magnetic sounding has proven elusive. Application of single-ocean-layer, spherically symmetric interior models has resulted in a joint degeneracy between the depth to the ocean layer, the thickness of that layer, and the conductivity of the ocean water. Important strides have been made by Khurana et al. (2002), Schilling (2006), and Hand and Chyba (2007), but existing studies have failed to break this degeneracy using the available measurements. Only for Europa have sufficient magnetic measurements been returned to encourage attempts to characterize a subsurface ocean, but the data have still been

too scarce to place significant limits on ocean properties. This state of affairs is unlikely to last much longer, with both *Europa Clipper* and *JUpiter ICy moons Explorer (JUICE)* planning extensive campaigns studying the Galilean moons—both harboring magnetometers—and numerous other missions in earlier stages of development.

Understanding and interpreting the detailed magnetic data returned by these and other future missions to icy worlds will require the techniques pioneered in this work, and they will also require detailed simulations of the plasma environment within which the spacecraft are immersed. Oscillations in the plasma and large-scale current structures created by their interaction with the planetary magnetic fields will also create magnetic signals that the spacecraft will measure. Most of the contributions to magnetic data from plasma are spurious signals and oscillations on much shorter time scales than those of the global induced field of the moons (Schilling et al., 2004). However, modeling the plasma flow near the moons has repeatedly been shown to play a critical role in accounting for detailed features in time-series spectra (Kabin et al., 1999; Dougherty et al., 2006; Paty and Winglee, 2006; Schilling et al., 2008; Rubin et al., 2015; Harris et al., 2021, *etc.*). Ultimately, comparable effect sizes from depth-dependence of ocean conductivity, the asymmetry expected in subsurface layers, and moon–plasma interactions will require a full accounting of all three in order to successfully characterize an icy moon through magnetic sounding.

The induced magnetic moments of quadrupole order and higher that will result for asymmetric oceans will have a greater influence for measurements taken nearer to a moon. Although certain asymmetric shapes can also affect the induced dipole moment, affecting the induced field at all distances, future work may be able to parameterize conditions under which the effects of depth-dependent properties and asymmetric conducting layers are negligible, or nearly so, such that their direct influence may be regarded as a simple source of noise in the magnetic data. Such an approach could be advantageous for modeling efforts that attempt to compare many thousands of simplified models to the data, so as to employ machine learning or Bayesian statistical methods. These techniques have proven valuable in anticipating the requirements for future missions, *e.g.* to the Uranus system (Cochrane et al., 2021). Nonetheless, large alterations of the magnetic field near a moon resulting from asymmetry could have a significant effect on plasma flow near that moon, which will

in turn alter the magnetic signals experienced by spacecraft even far from the moon. Future plasma modeling efforts must consider the full set of induced moments in order to more faithfully represent flow interactions near that moon.

Exploration of icy moons is still in its infancy. Computing power has continued to improve sharply in the past two decades, with new and existing statistical analysis techniques growing alongside. We now also look forward to missions in advanced stages of development that promise to return vastly more information than is currently available. The work collected here represents a large step forward in improving the physical accuracy of planetary induction models to better match modern computing power, statistical techniques, and the new data on the horizon. We are now able to investigate and answer questions regarding the realistic and expected effects of inter- and intraplanetary interactions in ways not previously possible. In future, the tools we have made available will be pivotal in exploiting magnetic interactions to characterize the hidden oceans of icy moons.

BIBLIOGRAPHY

M. Abramowitz and I. A. Stegun. *Handbook of mathematical functions with formulas, graphs, and mathematical tables*, volume 55. US Government printing office, tenth edition, 1972.

M. H. Acuña and N. F. Ness. The main magnetic field of Jupiter. *Journal of Geophysical Research*, 81(16):2917–2922, 1976.

C. B. Agnor and D. P. Hamilton. Neptune's capture of its moon Triton in a binary–planet gravitational encounter. *Nature*, 441(7090):192–194, 2006.

J. D. Anderson, G. Schubert, R. A. Jacobson, E. L. Lau, W. B. Moore, and W. L. Sjogren. Europa's differentiated internal structure: Inferences from four Galileo encounters. *Science*, 281(5385): 2019–2022, 1998. doi: 10.1126/science.281.5385.2019.

J. D. Anderson, R. A. Jacobson, T. P. McElrath, W. B. Moore, G. Schubert, and P. C. Thomas. Shape, mean radius, gravity field, and interior structure of Callisto. *Icarus*, 153(1):157–161, 2001.

G. Arfken, H. Weber, and F. Harris. *Mathematical Methods for Physicists*. Academic Press, seventh edition, 2012.

H. Arnold, L. Liuzzo, and S. Simon. Magnetic signatures of a plume at Europa during the Galileo E26 flyby. *Geophysical research letters*, 46(3):1149–1157, 2019. doi: 10.1029/2018GL081544.

C. S. Arridge and J. W. Eggington. Electromagnetic induction in the icy satellites of Uranus. *Icarus*, page 114562, 2021. ISSN 0019-1035. doi: 10.1016/j.icarus.2021.114562.

C. S. Arridge, N. Achilleos, J. Agarwal, C. B. Agnor, R. Ambrosi, N. André, S. V. Badman, K. Baines, D. Banfield, M. Barthélémy, M. M. Bisi, J. Blum, T. Bocanegra-Bahamon, B. Bon-

fond, C. Bracken, P. Brandt, C. Briand, C. Briois, S. Brooks, J. Castillo-Rogez, T. Cavalié, B. Christophe, A. J. Coates, G. Collinson, J. F. Cooper, M. Costa-Sitja, R. Courtin, I. A. Daglis, I. de Pater, M. Desai, D. Dirkx, M. K. Dougherty, R. W. Ebert, G. Filacchione, L. N. Fletcher, J. Fortney, I. Gerth, D. Grassi, D. Grodent, E. Grün, J. Gustin, M. Hedman, R. Helled, P. Henri, S. Hess, J. K. Hillier, M. H. Hofstadter, R. Holme, M. Horanyi, G. Hospodarsky, S. Hsu, P. Irwin, C. M. Jackman, O. Karatekin, S. Kempf, E. Khalisi, K. Konstantinidis, H. Krüger, W. S. Kurth, C. Labrianidis, V. Lainey, L. L. Lamy, M. Laneuville, D. Lucchesi, A. Luntzer, J. MacArthur, A. Maier, A. Masters, S. McKenna-Lawlor, H. Melin, A. Milillo, G. Moragas-Klostermeyer, A. Morschhauser, J. I. Moses, O. Mousis, N. Nettelmann, F. M. Neubauer, T. Nordheim, B. Noyelles, G. S. Orton, M. Owens, R. Peron, C. Plainaki, F. Postberg, N. Rambaux, K. Retherford, S. Reynaud, E. Roussos, C. T. Russell, A. M. Rymer, R. Sallantin, A. Sánchez-Lavega, O. Santolik, J. Saur, K. M. Sayanagi, P. Schenk, J. Schubert, N. Sergis, E. C. Sittler, A. Smith, F. Spahn, R. Srama, T. Stallard, V. Sterken, Z. Sternovsky, M. Tiscareno, G. Tobie, F. Tosi, M. Trieloff, D. Turrini, E. P. Turtle, S. Vinatier, R. Wilson, and P. Zarka. The science case for an orbital mission to Uranus: Exploring the origins and evolution of ice giant planets. *Planetary and Space Science*, 104:122–140, 2014. ISSN 0032-0633. doi: doi.org/10.1016/j.pss.2014.08.009.

F. Bagenal and V. Dols. The space environment of Io and Europa. *Journal of Geophysical Research: Space Physics*, 125(5):e2019JA027485, 2020.

F. Bagenal, E. Sidrow, R. J. Wilson, T. A. Cassidy, V. Dols, F. J. Crary, A. J. Steffl, P. A. Delamere, W. S. Kurth, and W. R. Paterson. Plasma conditions at Europa's orbit. *Icarus*, 261:1–13, 2015.

A. C. Barr and R. M. Canup. Constraints on gas giant satellite formation from the interior states of partially differentiated satellites. *Icarus*, 198(1):163–177, 2008.

C. B. Beddingfield and R. J. Cartwright. Hidden tectonism on Miranda's Elsinore Corona revealed by polygonal impact craters. *Icarus*, 343:113687, 2020.

J. W. Belcher, H. S. Bridge, F. Bagenal, B. Coppi, O. Divers, A. Eviatar, G. S. Gordon Jr, A. J. Lazarus, R. L. McNutt Jr, K. W. Ogilvie, J. D. Richardson, G. L. Siscoe, E. C. Sittler Jr., J. T.

Steinberg, J. D. Sullivan, A. Szabo, L. Villanueva, V. M. Vasyliunas, and M. Zhang. Plasma observations near Neptune: Initial results from Voyager 2. *Science*, 246(4936):1478–1483, 1989.

S. E. Billings and S. A. Kattenhorn. The great thickness debate: Ice shell thickness models for Europa and comparisons with estimates based on flexure at ridges. *Icarus*, 177(2):397–412, 2005.

O. Bollengier, J. M. Brown, and G. H. Shaw. Thermodynamics of pure liquid water: Sound speed measurements to 700 MPa down to the freezing point, and an equation of state to 2300 MPa from 240 to 500 K. *The Journal of Chemical Physics*, 151(5):054501, 2019.

H. S. Bridge, J. W. Belcher, B. Coppi, A. J. Lazarus, R. L. McNutt, S. Olbert, J. D. Richardson, M. R. Sands, R. S. Selesnick, J. D. Sullivan, R. E. Hartle, K. W. Ogilvie, E. C. Sittler Jr., F. Bagenal, R. S. Wolff, V. M. Vasyliunas, G. L. Siscoe, C. K. Goertz, and A. Eviatar. Plasma observations near Uranus: Initial results from Voyager 2. *Science*, 233(4759):89–93, 1986.

D. M. Brink and G. R. Satchler. *Angular momentum*. Clarendon Press, second edition, 1968.

B. Buffington, T. Lam, S. Campagnola, J. Ludwinski, E. Ferguson, and B. Bradley. Evolution of trajectory design requirement of NASA's planned Europa Clipper mission. In *68th International Astronautical Congress*, 2017.

R. Calvert, J. A. Cornelius, V. S. Griffiths, and D. I. Stock. The determination of the electrical conductivities of some concentrated electrolyte solutions using a transformer bridge. *The Journal of Physical Chemistry*, 62(1):47–53, 1958.

S. Campagnola, B. B. Buffington, T. Lam, A. E. Petropoulos, and E. Pellegrini. Tour design techniques for the Europa Clipper mission. *Journal of Guidance, Control, and Dynamics*, 42(12): 2615–2626, 2019. doi: 10.2514/1.G004309.

G. Carnielli, M. Galand, F. Leblanc, L. Leclercq, R. Modolo, A. Beth, H. L. F. Huybrighs, and X. Jia. First 3D test particle model of Ganymede's ionosphere. *Icarus*, 330:42–59, 2019. doi: 10.1016/j.icarus.2019.04.016.

M. H. Carr, M. J. S. Belton, C. R. Chapman, M. E. Davies, P. Geissler, R. Greenberg, A. S. McEwen, B. R. Tufts, R. Greeley, R. Sullivan, J. W. Head, R. T. Pappalardo, K. P. Klaasen, T. V. Johnson, J. Kaufman, D. Senske, J. Moore, G. Neukum, G. Schubert, J. A. Burns, P. Thomas, and J. Veverka. Evidence for a subsurface ocean on Europa. *Nature*, 391(6665):363–365, 1998.

R. J. Cartwright, C. B. Beddingfield, T. A. Nordheim, J. Roser, W. M. Grundy, K. P. Hand, J. P. Emery, D. P. Cruikshank, and F. Scipioni. Evidence for ammonia-bearing species on the uranian satellite Ariel supports recent geologic activity. *The Astrophysical Journal Letters*, 898(1):L22, 2020.

J. C. Castillo-Rogez, M. Hesse, M. Formisano, H. Sizemore, M. Bland, A. Ermakov, and R. Fu. Conditions for the long-term preservation of a deep brine reservoir in Ceres. *Geophysical Research Letters*, 46(4):1963–1972, 2019.

A. D. Chave. On the theory of electromagnetic induction in the Earth by ocean currents. *Journal of Geophysical Research: Solid Earth*, 88(B4):3531–3542, 1983.

G. Choblet, G. Tobie, C. Sotin, K. Kalousova, and O. Grasset. Heat transport in the high-pressure ice mantle of large icy moons. *Icarus*, 285:252–262, 2017.

C. J. Cochrane, S. D. Vance, T. A. Nordheim, M. Styczinski, A. Masters, and L. H. Regoli. In search of subsurface oceans within the uranian moons, 2021. URL https://arxiv.org/abs/2105.06087. Submitted to Journal of Geophysical Research: Planets.

E. U. Condon and G. H. Shortley. *The theory of atomic spectra*. Cambridge University Press, 1951.

J. Connerney, M. H. Acuña, and N. F. Ness. The magnetic field of Neptune. *Journal of Geophysical Research: Space Physics*, 96(S01):19023–19042, 1991.

J. E. P. Connerney, M. H. Acuña, and N. F. Ness. Modeling the jovian current sheet and inner magnetosphere. *Journal of Geophysical Research: Space Physics*, 86(A10):8370–8384, 1981.

J. E. P. Connerney, M. H. Acuña, N. F. Ness, and T. Satoh. New models of Jupiter's magnetic field constrained by the Io flux tube footprint. *Journal of Geophysical Research: Space Physics*, 103 (A6):11929–11939, 1998.

J. E. P. Connerney, S. Kotsiaros, R. J. Oliversen, J. R. Espley, J. L. Joergensen, P. S. Joergensen, J. M. G. Merayo, M. Herceg, J. Bloxham, K. M. Moore, S. J. Bolton, and S. M. Levin. A new model of Jupiter's magnetic field from Juno's first nine orbits. *Geophysical Research Letters*, 45 (6):2590–2596, 2018.

C. G. Constable and S. C. Constable. Satellite magnetic field measurements: applications in studying the deep Earth. *The state of the planet: Frontiers and challenges in geophysics*, 150:147–159, 2004a.

S. Constable and C. Constable. Observing geomagnetic induction in magnetic satellite measurements and associated implications for mantle conductivity. *Geochemistry, Geophysics, Geosystems*, 5(1), 2004b.

S. Constable and L. J. Srnka. An introduction to marine controlled-source electromagnetic methods for hydrocarbon exploration. *Geophysics*, 72(2):WA3–WA12, 2007.

S. Croft. Miranda geology and tectonics: A non-catastrophic interpretation. In *Lunar and Planetary Science Conference*, volume 18, 1987.

S. Croft, J. Lunine, and J. Kargel. Equation of state of ammonia-water liquid: Derivation and planetological applications. *Icarus*, 73(2):279–293, 1988.

M. Ćuk, M. El Moutamid, and M. S. Tiscareno. Dynamical history of the uranian system. *The Planetary Science Journal*, 1(1):22, 2020.

P. A. Davidson. *An introduction to magnetohydrodynamics*. American Association of Physics Teachers, 2002.

P. Dennery and A. Krzywicki. *Mathematics for physicists*. Dover, 2012.

F. Deschamps and C. Sotin. Thermal convection in the outer shell of large icy satellites. *Journal of Geophysical Research: Planets*, 106(E3):5107–5121, 2001.

S. D. Domagal-Goldman, K. E. Wright, K. Adamala, L. Arina de la Rubia, J. Bond, L. R. Dartnell, A. D. Goldman, K. Lynch, M. E. Naud, I. G. Paulino-Lima, K. Singer, M. Walther-Antonio, X. C. Abrevaya, R. Anderson, G. Arney, D. Atri, A. Azúa-Bustos, J. S. Bowman, W. J. Brazelton, G. A. Brennecka, R. Carns, A. Chopra, J. Colangelo-Lillis, C. J. Crockett, J. DeMarines, E. A. Frank, C. Frantz, E. de la Fuente, D. Galante, J. Glass, D. Gleeson, C. R. Glein, C. Goldblatt, R. Horak, L. Horodyskyj, B. Kaçar, A. Kereszturi, E. Knowles, P. Mayeur, S. McGlynn, Y. Miguel, M. Montgomery, C. Neish, L. Noack, S. Rugheimer, E. E. Stüeken, P. Tamez-Hidalgo, S. Imari Walker, and T. Wong. The Astrobiology Primer v2.0. *Astrobiology*, 16(8):561, 2016.

M. Dougherty, K. Khurana, F. Neubauer, C. Russell, J. Saur, J. Leisner, and M. Burton. Identification of a dynamic atmosphere at Enceladus with the Cassini magnetometer. *Science*, 311(5766): 1406–1409, 2006.

S. Duling, J. Saur, and J. Wicht. Consistent boundary conditions at nonconducting surfaces of planetary bodies: Applications in a new Ganymede MHD model. *Journal of Geophysical Research: Space Physics*, 119(6):4412–4440, 2014.

D. H. Eckhardt. Geomagnetic induction in a concentrically stratified Earth. *Journal of Geophysical Research*, 68(23):6273–6278, 1963.

A. R. Edmonds. *Angular momentum in quantum mechanics*. Princeton University Press, 1996. ISBN 9780691025896.

G. D. Egbert and A. Kelbert. Computational recipes for electromagnetic inverse problems. *Geophysical Journal International*, 189(1):251–267, 2012. doi: 10.1111/j.1365-246X.2011.05347.x.

E. B. Fainberg and B. S. Zinger. Electromagnetic induction in a non-uniform spherical model of the Earth. In *Annales de Geophysique*, volume 36, pages 127–134, 1980.

P. D. Feldman, M. A. McGrath, D. F. Strobel, H. W. Moos, K. D. Retherford, and B. C. Wolven. HST/STIS ultraviolet imaging of polar aurora on Ganymede. *The Astrophysical Journal*, 535(2): 1085, 2000.

C. Gissinger and L. Petitdemange. A magnetically driven equatorial jet in Europa's ocean. *Nature Astronomy*, 3(5):401–407, 2019. doi: 10.1038/s41550-019-0713-3.

C. R. Glein, F. Postberg, and S. D. Vance. The geochemistry of Enceladus: composition and controls. In P. M. Schenk, R. N. Clark, C. J. A. Howett, A. J. Verbiscer, and J. H. Waite, editors, *Enceladus and the Icy Moons of Saturn*, pages 39–56. University of Arizona Press, Tucson, 2018. ISBN 978-0816537075.

P. W. J. Glover. Geophysical properties of the near surface Earth: Electrical properties. In G. Schubert, editor, *Treatise on Geophysics*, volume 11, pages 89–137. Elsevier, second edition, 2015. doi: 10.1016/B978-0-444-53802-4.00189-5.

O. Grasset, M. K. Dougherty, A. Coustenis, E. J. Bunce, C. Erd, D. Titov, M. Blanc, A. Coates, P. Drossart, L. N. Fletcher, H. Hussmann, R. Jaumann, N. Krupp, J.-P. Lebreton, O. Prieto-Ballesteros, P. Tortora, F. Tosi, and T. Van Hoolst. JUpiter ICy moons Explorer (JUICE): An ESA mission to orbit Ganymede and to characterise the Jupiter system. *Planetary and Space Science*, 78:1–21, 2013.

A. V. Grayver, N. R. Schnepf, A. V. Kuvshinov, T. J. Sabaka, C. Manoj, and N. Olsen. Satellite tidal magnetic signals constrain oceanic lithosphere-asthenosphere boundary. *Science advances*, 2(9):e1600798, 2016.

M. Grey, J. Westlake, S. Liang, E. Hohlfeld, A. Crew, and R. McNutt. Europa PIMS prototype faraday cup development. In *2018 IEEE Aerospace Conference*, pages 1–15. IEEE, 2018. doi: 10.1109/AERO.2018.8396522.

W. M. Grundy, L. A. Young, J. R. Spencer, R. E. Johnson, E. F. Young, and M. W. Buie. Distribu-

tions of H_2O and CO_2 ices on Ariel, Umbriel, Titania, and Oberon from IRTF/SpeX observations. *Icarus*, 184(2):543–555, 2006.

H. Guo and H. Keppler. Electrical conductivity of NaCl-bearing aqueous fluids to 900 °C and 5 GPa. *Journal of Geophysical Research: Solid Earth*, 124(2):1397–1411, 2019.

K. P. Hand and C. F. Chyba. Empirical constraints on the salinity of the europan ocean and implications for a thin ice shell. *Icarus*, 189(2):424–438, 2007. doi: 10.1016/j.icarus.2007.02.002.

C. J. Hansen, D. E. Shemansky, L. W. Esposito, A. I. F. Stewart, B. R. Lewis, J. E. Colwell, A. R. Hendrix, R. A. West, J. H. Waite Jr, B. Teolis, and B. A. Magee. The composition and structure of the Enceladus plume. *Geophysical Research Letters*, 38(11), 2011.

C. D. K. Harris, X. Jia, J. A. Slavin, G. Toth, Z. Huang, and M. Rubin. Multi-fluid MHD simulations of Europa's plasma interaction under different magnetospheric conditions. *Journal of Geophysical Research: Space Physics*, 126(5):e2020JA028888, 2021. doi: 10.1029/2020JA028888.

O. Hartkorn and J. Saur. Induction signals from Callisto's ionosphere and their implications on a possible subsurface ocean. *Journal of Geophysical Research: Space Physics*, 122(11):11–677, 2017. doi: 10.1002/2017JA024269.

O. Hartkorn, J. Saur, and D. F. Strobel. Structure and density of Callisto's atmosphere from a fluid-kinetic model of its ionosphere: Comparison with Hubble Space Telescope and Galileo observations. *Icarus*, 282:237–259, 2017. doi: 10.1016/j.icarus.2016.09.020.

D. J. Hemingway and T. Mittal. Enceladus's ice shell structure as a window on internal heat production. *Icarus*, 332:111–131, 2019.

F. Herbert. Aurora and magnetic field of Uranus. *Journal of Geophysical Research: Space Physics*, 114(A11), 2009.

C. A. Hibbitts, J. E. Klemaszewski, T. B. McCord, G. B. Hansen, and R. Greeley. CO_2-rich impact craters on Callisto. *Journal of Geophysical Research: Planets*, 107(E10):14–1, 2002.

T. M. Hoehler, W. Bains, A. Davila, M. N. Parenteau, A. Pohorille, and R. Dotson. Life's requirements, habitability, and biological potential. In V. S. Meadows, G. N. Arney, B. E. Schmidt, and D. J. Des Marais, editors, *Planetary Astrobiology*, pages 37–70. University of Arizona Press, 2020.

M. Hofstadter, A. Simon, S. Atreya, D. Banfield, J. J. Fortney, A. Hayes, M. Hedman, G. Hospodarsky, K. Mandt, A. Masters, M. Showalter, K. M. Soderlund, D. Turrini, E. Turtle, K. Reh, J. Elliott, N. Arora, A. Petropoulos, and The Ice Giant Mission Study Team. Uranus and Neptune missions: A study in advance of the next Planetary Science Decadal Survey. *Planetary and Space Science*, 177:104680, 2019. ISSN 0032-0633. doi: 10.1016/j.pss.2019.06.004.

D. L. Hogenboom, J. S. Kargel, J. P. Ganasan, and L. Lee. Magnesium sulfate-water to 400 MPa using a novel piezometer: Densities, phase equilibria, and planetological implications. *Icarus*, 115(2):258–277, 1995.

T. S. Horbury, H. O'Brien, I. Carrasco Blazquez, M. Bendyk, P. Brown, R. Hudson, V. Evans, T. M. Oddy, C. M. Carr, T. J. Beek, E. Cupido, S. Bhattacharya, J.-A. Dominguez, L. Matthews, V. R. Myklebust, B. Whiteside, S. D. Bale, W. Baumjohann, D. Burgess, V. Carbone, P. Cargill, J. Eastwood, G. Erdös, L. Fletcher, R. Forsyth, J. Giacalone, K.-H. Glassmeier, M. L. Goldstein, T. Hoeksema, M. Lockwood, W. Magnes, M. Maksimovic, E. Marsch, W. H. Matthaeus, N. Murphy, V. M. Nakariakov, C. J. Owen, M. Owens, J. Rodriguez-Pacheco, I. Richter, P. Riley, C. T. Russell, S. Schwartz, R. Vainio, M. Velli, S. Vennerstrom, R. Walsh, R. F. Wimmer-Schweingruber, G. Zank, D. Müller, I. Zouganelis, and A. P. Walsh. The Solar Orbiter magnetometer. *Astronomy & Astrophysics*, 642:A9, 2020.

R. A. Horne and G. Frysinger. The effect of pressure on the electrical conductivity of sea water. *Journal of Geophysical Research*, 68(7):1967–1973, 1963.

G. S. Hubbard, F. M. Naderi, and J. B. Garvin. Following the water, the new program for Mars exploration. *Acta Astronautica*, 51(1-9):337–350, 2002.

H. Hussmann, F. Sohl, and T. Spohn. Subsurface oceans and deep interiors of medium-sized outer planet satellites and large trans-neptunian objects. *Icarus*, 185(1):258–273, 2006.

L. Iess, D. Stevenson, M. Parisi, D. Hemingway, R. Jacobson, J. Lunine, F. Nimmo, J. Armstrong, S. Asmar, M. Ducci, and P. Tortora. The gravity field and interior structure of Enceladus. *Science*, 344(6179):78–80, 2014.

J. D. Jackson. *Classical electrodynamics*. John Wiley & Sons, 1999. doi: 10.1119/1.19136.

X. Jia, R. J. Walker, M. G. Kivelson, K. K. Khurana, and J. A. Linker. Properties of Ganymede's magnetosphere inferred from improved three-dimensional MHD simulations. *Journal of Geophysical Research: Space Physics*, 114(A9), 2009.

X. Jia, M. G. Kivelson, K. K. Khurana, and W. S. Kurth. Evidence of a plume on Europa from Galileo magnetic and plasma wave signatures. *Nature Astronomy*, 2(6):459, 2018. doi: 10.1038/s41550-018-0450-z.

C. A. Jones and K. M. Kuzanyan. Compressible convection in the deep atmospheres of giant planets. *Icarus*, 204(1):227–238, 2009.

E. G. Jones and C. H. Lineweaver. To what extent does terrestrial life "follow the water"? *Astrobiology*, 10(3):349–361, 2010.

B. Journaux, I. Daniel, R. Caracas, G. Montagnac, and H. Cardon. Influence of NaCl on ice VI and ice VII melting curves up to 6 GPa, implications for large icy moons. *Icarus*, 226(1):355–363, 2013.

B. Journaux, I. Daniel, S. Petitgirard, H. Cardon, J.-P. Perrillat, R. Caracas, and M. Mezouar. Salt partitioning between water and high-pressure ices. Implication for the dynamics and habitability of icy moons and water-rich planetary bodies. *Earth and Planetary Science Letters*, 463:36–47, 2017.

B. Journaux, J. M. Brown, A. Pakhomova, I. E. Collings, S. Petitgirard, P. Espinoza, T. Boffa Ballaran, S. D. Vance, J. Ott, F. Cova, G. Garbarino, and M. Hanfland. Holistic approach for studying planetary hydrospheres: Gibbs representation of ices thermodynamics, elasticity, and the water phase diagram to 2,300 MPa. *Journal of Geophysical Research: Planets*, 125(1): e2019JE006176, 2020.

K. Kabin, M. R. Combi, T. I. Gombosi, A. F. Nagy, D. L. DeZeeuw, and K. G. Powell. On Europa's magnetospheric interaction: A MHD simulation of the E4 flyby. *Journal of Geophysical Research: Space Physics*, 104(A9):19983–19992, 1999.

K. Kalousová, C. Sotin, G. Choblet, G. Tobie, and O. Grasset. Two-phase convection in Ganymede's high-pressure ice layer—Implications for its geological evolution. *Icarus*, 299:133–147, 2018.

S. Kamata, F. Nimmo, Y. Sekine, K. Kuramoto, N. Noguchi, J. Kimura, and A. Tani. Pluto's ocean is capped and insulated by gas hydrates. *Nature Geoscience*, 12(6):407–410, 2019.

J. S. Kargel, J. Z. Kaye, J. W. Head III, G. M. Marion, R. Sassen, J. K. Crowley, O. P. Ballesteros, S. A. Grant, and D. L. Hogenboom. Europa's crust and ocean: origin, composition, and the prospects for life. *Icarus*, 148(1):226–265, 2000.

K. Khurana and the *Trident* Team. Single-pass magnetometric ocean detection at Triton. *Ocean Worlds 4*, 2168:6038, 2019.

K. K. Khurana. Euler potential models of Jupiter's magnetospheric field. *Journal of Geophysical Research: Space Physics*, 102(A6):11295–11306, 1997.

K. K. Khurana, M. G. Kivelson, D. J. Stevenson, G. Schubert, C. T. Russell, R. J. Walker, and C. Polanskey. Induced magnetic fields as evidence for subsurface oceans in Europa and Callisto. *Nature*, 395(6704):777–780, 1998.

K. K. Khurana, M. G. Kivelson, and C. T. Russell. Searching for liquid water in Europa by using surface observatories. *Astrobiology*, 2(1):93–103, 2002. doi: 10.1089/153110702753621376.

K. K. Khurana, M. G. Kivelson, K. P. Hand, and C. T. Russell. Electromagnetic induction from Europa's ocean and the deep interior. In R. T. Pappalardo, W. B. McKinnon, and K. Khurana, editors, *Europa*, pages 572–586. University of Arizona Press, Tucson, 2009. ISBN 978-0816528448.

M. G. Kivelson, K. K. Khurana, S. Joy, C. T. Russell, D. Southwood, R. J. Walker, and C. Polanskey. Europa's magnetic signature: Report from Galileo's pass on 19 December 1996. *Science*, 276 (5316):1239–1241, 1997.

M. G. Kivelson, K. K. Khurana, D. J. Stevenson, L. Bennett, S. Joy, C. T. Russell, R. J. Walker, C. Zimmer, and C. Polanskey. Europa and Callisto: Induced or intrinsic fields in a periodically varying plasma environment. *Journal of Geophysical Research: Space Physics*, 104(A3):4609–4625, 1999.

M. G. Kivelson, K. K. Khurana, C. T. Russell, M. Volwerk, R. J. Walker, and C. Zimmer. Galileo magnetometer measurements: A stronger case for a subsurface ocean at Europa. *Science*, 289 (5483):1340–1343, 2000. doi: 10.1126/science.289.5483.1340.

M. G. Kivelson, K. K. Khurana, and M. Volwerk. The permanent and inductive magnetic moments of Ganymede. *Icarus*, 157(2):507–522, 2002.

V. A. Krasnopolsky and D. P. Cruikshank. Photochemistry of Triton's atmosphere and ionosphere. *Journal of Geophysical Research: Planets*, 100(E10):21271–21286, 1995.

A. Kuvshinov. 3-D global induction in the oceans and solid Earth: recent progress in modeling magnetic and electric fields from sources of magnetospheric, ionospheric and oceanic origin. *Surveys in Geophysics*, 29(2):139–186, 2008.

B. N. Lahiri and A. T. Price. Electromagnetic induction in non-uniform conductors, and the determination of the conductivity of the Earth from terrestrial magnetic variations. *Philosophical Transactions of the Royal Society of London. Series A, Mathematical and Physical Sciences*, pages 509–540, 1939. doi: 10.1098/rsta.1939.0001.

V. Lainey, L. Duriez, and A. Vienne. Synthetic representation of the Galilean satellites' orbital motions from L1 ephemerides. *Astronomy & Astrophysics*, 456(2):783–788, 2006.

T. Lam, B. Buffington, and S. Campagnola. A robust mission tour for NASA's planned Europa Clipper mission. In *2018 Space Flight Mechanics Meeting*, 2018. doi: 10.2514/6.2018-0202.

E. Larionov and P. Kryukov. The conductivity of $MgSO_4$ aqueous-solutions in the range of temperatures 298–423 K and pressures 0.1–784.6 MPa. *Izvestiya Sibirskogo Otdeleniya Akademii Nauk SSSR Seriya Khimicheskikh Nauk*, 5:20–23, 1984.

M. Le Bars, D. Cébron, and P. Le Gal. Flows driven by libration, precession, and tides. *Annual Review of Fluid Mechanics*, 47:163–193, 2015.

J. Lieske. Galilean satellite ephemerides E5. *Astronomy and Astrophysics Supplement Series*, 129 (2):205–217, 1998.

L. Liuzzo, M. Feyerabend, S. Simon, and U. Motschmann. The impact of Callisto's atmosphere on its plasma interaction with the jovian magnetosphere. *Journal of Geophysical Research: Space Physics*, 120(11):9401–9427, 2015.

L. Liuzzo, S. Simon, M. Feyerabend, and U. Motschmann. Disentangling plasma interaction and induction signatures at Callisto: The Galileo C10 flyby. *Journal of Geophysical Research: Space Physics*, 121(9):8677–8694, 2016.

L. Liuzzo, S. Simon, M. Feyerabend, and U. Motschmann. Magnetic signatures of plasma interaction and induction at Callisto: The Galileo C21, C22, C23, and C30 flybys. *Journal of Geophysical Research: Space Physics*, 122(7):7364–7386, 2017.

L. Liuzzo, S. Simon, and M. Feyerabend. Observability of Callisto's inductive signature during the JUpiter ICy moons Explorer mission. *Journal of Geophysical Research: Space Physics*, 123 (11):9045–9054, 2018.

J. B. Marion and M. A. Heald. *Classical Electromagnetic Radiation*. Academic Press, New York, second edition, 1980. ISBN 0124722571.

B. Mauk, S. Krimigis, E. Keath, A. Cheng, T. Armstrong, L. Lanzerotti, G. Gloeckler, and D. Hamilton. The hot plasma and radiation environment of the uranian magnetosphere. *Journal of Geophysical Research: Space Physics*, 92(A13):15283–15308, 1987.

R. B. McCleskey, D. K. Nordstrom, J. N. Ryan, and J. W. Ball. A new method of calculating electrical conductivity with applications to natural waters. *Geochimica et Cosmochimica Acta*, 77:369–382, 2012.

T. J. McDougall and P. M. Barker. Getting started with TEOS-10 and the Gibbs seawater (GSW) oceanographic toolbox. *SCOR/IAPSO WG*, 127:1–28, 2011.

W. B. McKinnon. On convection in ice I shells of outer solar system bodies, with detailed application to Callisto. *Icarus*, 183(2):435–450, 2006.

H. J. Melosh, A. G. Ekholm, A. P. Showman, and R. D. Lorenz. The temperature of Europa's subsurface water ocean. *Icarus*, 168(2):498–502, 2004.

M. Melwani Daswani, S. D. Vance, M. J. Mayne, and C. R. Glein. A metamorphic origin for Europa's ocean. *Geophysical Research Letters*, 2021. under revision.

C. Michaut and M. Manga. Domes, pits, and small chaos on Europa produced by water sills. *Journal of Geophysical Research: Planets*, 119(3):550–573, 2014.

F. J. Millero, R. Feistel, D. G. Wright, and T. J. McDougall. The composition of Standard Seawater and the definition of the Reference-Composition Salinity Scale. *Deep Sea Research Part I: Oceanographic Research Papers*, 55(1):50–72, 2008.

T. Minami. Motional induction by tsunamis and ocean tides: 10 years of progress. *Surveys in Geophysics*, 38(5):1097–1132, 2017.

H. K. Moffatt. *Magnetic field generation in electrically conducting fluids*, volume 2. Cambridge University Press, 1978.

W. B. Moore and G. Schubert. The tidal response of Europa. *Icarus*, 147(1):317–319, 2000.

National Research Council. *Vision and Voyages for Planetary Science in the Decade 2013–2022*. The National Academies Press, Washington, DC, 2011. ISBN 978-0-309-22464-2. doi: 10.17226/13117.

A. Néri, F. Guyot, B. Reynard, and C. Sotin. A carbonaceous chondrite and cometary origin for icy moons of Jupiter and Saturn. *Earth and Planetary Science Letters*, 530:115920, 2020.

N. F. Ness, M. H. Acuña, K. W. Behannon, L. F. Burlaga, J. E. Connerney, R. P. Lepping, and F. M. Neubauer. Magnetic fields at Uranus. *Science*, 233(4759):85–89, 1986.

F. M. Neubauer. Alfvén wings and electromagnetic induction in the interiors: Europa and Callisto. *Journal of Geophysical Research: Space Physics*, 104(A12):28671–28684, 1999. doi: 10.1029/1999JA900217.

M. Neveu and A. R. Rhoden. Evolution of Saturn's mid-sized moons. *Nature astronomy*, 3(6):543–552, 2019.

H. Ni, Q. Chen, and H. Keppler. Electrical conductivity measurements of aqueous fluids under pressure with a hydrothermal diamond anvil cell. *Review of Scientific Instruments*, 85(11):115107, 2014.

F. Nimmo, P. C. Thomas, R. T. Pappalardo, and W. B. Moore. The global shape of Europa: Constraints on lateral shell thickness variations. *Icarus*, 191(1):183–192, 2007.

F. Nimmo, B. Bills, and P. Thomas. Geophysical implications of the long-wavelength topography of the saturnian satellites. *Journal of Geophysical Research: Planets*, 116(E11), 2011.

F. Nimmo, D. P. Hamilton, W. B. McKinnon, P. M. Schenk, R. P. Binzel, C. J. Bierson, R. A. Beyer, J. M. Moore, S. A. Stern, H. A. Weaver, C. B. Olkin, L. A. Young, K. E. Smith, and The

New Horizons Geology, Geophysics & Imaging Theme Team. Reorientation of Sputnik Planitia implies a subsurface ocean on Pluto. *Nature*, 540(7631):94–96, 2016.

R. T. Pappalardo, M. J. S. Belton, H. H. Breneman, M. H. Carr, C. R. Chapman, G. C. Collins, T. Denk, S. Fagents, P. E. Geissler, B. Giese, R. Greeley, R. Greenberg, J. W. Head, P. Helfenstein, G. Hoppa, S. D. Kadel, K. P. Klaasen, J. E. Klemaszewski, K. Magee, A. S. McEwen, J. M. Moore, W. B. Moore, G. Neukum, C. B. Phillips, L. M. Prockter, G. Schubert, D. A. Senske, R. J. Sullivan, B. R. Tufts, E. P. Turtle, R. Wagner, and K. K. Williams. Does Europa have a subsurface ocean? Evaluation of the geological evidence. *Journal of Geophysical Research: Planets*, 104(E10):24015–24055, 1999.

W. D. Parkinson. *Introduction to Geomagnetism*. Elsevier, 1983.

M. A. Pasek and R. Greenberg. Acidification of Europa's subsurface ocean as a consequence of oxidant delivery. *Astrobiology*, 12(2):151–159, 2012.

C. Paty and R. Winglee. Multi-fluid simulations of Ganymede's magnetosphere. *Geophysical research letters*, 31(24), 2004.

C. Paty and R. Winglee. The role of ion cyclotron motion at Ganymede: Magnetic field morphology and magnetospheric dynamics. *Geophysical research letters*, 33(10), 2006.

C. Paty, C. S. Arridge, I. J. Cohen, G. A. DiBraccio, R. W. Ebert, and A. M. Rymer. Ice giant magnetospheres. *Philosophical Transactions of the Royal Society A*, 378(2187):20190480, 2020.

R. Pawlowicz. The electrical conductivity of seawater at high temperatures and salinities. *Desalination*, 300:32–39, 2012.

A. P. Payan, C. S. Paty, and K. D. Retherford. Uncovering local magnetospheric processes governing the morphology and variability of Ganymede's aurora using three-dimensional multifluid simulations of Ganymede's magnetosphere. *Journal of Geophysical Research: Space Physics*, 120(1):401–413, 2015.

J. Plescia. Cratering history of Miranda: Implications for geologic processes. *Icarus*, 73(3):442–461, 1988.

R. M. Ponte, Q. Sun, C. Liu, and X. Liang. How salty is the global ocean: Weighing it all or tasting it a sip at a time? *Geophysical Research Letters*, 48(11):e2021GL092935, 2021. doi: 10.1029/2021GL092935.

A. R. Poppe, S. Fatemi, and K. K. Khurana. Thermal and energetic ion dynamics in Ganymede's magnetosphere. *Journal of Geophysical Research: Space Physics*, 123(6):4614–4637, 2018. doi: 10.1029/2018JA025312.

F. Postberg, S. Kempf, J. Schmidt, N. Brilliantov, A. Beinsen, B. Abel, U. Buck, and R. Srama. Sodium salts in E-ring ice grains from an ocean below the surface of Enceladus. *Nature*, 459 (7250):1098–1101, 2009.

L. C. Quick and B. D. Marsh. Heat transfer of ascending cryomagma on Europa. *Journal of Volcanology and Geothermal Research*, 319:66–77, 2016. doi: 10.1016/j.jvolgeores.2016.03.018.

N. Rambaux and J. Castillo-Rogez. Tides on satellites of giant planets. In J. Souchay, S. Mathis, and T. Tokieda, editors, *Tides in Astronomy and Astrophysics*, pages 167–200. Springer-Verlag Berlin Heidelberg, 2013. ISBN 978-3-642-32961-6. doi: 10.1007/978-3-642-32961-6_5.

N. Rambaux, J. C. Castillo-Rogez, J. G. Williams, and Ö. Karatekin. Librational response of Enceladus. *Geophysical Research Letters*, 37(4), 2010.

C. Ray, C. R. Glein, J. H. Waite, B. Teolis, T. Hoehler, J. A. Huber, J. Lunine, and F. Postberg. Oxidation processes diversify the metabolic menu on Enceladus. *Icarus*, 364:114248, 2021.

J. D. Richardson, J. W. Belcher, M. Zhang, and R. L. McNutt Jr. Low-energy ions near Neptune. *Journal of Geophysical Research: Space Physics*, 96(S01):18993–19011, 1991.

M. N. Ross and G. Schubert. Tidal heating in an internal ocean model of Europa. *Nature*, 325 (6100):133–134, 1987.

L. Roth, J. Saur, K. D. Retherford, D. F. Strobel, P. D. Feldman, M. A. McGrath, and F. Nimmo. Transient water vapor at Europa's south pole. *Science*, 343(6167):171–174, 2014. doi: 10.1126/science.1247051.

L. J. Rothschild and R. L. Mancinelli. Life in extreme environments. *Nature*, 409(6823):1092–1101, 2001.

M. Rubin, X. Jia, K. Altwegg, M. R. Combi, L. K. S. Daldorff, T. I. Gombosi, K. Khurana, M. G. Kivelson, V. M. Tenishev, G. Tóth, B. van der Holst, and P. Wurz. Self-consistent multifluid MHD simulations of Europa's exospheric interaction with Jupiter's magnetosphere. *Journal of Geophysical Research: Space Physics*, 120(5):3503–3524, 2015. doi: 10.1002/2015JA021149.

A. R. Sarid, R. Greenberg, G. V. Hoppa, T. A. Hurford, B. R. Tufts, and P. Geissler. Polar wander and surface convergence of Europa's ice shell: Evidence from a survey of strike-slip displacement. *Icarus*, 158(1):24–41, 2002.

J. Saur, D. Strobel, and F. Neubauer. Interaction of the jovian magnetosphere with Europa: Constraints on the neutral atmosphere. *Journal of Geophysical Research: Planets*, 103(E9):19947–19962, 1998.

J. Saur, F. M. Neubauer, and K.-H. Glassmeier. Induced magnetic fields in solar system bodies. *Space science reviews*, 152(1-4):391–421, 2010. doi: 10.1007/s11214-009-9581-y.

J. Saur, S. Duling, L. Roth, X. Jia, D. F. Strobel, P. D. Feldman, U. R. Christensen, K. D. Retherford, M. A. McGrath, F. Musacchio, A. Wennmacher, F. M. Neubauer, S. Simon, and O. Hartkorn. The search for a subsurface ocean in Ganymede with Hubble Space Telescope observations of its auroral ovals. *Journal of Geophysical Research: Space Physics*, 120(3):1715–1737, 2015.

P. Schenk, I. Matsuyama, and F. Nimmo. A very young age for true polar wander on Europa from related fracturing. *Geophysical Research Letters*, 47(17):e2020GL088364, 2020.

N. Schilling. *Time varying Interaction of Europa's Atmosphere-Ionosphere and its Conducting Ocean with the Jovian Magnetosphere*. PhD thesis, Universität zu Köln, 2006.

N. Schilling, K. K. Khurana, and M. G. Kivelson. Limits on an intrinsic dipole moment in Europa. *Journal of Geophysical Research: Planets*, 109(E5), 2004. doi: 10.1029/2003JE002166.

N. Schilling, F. M. Neubauer, and J. Saur. Time-varying interaction of Europa with the jovian magnetosphere: Constraints on the conductivity of Europa's subsurface ocean. *Icarus*, 192(1): 41–55, 2007. doi: 10.1016/j.icarus.2007.06.024.

N. Schilling, F. M. Neubauer, and J. Saur. Influence of the internally induced magnetic field on the plasma interaction of Europa. *Journal of Geophysical Research: Space Physics*, 113(A3), 2008.

B. Schmidt, D. Blankenship, G. Patterson, and P. Schenk. Active formation of 'chaos terrain' over shallow subsurface water on Europa. *Nature*, 479(7374):502–505, 2011.

C. Schmidt and C. E. Manning. Pressure-induced ion pairing in $MgSO_4$ solutions: Implications for the oceans of icy worlds. *Geochemical Perspectives Letters*, 3(1):66–74, 2017.

G. Schubert and K. M. Soderlund. Planetary magnetic fields: Observations and models. *Physics of the Earth and Planetary Interiors*, 187(3-4):92–108, 2011.

G. Schubert, J. Anderson, T. Spohn, and W. McKinnon. Interior composition, structure and dynamics of the Galilean satellites. In F. Bagenal, T. Dowling, and W. McKinnon, editors, *Jupiter: The Planet, Satellites and Magnetosphere*, pages 281–306. Cambridge University Press, 2004.

R. Schunk and A. Nagy. *Ionospheres: Physics, Plasma Physics, and Chemistry*. Cambridge University Press, 2009.

A. Schuster. The diurnal variation of terrestrial magnetism. *Philosophical Transactions of the Royal Society of London.(A.)*, 180:467–518, 1889.

M. Seufert, J. Saur, and F. M. Neubauer. Multi-frequency electromagnetic sounding of the Galilean moons. *Icarus*, 214(2):477–494, 2011. doi: 10.1016/j.icarus.2011.03.017.

A. P. Showman and R. Malhotra. Tidal evolution into the Laplace resonance and the resurfacing of Ganymede. *Icarus*, 127(1):93–111, 1997.

A. P. Showman and R. Malhotra. The Galilean satellites. *Science*, 286(5437):77–84, 1999.

K. Soderlund, B. Schmidt, J. Wicht, and D. Blankenship. Ocean-driven heating of Europa's icy shell at low latitudes. *Nature Geoscience*, 7(1):16–19, 2014.

K. M. Soderlund. Ocean dynamics of outer solar system satellites. *Geophysical Research Letters*, 46(15):8700–8710, 2019. doi: 10.1029/2018GL081880.

K. M. Soderlund, K. Kalousová, J. J. Buffo, C. R. Glein, J. C. Goodman, G. Mitri, G. W. Patterson, F. Postberg, M. Rovira-Navarro, T. Rückriemen, J. Saur, B. E. Schmidt, C. Sotin, T. Spohn, G. Tobie, T. Van Hoolst, S. D. Vance, and B. Vermeersen. Ice–ocean exchange processes in the jovian and saturnian satellites. *Space Science Reviews*, 216(5):1–57, 2020.

S. P. Srivastava. Theory of the magnetotelluric method for a spherical conductor. *Geophysical Journal International*, 11(4):373–387, 1966.

S. Stanley and G. A. Glatzmaier. Dynamo models for planets other than Earth. *Space science reviews*, 152(1-4):617–649, 2010.

G. Steinbrügge, D. M. Schroeder, M. S. Haynes, H. Hussmann, C. Grima, and D. D. Blankenship. Assessing the potential for measuring Europa's tidal Love number h_2 using radar sounder and topographic imager data. *Earth and Planetary Science Letters*, 482:334–341, 2018.

M. J. Styczinski and E. M. Harnett. Induced magnetic moments from a nearly spherical ocean. *Icarus*, 354(2):114020, 2021. doi: 10.1016/j.icarus.2020.114020.

R. Tajeddine, K. M. Soderlund, P. C. Thomas, P. Helfenstein, M. M. Hedman, J. A. Burns, and P. M. Schenk. True polar wander of Enceladus from topographic data. *Icarus*, 295:46–60, 2017.

P. Thomas, R. Tajeddine, M. Tiscareno, J. Burns, J. Joseph, T. Loredo, P. Helfenstein, and C. Porco. Enceladus's measured physical libration requires a global subsurface ocean. *Icarus*, 264:37–47, 2016.

G. Tobie, G. Choblet, and C. Sotin. Tidally heated convection: Constraints on Europa's ice shell thickness. *Journal of Geophysical Research: Planets*, 108(E11), 2003. doi: 10.1029/2003JE002099.

G. Tobie, A. Mocquet, and C. Sotin. Tidal dissipation within large icy satellites: Applications to Europa and Titan. *Icarus*, 177(2):534–549, 2005.

B. Travis, J. Palguta, and G. Schubert. A whole-moon thermal history model of Europa: Impact of hydrothermal circulation and salt transport. *Icarus*, 218(2):1006–1019, 2012.

G. L. Tyler, D. N. Sweetnam, J. D. Anderson, S. E. Borutzki, J. K. Campbell, V. R. Eshleman, D. L. Gresh, E. M. Gurrola, D. P. Hinson, N. Kawashima, E. R. Kursinski, G. S. Levy, G. F. Lindal, J. R. Lyons, E. A. Marouf, P. A. Rosen, R. A. Simpson, and G. E. Wood. Voyager radio science observations of Neptune and Triton. *Science*, 246(4936):1466–1473, 1989.

R. H. Tyler. Magnetic remote sensing of Europa's ocean tides. *Icarus*, 211(1):906–908, 2011. doi: 10.1016/j.icarus.2010.10.011.

R. H. Tyler, S. Maus, and H. Lühr. Satellite observations of magnetic fields due to ocean tidal flow. *Science*, 299(5604):239–241, 2003.

T. Van Hoolst, R.-M. Baland, and A. Trinh. The diurnal libration and interior structure of Enceladus. *Icarus*, 277:311–318, 2016.

S. Vance and J. M. Brown. Layering and double-diffusion style convection in Europa's ocean. *Icarus*, 177(2):506–514, 2005.

S. Vance and J. M. Brown. Thermodynamic properties of aqueous $MgSO_4$ to 800 MPa at temperatures from –20 to 100°c and concentrations to 2.5 mol kg^{-1} from sound speeds, with applications to icy world oceans. *Geochimica et Cosmochimica Acta*, 110:176–189, 2013.

S. Vance and M. Melwani Daswani. Serpentinite and the search for life beyond Earth. *Philosophical Transactions of the Royal Society A*, 378(2165):20180421, 2020.

S. Vance, M. Bouffard, M. Choukroun, and C. Sotin. Ganymede's internal structure including thermodynamics of magnesium sulfate oceans in contact with ice. *Planetary and Space Science*, 96:62–70, 2014.

S. D. Vance and J. Goodman. Oceanography of an ice-covered moon. In R. T. Pappalardo, W. B. McKinnon, and K. Khurana, editors, *Europa*, pages 459–482. University of Arizona Press, Tucson, 2009. ISBN 978-0816528448.

S. D. Vance, K. P. Hand, and R. T. Pappalardo. Geophysical controls of chemical disequilibria in Europa. *Geophysical Research Letters*, 43(10):4871–4879, 2016.

S. D. Vance, M. P. Panning, S. Stähler, F. Cammarano, B. G. Bills, G. Tobie, S. Kamata, S. Kedar, C. Sotin, W. T. Pike, R. Lorenz, H.-H. Huang, J. M. Jackson, and B. Banerdt. Geophysical investigations of habitability in ice-covered ocean worlds. *Journal of Geophysical Research: Planets*, 123(1):180–205, 2018. doi: 10.1002/2017JE005341.

S. D. Vance, G. Tobie, M. Melwani Daswani, and G. Choblet. Tidal signatures of geochemically rigorous interior structure for Ganymede. In *EPSC–DPS Joint Meeting*, 2019.

S. D. Vance, M. J. Styczinski, B. G. Bills, C. J. Cochrane, K. M. Soderlund, N. Gómez-Pérez, and C. Paty. Magnetic induction responses of Jupiter's ocean moons including effects from adiabatic convection. *Journal of Geophysical Research: Planets*, 126(2):e2020JE006418, 2021. doi: 10.1029/2020JE006418.

J. Velímský and Z. Martinec. Time-domain, spherical harmonic-finite element approach to transient three-dimensional geomagnetic induction in a spherical heterogeneous Earth. *Geophysical Journal International*, 161(1):81–101, 2005. doi: 10.1111/j.1365-246X.2005.02546.x.

J. R. Wait. On the theory of transient electromagnetic sounding over a stratified Earth. *Canadian Journal of Physics*, 50(11):1055–1061, 1972.

J. H. Waite, C. R. Glein, R. S. Perryman, B. D. Teolis, B. A. Magee, G. Miller, J. Grimes, M. E. Perry, K. E. Miller, A. Bouquet, J. I. Lunine, T. Brockwell, and S. J. Bolton. Cassini finds molecular hydrogen in the Enceladus plume: evidence for hydrothermal processes. *Science*, 356 (6334):155–159, 2017.

B. P. Weiss, V. Colicci, and J. B. Biersteker. Searching for subsurface oceans on the moons of Uranus using magnetic induction. In *2020 AGU Fall Meeting*, 2020. P074-07.

C. J. Weiss. Triangulated finite difference methods for global-scale electromagnetic induction simulations of whole mantle electrical heterogeneity. *Geochemistry, Geophysics, Geosystems*, 11 (11), 2010. doi: 10.1029/2010GC003283.

E. P. Wigner. *Gruppentheorie und ihre Anwendung auf die Quantenmechanik der Atomspektren*. Springer, 1931.

T. S. Zhang and A. Schultz. A 3-D perturbation solution for the EM induction problem in a spherical Earth—the forward problem. *Geophysical Journal International*, 111(2):319–334, 1992. doi: 10.1111/j.1365-246X.1992.tb00580.x.

P. Zhu, G. E. Manucharyan, A. F. Thompson, J. C. Goodman, and S. D. Vance. The influence of meridional ice transport on Europa's ocean stratification and heat content. *Geophysical Research Letters*, 2017.

C. Zimmer, K. K. Khurana, and M. G. Kivelson. Subsurface oceans on Europa and Callisto: Constraints from Galileo magnetometer observations. *Icarus*, 147(2):329–347, 2000. doi: 10.1006/icar.2000.6456.

M. Y. Zolotov. Oceanic composition on Europa: Constraints from mineral solubilities. In *Lunar and Planetary Science Conference*, page 2349, 2008.

M. Y. Zolotov and J. S. Kargel. On the chemical composition of Europa's icy shell, ocean, and underlying rocks. In R. T. Pappalardo, W. B. McKinnon, and K. Khurana, editors, *Europa*, pages 431–456. University of Arizona Press, Tucson, 2009. ISBN 978-0816528448.

M. Y. Zolotov and E. L. Shock. Composition and stability of salts on the surface of Europa and their oceanic origin. *Journal of Geophysical Research: Planets*, 106(E12):32815–32827, 2001.

VITA

Marshall John "Moosh" Styczinski was born in Dublin, California. In 2006, he graduated from Portola Jr/Sr High School in the Sierra Nevada mountains. While an undergraduate at the University of California, Davis, Marshall completed an Honors Thesis project focused on the restoration of an x-ray photoelectron spectrometer used for characterizing material layer properties. Marshall was ultimately awarded the "with Highest Honors" distinction for his Bachelor of Science in Physics.

For two years following completion of his B.S. in Physics, Marshall worked in laboratories at UC Davis. He studied radiation degradation of permanent magnets, repaired an evaporative deposition system, and created a scale mockup of the Large Underground Xenon detector to experiment with acoustic detection of bubbles within cryogenic fluids. During this time, Marshall also worked in Chooz, France to fill the Double Chooz experiment's "Far" neutrino detector with scintillator fluids.

In 2012, Marshall joined the University of Washington Physics doctoral program. In 2014, he joined the Physics Education Group (UWPEG), and studied ways to improve student understanding of electromagnetics concepts, especially with educational simulations. Throughout Marshall's first 6 years at University of Washington, he was a Teaching Assistant (TA) for a wide variety of courses. Marshall taught introductory physics most of all, including as a head TA—training the other TAs, writing exams, and helping to manage the large courses.

Also in 2014, Marshall joined the UW Astrobiology Program. After 3 years, Marshall made the difficult decision to leave UWPEG to pursue more astrobiology-relevant research. In 2017, he began working with Professor Erika Harnett and met Dr. Steven Vance of the Jet Propulsion Laboratory (JPL). The next year, Marshall joined Dr. Vance for an internship at JPL, beginning a longstanding and fruitful collaboration. In 2018, Marshall was also awarded a NASA Earth and Space Science Fellowship to study magnetic effects of possible asymmetry within Europa. In 2021, Marshall earned his Doctor of Philosophy in Physics.